Fluide et sismicité: de l'observation sismologique aux processus mécaniques

Louis De Barros

UNIVERSITE DE LA COTE D'AZUR

Ecole Doctorale Sciences Fondamentales et Appliquées

DS3 : Sciences de la Terre et de l'Univers, Espace

Habilitation à Diriger les Recherches

Fluide et sismicité :

De l'observation sismologique aux processus mécaniques

Louis De Barros

Geoazur (UMR 7329), Sophia-Antipolis

Soutenue le 25 Juin 2020 au laboratoire Geoazur devant le jury composé de :

Jean-Paul Ampuero	DR IRD (Géoazur, Université Côte d'Azur)	Examinateur
Françoise Courboulex	DR CNRS (Géoazur, Université Côte d'Azur)	Examinateur
Jean-Robert Grasso	Physicien (ISTerre, Université Grenoble Alpes)	Examinateur
Philippe Jousset	Chercheur (GFZ Postdam)	Rapporteur
Hélène Lyon-Caen	DR CNRS (Ecole Normale Supérieure)	Rapporteur
David Marsan	Professeur (ISTerre, Université Savoie Mont Blanc)	Rapporteur

CONTENU

RESUME

Il est maintenant communément admis que les perturbations de fluide dans la croûte terrestre génèrent des tremblements de terre. Par exemple, des essaims sismiques accompagnent les montées de magmas ou les activités anthropiques d'exploitations de réservoirs. La compréhension du lien entre les fluides et les séismes reste imparfaite, même si elle est indispensable pour améliorer la surveillance des processus dynamiques en profondeur, et améliorer l'anticipation des risques.

Plusieurs observations permettent d'affiner ce lien en renseignant sur les processus fluide/solide en profondeur. Il est en effet possible d'utiliser des techniques d'imagerie spécifique pour localiser les fluides en profondeur. Les distributions spatio-temporelle des essaims sismiques ou les formes d'ondes « non conventionnelles » renseignent sur les processus de diffusions de pression fluide, ou sur la présence de glissements lents. Enfin, les observations multi-paramètres, possibles lors d'expériences contrôlées de sismicité induite, permettent de contraindre les couplages hydro-mécaniques et sismologiques.

Ces différentes observations, multi-échelles et multi-objets, m'ont permis d'apporter de nouvelles contraintes sur le lien de causalité existant entre fluide et séismes. En particulier, j'ai montré que ce lien n'est pas forcément direct. Les fluides semblent en effet principalement induire des glissements lents et déformations asismiques, qui déclenchent à leur tour des séismes par transfert de contraintes.

Mots clefs :

Sismicité induite ; volcans, réservoirs, zones tectoniquement actives ; expériences in-situ ; essaim sismique ; sismicité « non conventionnelle » ; déformations lentes et asismiques ; couplage fluide/déformation/séismes

Merci à tous les enseignants et collègues qui ont su me transmettre leur passion et qui me donnent quotidiennement le gout pour la recherche scientifique.

PREAMBULE

Ce mémoire d'habilitation à diriger des recherches dresse un bilan des activités de recherches que j'ai menées depuis l'obtention de mon doctorat soutenu en 2007 à l'Université de Grenoble, (laboratoire ISTerre, ex. LGIT). Les travaux présentés ici ont été obtenus lors de 4 années de post-doctorat à l'University College Dublin (équipe dirigée par C. Bean), et à l'Université de la Côte d'Azur depuis mon recrutement comme maître de conférences en 2012 au laboratoire Géoazur.

Lors de ces 12 années de recherche, j'ai navigué entre l'imagerie sismique des phases fluides, la caractérisation des signaux volcano-sismologiques, le développement et l'analyse d'expérience de sismicité induite par injection de fluides et la caractérisation des processus à l'origine de la micro-sismicité tectonique. Ces activités, a priori disparates, ont toutes été conduites dans le but de comprendre le rôle des fluides dans les processus dynamiques de la croûte terrestre. Plus précisément, les objectifs sont donc 1) de comprendre comment les fluides influencent les ruptures sismiques et 2) de pouvoir utiliser les signatures sismiques pour suivre les migrations de fluide. Pour cela, je me suis intéressé à différents objets géologiques (réservoirs, volcans, zones tectoniquement actives), et à différentes échelles (expériences in-situ décamétriques jusqu'aux zones tectoniques plurikilométriques).

De tels travaux ne peuvent être réalisés seuls. Comme ces travaux sont à l'interface entre la sismologie et l'hydromécanique, j'ai en particulier développé des collaborations fortes avec des chercheurs en hydromécaniques et avec d'autres sismologues, que ce soit au sein de Géoazur, ou internationalement. Ces échanges se sont fait dans le cadre de différents projets dans lesquels j'ai été impliqué (projets européens : VOLUME, etc ; ANR : SEAFOOD, etc.), ou fortement investi (ANR JCJC HYDROSEIS, PI. F. Cappa; Fluids and Faults, financement Total). Durant ma carrière, j'ai aussi co-encadré 5 doctorants et 1 post-doctorat, et collaboré activement au suivi de 4 autres thèses. J'ai aussi encadré des stages d'étudiants à différents niveaux, de la L3 au M2. Ces travaux m'ont permis de publier 33 articles de rang A, dont 18 en 1er auteur ou derrière un étudiant.

Après une introduction qui replace mes travaux dans leur contexte scientifique et affine le contour des problématiques sur lesquelles j'ai travaillé et l'originalité de mes travaux (Chapitre 1), je présente une synthèse des principaux résultats obtenus (Chapitre 2). Enfin, le dernier chapitre (Chapitre 3) explore quelques pistes de travail, commencées ou envisagées, pour essayer de mieux répondre aux questions que je me pose. Un curriculum vitae détaillé et la liste complète de mes publications sont donnés en annexes de ce document.

1. INTRODUCTION

1.1. Contexte scientifique et sociétal

1.1.1. Fluides dans la croûte terrestre

La croûte terrestre contient de nombreux vides, saturés de différents fluides, de différentes origines :

- Au niveau des volcans, les fluides magmatiques, provenant de l'interface noyau-manteau (points chauds), de la déshydratation de la plaque plongeante en contexte de subduction ou des remontées magmatiques du manteau supérieur, sont stockés dans des chambres magmatiques, avant de générer des éruptions volcaniques en surface. Ces fluides sont complexes, avec une phase magmatique et une phase gazeuse, et vont évoluer chimiquement avec les roches encaissantes tout au long de leur remontée. Ce fluide chaud peut aussi interagir avec l'eau dans les édifices volcaniques, conduisant à des éruptions phréatiques.
- La croûte est aussi faillée et fracturée, permettant le stockage et la circulation d'eau. En particulier, les failles, qui découpent la croûte à toutes les échelles, sont entourées d'une zone endommagée et fracturée, permettant la circulation d'eau météorique vers la profondeur, ou la remontée de fluides (eau, CO_2) profonds.
- La croûte superficielle est, non seulement fracturée et faillée, mais aussi poreuse. Des hydrocarbures, sous forme gazeuse ou liquide peuvent avoir migré de la roche mère dans laquelle ils se sont formés, vers des pièges géologiques. Les hydrocarbures de ces réservoirs sont exploités, de manière conventionnelle ou par fracturation hydraulique pour augmenter leur mobilité. Inversement, ces pièges à hydrocarbures peuvent être utilisés pour du stockage géologique, par exemple de CO_2. Enfin, les sols et roches superficielles sont à l'interface avec l'hydrosphère, et contiennent donc des aquifères, qui sont exploités pour les ressources en eau.

Les fluides saturant les roches de la croûte supérieure correspondent donc à des enjeux sociétaux forts :

- Ce sont en effet des ressources. Les hydrocarbures sont toujours massivement utilisés pour produire de l'énergie, des matériaux (plastiques, bitumes, etc.) ou des composés chimiques. Le développement récent de la géothermie haute enthalpie nécessite aussi la mise en circulation d'eau à grande profondeur. L'accès à l'eau potable passe au moins en partie par l'exploitation des aquifères souterrains, et donc par leur suivi et protection face aux pollutions chimiques et intrusions d'eau saline.
- Ils interviennent dans les risques naturels. Evidemment, la remontée des fluides magmatiques est la cause des éruptions volcaniques. La présence d'eau est aussi un facteur important dans le déclenchement de la rupture sismique et dans les glissements de terrains, par la mise en pression et déstabilisation de fractures et failles.

Que ce soit pour des problèmes de ressources ou de risques naturels, il est donc primordial de connaitre la distribution des fluides en profondeur, mais aussi de caractériser comment s'effectue leur migration. Mais il est aussi indispensable de comprendre comment le fluide interagit avec le milieu solide encaissant, pouvant générer des ruptures des roches.

1.1.2. Fluides et séismes

Sismicité et éruptions volcaniques

Le lien entre fluide et solide est connu depuis longtemps, en particulier dans les zones volcaniques, où déformations de l'édifice volcaniques et séismes sont observés avant l'éruption. Par exemple,

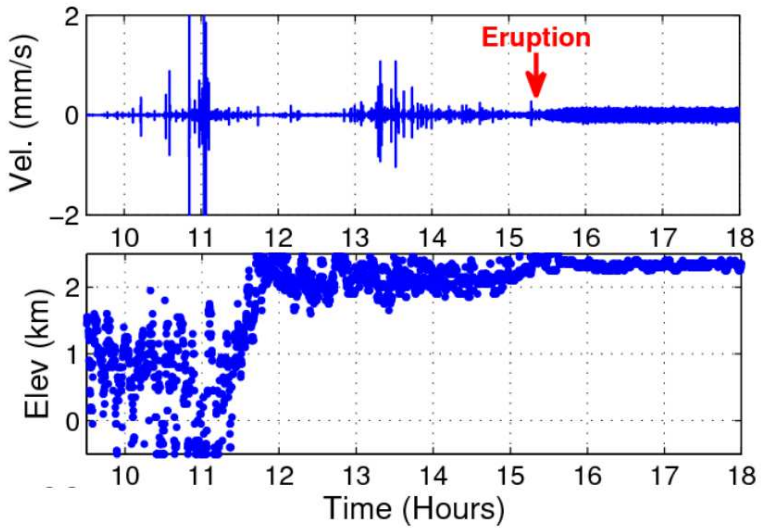

***Figure 1**: Crise sismique précédant l'éruption du 14 octobre 2010 du Piton de la Fournaise (La Réunion), et profondeur de la sismicité (**De Barros et al., 2013a**).*

des séismes furent ressentis par la population de Pompéi avant l'éruption du Vésuve, mais ne furent pas interprétés comme des précurseurs d'une activité volcanique. L'installation de stations sismiques à proximité des volcans a permis très tôt l'observation de ce lien séismes-éruptions et son utilisation dans l'anticipation des éruptions (Stearns, 1925; Tokarev, 1963). Il est maintenant reconnu que la montée de lave s'accompagne de ruptures dans le milieu encaissant, générant une forte sismicité. Celle-ci est un des outils principaux de surveillance et de prévision des éruptions. Par exemple, la Figure 1 présente la sismicité ayant lieu avant l'éruption du 14 octobre 2010 sur le Piton de la Fournaise, ainsi que la migration verticale des hypocentres **(De Barros et al., 2013a**). De nombreux évènements sismiques précèdent une phase de quiescence avant l'éruption. La crise sismique pré-éruptive suit globalement le même schéma sur tous les volcans, même si sa durée peut varier de quelques heures à plusieurs années (McNutt, 2005).

Sismicité induite par les activités anthropiques

Les premières corrélations entre perturbations de la pression fluide et tremblements de terre datent des années 1960, suite aux injections de fluides à plus de 3500 m au Rocky Moutain Arsenal, Colorado (Healy et al., 1968). Les cas avérés de sismicité induite par des activités anthropiques sont maintenant très nombreux (*Figure 2*). Le risque lié à la sismicité induite est vraiment devenue une thématique d'actualité, tant sociétale que scientifique, suite à l'augmentation exponentielle de l'activité sismique dans le centre des Etats-Unis, en particulier dans l'état de Oklahoma. Ces zones, à très faible déformation tectonique, ont vu leur taux de sismicité multiplié par 30 depuis 2008 (Ellsworth, 2013; Keranen et al., 2014). Des séismes de magnitude proche de 6, produisant des dégâts mineurs, ont aussi été enregistrés. Cette augmentation de la sismicité est associée aux injections de très grands volumes d'eaux usées, résidus de l'extraction des gaz par fracturation hydraulique des schistes. En dehors de cette zone, les exemples de sismicité induite liée aux exploitations de réservoirs d'hydrocarbures, sont nombreux (*Figure 2).* Dans la province de l'Alberta (Canada), la fracturation hydraulique elle-même semble avoir généré des séismes de magnitude jusqu'à 3.9, avec plusieurs semaines de retard (Bao and Eaton, 2016; Eyre et al., 2019). De même que les injections d'eau, les injections de gaz, que ce soit pour du stockage d'hydrocarbures gazeux ou pour la séquestration de CO2, peuvent aussi induire des séismes (Verdon and Stork, 2016). Enfin, l'exploitation classique des hydrocarbures peut générer des tremblements de terres. Par exemple, au Pays-Bas, l'exploitation du gaz sur le site de Groningen conduit à un affaissement du réservoir, et à l'occurrence de nombreux séismes (M< 3.5) depuis 1991 (van Thienen-Visser and Breunese, 2015). Ces séismes ont été une source d'inquiétude pour la population, aggravée par une perception erronée par la population et une gestion maladroite de la crise (Sintubin, 2018). En France, une sismicité modérée (Ml<4.2) a été induite par la déplétion du réservoir de gaz de Lacq entre 1970 et 2011 (Bardainne et al., 2008). Cette sismicité a ensuite été réactivée par l'injection de CO2 dans ces anciens réservoirs de gaz en 2011-2014 (Payre et al., 2014).

L'exploitation des champs géothermiques profonds induit aussi des séismes, potentiellement dangereux (Zang et al., 2014). Le site test de Soultz-sous-forêt a été un des premiers sites où la sismicité induite a été observée et caractérisée suite à des stimulations hydrauliques (Bourouis and Bernard, 2007; Cornet et al., 1998; Schmittbuhl et al., 2014). En 2006, la stimulation à plus de 5 km de profondeur près de la ville de Bale a induit des séismes ressentis par la population, ce qui a conduit à l'arrêt du projet de géothermie (Deichmann and Giardini, 2009). Plus récemment (2017), le séisme (M5.5) de Pohang en Corée est suspecté d'avoir été induit par le champ géothermique à proximité (Grigoli et al., 2018). Cet événement est le second séisme le plus fort qu'est connu cette zone tectoniquement calme.

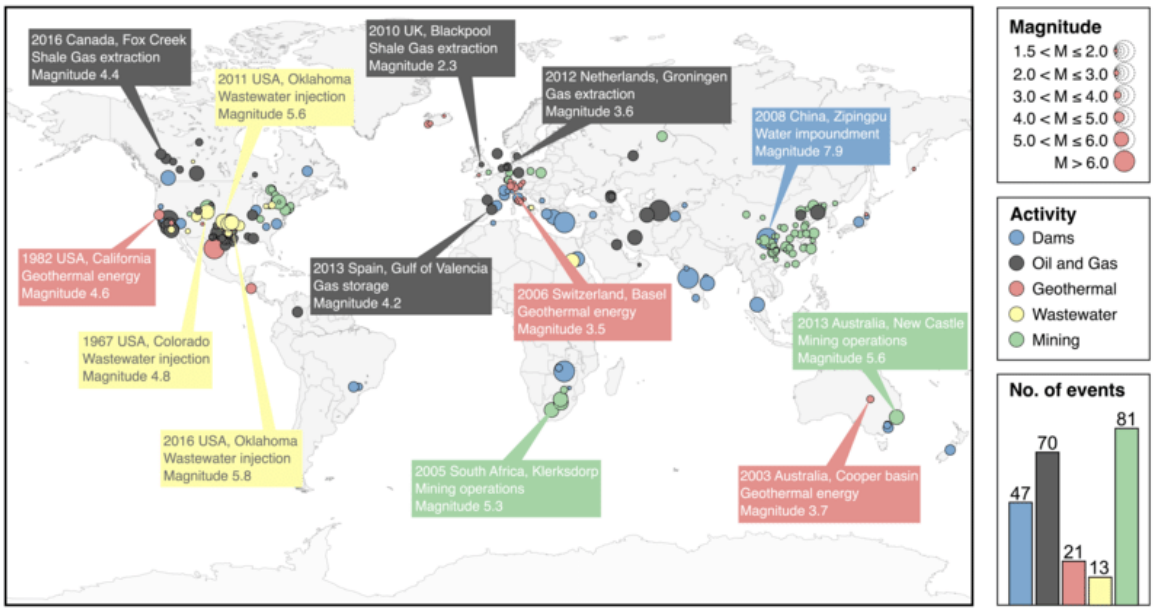

***Figure 2**: Cas principaux de sismicité induite observée dans le monde, et associée à différentes activités anthropiques. La magnitude est celle du plus grand événement. Le nombre d'événements se rapporte aux nombres de sites où de la sismicité induite a été observée (Davies et al., 2013; figure de Grigoli et al., 2017)*

Tous ces cas de sismicité induites sont reliés à des perturbations des fluides en profondeur. Cependant, des modifications de la pression fluide en surface génèrent aussi des séismes (Gupta, 2002). C'est le cas pour la mise en eau de barrages. Par exemple, le remplissage de barrages en France s'est accompagné de séismes de magnitude aussi forte que M4.9 (Grasso et al., 2018). Des tremblements de terre destructeurs ont aussi été générés, tel le séisme de Koyna en Inde (Gupta, 2002). Le lien entre le séisme de Wenchuan (Chine, 2008, M7.9), qui a fait plus de 100 000 morts, et la mise en eau du barrage de Zipingpu est toujours une question ouverte (Ge et al., 2009).

Fluides et séismes tectoniques

Le déclenchement des séismes d'origine tectonique est aussi impacté par la présence des fluides. La corrélation est ici rendue difficile par le manque de connaissance sur les fluides en présence dans les failles à plusieurs kilomètres de profondeur. Les observations sur le rôle des fluides sont donc généralement indirectes. Des imageries sismiques montrent des anomalies de vitesses pouvant être reliées à la présence de fluide autour de la faille ayant généré le séisme de Kobé en 1995 (Zhao et al., 1996). En inversant les mécanismes de la sismicité, Terakawa et al. (2010) montrent que des zones de surpression fluide (possiblement de CO2) ont conduit à la séquence sismique de l'Aquila en 2009 (M6.2). Suite à des chocs principaux, un des mécanismes possibles pour expliquer les répliques est lié au rééquilibrage des pressions de fluide (**De Barros et al., 2019a**; Nur and Booker, 1972).

En plus de leur influence dans les séquences chocs principaux/répliques, les fluides ont un rôle certain dans la genèse des essaims sismiques. Ceux-ci sont caractérisés par une dense concentration de séismes, localisés dans l'espace et le temps, avec le tremblement de terre de plus forte

magnitude au sein de la séquence. Ils peuvent évoluer vers des tremblements de terre de plus fortes magnitudes (par exemple, séisme de l'Aquila, 2009 ; Chiaraluce et al., 2011), ou s'arrêter. Ils accompagnent aussi les éruptions volcaniques, les injections anthropiques de fluide, ou les glissements lents en zone de subduction. Pour maintenir une telle activité sismique pendant des heures, jours, voire semaines, un « moteur » est nécessaire. Ils sont donc attribués à une interaction avec les fluides et/ou les glissements lents. Les fluides ont donc été impliqués pour expliquer les processus de nombreux essaims sismiques (Bräuer et al., 2009), tels la sismicité dans le sud de la Californie (Chen et al., 2012), l'Ubaye (Leclère et al., 2013), le golfe de Corinthe (Duverger et al., 2015), la Bohème (Parotidis et al., 2003), etc… Cependant, les raisons pour lesquelles une zone s'exprime sous formes d'essaims, et non comme une suite choc principal/répliques, restent mal comprises.

Que ce soit dans les volcans, les zones tectoniquement actives ou les réservoirs, les perturbations de pression des fluides induisent des séismes. Les fluides semblent en effet participer à la nucléation de larges tremblements de terres, mais aussi générer des essaims de séismes de magnitude modéré.

1.1.3. Fluides et mécanismes de ruptures

Fluide et rupture

Le rôle de la pression de fluide P dans une rupture cisaillante est décrit de manière simple par le critère de Mohr-Coulomb : $\tau = (\sigma - P)\tan\varphi$. Il y a donc glissement lorsque la contrainte cisaillante τ devient égale au produit de la contrainte normale effective (contrainte normale σ réduite de la pression P) par un coefficient de friction $\mu=\tan\varphi$. La rupture peut donc être atteinte de deux manières (*Figure 3*, Ellsworth, 2013) : soit en augmentant la pression dans la faille, ce qui diminue la contrainte normale effective, soit par une perturbation de contraintes, qui peut être due à une déformation (poro-thermo-)élastique ou à une modification des charges. En plus de ces mécanismes, il a récemment été montré que les déformations asismiques, et les transferts de contraintes associés, sont un facteur efficace dans le déclenchement de séismes (Cappa et al., 2019; **De Barros et al., 2018**; Guglielmi et al., 2015b). Le lien entre les fluides et la sismicité induite ne peut donc pas se résumer à l'influence directe de la pression sur la contrainte effective.

En fonction de la perturbation de pression, différents modes de rupture peuvent être observés (Cornet, 2016) :

- Ruptures ponctuelles dans un massif poro-élastique : à faible pression, le fluide va diffuser et induire des ruptures de zones localisées pour lesquelles le critère de rupture est atteint par diminution de la contrainte effective ou augmentation de la contrainte cisaillante.
- Réactivation de failles en cisaillement : la pression de fluide va permettre le glissement cisaillant sur de grandes surfaces de failles préexistantes.
- Réactivation de failles en mode I : à plus forte pression, la contrainte effective mineure peut devenir négative. La réactivation des failles va donc se faire avec une composante normale,

plus ou moins forte.

- Hydro-fracturation : à très forte pression, et en l'absence d'hétérogénéités géologiques, la pression peut déclencher une rupture de la matrice rocheuse, avec une composante normale dominante.

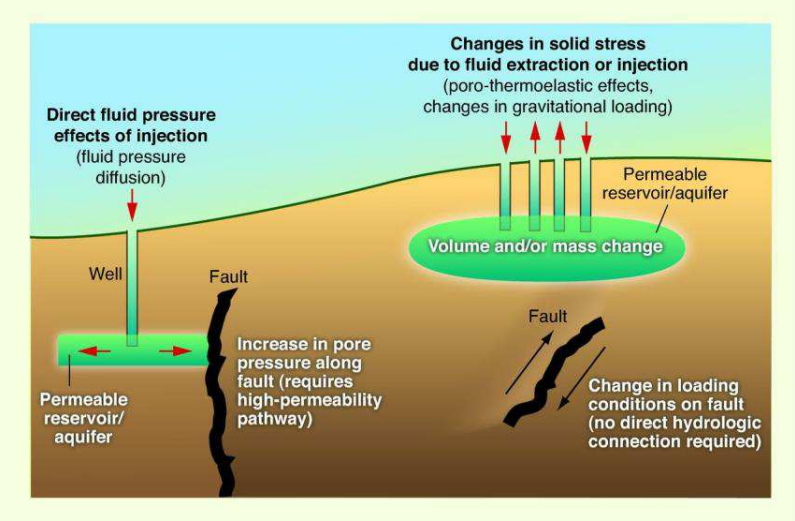

***Figure 3**: Schéma des mécanismes par lesquels les fluides peuvent induire des séismes, c'est-à-dire par augmentation directe de la pression, ou par modification des conditions de chargement de la faille (figure de Ellsworth, 2013) .*

Les ruptures mécaniques induites par augmentation de la pression fluide ou par perturbation de l'état de contraintes peuvent être décrites par la théorie de Mohr-Coulomb. Cependant, les différents modes de rupture induite par les fluides peuvent être sismiques ou non, c'est-à-dire qu'ils peuvent ou non émettre des ondes détectables par des capteurs sismologiques.

Fluide et déformation asismique :

La loi de Mohr-Coulomb permet donc de décrire l'occurrence des ruptures, mais ne renseigne pas sur son caractère sismique. Le glissement peut en effet se produire à une vitesse trop faible pour générer des ondes sismiques. Une telle déformation asismique est caractéristique de la déformation dans les parties ductiles de la croûte. Elle est maintenant vue comme non négligeable, même dans la partie sismogène de la croûte. En effet, le développement des réseaux GPS a permis de montrer que seul un faible pourcentage de la déformation était sismique dans les zones de subduction (Liu and Rice, 2007; Perfettini et al., 2010). Cette déformation peut s'exprimer par un mouvement lent et continu ou par des épisodes de glissements lents (Schwartz and Rokosky, 2007), séparant des périodes où l'interface est bloquée. Alors que certaines zones de la faille de San-Andreas glissent lors de tremblements de terre de magnitude 6 et plus, d'autres zones, non couplées, glissent asismiquement (Linde et al., 1996). Dans les volcans, la majorité de la déformation est aussi asismique, phénomène accentué par les hautes températures en jeu. En particulier, la phase finale

de propagation du magma vers la surface, accompagnée de très large déformation de l'édifice volcanique, n'exprime que très peu de sismicité **(De Barros et al., 2013a**; McNutt, 2005). De grands glissements sur des failles peuvent ainsi se produire sans émissions d'ondes (Cervelli et al., 2002).

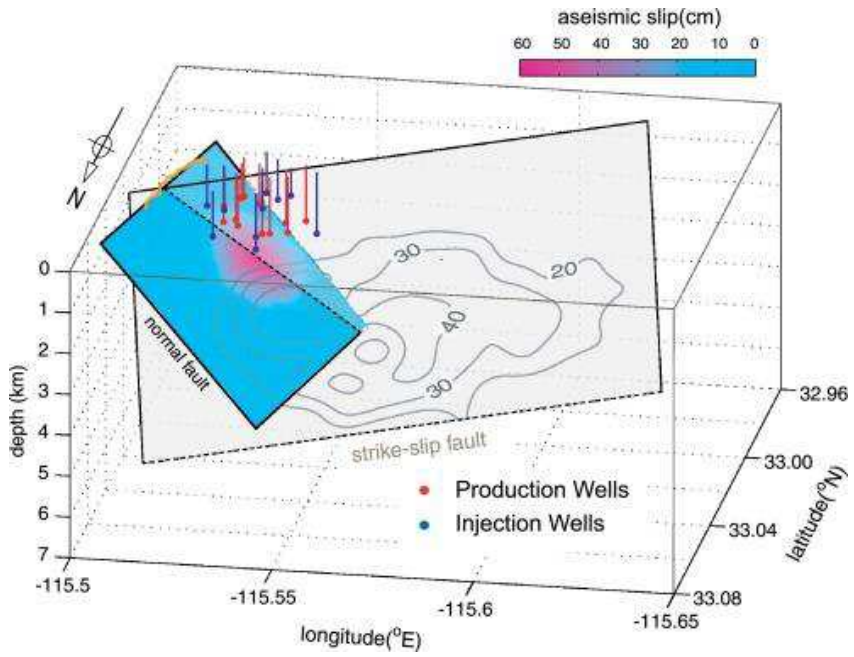

***Figure 4**: Le champ géothermique de Brawley (Californie), a induit des séismes en décrochement de magnitude 5+ (contours de glissement) sur une faille en profondeur. Ces séismes ont été déclenchés par le glissement asismique d'une faille normale, qui a été directement induit par les injections (Wei et al, 2015).*

De nombreux cas d'injection de fluides ont été associés à une déformation principalement asismique (Grasso and Wittlinger, 1990; Schmittbuhl et al., 2014; Scotti and Cornet, 1994,…). Par exemple, la comparaison des déformations mesurées en forage et de la sismicité induite lors d'une injection à Soultz-Sous-Forêts démontre la prédominance des déformations asismiques (Cornet et al., 1998). L'exploitation géothermique de Brawley (Californie) a généré des séismes de magnitude 5+, mais à 5 kms sous le réservoir. Les déformations de surface ont permis de montrer que cette sismicité a été générée en réponse à un large glissement asismique, directement induit par les perturbations des fluides (*Figure 4*, Wei et al., 2015). Des analogies dans la distribution de la sismicité induite avec les glissements lents de la faille de San Andreas, et les bilans énergétiques, suggèrent une large composante asismique lors des injections à Cotton Valley (Rutledge et al., 2004). Enfin, les expériences in-situ de réactivation de failles à une échelle décamétrique ont montré que la déformation était majoritairement asismique, en particulier au voisinage du point d'injection **(De Barros et al., 2018**; Guglielmi et al., 2015b).

Pour prendre en compte le comportement sismique ou asismique de la rupture, il est nécessaire de prendre en compte la dépendance de la friction au glissement (slip weakening/strenghtening) ou à la vitesse de glissement (rate-and-state, Dieterich, 1992). La variation du coefficient de friction est

ensuite introduite dans la loi de Mohr-Coulomb. La pression fluide a deux effets notables dans ces lois de friction : 1) la variation des paramètres frictionnels et 2) l'augmentation de la taille de nucléation avec la pression (Scuderi and Collettini, 2016). Ces deux effets expliquent pourquoi la déformation est principalement asismique au niveau de l'injection (*Figure 5*, Cappa et al., 2019).

Une part importante de la déformation est donc asismique. La présence de cette composante asismique complexifie notre compréhension de la rupture, principalement car celle-ci n'est pas visible dans les données sismiques.

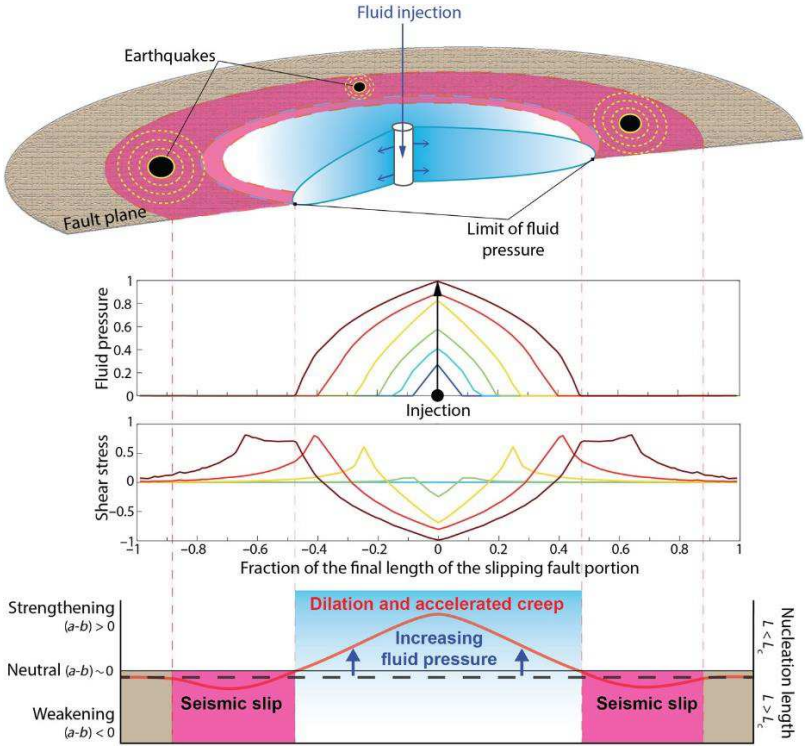

***Figure 5** : Schéma conceptuel de l'évolution d'une faille soumise à une injection d'eau, d'après des observations expérimentales et des modélisations numériques (Cappa et al., 2019). La zone pressurisée près de l'injection montre un glissement asismique, associé à un comportement neutre ou stable dans la loi de « rate and state ». La chute de contrainte cisaillante dans cette zone génère un transfert de contraintes sur ses bords, qui présentent un comportement fragile, et donc sismique.*

Couplage hydro-mécanique : lien fluide-séisme-déformation

La relation entre fluide et déformation n'est pas unilatérale, un couplage existe entre eux. Le fluide induit des ruptures, mais les ruptures modifient la pression et la circulation du fluide. Par exemple, un glissement peut s'accompagner d'une phase de dilatance ou d'une composante normale. Cette variation de volume va faire diminuer la pression dans la faille, et donc peut arrêter la rupture. Ce phénomène de « dilatant-strenghtening » conduit donc à des glissements lents, contraints par la vitesse de propagation des fluides dans la faille (Segall et al., 2010).

La perméabilité d'une faille en glissement, sismique ou asismique, est aussi considérablement augmentée (Crawford et al., 2008), ce qui peut conduire à modifier les chemins de circulations de fluide, et à des rééquilibrages de pression. Ainsi, la faille, peu perméable avant glissement, va se conduire comme un drain lors du glissement, ce qui modifie très fortement la distribution de pression le long de la faille (« Fault-valve behaviour », Sibson, 1990).

Enfin, toute déformation, qu'elle soit élastique, sismique ou asismique, va induire un transfert de contraintes dans le milieu environnant. Les transferts de contraintes liés aux déformations poro-élastiques sont de faibles amplitudes, mais peuvent être suffisantes pour générer de la sismicité sur des failles déjà proches de la rupture. Ainsi, les perturbations de pression dans les failles sismogènes de l'Oklahoma étant très faibles, une part de la sismicité de cette zone est expliquée par des perturbations poro-élastiques des contraintes sur des failles proches de la rupture (Chang and Segall, 2016; Goebel et al., 2017).

Le phénomène de transfert de contraintes est bien connu pour les séismes, car il est responsable des répliques (Stein, 1999), pouvant générer des tremblements de terre en cascade (Marsan and Lengliné, 2008). En plus d'un déclenchement direct de la sismicité, ces transferts de contraintes peuvent générer des glissements lents (Rolandone et al., 2018) et des modifications de la pression et de la circulation des fluides (**De Barros et al., 2019a**; Miller et al., 2004). Ces phénomènes peuvent générer à leur tour des évènements sismiques. Cependant, les modifications de contraintes reliées aux déformations lentes et asismiques sont bien moins connues, entre autres car les déformations asismiques sont difficilement observables. Les modélisations numériques hydromécaniques montrent cependant une augmentation de la contrainte cisaillante au front du glissement asismique, qui peut induire des séismes dans la zone non pressurisée autour de l'injection (*Figure 5*, Cappa et al., 2019). Cette interprétation a été développée dans le cas du site géothermal de Brawley (*Figure 4*, Wei et al., 2015) et lors d'expériences contrôlées d'injection (**De Barros et al., 2018**).

Les perturbations de contraintes peuvent aussi être transitoire. Ainsi, le passage des ondes sismiques peut modifier les contraintes s'exerçant sur une faille, et/ou mettre en pression les fluides la saturant. Si la faille est dans un état critique, elle peut alors glisser. Bien que l'amplitude de ces perturbations reste faible, les observations de tels déclenchements dynamiques sont nombreuses (**De Barros et al., 2017**; Hill and Prejean, 2015).

Ces différents exemples montrent qu'il existe un couplage très fort entre pression fluide, déformation et séismes (*Figure 6*). L'interaction entre les séismes et les fluides est un jeu à 3 acteurs, où déformation lente, séismes et fluides interfèrent de manière complexe au cours du temps, à travers des transferts de contraintes et des perturbations des pressions. Dans la mesure du possible, il est donc nécessaire d'étudier de manière globale rupture sismique et processus hydromécaniques.

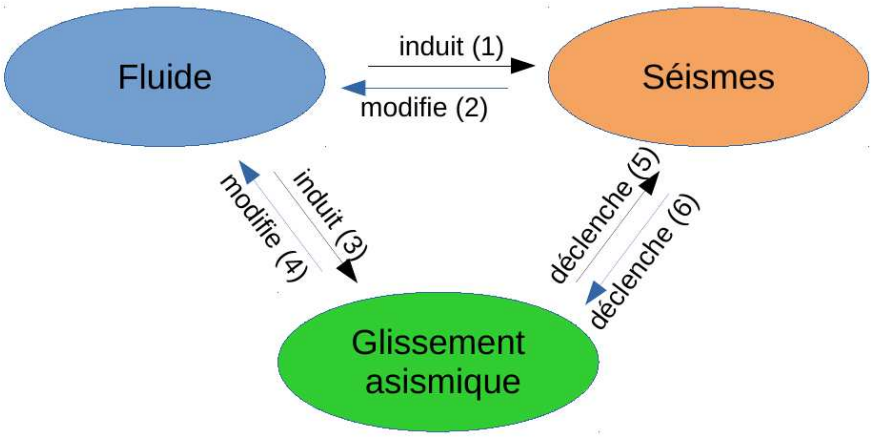

***Figure 6**: Schéma simplifié des interactions existant entre les fluides, les séismes et les glissements asismiques. Les fluides induisent des séismes et des glissements asismiques par diminution des contraintes effectives et/ou perturbations poro-élastiques du champ de contraintes (1,3). En retour, ces glissements vont modifier la circulation et la pression des fluides (2,4). Enfin, par transfert de contraintes, les glissements asismiques déclenchent des séismes, et inversement (5,6).*

1.1.4. Quelles observations ?

Pour mieux comprendre ces interactions complexes, il est souhaitable d'avoir des mesures à la fois des fluides, de la déformation et des émissions sismiques. De telles observations existent en laboratoire. Par exemple, Schubnel et al. (2007) ont enregistré les émissions acoustiques lors de ruptures induites par augmentation de la pression fluide sur des échantillons de grès dans une presse triaxiale. Cependant, la taille des échantillons et leur préparation font que les matériaux utilisés dans de telles expériences n'ont pas toute la complexité structurale des formations géologiques. Dans les environnements naturels, les observations multi-paramètres sont rares et souvent incomplètes. Dans les réservoirs, seule une information parcellaire est disponible sur les fluides, avec la pression et le débit mesurés en tête de puits avec un échantillonnage temporel lâche. Peu d'informations existent sur la déformation, car les mesures en puits sont rares et les déformations en surface souvent très faibles. Les localisations de failles et l'état de contraintes sont aussi imparfaitement connus. Dans les zones tectoniques, seules les larges déformations sont observées de la surface. Le GPS et l'INSAR renseignent sur les mécanismes des tremblements de terre de magnitude 6+, mais ne peuvent résoudre les déformations associées à de plus faibles magnitudes ou à des essaims sismiques. De plus, la géométrie des failles portant les séismes de magnitude faible à modérée est généralement inconnue. La présence de fluide dans les failles n'est que supposée, avec des observations indirectes. Sur les volcans actifs, des fluides complexes (eau, gaz et magma) sont présents, mais leur localisation n'est qu'imparfaitement connue. La forte déformation de l'édifice avant la rupture est mesurable, mais elle moyenne une complexité de processus (déformation poro-élastique, glissement gravitaire, etc.) dans un milieu géologique

extrêmement hétérogène. En résumé, quel que soit l'objet géologique considéré, les observations que nous pouvons avoir sont parcellaires, incomplètes et en général acquises à la surface, c'est-à-dire loin des processus.

Pour pouvoir appréhender la complexité de la rupture sismique, il y a donc une **nécessité d'observations multi-paramètres (fluide, déformation, sismicité et éléments structuraux de la géologie), à très proche distance, et avec une bonne résolution temporelle.** Dans cette optique, des développements instrumentaux peuvent être nécessaires, pour renforcer les observations possibles. Par exemple, les récents développements techniques d'interrogations de fibres optiques permettent d'envisager les mesures conjointes de déformation et de sismicité dans des environnements difficiles tels les fonds marins (**Sladen et al., 2019**) ou les volcans actifs (Jousset et al., 2018). Le récent développement d'une sonde de forage, basée sur un réseau de fibres optiques, permet de mesurer les déformations en forages, couplées à des mesures de pression et de débit d'injection (SIMFIP, Guglielmi et al., 2014). Cette sonde a ainsi permis de reproduire les processus naturels de sismicité induite lors d'expériences in-situ, à une échelle intermédiaire (mètres à dizaine de mètres). Il est alors possible d'installer un réseau de suivi dense, à proximité de perturbations (injections de fluide) contrôlées.

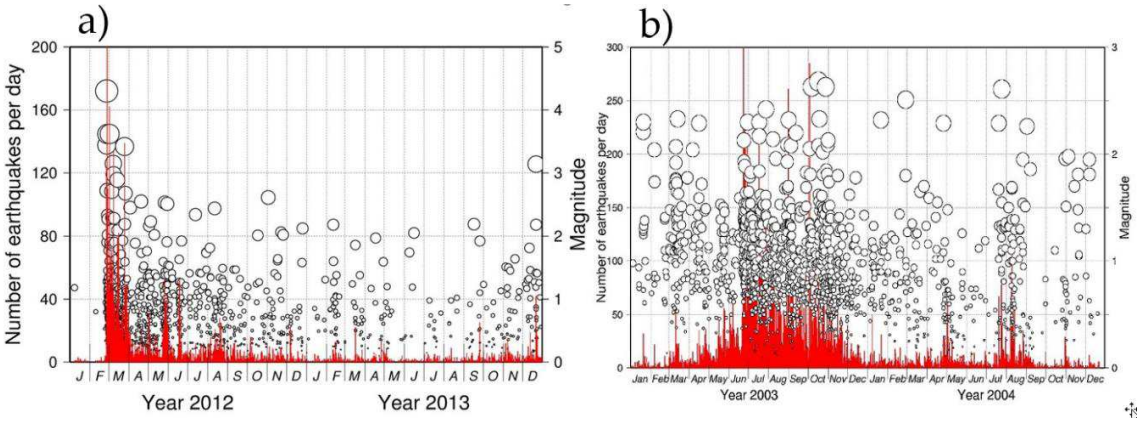

Figure 7: Distribution temporelle des événements sismiques enregistrés dans la région de l'Ubaye. a) Séismes de magnitude 4.3 et ses répliques (Thouvenot et al., 2016) ; b) essaim sismique de Jausiers en 2003-2004 (Jenatton et al., 2007).

Pour contrebalancer ce manque d'observations sur les fluides à proximité des sources sismiques, des observations sismologiques indirectes peuvent aussi être utilisées. L'interaction fluide-déformation-séismes peut ainsi se voir dans la **distribution spatiale, temporelle et de magnitude de la sismicité.** Les séquences sismiques s'organisent généralement autour d'un séisme principal, mais peuvent au contraire apparaître comme des essaims sismiques (*Figure 7)*. Cette différence d'organisation suggère des forçages et processus différents au niveau de la source. La migration de la sismicité indique soit des diffusions de fluide soit des glissements lents. Ainsi, l'augmentation de la distance des séismes au point d'injection avec le temps est classiquement reliée à la diffusion de la pression fluide (Shapiro et al., 1997a). Un tel modèle ne prend cependant pas en compte les déformations lentes et les transferts de contraintes associés, et est donc perfectible. Des anomalies

dans les distributions de magnitude (loi de Gutemberg-Richter), dans le nombre de répliques (loi d'Omori, Utsu and Ogata, 1995), dans les chutes de contraintes (Lengliné et al., 2014), dans les distributions de temps et de distance inter-évènements (Hainzl and Ogata, 2005; Schoenball et al., 2015) ou dans la dispersion des mécanismes des sources (Leclère et al., 2013) suggèrent la présence de processus complexes au niveau des sources des séismes. L'interprétation de ces anomalies reste cependant ambiguë : les fluides sont souvent mis en avant, mais des glissements lents (ou autres processus ?) peuvent aussi exister. Et de manière générale, il n'y a pas de vérification directe possible, rendant ces interprétations toujours délicates.

Enfin, des **événements sismiques (sismicité non conventionnelle), avec des formes d'ondes très différentes de celles des tremblements de terre** (*Figure 8*), sont des marqueurs de processus différents de la rupture rapide et cisaillante à l'origine des séismes. Depuis plusieurs décennies, les trémors (Aki et al., 1977), événements longues et très longues périodes (Chouet, 1996) sont observés sur les volcans actifs, et servent à anticiper les éruptions. Ils sont classiquement interprétés comme la résonance de cavités remplies de fluides (gaz, lave ou eau). Cependant, des processus alternatifs, plus compatibles avec la sismologie non-volcanique, ont été proposés (glissement lents, **Bean et al., 2014**; ruptures répétitives, Dmitrieva et al., 2013). Les mécanismes de ces signatures sont donc toujours en débat. Des signatures sismiques non conventionnelles sont aussi observées dans des environnements non volcaniques. Des trémors et des signatures longues périodes ont été observés lors de glissements lents dans les zones de subduction ou sur certaines failles (Obara et al., 2004; Shelly et al., 2007). Pourquoi certaines zones de subduction glissent sous forme de tremblements de terre, de glissement lent périodique (avec signature sismique ou non), ou de déformation continue est toujours une question ouverte. En particulier, par analogie avec les signatures volcaniques, le rôle des fluides dans la genèse de cette sismicité est toujours débattu (Shapiro et al., 2018). Des signatures non conventionnelles, souvent appelées LPLD (« Long Period Long Duration ») ont aussi été observés lors des exploitations de réservoirs, en particulier lors des fracturations hydrauliques dans des argilites (Das and Zoback, 2013; Kumar et al., 2017a). Initialement attribués à des glissements lents, l'existence de telles signatures a cependant été mise en doute (Zecevic et al., 2016a). De manière générale, la difficulté de détection et d'analyse de ses signatures font que leurs mécanismes restent débattus, pouvant être reliés aux fluides et/ou aux déformations lentes.

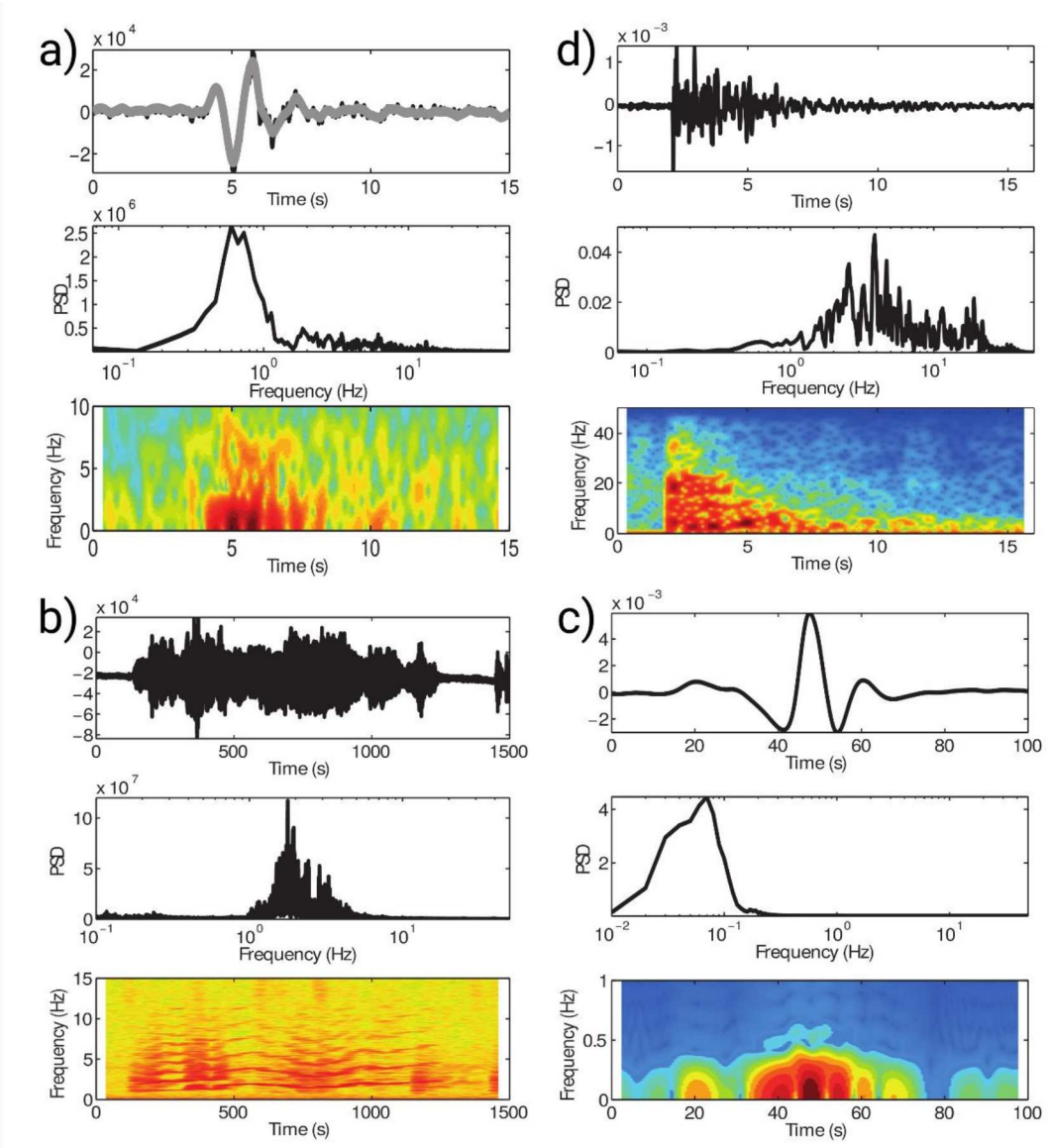

Figure 8: *Exemples de différentes formes d'ondes, avec leur spectre et spectrogramme enregistrées dans des environnements volcaniques. a) Evènement à basses fréquences (Long Period, LP), Etna* ***(De Barros et al., 2009)*** *; b) Evènement Volcano-Tectonique (VT), Piton de la Fournaise,* ***(De Barros et al., 2013a)*** *; c) Trémor, Arenal* ***(Davi et al., 2012)*** *; d)Evènement à très basses fréquences (Very Long Période, VLP), Etna, (Zuccarello et al., 2013).*

1.2. Parcours scientifique

1.2.1. Problématique scientifique

Mes activités de recherche depuis ma thèse portent donc sur la **signature sismique des processus d'interaction entre fluides et solides** dans la subsurface terrestre. Je m'intéresse en particulier à l'influence des fluides dans les processus de nucléation des séismes. Inversement, l'objectif est aussi l'utilisation de micro-sismicité induite et son évolution spatio-temporelle, pour améliorer le suivi des fluides en profondeur, et ainsi optimiser 1) l'anticipation des risques sismique et volcanique et 2) l'accessibilité aux ressources. Pour améliorer notre connaissance du rôle des fluides dans la genèse des séismes, de nombreuses questions restent ouvertes, et nécessitent de nouveaux éclairages :

- Où se situent les fluides dans des milieux fortement hétérogènes ?
- Comment les fluides participent aux déformations ? Quels modes de ruptures induisent-ils (sismiques ou asismiques) ?
- Quel est le lien entre les fluides et la taille des séismes ?
- Pourquoi observe-t-on des essaims sismiques et/ou de larges événements associés aux fluides ?
- Quelles observations peuvent nous renseigner sur le rôle du fluide ? Formes d'ondes ? distribution spatio-temporelle ? etc.
- Quelles sont les interactions entre fluide et glissement lent ?
- etc.

En résumé, le fil conducteur qui motive ma recherche scientifique est : quels sont les mécanismes d'interactions entre les fluides, les déformations lentes et les séismes ? Et pour répondre à cette question, il est aussi intéressant de la prendre à l'envers : quelles sont les observations sismiques (éventuellement de déformation et de fluide) permettant de suivre (et d'anticiper) ces interactions ?

1.2.2. Originalités de mon approche

Mon approche est originale à plusieurs niveaux :

- Premièrement, je me suis intéressé à cette problématique sur **différents objets géologiques** (réservoirs, volcans, zones tectoniques, *Figure 9*). Bien que les conditions de pressions, de température, les types de fluides et les conditions géologiques diffèrent, des similarités existent dans la sismicité et dans les processus la générant. La mise en perspective des observations entre différents objets peut donc permettre d'extraire les éléments communs, et donc génériques, existants dans les processus fluide-solide. Suivant la même idée, l'exploration des réponses de failles à **différentes échelles spatiales** permet d'extraire les comportements les plus généraux possibles. En particulier, j'ai travaillé à une échelle décamétrique lors d'expériences d'injection de fluide. Inhabituelle et originale, cette échelle permet d'avoir une bonne connaissance du milieu géologique et une instrumentation proche tout en restant dans un milieu naturel. Intermédiaire entre le

laboratoire et le réservoir, elle concilie donc les avantages de ces deux échelles, et permet ainsi de relier ces approches.

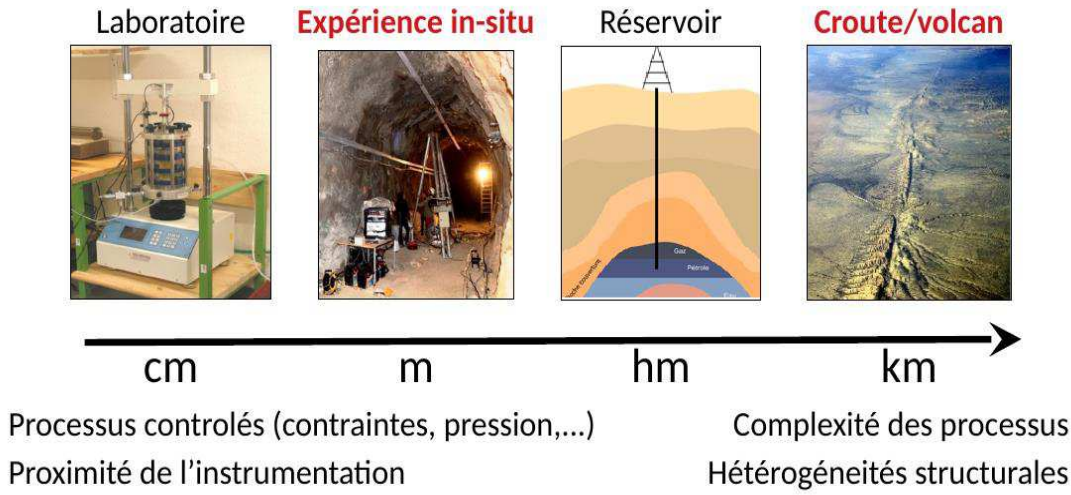

***Figure 9**: Différentes échelles et objets dans lesquels se retrouvent des processus liés aux fluides. Ces différentes échelles et objets ont chacun leur intérêt et inconvénients dans l'appréhension des processus. J'ai travaillé sur les échelles du mètre au kilomètre, principalement sur les expériences in-situ, volcans et zones d'activités tectoniques.*

- Deuxièmement, j'ai travaillé à la fois sur l'**imagerie et les sources sismiques** comme marqueurs des processus fluides-solides. J'ai en effet cherché, par des techniques d'imagerie, à obtenir des informations sur les fluides en profondeur, que ce soit pour des réservoirs poreux ou des chambres magmatiques. Ces dernières années, je me suis cependant plus intéressé à l'analyse et à l'interprétation des sources de la micro-sismicité pour obtenir des informations sur les fluides. Durant mon parcours, j'ai donc balayé différentes approches de la sismologie.

- Pour la compréhension de source des séismes, la sismologie apporte des observations, mais ne permet pas seule de résoudre la question. Il est donc nécessaire de coupler les interprétations sismologiques notamment avec des modèles hydro-mécaniques. Depuis mon recrutement à Géoazur, j'ai donc souhaité travaillé à **l'interface entre sismologie et hydro-mécanique**, en développant notamment des collaborations étroites avec des experts en hydro-mécanique. En particulier, ces collaborations se sont concrétisées par la réalisation des expériences de réactivation de failles, où données hydrauliques, mécaniques, géologiques et sismologiques ont été simultanément acquises et interprétées.

- Enfin, j'ai utilisé **une diversité d'approches méthodologiques**. Mon approche principale se base sur l'analyse des données sismologiques, impliquant traitement du signal et

problèmes inverses. Dans ce but, j'ai dû développer ou adapter des méthodes pour améliorer le traitement de données. J'ai aussi travaillé sur le développement et utilisé des approches numériques. Enfin, j'ai participé à la conception d'expériences originales et innovantes de réactivation de failles par injection de fluide en environnement naturel, notamment par la conception des réseaux instrumentaux de surveillance.

1.2.3. Cadre collaboratif

Pour réaliser ces travaux de recherches, j'ai cherché à développer des collaborations scientifiques avec des experts dans des domaines complémentaires à mes compétences, que ce soit en local ou à l'international. Le travail avec d'autres sismologues est facilité par un vocabulaire, des outils et des questions communes. Pour mettre en commun des points de vue différents sur des questions communes, j'ai aussi développé des collaborations fortes avec des hydro-mécaniciens, spécialistes de la mécanique de la rupture, depuis mon recrutement à Géoazur. Les coauteurs de mes articles scientifiques montrent la diversité des collaborations établies. Parmi ces collaborateurs avec lequel j'ai travaillé depuis ma thèse, je souhaite en particulier mentionner (et remercier):

- Au niveau national : F. Cappa, D. Rivet, A. Deschamps, F. Courboulex, A. Sladen, M. Godano, I. Manighetti, H. Agurto, J.P. Ampuero, C. Larroque, Q. Blétery (Géoazur) ; J. Virieux, A. Helmstetter, S. Garambois, J.-P. Métaxian, J.-R. Grasso, (ISTerre) ; O. Lengliné (EOST); P. Henry (Cerege); G. Daniel (EDF); C. Duverger (CEA); H. Jomard (IRSN); P. Dublanchet (Mines PSL); etc.
- Au niveau international : Y. Guglielmi, M. Schoenball (Berkeley); C. Bean, I. Lokmer G. O'Brien (Dublin), Y. Huang (U. Michigan); L. Zuccarello, G. Saccorroti (INGV); etc.

Ce travail scientifique est aussi passé par l'encadrement d'étudiants, dont 8 étudiants de licence et 6 étudiants de master. J'ai aussi directement encadré 5 doctorants (M. Zecevic, T. Eyre, L. Duboeuf, N. Wynants, M. Baques) et collaboré sur l'encadrement de 4 autres thèses. Enfin, J'ai supervisé 2 ans de postdoctorat de D. Rivet, qui a ensuite été recrutée à Géoazur (CNAP-OCA).

Enfin, une partie de cette activité de recherche s'est faite dans le cadre de projets de recherche. J'ai en effet participé à plusieurs projets, financés par l'Europe (VOLUME, PI C. Bean ; QUEST ITN, PI H. Igel ; REAKT, PI P. Bernard), par l'ANR (SEAFOOD, PI A. Sladen ; EPOST, PI M. Vergnole) ou par le monde industriel (HPMS-Ca, Total, PI Y. Guglielmi ; Tullow Oil, PI C. Bean). En particulier, j'ai été fortement impliqué dans 3 projets :

- **Projet « Fluides et Failles »,** 2012-2017, financement Total (budget : 1.8 M€), PI C. Gout & P. Henry,

Au sein de ce projet, j'ai été responsable du WP4 « Surveillance sismique » avec un budget de 550k€. L'objectif de ce projet est la compréhension de la réponse des failles argileuses à une perturbation de pression de fluide. Des injections d'eau à haute pression ont permis de réactiver différentes zones d'une faille traversant les argilites de la plate-forme expérimentale de Tournemire (IRSN, 12). L'instrumentation de surveillance a permis d'analyser la micro-sismicité induite et de suivre les variations des vitesses sismiques associées au mouvement de faille, en collaboration avec la société

Magnitude (84) et avec des hydro-mécaniciens (CEREGE Marseille, ISTerre Grenoble, ENS Paris). Le travail de Post-doctorat de D. Rivet (2014-2015) a été financé sur ce projet.

- **ANR JCJC HYDROSEIS:** 2014-2019, financement ANR JCJC (budget 310 k€), PI F. Cappa *(https://projets.oca.eu/en/hydroseis-home)*

Au sein de ce projet, j'ai été responsable du WP2 « expérience et analyse des données », budget 160k€. Ces expériences de sismicité induite ont été réalisées en 2015 dans un massif de calcaire fracturé (LSBB, Rustrel). L'instrumentation dense et variée (pression, déformation, sismicité) a permis l'acquisition de données hydromécaniques et sismologiques uniques en leur genre. Ce projet a été mené en collaboration avec le projet HPMS-Ca (PI : Y. Guglielmi), financé par Total SA. Pour le bon déroulement de ce projet, j'ai obtenu une bourse de thèse (L. Duboeuf, financement MESR) et un an de post-doctorat (D. Rivet, 2016-2017, financement UNS).

- **Projets UBAYE :** 2019-2022, financement IRSN-CEA, PI L. De Barros et F. Courboulex, budget 165 k€

L'objectif de ce projet est de comprendre pourquoi cette zone des Alpes du sud a un taux anormalement fort de séismes, avec des alternances chocs principaux et essaims sismiques. En particulier, l'accent sera mis sur la caractérisation des processus et des forçages de la sismicité, en étudiant en détail la sismicité en 2014 pour extrapoler et comparer les résultats à une plus grande échelle temporelle et à d'autres zones similaires. Ce projet finance la thèse de M. Baques.

1.3. Bilan

Mes activités de recherche concernent la compréhension des interactions entre fluide et séismes, en lien avec les déformations asismiques. Cette thématique de recherche a des applications fortes pour l'exploitation des ressources (géothermie, etc.) et pour l'anticipation des risques sismiques et volcaniques.

Durant ma carrière, je me suis intéressé à différentes échelles et à différents objets géologiques, avec pour objectif d'extraire les processus hydromécaniques les plus génériques possibles. Dans la suite de ce manuscrit, je souhaite donc mettre en parallèle les observations et interprétations faites sur les différents objets sur lesquels j'ai travaillé.

Pour répondre à cette problématique, J'ai utilisé des modélisations numériques, réalisé des expériences contrôlées et analysé des signaux sismologiques, mais les observations restent la base de mon approche. En effet, le lien fluide/sismicité/glissement asismique peut s'étudier à partir d'expériences contrôlées, de l'imagerie des hétérogénéités du milieu, par la distribution de la sismicité ou par des signatures sismiques non conventionnelles (*Figure 10*). J'organiserai donc les résultats de mon travail dans la suite de ce manuscrit à partir de ces différentes classes d'observations.

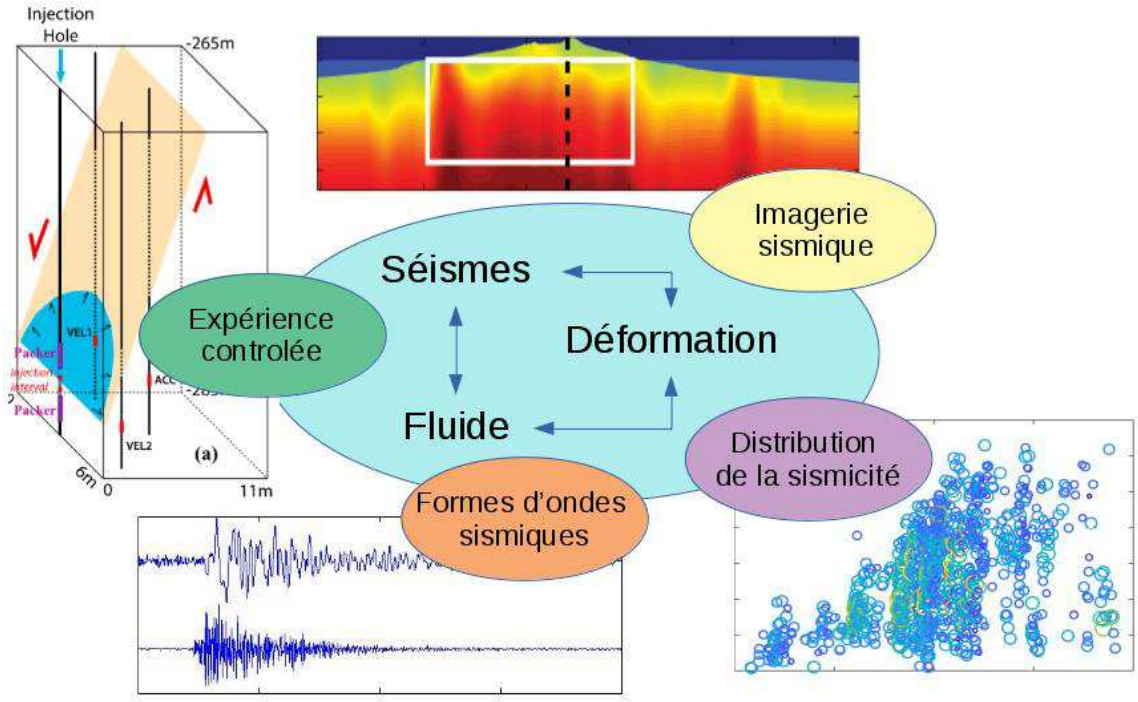

***Figure 10**: Résumé de mon travail de recherche. Ma problématique principalement sur laquelle j'ai travaillé concerne les relations entre fluide, séismes et déformation asismiques. Pour répondre à cette question, j'ai 1) développé des expériences de sismicité induite, 2) cherché à imager les phases fluides/solides des milieux de la subsurface, 3) analysé des formes d'ondes d'évènements non conventionnels et 4) regardé la distribution spatiale, temporelle et d'énergie de la micro-sismicité.*

2. SYNTHESE DES TRAVAUX DE RECHERCHES

Ce chapitre présente une synthèse des principaux résultats scientifiques que j'ai obtenus dans mon parcours. Il est construit autour d'une sélection d'articles, choisis pour leur représentativité de mes travaux et questions.

Il est organisé à partir des observations ayant permis ces travaux (*Figure 10*), en essayant dans la mesure du possible de mettre en parallèle différents objets et échelles. Il est donc constitué de 4 parties. La première se focalise sur les résultats des expériences in-situ pour affiner les couplages sismo-hydro-mécaniques. La deuxième présente quelques résultats obtenus en imagerie, en utilisant des théories poro-élastiques dans les réservoirs et pour les stockages volcaniques. La troisième partie s'intéresse aux formes d'ondes non conventionnelles, principalement sur les volcans, mais aussi dans les réservoirs. Enfin, la dernière partie s'intéresse à l'organisation spatiale et temporelle de la sismicité induite par les fluides.

2.1. Couplage sismo-hydro-mécanique : approches expérimentales

Articles publiés dans ce thème

Wynants-Morel, N., Cappa, F., De Barros, L., Ampuero, J.P., 2020. Stress Perturbation From Aseismic Slip drives The Seismic Front During Fluid Injection In A Permeable Fault. *Journal of Geophysical Research: Solid Earth*, In review

Huang Y., L. De Barros, F. Cappa, 2019. Illuminating the rupturing of microseismic sources in an injection-induced earthquake experiment, *Geophysical Research Letters*, doi: 10.1029/2019GL083856

De Barros, L., F. Cappa, Y. Guglielmi, L. Duboeuf, J.-R. Grasso (2019) Energy of injection-induced seismicity predicted from in-situ experiments, *Scientific Reports*, 10.1038/s41598-019-41306-x

De Barros, L., Guglielmi, Y., Rivet, D., Cappa, F., & Duboeuf, L. (2018). Seismicity and fault aseismic deformation caused by fluid injection in decametric in-situ experiments. *Comptes Rendus Geoscience*, *350*(8), 464-475.

Duboeuf+, L., De Barros, L., Cappa, F., Guglielmi, Y., Deschamps, A., & Seguy, S. (2017). Aseismic motions drive a sparse seismicity during fluid injections into a fractured zone in a carbonate reservoir. Journal of Geophysical Research: Solid Earth, 122(10), 8285-8304.

Rivet D., De Barros L., Guglielmi Y., Cappa F., Castilla R., Henry P.,(2016) Seismic velocity changes associated with aseismic deformations of a fault stimulated by fluid injection, *Geophysical Research Letters,* 43(18), 9563-9572.

De Barros, L., G Daniel, Y Guglielmi, D Rivet, H Caron, X Payre, et al. (2016), Fault structure, stress, or pressure control of the seismicity in shale? Insights from a controlled experiment of fluid-induced fault reactivation, J. Geophys. Res. Solid Earth, 121, 4506–4522, doi:10.1002/2015JB012633.

Derode+, B., Guglielmi, Y., De Barros, L., & Cappa, F. (2015). Seismic responses to fluid pressure perturbations in a slipping fault. *Geophysical Research Letters*, *42*(9), 3197-3203.

Ce chapitre met l'accent sur les couplages existant entre sismicité, fluide et déformation. Il s'appuie donc principalement sur les données des expériences in-situ, pour lesquelles des observations multiparamétriques existent (0). Ces expériences originales m'ont en particulier permis de montrer l'importance prépondérante des comportements asismiques dans les réponses des failles à des perturbations fluides (2.1.2). Je suggère donc un nouveau modèle dans lequel la sismicité est plutôt déclenchée par les transferts de contraintes du glissement asismique que par les fluides. Enfin, les mesures multiparamétriques, et les modélisations numériques permettent de quantifier le lien entre sismicité et réponses hydro-mécaniques (2.1.3).

2.1.1. Expériences de réactivation de failles

Pour améliorer la compréhension de la sismicité induite, depuis mon recrutement à Géoazur, j'ai développé une démarche expérimentale, en travaillant sur des expériences, à une échelle décamétrique, de réactivation de failles naturelles par des injections d'eau sous pression. D'un point de vue sismologique, il s'agit donc d'expériences contrôlées de sismicité induite. Ces expériences ont lieu dans des tunnels, pour accéder à la roche en profondeur et avoir un état de contraintes favorisant un glissement des structures géologiques présélectionnées. Ces structures testées appartiennent à la zone endommagée de failles kilométriques : ce sont des failles secondaires, des fractures, des zones intactes, voire la totalité de la zone de faille dans sa largeur. Des forages permettent d'accéder aux zones de tests, et de 1) caractériser la géologie et les structures, 2) injecter de l'eau, et 3) installer un système de surveillance à très proche distance des injections. Dans le forage d'injection (*Figure 11*), la sonde SIMFIP, développée par Y. Guglielmi (Guglielmi et al., 2014) permet d'isoler une zone dans laquelle l'eau pressurisée est injectée. En plus de la pression et du débit, la déformation à l'injection est mesurée dans les 3 directions, à partir d'un réseau de fibres optiques (réseau de Bragg).

A des distances métriques des zones d'injection, un réseau dense et multiparamétrique de capteurs de surveillance est installé. Il permet des mesures de déformations, de la sismicité et de pressions fluides. En particulier, la sismicité a été enregistré par un grand nombre de capteurs (jusqu'à 35 au LSBB) : géophones (10-500 Hz), accéléromètres (0.01-4 kHz) et capteurs acoustiques (0.1-10 kHz). La mesure conjointe des déformations et de ces capteurs sismiques permet d'avoir une réponse fréquentielle allant du statique aux hautes fréquences (~10 kHz).

Plusieurs expériences, dans différents contextes géologiques, ont été réalisées :

1- Une expérience préliminaire a été réalisée en 2010 au LSBB à Rustrel (Guglielmi et al., 2015a), avant mon arrivée à Géoazur. Cependant, le nombre et le choix des capteurs sismiques n'ont pas permis une analyse fine et certaine de la sismicité (**Derode et al., 2015**). J'ai été fortement impliqué dans la conception, réalisation et analyse d'une deuxième expérience en 2015 (financement ANR Hydroseis, et Total HPMS-Ca), avec un réseau dense de surveillance (**Duboeuf et al., 2017**; **Huang et al., 2019**).

2- Dans les argilites de Tournemire (Plateforme expérimentale de l'IRSN, Aveyron), des injections ont été réalisées dans différentes structures d'une zone de faille, puis dans la totalité de celle-ci, avec une surveillance dense autour (financement Total Fluide et Faille, **De Barros et al., 2016**; Guglielmi et al., 2015b; **Rivet et al., 2016**).

3- Des tests préliminaires de réactivation d'une zone de faille dans les argilites du Mont Terri, avec un nombre limité de capteurs (FS, Guglielmi et al., 2017; **Nussbaum et al., 2017**), a servi de base pour la conception d'une expérience avec une instrumentation dense (FS-B, financement consortium d'entreprises) dont la réalisation est prévue début 2020.

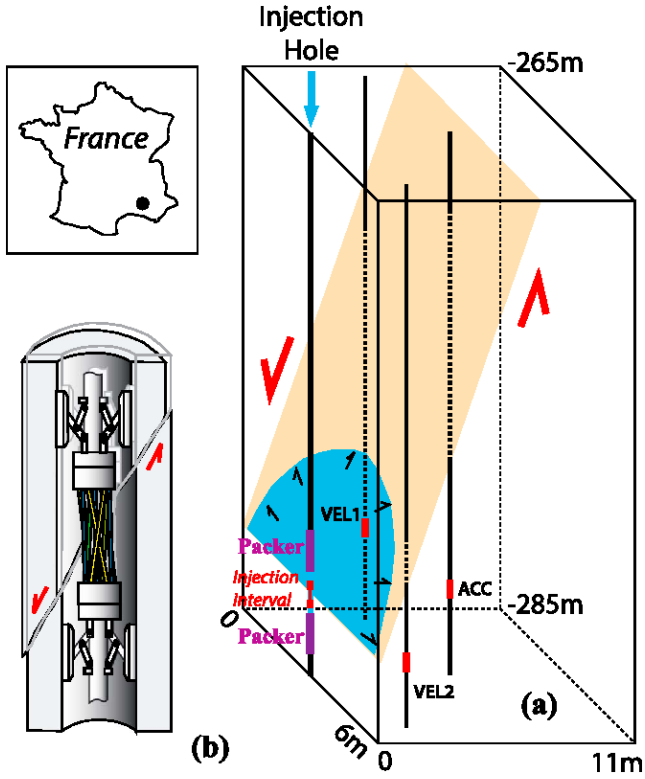

Figure 11 *: Schéma conceptuel des expériences d'injection (a) au LSBB. De la galerie, des forages permettent d'accéder à la zone de faille à tester, pour réaliser les injections de fluide grâce à la sonde SIMFIP (b). Cette sonde permet d'isoler, entre 2 packers, une zone de dans laquelle l'injection est réalisée, et de mesurer la déformation en 3D par un réseau de fibres optiques. Autour de l'injection, d'autres forages permettent d'installer un réseau de surveillance à proximité des injections (Figure de* ***Derode et al., 2015****)*

Ces expériences sont novatrices et uniques pour plusieurs aspects :

1- L'échelle de l'expérience, qui permet de connaitre le contexte géologique et de sélectionner précisément les structures géologiques à tester.

2- La densité et la proximité des observations multiparamétriques, permettant un contrôle des conditions expérimentales et une analyse a posteriori fine.

3- Les collaborations entre géologue, hydro-mécaniciens et sismologues mises en place pour la conception, le déroulement et l'analyse des expériences.

2.1.2. Une déformation principalement asismique

Des évènements sismiques sont enregistrés en réponse aux injections. Cependant, ils sont peu nombreux, avec 34 et 215 signaux enregistrés lors des 5 tests de Tournemire et les 11 tests de Rustrel, respectivement. De plus, ces événements sont caractérisés par une magnitude faible, comprise entre Mw=-4.2 et -3.1, c'est-à-dire intermédiaire entre la sismicité observée dans les réservoirs (~-2.5 < Mw < 0) et celle déclenchée lors d'essais en laboratoire (M<-5). Leur fréquence coin, supérieure à 0.8 kHz, conduit à des tailles de sources < 0.3 m et à des déformations micrométriques. Cependant, dans la majorité des tests, une déformation plastique et irréversible, avec des glissements pouvant atteindre 0.4 mm, est observée à l'injection, et s'étend sur des surfaces décamétriques.

Lors des injections dans les argilites de Tournemire, entre 0 et 12 événements par tests ont été détectés. Ces événements sont localisés loin (entre 3 et 25 mètres) et au sud des injections, et dans le compartiment ouest de la faille. Il n'y a en particulier pas de sismicité autour de l'injection, malgré les déformations plastiques observées. De plus, les mécanismes de ces signaux suggèrent que la majorité des sources sismiques sont sur l'unique famille de structures géologiques qui possède un remplissage de calcite (**De Barros et al., 2016**).

Sur les 11 tests de Rustrel, seuls 6 présentent une déformation résiduelle à l'injection. Ces 6 tests ont induit 215 évènements, distribués de manière très hétérogène entre les tests. Comme à Tournemire, il n'y a pas d'évènements dans la zone autour de l'injection (**Duboeuf et al., 2017**). De plus, la confrontation des localisations et mécanismes de ces signaux avec les éléments géologiques montrent que les sources sismiques ne sont pas localisées sur les structures dans lesquelles le fluide est injecté (Duboeuf, 2018; **Huang et al., 2019**).

Pour ces deux expériences, nous avons fait des bilans d'énergie sismique, de déformation et hydraulique. Moins de 1 % de l'énergie injectée dans le système (énergie hydraulique) est convertie en déformation, et de 10^{-3} à 1 % de l'énergie de déformation est associée à l'émission de signaux sismiques (**De Barros et al., 2019b, 2018**). La déformation est donc principalement asismique. Des ordres de grandeurs similaires ont été trouvés, à la fois lors d'expériences de laboratoire, et lors d'exploitation de réservoirs.

De telles observations pourraient être spécifiques à notre échelle de mesure. En particulier, les faibles chutes de contraintes de cette sismicité pourraient être reliées à la faible envergure des perturbations, dans un milieu où les contraintes initiales sont faibles. En calculant de manière fine les propriétés de sources sur des événements similaires, et en les comparant à des analyses similaires faites sur la sismicité de l'Oklahoma, nous avons montré que la sismicité de ces expériences était conforme aux lois statistiques d'échelle communément admises **(Huang et al., 2019**).

Toutes ces observations nous ont conduits à proposer un nouveau modèle **(De Barros et al., 2018, 2016; Duboeuf et al., 2017**) pour expliquer la sismicité induite. La déformation induite autour de l'injection est asismique. Cette déformation va induire des perturbations de contrainte à sa périphérie. Un séisme aura lieu si ces perturbations, dans l'état de contraintes local, déclenchent un

glissement sur une structure géologique ayant des propriétés de friction adéquate. La sismicité apparait donc comme une conséquence indirecte du fluide, et n'est qu'un acteur secondaire dans la déformation induite par les fluides. Elle est donc contrôlée à la fois par le développement d'un glissement asismique, et par le nombre et propriétés des failles. Ce modèle a ensuite été validé par des expériences en laboratoire et des modélisations numériques (Cappa et al., 2019**; Wynants-Morel et al., submitted**), ainsi que par des observations à l'échelle du réservoir (Eyre et al., 2019).

Article sélectionné

L'article suivant résume les différentes observations sismologiques et les résultats obtenus en les confrontant aux mesures hydro-mécaniques lors des expériences contrôlées de réactivation de failles réalisées à Tournemire, Rustrel et Mont Terri. Il met en particulier l'accent sur l'importance de la déformation asismique, et sur son rôle dans la sismicité induite.

De Barros, L., Guglielmi, Y., Rivet, D., Cappa, F., & Duboeuf, L. (2018). Seismicity and fault aseismic deformation caused by fluid injection in decametric in-situ experiments. *Comptes Rendus Geoscience*, *350*(8), 464-475.

C. R. Geoscience 350 (2018) 464–475

Contents lists available at ScienceDirect

Comptes Rendus Geoscience

www.sciencedirect.com

Internal Geophysics (Seismology)

Seismicity and fault aseismic deformation caused by fluid injection in decametric in-situ experiments

Louis De Barros [a,*], Yves Guglielmi [b], Diane Rivet [a], Frédéric Cappa [a,c], Laure Duboeuf [a]

[a] Université Côte d'Azur, CNRS, Observatoire de la Côte d'Azur, IRD, Géoazur, Sophia Antipolis, 06560 Valbonne, France
[b] Earth and Environmental Science Area, Lawrence Berkeley National Laboratory, Berkeley, CA, USA
[c] Institut universitaire de France, 75231 Paris cedex 05, France

ARTICLE INFO

Article history:
Received 1st June 2018
Accepted after revision 20 June 2018
Available online 1 September 2018

Handled by Vincent Courtillot

Keywords:
Fluid-induced seismicity
In-situ decametric experiments
Aseismic deformation
Stress transfer

ABSTRACT

Seismicity induced by fluid perturbations became an important societal concern since felt earthquakes (M_w up to 6) occurred after anthropogenic activities. In order to mitigate the risks associated with undesired seismicity, as well as to be able to use the micro-seismicity as a probe for in-depth investigation of fluid-driven processes, it is of crucial importance to understand the links between seismicity, fluid pressure and flow. We have developed a series of in-situ, decameter-scale experiments of fault zone reactivation by controlled fluid injection, in order to improve the near-source geophysical and hydromechanical observations. The deployed geophysical monitoring close to the injection allows one to cover the full frequency range of the fault responses from the static deformation to the very high-frequency seismic emissions (up to 4 kHz). Here, we focus on the microseismicity ($M_w \sim -4$ to -3) recorded during two fluid injection experiments in low-permeable shale and highly-fractured limestone formations. In both experiments, the spatio-temporal distribution of the seismic events, the energy balance, and the seismic velocity changes of the fractured medium show that most of the deformation does not actually emit seismic signals. The induced deformation is mainly aseismic. Based on these high-resolution multiparametric observations in the near-field, we therefore proposed a new model for injection-induced seismicity: the seismicity is not directly induced by the increasing fluid pressure, but it is rather triggered by the stress perturbations transferred from the aseismic motion caused by the injection.

1. Introduction

Fluids are present in the upper crust and are usually related to either underground resources (water, oil, and gas) or natural hazards. One major probe to infer where fluids are present and how they are moving at depth is through seismic monitoring and imaging. For instance, in natural hazard assessment, seismicity is indeed used to monitor volcanic eruptions and magma upwelling (De Barros et al., 2013; McNutt, 2005). Anthropogenic activities in reservoir operations such as fluid storage or extraction also induce seismicity. For examples, induced seismicity has been observed in deep geothermal fields

* Corresponding author. Norsar, Gunnar Randers vei 15, PO Box 52, N2027 Kjeller, Norway.
E-mail address: debarros@geoazur.unice.fr (L. De Barros).

https://doi.org/10.1016/j.crte.2018.08.002

(e.g., Lengliné et al., 2017; Wei et al., 2015), during gas storage into depleted reservoir (e.g., Cesca et al., 2014), and induced by CO_2 geological storage (Payre et al., 2014) or gas and hydrocarbon extraction (Albano et al., 2017; Bardainne et al., 2008). In recent years, unconventional shale gas exploitation strongly increases the seismicity rate around the reservoirs, in particular in the central United States and Western Canada (e.g., Bao and Eaton, 2016). While in Oklahoma (USA) the seismicity is mainly induced by the large volume of waste water injected below the shale layers (e.g., Keranen et al., 2014; Schoenball and Ellsworth, 2017), the seismicity in Western Canada might be produced by the fracking process itself (Atkinson et al., 2016). Earthquakes are also observed during and after hydraulic dam fillings (e.g., Gupta et al., 2017). Recent observations at fluid injection sites indicated that induced earthquakes can reach magnitudes up to $M_w \sim 6$, as the Prague and Pawnee earthquakes in Oklahoma (USA). Therefore, seismic hazard due to anthropogenic activity is a major concern and should be mitigated.

It is now well known that fluid pressure induces failures, by decreasing the effective normal stress acting on faults and fractures, which brings the stress state close to the failure envelope. Therefore, when the fluid pressure reaches a failure threshold, an earthquake occurs if sufficient frictional weakening occurs. Within this idea, the seismicity should follow the fluid pressure diffusion, and the measure of the seismicity front could lead to an estimation of the diffusivity of the medium (Shapiro, 2015). Consequently, as the size of the pressurized volume increases with the volume of injected fluids, the length of the faults which get close to failure also increases. Therefore, the maximum magnitude of the induced seismicity should scale with the injected volume (McGarr, 2014).

However, the response of a faulted medium to fluid pressure perturbation can be much more complex. Firstly, the seismicity may occur far and much deeper from the injection, as observed in Oklahoma, where wastewater disposals induced seismicity more than 40 km away from the injection (Schoenball and Ellsworth, 2017; Yeck et al., 2017). The seismicity may also be delayed in time, with the largest event occurring after the shut-in of the injection, as observed at the Basel geothermal field (Mukuhira et al., 2013). Furthermore, only a fraction of the energy injected into the reservoirs is converted to seismicity, as a large part of the deformation may not express seismic signatures (Guglielmi et al., 2015a; Schmittbuhl et al., 2014). For instance, a large aseismic motion was induced by the geothermal field of Brawley in southern California (Wei et al., 2015), which, in turn, triggered two $M \sim 5$ earthquakes. At the laboratory scale, Goodfellow et al. (2015) showed that the seismic energy represents less than $1.25 \cdot 10^{-4}$% of the injection energy during hydraulic fracture tests, highlighting that aseismic deformation represents a large part of rupture mechanisms.

Therefore, the relationships between fluids, earthquakes and aseismic deformation are still under debate, and detailed observations near injection wells are rare, even if the understanding of induced seismicity is crucial for reservoir engineering and hazard mitigation. In order to get well-constrained data close to injection and to investigate the seismological and hydromechanical behavior of the pressurized rock volume, we have developed a series of innovative in-situ experiments at a decameter scale. The main idea is to reactivate well-identified geological structures belonging to mature fault zones in shale and limestone at about 300 m depth. To do so, high-pressure water is directly injected into them. Around the injection zone, a dense network of geophysical sensors allows the simultaneous monitoring of the hydrological, mechanical, and seismological responses of the ruptured faults over a broad frequency band, from static to high frequency (10 kHz). Such experiments therefore benefit from realistic in-situ conditions, well-characterized geological structures, controlled hydraulic perturbations, and a multi-parametric monitoring network at close distance (meter to decameter) from the injection.

In this paper, we first describe the two injection experiments performed in fault zones nested in low- and high-permeability rocks, together with the seismic and hydromechanical responses of the tested geological structures. Importantly, these experiments provide new complete dataset for seismological and hydromechanical characterization and show unequivocally that most of the deformation induced by the fluid injection is aseismic. In the light of the coupled analysis of the data, we therefore suggest that the seismicity is only a secondary response to the fluid pressure, and that seismicity is rather triggered by aseismic deformation caused by the injection.

2. Data and experiments

2.1. Geological context and injection procedure

The experiments aim at injecting high-pressure water (1 to 5 MPa) into selected existing geological features (e.g., fault, fracture, bedding plane), in order to induced slips on the tested structures. Those experiments took place in underground research laboratories, at about 300 m depth. This depth allows a stress state that favors shear motions of the tested structures. From the galleries, boreholes were drilled, to intersect the different geological structures of a mature fault zone. Inside the injection borehole, the SIMFIP probe (Guglielmi et al., 2013) isolated a 2.5-m-long chamber with a straddle packer system. The probe is a new borehole tool that allows water injection together with simultaneous measurements of the fluid pressure and of 3D mechanical displacements. With this probe, water was injected into the geological structures that crosscut the sealed section of the borehole. The injection sequences were design to (1) test the pore-elastic response of the medium with low-pressure injections (e.g., pulse tests of short duration, some minutes) and (2) induce the mechanical shearing and opening of existing fractures with a step-by-step increasing pressure. The pressure increase however stays below the fracturing pressure, since the aim of such experiments is to reactivate existing faults and is not to induce fluid driven hydro-fractures.

The first experiment of this type was performed in 2010 into the fractured limestone of the Low Noise

Underground Laboratory of Rustrel (southern France). The experiment consisted in injecting water in a high-permeable fault zone. The hydromechanical and seismological measurements showed unprecedented and direct evidence of an aseismic motion preceding seismic failures (Guglielmi et al., 2015a). However, this experiment suffered from a very limited number of seismic sensors, which prevented the in-depth analysis of the seismic responses (Derode et al., 2015). To resolve this limitation, similar experiments took place again in the same facility, in 2015, with a denser monitoring network made up of 31 seismic sensors around the injection (from 1 to 20 m) (Duboeuf et al., 2017). Injections were performed at 11 different locations (Fig. 1A), to test the responses of either (1) the sub-horizontal bedding planes that separate layers with different facies, and (2) the minor faults or fractures, belonging to the extended damage zones of a kilometer-long fault (Jeanne et al., 2012). Results confirmed that most deformation is aseismic in these experiments, with seismicity mainly occurring at distance (1 to 12 m) from the injection.

In order to test another lithology and investigate seismicity in low-permeable formations, a set of experiments (De Barros et al., 2016; Guglielmi et al., 2015b) was conducted in 2014 in the Toarcian shale of the IRSN underground experimental platform of Tournemire (France). Here, the injection borehole fully crossed a kilometer-long fault zone, and 4 injections were performed

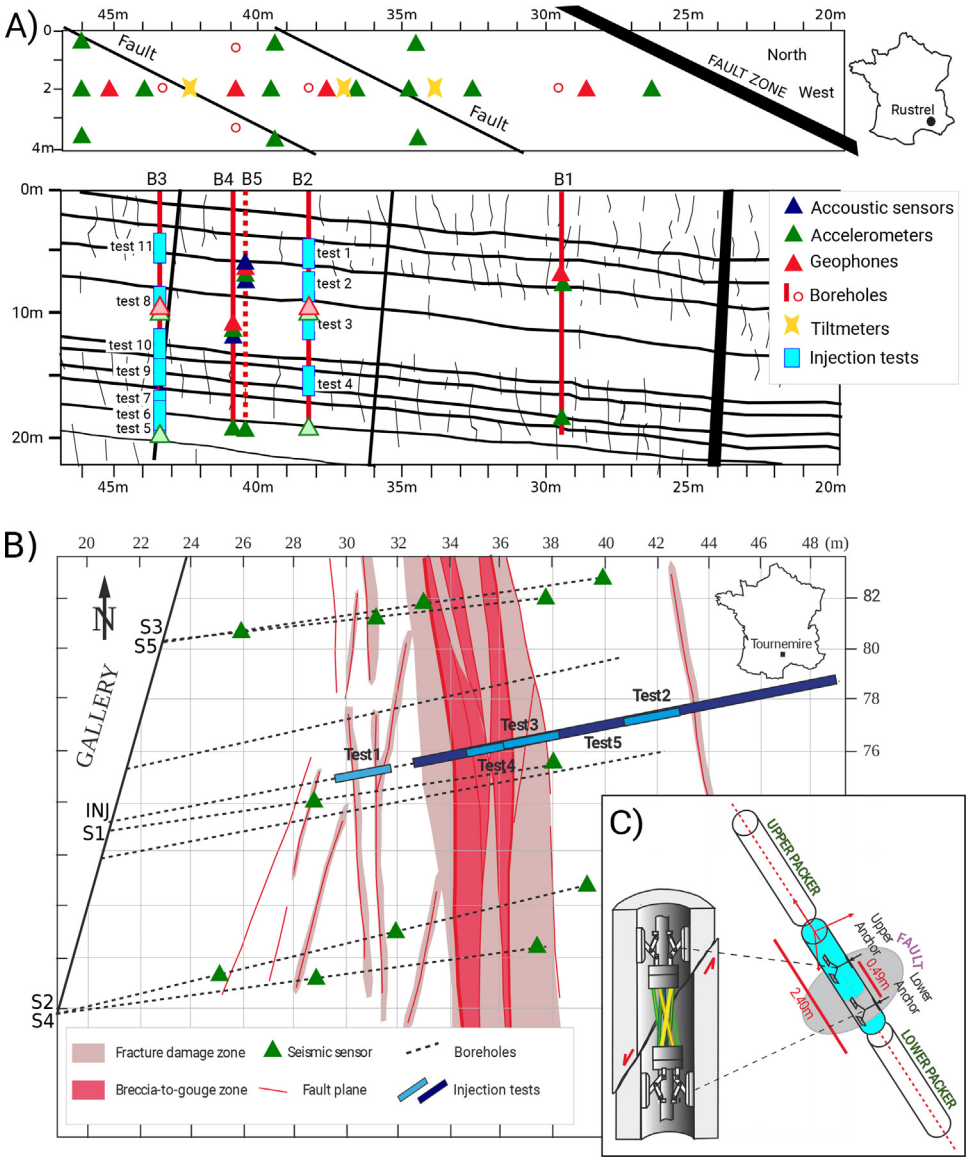

Fig. 1. Experimental setup of the experiments. A. Map view of the gallery and vertical cross-section, showing the locations of the monitoring network and the injection tests, in the Rustrel limestone (see Duboeuf et al. (2017) for details). B. Map view of the experiment in the Tournemire shale with the schematic structures of the fault zone and the location of the injection tests and the seismic sensors (see De Barros et al. (2016) for details). C. Schematic view of the SIMFIP injection probe, and details on the optic-fiber strainmeter anchored in the injection chamber.

in different geological structures: (1) minor faults in the damaged zones, (2) the unfractured medium, (3) fractures in the damaged zone, and (4) the fault core (Fig. 1B). In top of the responses of those isolated structures, the full thickness of the fault zone, including the fault core and the western damages zone, was tested using a 15-m-long portion of the borehole as injection.

2.2. Monitoring network and data

Both injection experiments (limestone in Rustrel, 2015 and shale in Tournemire, 2014) were instrumented with a dense monitoring network in order to record in high detail the hydrological, mechanical, and seismological responses (Fig. 2) of the hydraulically-stimulated structures. Inside the injection chamber, the newly developed SIMFIP probe allowed the simultaneous measurements of the injected pressure, the flow rate, and the 3D motions of the injected structures. This borehole strainmeter (Fig. 1c), based on optical-fiber Bragg grating measurements, was anchored on the borehole walls, independently from the injection system (Guglielmi et al., 2013). It captured deformations as small as 1 μm/m. At a few meters from the injection, deformation was also recorded by three two-components tiltmeters set on the gallery floor in the Rustrel experiment. At Tournemire, a borehole was equipped with 40 extensometric gauges, distributed on a 12-m-long probe.

Surrounding the injection, the seismicity was mainly recorded by a dense network of 22 and 16 accelerometers, for the Rustrel (Fig. 1A) and Tournemire (Fig. 1B) experiments, respectively. These sensors, with a flat response between 2 Hz and 4 kHz, were preferred to classical geophones, in order to have a much wider and higher frequency response. Fig. 3 shows the time and the frequency signature of a seismic event recorded at Rustrel. Below ~ 500 Hz, accelerometers and seismometers have similar responses. Above this frequency, while the geophone is losing sensitivity, the accelerometers fully catch the event waveform, including its frequency corner at around 1.2 kHz. To complement this backbone network at lower and higher frequency, a few geophones (10–800 Hz) and acoustic sensors (10 Hz–10 kHz) were also deployed (Fig. 1).

All these data were synchronously recorded, at sampling frequencies going from 1 kHz for hydrological and mechanical data to 2, 10 or 20 kHz for seismological data. Fig. 2 summarizes this multi-parameter dataset, by showing data recorded by different sensors during part of an injection in Rustrel (2015). In addition to the pressure and flow rate, which are more commonly recorded during reservoir-scale fluid injection, the variety of sensors used here allow one to span the full frequency range of the fault responses from the static deformation to the very high-frequency seismic emissions.

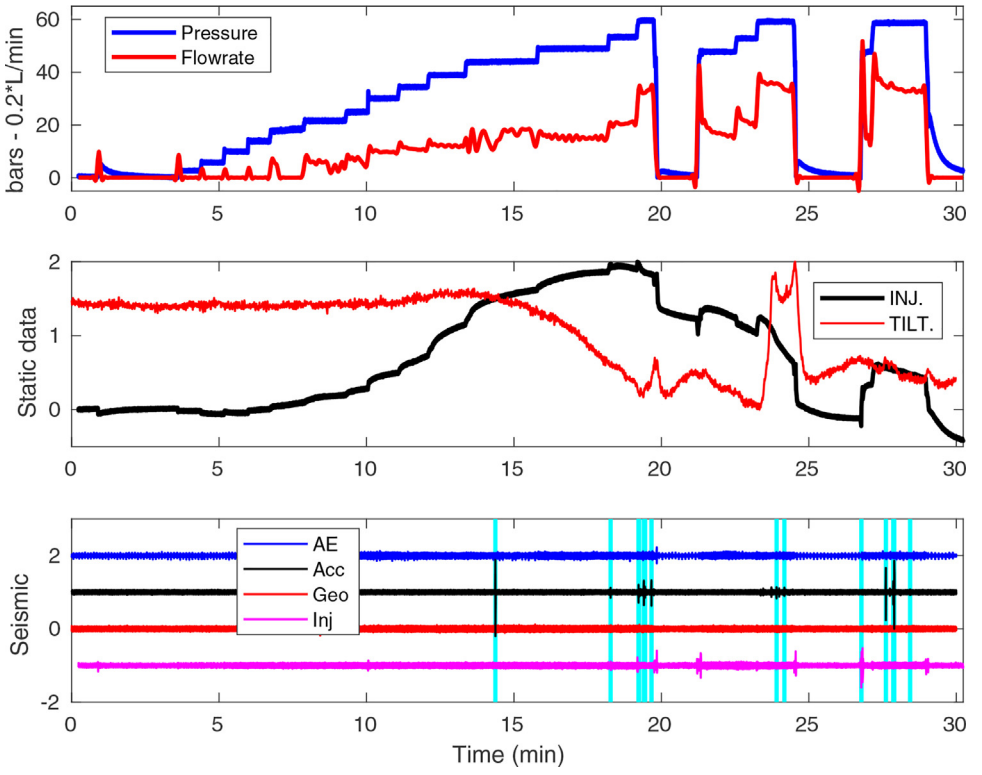

Fig. 2. Example of data recorded during step-rate injections in test 11, Rustrel. Top panel: hydraulic data, with pressure and flow rate at the injection; middle panel: quasi-static data, with one component of the deformation (INJ) at the injection point and of a tiltmeter (TILT) set on the gallery floor; bottom panel: high-frequency data, with high-pass filtered deformation (Inj, 10–500 Hz) at the injection point, geophone (Geo, 10–800 Hz), accelerometric (Acc, 0.1–4 kHz) and acoustic (AE, 0.2–10 kHz) data. The light blue vertical lines show the detected seismic events.

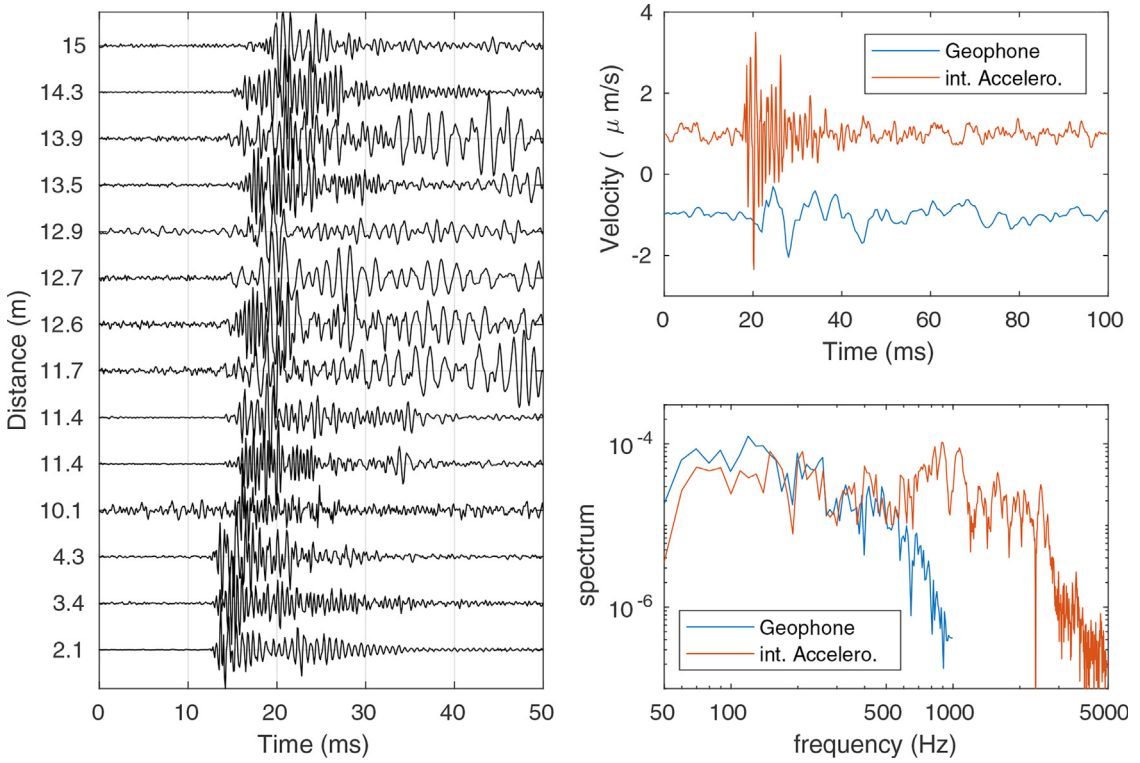

Fig. 3. Example of a $M_w \sim -3.6$ seismic event recorded in the Rustrel experiment. (Left) Accelerometric data, sorted accordingly to the hypocentral distance. (Right) Waveforms and spectrum, recorded by a geophone and an accelerometer (after time integration) set at the same location. The corner frequency of this event is around 1.2 kHz.

Finally, in both experiments, active seismic sources were also installed. The repetitive signals from these sources (hammer shots in Tournemire and vibrating device in Rustrel) are then used to monitor small velocity changes associated with medium perturbations during fluid injections and fault reactivations.

3. Experimental results

3.1. Seismic signatures

In both experiments, seismic events were detected by amplitude threshold methodsand then checked by eye-screening. In the Tournemire dataset, to identify small amplitude signals, the already detected events were used as templates and cross-correlated with the continuous seismic records (template-matching, Gibbons and Ringdal, 2006). At the end, only 34 events were detected in the Tournemire dataset during three injection tests (De Barros et al., 2016). The other two tests show no or single seismic emission. Out of the 11 tests performed in Rustrel, six tests show seismicity, with a total of 215 events (Duboeuf et al., 2017). An example of seismic event is shown in Fig. 3.

P- and S-wave arrival times and P-polarizations were used to get an absolute location for 24 events in the Tournemire experiment. One hundred and thirty-seven events from Rustrel were located both absolutely and relatively using arrival times and inter-event delays measured between similar events. The focal mechanisms, assuming a pure double-couple mechanism, were determined using either the first peak amplitudes for 16 events in the Tournemire dataset, or the first-motion polarity for 59 events in Rustrel.

The event magnitudes lie between $M_w = -3.2$ and $M_w = -4.2$. For both experiments, the detection threshold is around $M_w \sim -4$, at least around the injections. Frequency corners are found to be greater than 1 kHz, which leads to rupture area with an estimated radius of about 0.1 m to 0.3 m for a circular crack. Such seismicity is quite small compared to reservoir-scale seismicity, usually greater than $M_w \sim -3$ or tectonic seismicity ($M_w > 0$). However, such magnitude and source size are consistent with classical scaling laws for shearing events (e.g., Madariaga, 1976), with a stress drop of about 0.1 MPa. No major differences in magnitudes or frequency corners were observed between experiments.

Unconventional seismicity, like low-frequency events, tremor signals or long-period/long-duration signals have been observed around fluid injection in reservoirs (e.g., Kumar et al., 2017). They are interpreted as the seismic signature of slow-slip failures, but their existence and interpretation are still under debate (Zecevic et al., 2016). In the datasets recorded during the 2010 Rustrel experiments, Derode et al. (2015) identified such events. The source process behind them was, however, not clear, as the number of sensors did not allow a detailed analysis. Some low frequency events, with a peaked frequency content

at ~400 Hz, were also detected in the Tournemire dataset. However, the location of those events showed that they occurred in or around boreholes. They are likely to be produced by borehole wall resonance induced by pressure change (Tary et al., 2014). Therefore, unconventional seismic signals cannot be clearly linked to the fault reactivation in our datasets.

3.2. Deformation at the injection points

Hydromechanical responses strongly differ between the two experimental sites. In the shale of Tournemire, at low pressure, the flow rate was very small, indicating a very low initial fracture permeability. Once a pressure threshold was reached, the tested fractures slipped with some dilatancy, leading to a strong increase in flow rate and permeability. This pressure threshold, called Fracture Opening Pressure (FOP; Zoback, 2010), clearly separated the poro-elastic behavior near the injection borehole, from the plastic behavior on one or a few fractures which could extend several meters from the injection. Logically, seismicity only occurred once the FOP was reached. Maximum displacement measured between 0.08 and 0.55 mm with the SIMFIP probe was observed at the injections. At the end of the tests, the 0.05 to 0.52 mm residual displacements confirmed that a plastic motion was induced for all tests, even if two out of the five tests did not show any measurable seismic events, highlighting that aseismic motions occur during injections.

The fractured limestone of Rustrel, belonging to the unsaturated zone of the massif, behaves differently. Before any injections were performed, some fractures already had a millimeter opening. Therefore, even at low pressure, the flow rate was high: for four tests, injecting in highly permeable fractures led to a 70 L/min flow rate, while injection pressure remained below 2 MPa. No clear failures were observed in those tests, and no seismicity occurred. On the contrary, for six other tests, the pressure reached high value (5.5 MPa), with a flow rate increasing with pressure. Within these six tests, we observed a strong increase of permeability for two of them. A 20-fold permeability increase was also measured between the beginning and the end of the test performed in Rustrel in 2010 (Guglielmi et al., 2015a). Mechanical failures at the injection points are confirmed by residual displacements of 0.01 to 0.05 mm. However, contrary to the Tournemire tests, the pressure threshold between the poro-elastic and the plastic responses cannot be clearly defined using either the hydraulic or the deformation data. It suggests a transitional behavior, rather than the binary open/close process observed in the Tournemire experiments. For those six tests, as well as for the 2010 test, at least a few seismic events, and up to 120 events, have been observed.

3.3. Partitioning between seismic and deformation energy

Our observations show that the seismicity is unevenly distributed among tests. Some tests are fully aseismic, even if residual displacements are measured at the injection points, indicating a plastic motion on the injected structures. Moreover, there is a clear lack of seismicity near the injections, and the seismicity is also unevenly distributed in space, with some areas without any seismic sources. As instance, the seismicity in the Tournemire experiments occurred only in the eastern damage zone of the main fault. We can therefore wonder what fraction of the deformation is actually emitting seismic signals.

To evaluate the contribution of the seismicity to the deformation, seismic moments are compared to an equivalent moment computed from the deformation (Fig. 4). The latter can be computed as $M_0^{def} = \mu\ D\ S$, with μ the shear modulus. The displacement D, measured at the injections, can be a fraction of either the maximum or the residual displacement, by considering either the total motion or only the shearing part. The surface S of the shearing zone can be estimated by assuming that the seismic events are all located either inside or around it. Therefore, both D and S are rough estimations. They, however, show that less of 0.1% of the deformation energy is actually emitting seismicity in the Tournemire shale. This ratio is higher, but still very small, in the Rustrel limestone, as seismicity represents less than 6% in average. Therefore, in both cases, most of the deformation is aseismic during fluid injections.

Based on our observations, we suggest that not considering aseismic deformation induced by injections can lead to an overestimation of the maximum magnitude prediction as proposed by McGarr (2014). The authors linked the maximum seismic moment M_0^{max} of induced earthquakes to the injected volume V by $M_0^{max} = \mu\ V$, with V the injected volume. The maximum seismic moment observed here is indeed linearly related to the volume (Fig. 4). However, the McGarr (2014) theoretical predictions are six orders of magnitudes above our observations. This strong discrepancy may be explained by the strong aseismic component of the deformations, as McGarr (2014) considered that all deformations are emitting seismicity.

3.4. Location of the deformation

Repetitive, active seismic sources were shot during the experiments to image seismic velocity perturbations that testify to changes in the mechanical properties of the fault zone. Monitoring seismic velocity changes has proven its efficiency in giving valuable information about active fault behavior with either seismic slip (e.g., Brenguier et al., 2008), aseismic motion (e.g., Rivet et al., 2011), or pore-pressure changes (e.g., Hillers et al., 2015). In such injection experiments, with a dense monitoring network around the fault, seismic velocity change measure aims to detect aseismic deformation processes distributed around the reactivated structures.

The active seismic signals recorded during injection periods were compared with reference signals recorded prior to the tests and considered as the baseline responses of the medium. The delay betweensignals are then inferred from the phase differences by interferometric techniques. As P- and S-waves do not have the same sensitivity with respect to deformation and fluid content, we measured travel-time changes for both phases separately. Using tomography methods, these P- and S- wave velocity

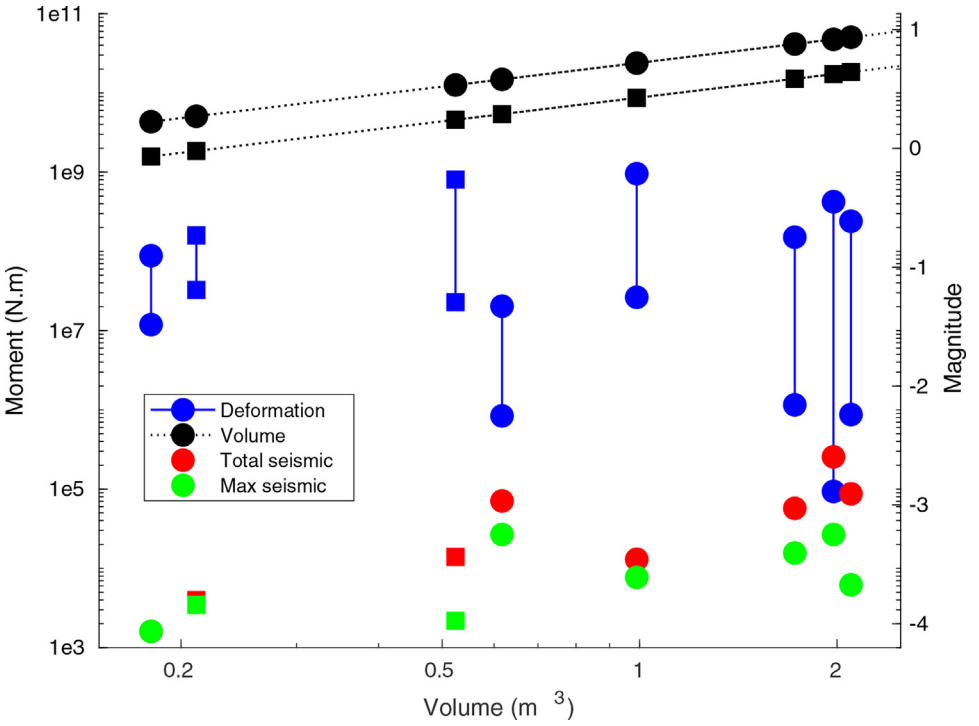

Fig. 4. Cumulated and maximum seismic moment (red and green symbols), deformation moment and predicted volume moment (blue and black symbols) versus injected volume V for the different tests of Rustrel (square) and Tournemire (circle). The volume moment is the maximum seismic moment following McGarr (2014) relationships, as $M_0^{max} = \mu V$. The shear moduli μ are different for Tournemire and Rustrel. The deformation moment is computed by $M_0^{def} = \mu S D$. Uncertainties on the rupture surface S and the displacement D measured at the injection give the error bars.

changes were located in the medium, by converting travel-time differences to velocity changes (Rivet et al., 2016).

Fig. 5 presents images of the seismic velocity changes measured during the first injection test of Tournemire experiment in a set of minor, secondary faults belonging to the western damaged zone and located at the center of the seismic sensor array. This test does not show clear seismic emissions, despite plastic deformations observed at the injection point. First, below the FOP (i.e. before plastic deformation on the injected structures), both P- and S-waves show a slight increase around the injection chamber (Fig. 5a,c). The pressure in the chamber makes it inflate, which increases the stress in the surrounding medium. Above the FOP, velocity perturbations are much stronger (up to 5%, Fig. 5b,d). A strong decrease of P- and S-waves is associated with the dilatancy of the minor faults that are aseismically slipping in response to the injection. The plurimetric extension of the perturbations (i.e. of the slipping area), is confirmed by numerical modeling of fluid-assisted stress perturbations (Rivet et al., 2016). The dilatant shear on these faults induces a stress transfer, with a stress increase in the surrounding areas, associated with a positive perturbation of the velocity.

The seismic velocity changes are therefore related either to the dilatancy of the slipping faults or to the opening/closing of micro-cracks due to stress perturbations. As no seismicity was recorded during this test, velocity changes appear as a good probe to monitor (1) aseismic deformation and (2) stress transfer. Across the tested fault, averaging the positive and negative perturbations leads to a small decrease of velocity of about 0.1%. This agrees with the perturbations measured across tectonic fault zones, and induced by earthquakes (Brenguier et al., 2008). Therefore, the small negative perturbations observed after earthquakes might be a spatial average of stronger and localized perturbations.

4. Discussion

Our experiments only induced a sparse seismicity, despite plastic behaviors at the injections. Particularly, there is a lack of seismic events near the injection points and an uneven spatial distribution around. The number of seismic events strongly differs from one test to another, with some tests without any seismicity. Therefore, the spatio-temporal distribution of the seismicity is very heterogeneous. Assuming that the fluid pressure, which reduces the effective stress, directly triggers the seismicity, the earthquakes should move away from the injection with the square (or cubic) root of time for a poro-elastic diffusion of the fluid (Shapiro, 2015). Such distance-time plot is given in Fig. 6, with a normalized diffusivity to make the different tests comparable. The actual diffusivity is found to range between 0.0015 and 0.13 m/s^2 among tests, which agrees with values usually measured in geothermal areas. However, this diffusive pattern is not clear, as seismicity does not gather behind a seismic front. For some tests (e.g., test 2, Rustrel), seismicity occurred clustered in

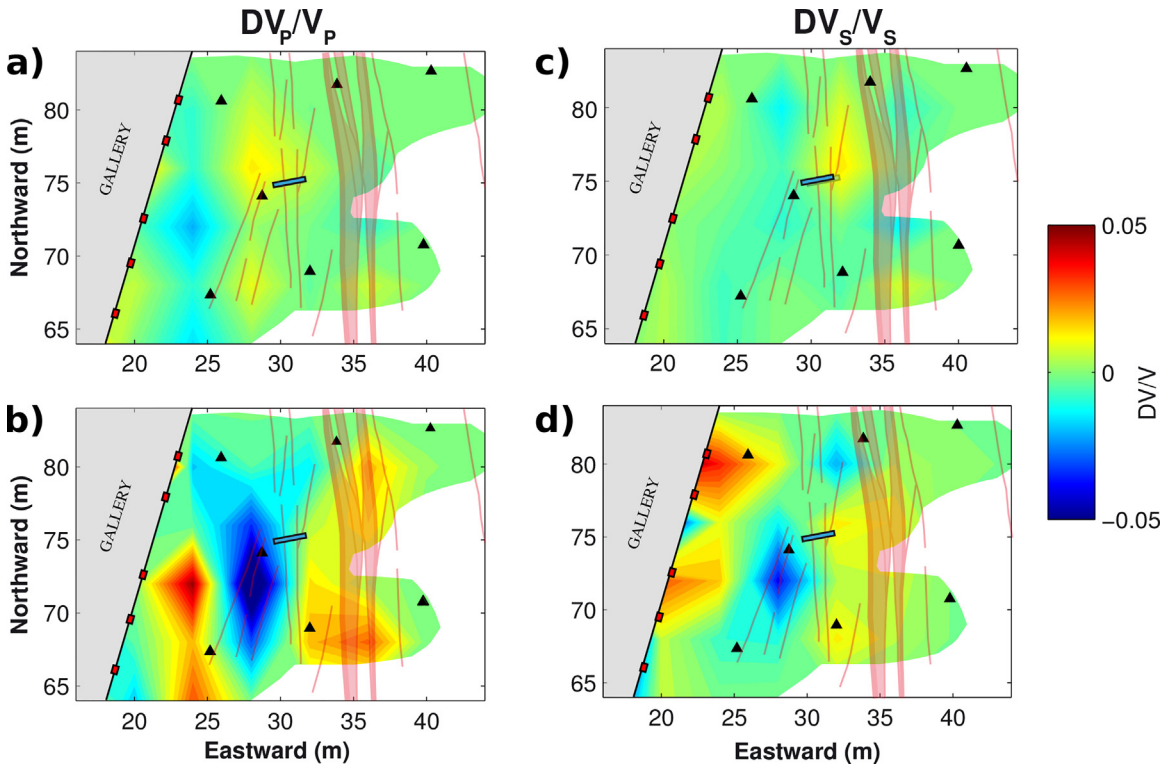

Fig. 5. Map view of the P- (left panels, a and b) and S-wave (right panel, c and d) velocity variations observed during test 1, Tournemire (see Fig. 1A). The blue rectangle shows the injection chamber. a and c: velocity changes for an injection pressure below the FOP; b and d: velocity changes for an injection pressure above the FOP, i.e. when aseismic failures were observed.

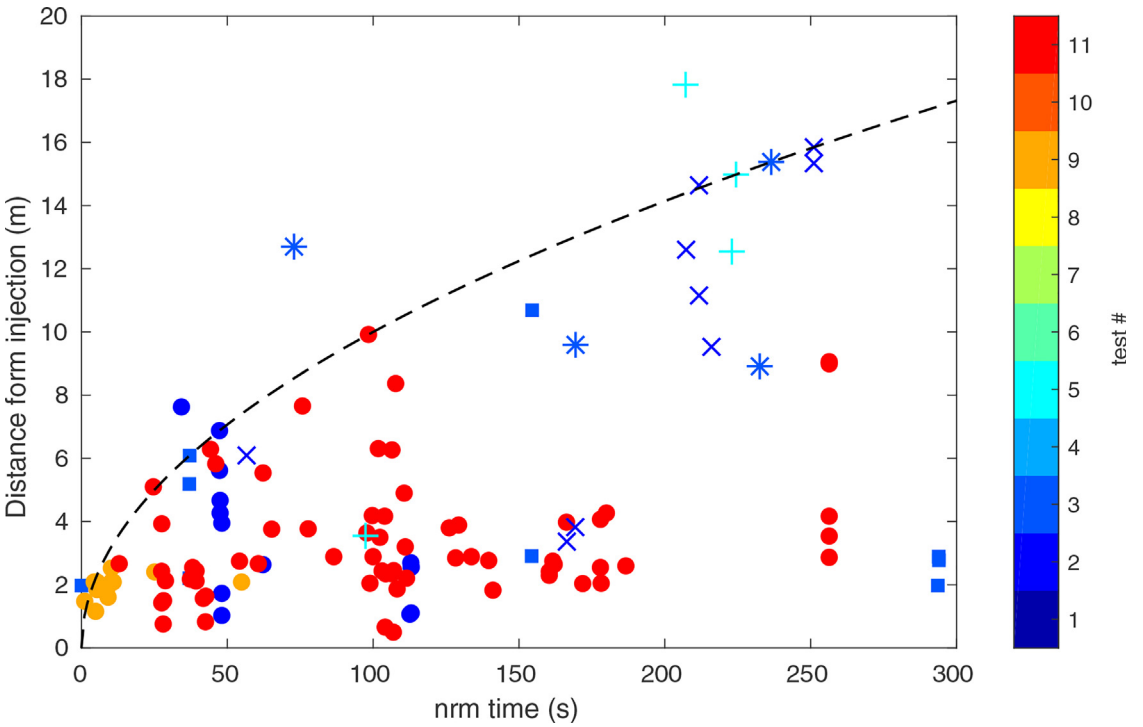

Fig. 6. Spatio-temporal distribution of the seismicity. Distance R between hypocenters and injection points versus time t where the pressure is above σ_3. The time has been normalized, in order to make the different tests comparable, with a diffusivity $D = 1$ m/s^2. This normalization coefficient is the mean for the three events with the largest diffusivity. The dotted line is therefore the theoretical prediction $R = \mathrm{sqrt}(4\pi Dt)$, with $D = 1$ m/s^2. The color-code stands for the test number, in either Tournemire (cross symbols) or Rustrel (filled symbols).

time but spatially scattered. Test11 seismicity (Rustrel) seems to follow two different diffusive patterns, with a higher diffusivity at early time than later in the test, which is inconsistent with the observed increase of permeability. Therefore, a poro-elastic diffusion is too simple to model the full complexity of the medium response. On top of that, the medium is changing with fluid injection, as new fluid paths are created. The intertwined relationships between injection parameters, geological settings, aseismic deformation and seismicity are therefore complex.

Based on our original experiments, the respective role of lithological, hydraulic and frictional properties of the fault zone can be better constrained. Firstly, we observe that the lithological properties influence the seismic behavior. For similar fluid perturbations, seismicity production is smaller in the Tournemire shale than in the Rustrel limestone. Similar experiments, also at decametric scale, but in crystalline rocks reveal a much numerous seismicity (Jalali et al., 2017; Zang et al., 2016). Besides, in the Tournemire shale, 11 out of 16 events with computed mechanisms occurred on the same family of fractures (Fig. 7), which are the only ones in the area with a calcite filling. While the shale has a rate-strengthening behavior, the calcite fillings may be rate-weakening. Therefore, seismicity occurred only on geological structures with an adequate mineralogy and frictional behaviors. In Rustrel, more numerous seismicity is observed in the layers with the highest density of fractures. The density and frictional properties of the fractures around the injection are then one controlling factor of seismicity production.

Fracture permeability also has a strong effect on seismicity. For both experiments, injections into areas with higher permeability fractures induce very little seismicity. As the fluid flows rapidly out the injected area, the volume invaded by the fluids is too large to allow a pressure higher than the FOP away from the injection. Therefore, no failures and no seismicity could happen. Finally, at the experiment scale, the fault zone is very heterogeneous, such as the seismicity distribution. The fault core seems indeed to act as a barrier for the fluid and for the stress field. It leads to heterogeneous hydraulic responses and stress concentration and rotation (Faulkner et al., 2006). Those heterogeneities, together with the permeability differences, may explain the asymmetric distribution of seismicity between the two sides of the fault core in the Tournemire shale (De Barros et al., 2016).

The stress field may also impact the seismic behavior. The seismic events show very scattered mechanisms for both experiments. Particularly, for Tournemire test 2, 7 mechanisms were computed for events that share similar horizontal location. Those events show similar nodal planes, but opposite polarities. The four left-handed strike slip mechanisms (Fig. 7a) agree with the local stress field measured by Cornet (2000) and confirmed by Guglielmi et al. (2015b). The three remaining events show an opposite mechanism (right-handed mechanism, Fig. 7b). As the fluid pressure equivalently reduces the effective stress of all normal components, such events with opposite slip-direction cannot be directly induced by a fluid-pressure increase. An additional forcing, likely the aseismic deformation, should interfere in order to strongly perturb the local stress field.

A strong aseismic motion was observed, when comparing deformation at the injection, induced seismicity, and medium perturbations imaged through seismic velocity changes. The strong discrepancy between seismic moment and either deformation energy or McGarr (2014) relationships clearly shows that most of the deformation is not emitting seismicity. Such small seismic-to-aseismic ratio

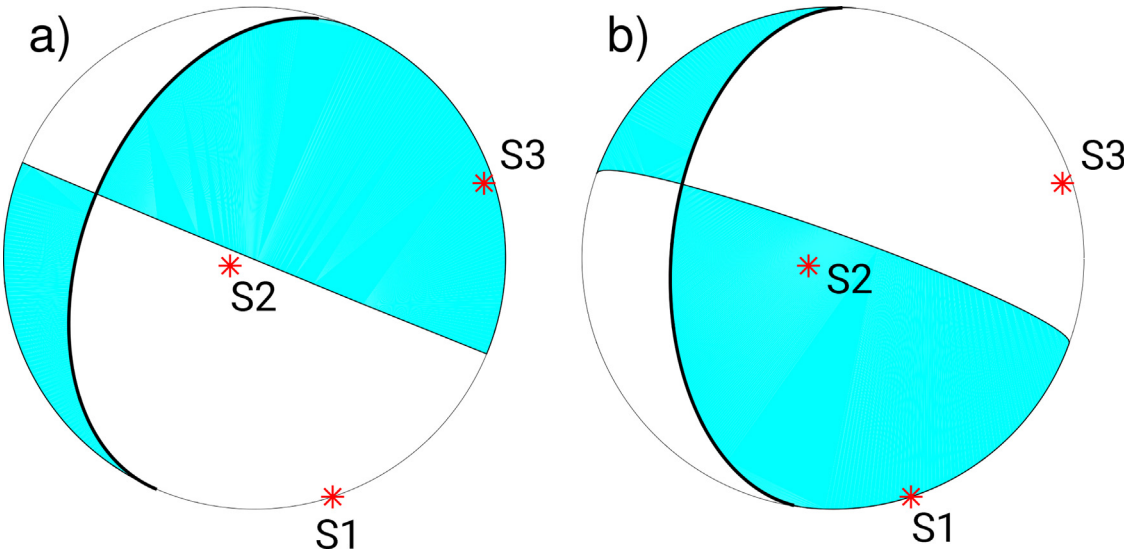

Fig. 7. Example of mechanisms computed for two seismic events in Tournemire. The bold lines are the fault planes, which are N150–180, 30–60°W structures with calcite fillings. The local stress field (S1 = 4 ± 2 MPa, S2 = 3.8 ± 0.4 MPa and S3 = 2.1 ± 1 MPa) was measured by Cornet (2000) and confirmed by Guglielmi et al. (2015b). Out of the computed mechanisms in the Tournemire test 2, four events have a mechanism similar as the left-handed strike-slip given in (a), and three events follow a right-handed strike-slip mechanism (b).

has been observed at the laboratory scale (Goodfellow et al. (2015), during reservoir monitoring (e.g., Calò et al., 2011; Schmittbuhl et al., 2014) or in subduction areas (e.g., Vallée et al., 2013).

In our experiments, deformation is particularly observed aseismic at the injection points. Therefore, it is firstly induced before any seismic failures (Guglielmi et al., 2015a). Both velocity change measurements and numerical modeling show that this aseismic motion may propagate over a distance of tens of meters away from the injection points (Guglielmi et al., 2015b; Rivet et al., 2016). Around it, the stress field should be perturbed, by Coulomb failure stress change, in the same way as for earthquakes (Stein, 1999). Moreover, this stress transfer around mainshocks triggered aftershocks, whose number decay with time follows an Omori's law. Here, stacking the event distributions for all tests, we also observed a $1/t$ decay of the number of seismic events (Fig. 8). Therefore, the observed seismicity seems to be "aftershocks" of the aseismic motion. In other words, the main slow failure induced at the injection modifies the stress field, strongly enough to trigger opposite-slip seismic events.

We can therefore propose a new model to explain how fluid perturbations induce seismicity (Fig. 9). The increase of fluid pressure and the associated reduction in effective normal stress induce large, aseismic failures. These aseismic deformations modify the fracture permeability and open new paths for the fluid flow. The volume to pressurize becomes larger, with new aseismic deformations once the pressure level becomes high enough. The fluid propagation could follow a fault-valve-like process as proposed by Sibson (1990), except that failures do not generate seismicity. It could also be modified by sudden shifts from highly channeled to large pressurized patches. In that case, the evolution of permeability with stress and strain could be an important mechanism driving the growth of aseismic fault rupture (Jeanne et al., 2018). The seismicity is likely a consequence of the main failures: the stress transferred from the aseismic deformation modifies the local stress field, which generates seismicity on

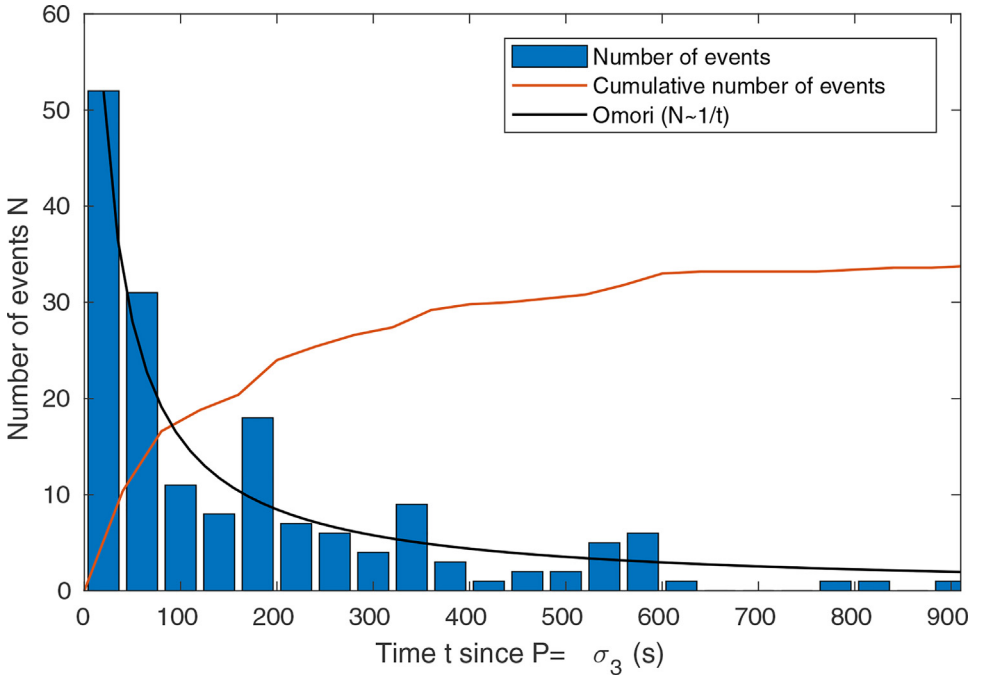

Fig. 8. Stacked time distribution of the seismic events for all tests. The time is defined as the time when the injection pressure is above σ_3. The red line is the cumulative number of events (divided by 5 for the sake of clarity). The black line is the Omori's law ($N(t) \sim 1/t$), which best fits the distribution.

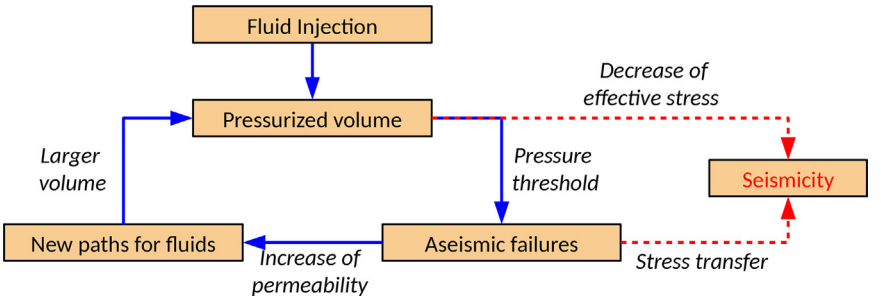

Fig. 9. Schematic view of the dual processes for fluid-induced seismicity, as inferred from the in-situ experiments.

structures with adequate rate-weakening frictional behaviors. It means that the seismicity may surround the main deformation area, and can eventually be outside the pressurized area. Moreover, as the pressurized zone increases with injected volume, the seismic cloud size also increases with time, leading to an apparent diffusivity of the seismicity.

However, from the saturated area, fluid diffusion may also occur, and may directly induce seismicity by decreasing effective stress. Therefore, a dual process, by either stress perturbations or increase in fluid pressure, may lead to seismicity. The balance between those two processes mainly depends on the pressure level, the variations of the medium permeability with stress and strain, and the injection time (Cornet, 2016; Jeanne et al., 2018). In our experience, seismicity seems mostly dominated by stress perturbation processes, but a lower-pressure fluid, injected during a longer time might generate a seismic front that follows fluid diffusion.

Aseismic deformation is therefore dominating the hydraulic responses of reservoirs (i.e. the fluid-flow paths). Thus, it is of crucial importance to monitor deformation during reservoir stimulation, by using either borehole instruments (strainmeters, extensometers, etc.), or surface measurements when possible. Monitoring velocity changes prove to be a promising tool to infer in-situ aseismic deformation and stress changes (Calò et al., 2011; Hillers et al., 2015; Rivet et al., 2016). On the contrary, the use of induced seismicity may not be a direct probe for the fluid, as it depends, among other parameters, on the injection properties, on the local stress field and on the density, the frictional and strength properties, and the permeability of the fractures. Therefore, great care should be taken in interpreting fluid extension from the spatio-temporal distribution of seismicity.

5. Conclusion

Two experiments of fault reactivation by fluid pressure injections were performed in shale (Tournemire site) and limestone (Rustrel site). The multi-parameter and dense monitoring network allowed the close observations of the hydro-mechanical and seismological responses of the injected structures, from the static deformation to the high-frequency (10-kHz) acoustic emissions. While plastic deformation was observed after most of the injections, only a sparse seismicity was observed. Its uneven spatio-temporal distribution, the energy budget and the seismic velocity changes show that more than 95% of the deformation is indeed aseismic. Seismicity rather seems to be a response to the stress transferred from this large aseismic deformation, than to the fluid pressure. Therefore, a dual process of stress transfer from aseismic deformation and poro-elastic diffusion of pressure leads to a complex seismic behavior. Moreover, the seismic emissions depend, not only on the injected volume, but also on the local stress field, on the geological heterogeneities, on the fracture permeability and frictional properties, and on their stress – strain dependency. Therefore, the spatio-temporal distribution of the seismicity in, e.g., reservoirs may mainly map the aseismic deformation, together with lithological heterogeneities. Therefore, in order to improve reservoir monitoring and seismic hazards mitigation, it is of crucial importance to better monitor and understand the deformation that are not recorded by conventional seismic instruments.

Acknowledgments

Tournemire experiment was funded by TOTAL SA through "Fluids and Faults" project (PIs: Claude Gout, Raymi Castilla and Pierre Henry). Rustrel experiment was supported by the "Agence nationale de la recherche" (HYDROSEIS project, PI. F. Cappa, ANR-13-JS06-0004-01) and by Total SA (HPMS-Ca project, Albion, PI. G. Massonat). We thank the IRSN (French Institute of Radioprotection and Nuclear Safety) for their dedicated help and access to the IRSN Tournemire platform, and the low-noise underground laboratory (LSBB) of Rustrel for logistical help during the experiment. SITES Company (J. Durand, H. Caron, and Y. Zouhair) is acknowledged for installing and maintaining the SIMFIP probe, sensors, and acquisition during the experiment. We thank the Magnitude Company (Sainte-Tulle, France office) for the Tournemire microseismic data processing. Louis De Barros deeply thanks the French Academie des Sciences for awarding him the Gouilloud–Schlumberger prize.

This paper is invited in the frame of Académie des Sciences 2017 Prizes (Grand prix Gouilloud-Schlumberger 2017). It has been reviewed/approved by Michel Campillo and Vincent Courtillot.

References

Albano, M., Barba, S., Tarabusi, G., Saroli, M., Stramondo, S., 2017. Discriminating between natural and anthropogenic earthquakes: insights from the Emilia Romagna (Italy) 2012 seismic sequence. Scientific Reports 7 (1), 282.

Atkinson, G.M., Eaton, D.W., Ghofrani, H., Walker, D., Cheadle, B., Schultz, R., Liu, Y., 2016. Hydraulic fracturing and seismicity in the Western Canada Sedimentary Basin. Seismol. Res. Lett. 87 (3), 631–647.

Bao, X., Eaton, D.W., 2016. Fault activation by hydraulic fracturing in western Canada. Science aag 2583.

Bardainne, T., Dubos-Sallée, N., Sénéchal, G., Gaillot, P., Perroud, H., 2008. Analysis of the induced seismicity of the Lacq gas field (Southwestern France) and model of deformation. Geophys. J. Int. 172 (3), 1151–1162.

Brenguier, F., Campillo, M., Hadziioannou, C., Shapiro, N.M., Nadeau, R.M., Larose, E., 2008. Postseismic relaxation along the San Andreas fault at Parkfield from continuous seismological observations. Science 321 (5895), 1478–1481.

Calò, M., Dorbath, C., Cornet, F.H., Cuenot, N., 2011. Large-scale aseismic motion identified through 4-DP-wave tomography. Geophys. J. Int. 186 (3), 1295–1314.

Cesca, S., Grigoli, F., Heimann, S., González, A., Buforn, E., Maghsoudi, S., Dahm, T., 2014. The 2013 September–October seismic sequence offshore Spain: a case of seismicity triggered by gas injection? Geophys. J. Int. 198 (2), 941–953.

Cornet, F.H., 2000. Détermination du champ de contrainte au voisinage du laboratoire souterrain de Tournemire, Rapp. N°98 N33/0073. Rapport du laboratoire de mécanique des roches, Institut de physique du globe de Paris.

Cornet, F.H., 2016. Seismic and aseismic motions generated by fluid injections. Geomechanics for Energy and the Environment, 5, pp. 42–54.

De Barros, L., Bean, C.J., Zecevic, M., Brenguier, F., Peltier, A., 2013. Eruptive fracture location forecasts from high-frequency events on Piton de la Fournaise Volcano. Geophys. Res. Lett. 40 (17), 4599–4603.

De Barros, L., Daniel, G., Guglielmi, Y., Rivet, D., Caron, H., Payre, X., Barbieri, E., 2016. Fault structure, stress, or pressure control of the

seismicity in shale? Insights from a controlled experiment of fluid-induced fault reactivation. J. Geophys. Res.: Solid Earth 121 (6), 4506–4522.
Derode, B., Guglielmi, Y., De Barros, L., Cappa, F., 2015. Seismic responses to fluid pressure perturbations in a slipping fault. Geophys. Res. Lett. 42 (9), 3197–3203.
Duboeuf, L., De Barros, L., Cappa, F., Guglielmi, Y., Deschamps, A., Seguy, S., 2017. Aseismic motions drive a sparse seismicity during fluid injections into a fractured zone in a carbonate reservoir. J. Geophys. Res: Solid Earth 122 (10), 8285–8304.
Faulkner, D.R., Mitchell, T.M., Healy, D., Heap, M.J., 2006. Slip on weak faults by the rotation of regional stress in the fracture damage zone. Nature 444 (7121), 922–925.
Gibbons, S.J., Ringdal, F., 2006. The detection of low magnitude seismic events using array-based waveform correlation. Geophys. J. Int. 165 (1), 149–166.
Goodfellow, S.D., Nasseri, M.H.B., Maxwell, S.C., Young, R.P., 2015. Hydraulic fracture energy budget: Insights from the laboratory. Geophys. Res. Lett. 42 (9), 3179–3187.
Guglielmi, Y., Cappa, F., Lançon, H., Janowczyk, J.B., Rutqvist, J., Tsang, C.F., Wang, J.S.Y., 2013. ISRM suggested method for step-rate injection method for fracture in-situ properties (SIMFIP): Using a 3-components borehole deformation sensor. In: The ISRM Suggested Methods for Rock Characterization, Testing and Monitoring: 2007–2014. 179–186.
Guglielmi, Y., Cappa, F., Avouac, J.P., Henry, P., Elsworth, D., 2015a. Seismicity triggered by fluid injection–induced aseismic slip. Science 348 (6240), 1224–1226.
Guglielmi, Y., Elsworth, D., Cappa, F., Henry, P., Gout, C., Dick, P., Durand, J., 2015b. In situ observations on the coupling between hydraulic diffusivity and displacements during fault reactivation in shales. J. Geophys. Res.: Solid Earth 120 (11), 7729–7748.
Gupta, H.K., Arora, K., Rao, N.P., Roy, S., Tiwari, V.M., Patro, P.K., Srihari, M., 2017. Investigations of continued reservoir triggered seismicity at Koyna, India. Geological Society, London. Spec. Publ. 445 (1), 151–188.
Hillers, G., Ben-Zion, Y., Campillo, M., Zigone, D., 2015. Seasonal variations of seismic velocities in the San Jacinto fault area observed with ambient seismic noise. Geophys. J. Int. 202 (2), 920–932.
Jalali, M.R., Gischig, V., Doetsch, J., Krietsch, H., Amann, F., Klepikova, M., 2017. Mechanical Hydraulic and Seismological Behavior of Crystalline Rock as a Response to Hydraulic Fracturing at the Grimsel Test Site. In: 51st US Rock Mechanics/Geomechanics Symposium. American Rock Mechanics Association.
Jeanne, P., Guglielmi, Y., Cappa, F., 2012. Multiscale seismic signature of a small fault zone in a carbonate reservoir: Relationships between VP imaging, fault zone architecture and cohesion. Tectonophysics 554, 185–201.
Jeanne, P., Guglielmi, Y., Rutqvist, J., Nussbaum, C., Birkholzer, J., 2018. Permeability Variations Associated With Fault Reactivation in a Claystone Formation Investigated by Field Experiments and Numerical Simulations. J. Geophys. Res.: Solid Earth 123, http://dx.doi.org/10.1002/2017JB015149.
Keranen, K.M., Weingarten, M., Abers, G.A., Bekins, B.A., Ge, S., 2014. Sharp increase in central Oklahoma seismicity since 2008 induced by massive wastewater injection. Science 345 (6195), 448–451.
Kumar, A., Zorn, E., Hammack, R., Harbert, W., 2017. Long-period, long-duration seismicity observed during hydraulic fracturing of the Marcellus Shale in Greene County, Pennsylvania. Leading Edge 36 (7), 580–587.
Lengliné, O., Boubacar, M., Schmittbuhl, J., 2017. Seismicity related to the hydraulic stimulation of GRT1, Rittershoffen, France. Geophys. J. Int. 208 (3), 1704–1715.
Madariaga, R., 1976. Dynamics of an expanding circular fault. Bull. Seismol. Soc. America 66 (3), 639–666.
McGarr, A., 2014. Maximum magnitude earthquakes induced by fluid injection. J. Geophys. Res.: Solid Earth 119 (2), 1008–1019.
McNutt, S.R., 2005. Volcanic seismology. Annu. Rev. Earth Planet. Sci. 32, 461–491.
Mukuhira, Y., Asanuma, H., Niitsuma, H., Häring, M.O., 2013. Characteristics of large-magnitude microseismic events recorded during and after stimulation of a geothermal reservoir at Basel, Switzerland. Geothermics 45, 1–17.
Payre, X., Maisons, C., Marblé, A., Thibeau, S., 2014. Analysis of the passive seismic monitoring performance at the Rousse CO_2 storage demonstration pilot. Energy Procedia 63, 4339–4357.
Rivet, D., Campillo, M., Shapiro, N.M., Cruz-Atienza, V., Radiguet, M., Cotte, N., Kostoglodov, V., 2011. Seismic evidence of nonlinear crustal deformation during a large slow slip event in Mexico. Geophys. Res. Lett. 38 (8.) .
Rivet, D., De Barros, L., Guglielmi, Y., Cappa, F., Castilla, R., Henry, P., 2016. Seismic velocity changes associated with aseismic deformations of a fault stimulated by fluid injection. Geophys. Res. Lett. 43 (18), 9563–9572.
Schmittbuhl, J., Lengliné, O., Cornet, F., Cuenot, N., Genter, A., 2014. Induced seismicity in EGS reservoir: the creep route. Geothermal Energy 2 (1), 14.
Schoenball, M., Ellsworth, W.L., 2017. A Systematic Assessment of the Spatiotemporal Evolution of Fault Activation Through Induced Seismicity in Oklahoma and Southern Kansas. J. Geophys. Res.: Solid Earth.
Shapiro, S.A., 2015. Fluid-induced seismicity. Cambridge University Press.
Sibson, R.H., 1990. Conditions for fault-valve behaviour. Geological Society London. Spec. Publ. 54 (1), 15–28.
Stein, R.S., 1999. The role of stress transfer in earthquake occurrence. Nature 402 (6762), 605.
Tary, J.B., Baan, M., Eaton, D.W., 2014. Interpretation of resonance frequencies recorded during hydraulic fracturing treatments. J. Geophys. Res.: Solid Earth 119 (2), 1295–1315.
Vallée, M., et al., 2013. Intense interface seismicity triggered by a shallow slow slip event in the Central Ecuador subduction zone. J. Geophys. Res.:Solid Earth 118, 2965–2981.
Wei, S., Avouac, J.P., Hudnut, K.W., Donnellan, A., Parker, J.W., Graves, R.W., Eneva, M., 2015. The 2012 Brawley swarm triggered by injection-induced aseismic slip. Earth Planet. Sci. Lett. 422, 115–125.
Yeck, W.L., Hayes, G.P., McNamara, D.E., Rubinstein, J.L., Barnhart, W.D., Earle, P.S., Benz, H.M., 2017. Oklahoma experiences largest earthquake during ongoing regional wastewater injection hazard mitigation efforts. Geophys. Res. Lett. 44 (2), 711–717.
Zang, A., Stephansson, O., Stenberg, L., Plenkers, K., Specht, S., Milkereit, C., Dahm, T., 2016. Hydraulic fracture monitoring in hard rock at 410 m depth with an advanced fluid-injection protocol and extensive sensor array. Geophys. J. Int. 208 (2), 790–813.
Zecevic, M., Daniel, G., Jurick, D., 2016. On the nature of long-period long-duration seismic events detected during hydraulic fracturing. Geophysics 81, KS109–KS117.
Zoback, M.D., 2010. Reservoir Geomechanics. Cambridge University Press, Cambridge, UK, 459 p.

2.1.3. Relations sismicité et paramètre hydro-mécaniques

Dans un objectif de limiter les risques associés à la sismicité induite, il est nécessaire d'anticiper la magnitude maximale pouvant être induite, à partir des paramètres d'injection et des propriétés connus de la faille. Pour cela, une relation linéaire entre magnitude maximale et volume injecté a été proposée par McGarr (1976). Cette relation a depuis été largement débattue (Eaton and Igonin, 2018; Galis et al., 2017; McGarr and Barbour, 2018; Van der Elst et al., 2016). De plus, l'énergie sismique induite dépend de nombreux autres paramètres, en plus du volume. En particulier, elle dépend de l'état de contraintes sur la faille (Garagash and Germanovich, 2012; Snee and Zoback, 2016; **Wynants-Morel et al., submitted**; etc) ou des propriétés mécaniques des failles et du réservoir (McClure and Horne, 2014; Pei et al., 2018; Schultz et al., 2018; etc)

De plus, les modèles reliant volume et sismicité ne considère pas que seule une part faible de la déformation est sismique (**Duboeuf et al., 2017**; McGarr and Barbour, 2018). En effet, moins de 1e-5 % de l'énergie injectée est dissipée par des séismes lors de nos expériences. La prise en compte de ce partitionnement sismique/asismique peut se faire en utilisant un index sismologique (Van der Elst et al., 2016), déterminé de manière empirique, a posteriori. Pour affiner ces modèles, nous avons profité de la richesse et de la diversité des mesures acquises lors de nos expériences, sur deux sites et deux matériaux géologiques différents (argilites et calcaires). La mesure simultanée et haute fréquence de la déformation, sismicité et paramètres d'injection permet de rechercher des relations entre ces paramètres. Nous avons montré ainsi qu'il est possible de corriger les relations moments sismiques en y intégrant la déformation au point d'injection. Alternativement, comme la sismicité a lieu en périphérie du glissement asismique, la distance minimale entre injection et sismicité permet d'estimer la quantité de déformation, et ainsi d'anticiper le moment sismique qui peut être relâché (**De Barros et al., 2019b**).

Article sélectionné

Après une comparaison entre énergie sismique, de déformation et hydraulique, l'article suivant propose de nouvelles relations pour anticiper l'énergie sismique relâchée en tenant compte de la déformation asismique.

De Barros, L., F. Cappa, Y. Guglielmi, L. Duboeuf, J.-R. Grasso (2019) Energy of injection-induced seismicity predicted from in-situ experiments, *Scientific Reports*, 10.1038/s41598-019-41306-x

SCIENTIFIC REPORTS

OPEN

Energy of injection-induced seismicity predicted from *in-situ* experiments

Received: 29 November 2018
Accepted: 4 March 2019
Published online: 21 March 2019

Louis De Barros[1], Frédéric Cappa[1,2], Yves Guglielmi[3], Laure Duboeuf[4] & Jean-Robert Grasso[5]

The ability to predict the magnitude of an earthquake caused by deep fluid injections is an important factor for assessing the safety of the reservoir storage and the seismic hazard. Here, we propose a new approach to evaluate the seismic energy released during fluid injection by integrating injection parameters, induced aseismic deformation, and the distance of earthquake sources from injection. We use data from ten injection experiments performed at a decameter scale into fault zones in limestone and shale formations. We observe that the seismic energy and the hydraulic energy similarly depend on the injected fluid volume (V), as they both scale as $V^{3/2}$. They show, however, a large discrepancy, partly related to a large aseismic deformation. Therefore, to accurately predict the released seismic energy, aseismic deformation should be considered in the budget through the residual deformation measured at the injection. Alternatively, the minimal hypocentral distance from injection points and the critical fluid pressure for fault reactivation can be used for a better prediction of the seismic moment in the total compilation of earthquakes observed during these experiments. Complementary to the prediction based only on the injected fluid volume, our approach opens the possibility of using alternative monitoring parameters to improve traffic-light protocols for induced earthquakes and the regulation of operational injection activities.

Over the last decades, important increases in the seismicity rates have been observed in relation with anthropogenic activities, especially underground fluid injections and productions[1]. Recent examples include earthquakes related to wastewater disposal[1,2], hydraulic fracturing[3], CO_2 sequestration[4], gas storage and extraction[5], and geothermal energy[6,7]. For instance, wastewater injections, associated with shale gas extraction, have induced earthquakes with magnitude up to 5.8 in Oklahoma (USA). In this area, the yearly rate of $M_w \geq 3$ earthquakes has changed from 1.6/year over the past century to more than 850/year in 20152. Geothermal activity may also induce large earthquakes, as the magnitude $M_w = 3.4$ earthquake felt in the Basel city, Switzerland[8]. A $M_w = 5.4$ earthquake is also suspected to be induced by geothermal activity, near Pohang (South Korea) in 2017, in a very low seismicity area[9,10]. Thus, a large number of studies indicate that anthropogenic activity increases the risk of earthquakes that can potentially damage surrounding infrastructures and impact population.

In order to understand and mitigate the seismic risk associated with fluid storage and extraction in deep reservoir formations, it is of crucial importance to anticipate the seismic energy induced by fluid perturbations[11]. Since the pioneering linear relationship proposed by McGarr[12,13], it is now well accepted that the induced seismic moment (M_o) scales with the injected fluid volume (V). However, several authors recently showed that the moment depends rather on $V^{3/2}$ than on V. Indeed, Galis *et al.*[14]. Used earthquake dynamic rupture simulations to show that the rupture arrest along a fault pressurized by local fluid injection is controlled by a competition between injection pressure and tectonic prestress. Previously, by revisiting the seismogenic index[15], Van der Elst *et al.*[16] statistically found a $V^{3/2b}$ correlation with the seismic moment, where b is the Gutenberg-Richter exponent. Similarly, Schultz *et al.*[17] showed that the number of events induced in the Duverner play (Canada) scales with the volume, or identically[18], that the seismic moment scales with $V^{3/2}$.

Furthermore, recent observations, acquired either in the laboratory[19], during *in-situ* injection experiments[20–22] or at the reservoir scale[23] showed that the seismic moment is overestimated by several orders of magnitude by

[1]Université Côte d'Azur, CNRS, Observatoire de la Côte d'Azur, IRD, Géoazur, France. [2]Institut Universitaire de France, Paris, France. [3]Lawrence Berkeley National Laboratory, Berkeley, USA. [4]NORSAR, Gunnar Randers vei 15, PO Box 52, N2027, Kjeller, Norway. [5]Université Grenoble Alpes, CNRS, OSUG, IRD, Isterre, France. Correspondence and requests for materials should be addressed to L.D.B. (email: debarros@geoazur.unice.fr)

the McGarr's model[13] prediction. One reason for this discrepancy is due to the assumption that every failure is seismic and confines within the pressurized volume. However, in many situations, only a small fraction of the deformation induced by fluid pressurization is observed to be seismogenic[6,7,20,21,24–27]. When considering together the seismic and aseismic motions, this discrepancy reduces significantly[28]. Thus, improving the anticipation of the seismic moment released during fluid injection requires an accurate quantification of the seismogenic context as well as the seismic and aseismic behavior of fault zones. The seismogenic index[15] (see method for its definition), together with the injected volume or the pressure rate, has been used to this aim to forecast the evolution on the injection-induced earthquakes in Oklahoma[29,30]. This parameter empirically gathers information on the stress state, the fault network and its frictional properties. Therefore, despite its strong potential for forecast purpose, it does not bring insights on the physics of the induced seismicity process.

Moreover, previous works have also shown that the characteristics of induced seismicity depend not only on the injected volume, but also on the reservoir geological structure[17,31,32], the depth of injection and the stress state[33–35], the density and frictional properties of faults[26,36] and the hydraulic properties of the reservoir/fault system[37,38]. Therefore, understanding induced seismicity only based on the measurement of the injected fluid volume can be problematic. To anticipate the released seismic energy induced by fluid perturbations at depth, quantifying the relationships between seismicity, injection parameters, rock deformation and reservoir structure is fundamental. Here, we focus on estimating what monitoring data contribute in the released seismicity, while considering the aseismic component of the deformation in the energy budget.

In this study, we have first acquired simultaneously measurements of fluid pressure, flow rate, deformation and seismicity during a series of ten *in-situ* injection experiments at a decameter scale in fault zones into permeable limestone[20] and low-permeable shales[26], accessed from underground laboratories at about 300 m depth. Such experiments have an intermediate scale between the laboratory and the reservoir. They benefit, therefore, from *in-situ* conditions and deals with the full complexity of the geological material responses. They also benefit from a proximal (m) and dense monitoring network, allowing a precise characterization of the geology, hydro-mechanical and seismic conditions. From those experiments, we then evaluated the relationships between the seismic moment, injection parameters and induced deformation for this unique quantitative data set. Through our investigations, we show that the seismic energy scales as the hydraulic energy with the injected fluid volume as $V^{3/2}$ when the aseismic deformation is included in the energy budget. Furthermore, our model better predicts the seismic moment when the critical fluid pressure for fault reactivation and the minimal hypocentral distance from injection points are considered.

Fluid Injection Experiments Into Fault Zones

The aim of these controlled experiments of fluid injections was to reactivate selected existing geological discontinuities (fault segments, fractures, etc.) belonging to the extended damaged zone of kilometer-long faults. The response to two different geological contexts were explored. A first set of experiments[26] took place in 2014 in shale rocks, accessed through the IRSN (Institut de Radioprotection et de Sureté Nucléaire) experimental platform of Tournemire (France). The second experiment[20] was performed in 2015 into the highly permeable fractured limestone of the Low Noise Underground Laboratory of Rustrel (LSBB, France). Both underground laboratories are situated between 200 m and 300 m depth. At these depths, the stress state ($2.1\,\text{MPa} < \sigma_3 < 3\,\text{MPa}$, and $4\,\text{MPa} < \sigma_1 < 6\,\text{MPa}$) favors shearing motions on the tested structures. From the tunnel walls, boreholes were drilled both for the injections and the monitoring network (see Fig. 1). Inside the injection boreholes, the SIMFIP (Step-rate Injection Method for Fracture *In-situ* Properties) probe[39] was used to inject water into a sealed section of the borehole in order to induce mechanical failures on the geological structures that crosscut the injection chamber. Eleven and five different locations of the probe in Rustrel and Tournemire sites, respectively, allowed testing the responses of either secondary faults, minor fractures, part of the main fault core, or sub-horizontal bedding planes that separate layers with different facies. With a maximum injection pressure between 2.2 and 6.0 MPa, (i.e., values below σ_3 plus the rock cohesion[24,40]), failures occurred only on optimally-oriented natural pre-existing structures, without inducing any new fractures.

In these experiments, a dense monitoring network surrounded these injections (14-to-22 accelerometers; see supplementary methods for more details on the experiment and the data analysis). In the injection chamber, the newly developed SIMFIP probe allowed the simultaneous measurements of the injected pressure, the flow-rate, and the 3D displacements of the tested structures[39] (Supplementary Fig. S1). Results show that for the 5 Tournemire tests and 6 of the Rustrel tests, a residual displacement was observed at the end of the injections, which shows that failure was reached for those tests. We discard from this analysis the remaining 5 tests in Rustrel because of technical issues or lack of clear failure signatures, and one fully aseismic test from Tournemire. Ten tests are therefore used in the following, among which eight tests have a complete dataset. Around the injection, the seismicity was mainly recorded by a dense network of accelerometers[20,26], which allow the detection, location and the magnitude computation of the seismic events. 34 and 215 events were recorded in the Tournemire and Rustrel experiments, respectively, with magnitude lying between −3.2 and −4.2. They are unevenly distributed among tests (see Fig. 1), as between none and 117 events were recorded. Their spatio-temporal distribution is also very heterogeneous. Particularly, no seismicity occurred close to the injection points despite mechanical failures monitored by the SIMFIP probe, highlighting a large aseismic component of the deformation[20,21,26].

Therefore, these experiments lead to gather a unique monitoring dataset in a catalog (Supplementary Table S6) that includes injection parameters (pressure, flow-rate), 3D-displacement at the injection, and seismicity. Particularly, the aseismic deformation at the injection is here directly measured and compared to the seismic emissions. Finally, these data were recorded within two very different geological contexts, very low permeable shale and high permeable limestone.

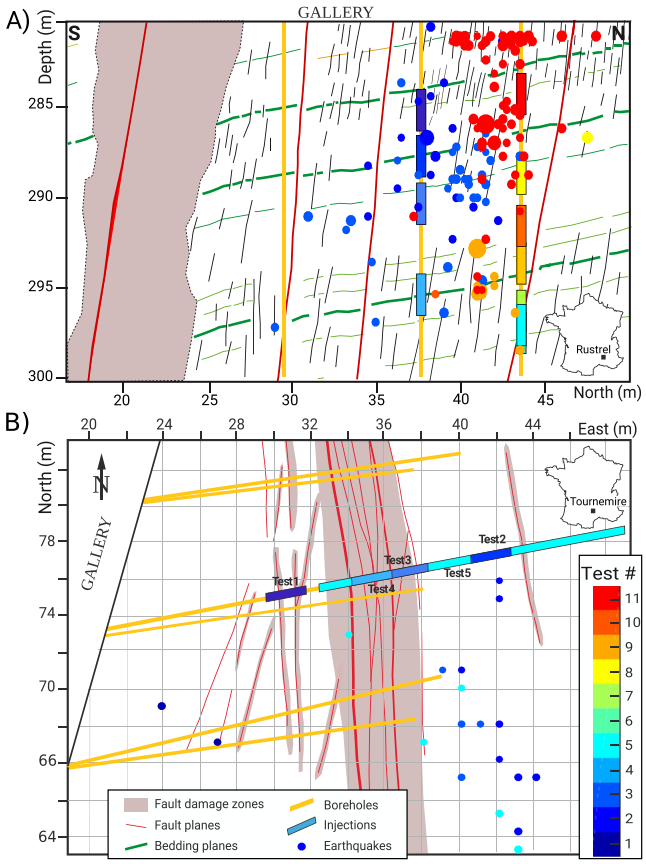

Figure 1. Experimental set-ups. Earthquake locations, colored by test number, and sized by magnitude projected in (**A**) a vertical cross-section view for the Rustrel (LSBB) experiment, and (**B**) a map view for the Tournemire experiment. The simplified geological structures (including faults identified from borehole logs, outcrops, and plugs), the monitoring boreholes and the injection locations are also indicated.

Results

Energy budget. For each test, the maximum moment M_0^{max} is the moment of the event with the largest magnitude, while the total moment M_0^{tot} is the sum of the moments of all detected events. As the detection threshold is similar in both experiments, M_0^{tot} corresponds to the cumulated moments of all events with magnitude $M_w > -4$[20,26]. According to Wyss[41], M_0^{tot} and M_0^{max} are theoretically proportional. Both moments, together with the predicted models from van der Elst *et al.*[16], Galis *et al.*[14] and McGarr and Barbour[28] can be converted to energy (see Methods). They are then compared with the hydraulic energy *Eh*, which represents the energy injected into the medium, and with the deformation moment M_0^{def} (see Methods).

We here observed that both the hydraulic moment *Eh* and the total moment M_0^{tot} similarly scales with the volume to a power close to 3/2 (Fig. 2). It suggests that the seismic energy is a proportional fraction of the injected energy. A lower exponent is found in the relationship between M_0^{max} and the volume. However, a 3/2 power is within the uncertainty range ($\sigma = 0.26$, inferred through bootstrap analysis). Therefore, these relationships agree with the theoretical predictions of Galis *et al.*[14] and Van der Elst *et al.*[16]. However, there is a ~8 order of magnitude difference between the hydraulic and the observed seismic moments: the seismic energy only represents 4E-7% to 1.5E-5% of the energy brought during injections. This falls in the lower end of the reservoir responses, where the ratio seismic-to-hydraulic energy is observed to range between 8E-6% and 2%[42].

A 5 order of magnitude difference is also noted between our observations and either Galis *et al.*[14] or McGarr[13] model. This discrepancy mainly comes from the fact that these models assume that all deformation is seismic, which is contradicted by observations[20,28]. The seismic moment is indeed only a small fraction (between 4e-3% and 1% in average) of the deformation moment, indicating that the induced deformation is mainly aseismic. Despite the very large uncertainties in the deformation moment, the predicting models of Galis *et al.*[14] and McGarr[13] models are at the upper bounds of these moments: they are therefore efficient to predict the total deformation, but not the released seismic moment.

The van der Elst[16] model perfectly fits the M_0^{tot} trend thanks to the use of the seismogenic index Σ as a free parameter. We find here a mean value of $\Sigma = -3$, consistently with reservoir measurements[42] where Σ ranges between -10 and 1. This parameter characterizes the seismogenic state of a reservoir, and, hence, considers the amount of aseismic response. In details, this parameter varies between -2.7 and -3.6 in the Rustrel experiments, and between -3.2 and -4.9 in the Tournemire shale. Therefore, extrapolating this parameter from one injection

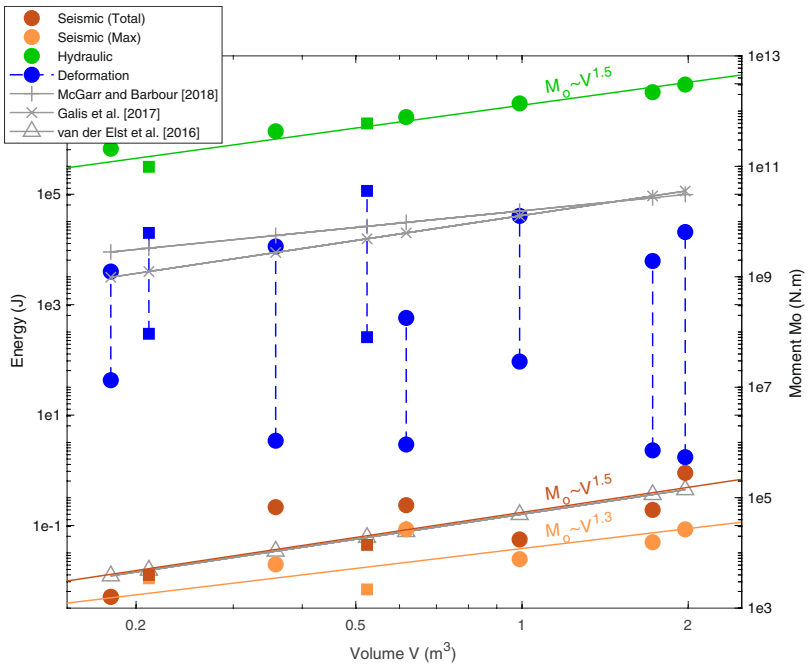

Figure 2. Seismic energy versus injected fluid volume. Maximum and total released seismic and hydraulic energy computed for the different tests performed in Rustrel ("o" symbols) and Tournemire ("□" symbols). Their best fitting trends are drawn as colored plain lines. Gray lines show the moment predictions converted to energy (upper bounds of M_0^{tot} from Mc Garr and Barbour[28], M_0^{max} from Galis *et al.*[14] and van der Elst *et al.*[16]).

to another may lead to errors in magnitude estimate greater than one, as it depends not only on the stress state, but also on the local fault architecture and on its frictional and hydromechanical properties. To summarize, the seismic energy and the injected energy show the same trend with the volume, but this latter parameter is not sufficient to accurately predict the released seismic energy, as the seismogenic state, including the aseismic motion, should be considered.

Sensitivity of the seismicity to injection and reservoir parameters. The seismic productivity, i.e. the released seismic energy, firstly scales with the volume. However, it may also depend on the reservoir properties, as fault responses to a fluid perturbation may be partly aseismic. We therefore explore the sensitivity of the released energy (or equivalently to the released moment) to the different parameters commonly used in reservoir engineering. Figure 3 shows the main results for the total seismic moment, with a fitting trend when the coefficient of determination R^2 is above 0.6. The best fit solutions are obtained when using the total seismic moment although similar results were observed using either the maximum seismic moment (Supplementary Fig. S3) or the number of events (Supplementary Fig. S4).

Seismicity and injection parameters: injected volume (V), fluid pressure (P), flowrate (Q) and hydraulic energy (Eh). As already stated, the total seismic moment is found to depend on the injected volume (Fig. 3a), with $M_0^{tot} \propto V^{3/2}$ ($R^2 = 0.77$). The former also scales with the hydraulic energy ($M_0^{tot} \propto Eh$, $R^2 = 0.72$, Fig. 3b). As expected, the more energy is injected, the larger the seismic energy is. In our experiments, but within two very different geological contexts, the seismic-to-injected energy ratio is constant at first order, and both scales with $V^{3/2}$.

Seismic moment also scales with the maximum injection pressure P as $M_0^{tot} \propto P^2$ (Fig. 3e), but with a poorer fit ($R^2 = 0.68$). This is not surprising, as the hydraulic energy also depends on pressure. However, the range of pressure variations is usually quite narrow, varying between the hydrostatic and the lithostatic pressures, which can reduce the effect of this parameter. As the stress state is not very different between both experiments ($\sigma_3 = 2.1$ MPa and $\sigma_3 = 3$ MPa), the correlation with a pressure-to-stress ratio (e.g. P/σ_3), rather than with the pressure alone, cannot be tested.

Moreover, as the seismogenic index Σ[15], seismic energy scales neither with the maximum flowrate nor with the injection duration (Fig. 3c,f). Similarly, no association between the flowrate and the seismicity is noticed for hydraulic fracturing cases[17], contrary to wastewater disposal sites[37]. This discrepancy may come from the difference in injection rates[17]. Therefore, this parameter may be a control parameter when the fluid migration is dominated by poro-elastic diffusion, but not when large fault reactivation (or bulk fracturing) is induced.

Seismicity and total/residual displacements at the injection (Umax/Ures). The relationship between released seismic energy and displacement at the injection is very surprising (Fig. 3j,k). Seismic moment and maximum displacement at the injection point, which contains both poro-elastic and plastic motions, do not present a clear link. However, there is a clear, but counter-intuitive, relationship with the residual (i.e. plastic) displacement:

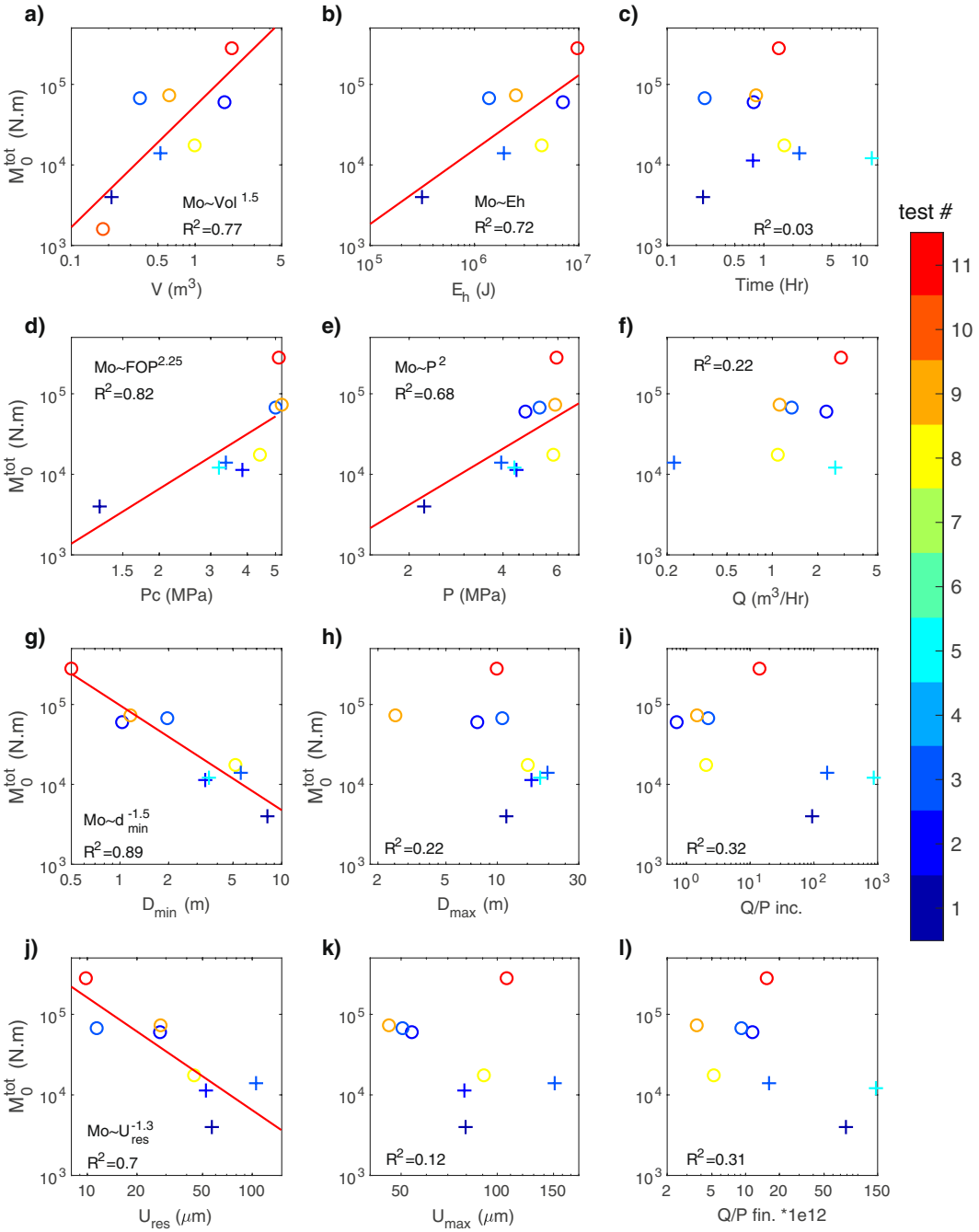

Figure 3. Released seismic moment and monitoring parameters. Total released seismic moment versus (**a**) Injected volume *V*. (**b**) Hydraulic energy *Eh*. (**c**) Injection duration time. (**d**) Critical Pressure *Pc*. (**e**) Maximum injection pressure *P*. (**f**) Maximum flowrate *Q*. (**g**) Minimal hypocentral distance from the injection D_{min}. (**h**) Maximal hypocentral distance from the injection D_{max}. (**i**) Ratio of the final over the initial Flowrate-Pressure ratio Q/P_{inc} (i.e. proxy for increase of permeability). (**j**) Residual displacement at the injection U_{res}. (**k**) Maximum displacement at the injection U_{max}. (**l**) Final Flowrate over Pressure ratio, i.e. proxy for final permeability Q/P_{fin}. Colorscale refers to the test number in either Rustrel ("o" symbols) or Tournemire ("+" symbols) experiments. Red lines show the best fitting lines for which R^2 is greater than 0.6.

$M_0^{tot} \propto U_{res}^{3/2}$ ($R^2 = 0.69$). For a fast-rupture earthquake, a large deformation implies a large energy release[43]. However, as the displacement is here observed to be aseismic near the injection[20,26], the released seismic energy is inversely related to the amount of aseismic deformation. Therefore, the larger the displacements are at the injection, the more energy is used in aseismic deformation, and less energy is available for seismic slips.

Seismicity and critical pressure (Pc). The critical pressure is defined as the pressure required to reach the elasto-plastic failure limit. As failures are associated with an increase of permeability and of flowrate at constant

pressure, it is the pressure for which the fractures start to hydraulically open above a critical stress[39,40]. Hence, it can be measured either as a change of trend in the pressure-flowrate response, by a change in the displacement direction at the injection, or by a loss of linearity in the displacement versus pressure relationship (Supplementary Methods and Fig. S2). Thus, this parameter quantifies the ability to reactivate a set of geological structures, depending on their orientation towards the stress state and on their frictional properties.

Here, we find a relationship (Fig. 3d) with the seismic moment: $M_0^{tot} \propto Pc^{2.25}$ ($R^2 = 0.84$). Therefore, the higher the pressure required to reactivate the structures is, the higher the seismic energy is. As for the pressure, *Pc* and the stress state or the stress deviator should be intrinsically linked, but the similarity in the regional stress field in our experiments does not allow exploring this correlation.

Seismicity and permeability. Assuming that the fluid flows in a set of fractures and that the permeability is linked to the mechanical opening of some of these fracture through the Darcy's law, the hydraulic conductivity is proportional to the flowrate-over-pressure ratio (*Q*/*P*, see Methods). This ratio is measured at the beginning and at the end of every injection test, and its increase is related to the increase in hydraulic conductivity. While a 50-to-500 times permeability increase is observed for the Tournemire tests, Rustrel tests show no or much smaller permeability changes, with less than a 20-times increase. This is related to the very different hydraulic properties of carbonates and shales host rocks. Thus, despite a general trend showing a decrease of the released moment with the increasing permeability, there is no significant relationship between these quantities (Fig. 3i,l). Same results were observed in controlled injections[44] in the Grimsel granite (Switzerland). Therefore, seismicity moment cannot be used to infer the permeability changes in reservoir monitoring. However, permeability and permeability changes may play a role in the aseismic deformation[45] and in the spatio-temporal distribution of the seismicity[46].

Seismicity and distance to the injection (D_{min}). An interesting observation in this series of experiments is the lack of seismicity close to the injections. All events were deported, with the closest events between 0.4 to 9 m from the injection well centers. Importantly, the seismic moment scales with the distance of the closest event to the injection (Fig. 3g), with $M_0^{tot} \propto D_{min}^{-1.5}$ and a very good fit ($R^2 = 0.89$). Note that, within each test, the closest event is usually not the largest one nor the first one. Intuitively, the furthest the events are, the lowest the fluid and stress perturbations are and the smallest the released seismic energy is. As the deformation is seen to be aseismic at the injection, the distance D_{min} represents the size of the aseismic volume around the injection, which explains its scaling with the residual displacement (Supplementary Fig. S5). D_{min} also depends on the injected volume ($D_{min} \propto V^{-1}$), and with a lower fit quality, on the injection pressure. The seismic moment also links with the mean hypocentral distance from the injection with a poorer fit, but not with the maximal distance to the injection (Fig. 3h).

Multi-parameter relationships between induced moment and monitoring data. Seismic moments correlate, not only with the injected volume, but also with the injection pressure, the residual displacement, the critical pressure, and the minimal hypocentral distance to the injection. On the contrary, the seismic moment depends neither on the injection duration, on the flowrate or on the permeability. So far, we looked for a direct correlation between the seismic moment and a single parameter, as if the monitoring parameters were independent from each other. However, trade-offs exist among them (Supplementary Fig. S5). That is why we now investigate the relationships of M_O^{tot} with 2 to 3 parameters together. As all the relationships are power functions, this problem reduces to a linear inverse problem in a log-log scale, assuming a relationship of the form:

$$\log(M_0^{tot}) = a + b\log(V) + c\log(P) + d\log D_{min} + e\log(U_{res}) + f\log(Pc) \quad (1)$$

where *a* to *f* are the unknowns to determine. Some of these parameters are fixed to 0, in order to explore all the possible combinations of 2 or 3 parameters that allow the reconstruction of M_0^{tot} (Fig. 4).

Among the relationships that include the volume, the following one leads to a good fit ($R^2 = 0.8$):

$$M_0^{tot} = A V^{\frac{3}{2}} P^{\frac{2}{3}} U_{res}^{-1} \quad (2)$$

with $A = 10^{-5}$. This relation is interesting, as the exponent of the volume is 3/2 like the hydraulic energy. As the same volume exponent was found for single parameter correlation, it means that there is no trade-off between the volume and either the pressure or the residual deformation. The seismicity increases with the volume, but it is counterbalanced by the pressure and the deformation at the injection to take into account the non-seismic processes. Comparing this relationship with the seismogenic index[15] leads to:

$$\sum = C - \frac{4}{9b}\log(P) - \frac{2}{3b}\log(U_{res}) \quad (3)$$

where *b* is the Gutenberg-Richter exponent and C is a constant with respect to the tested parameters. As Shapiro *et al.*[15] found this index constant with respect to the injection parameters, a trade-off only depending on the seismotectonic context should exist between *P* and U_{res}. However, this link cannot be clearly established here (Supplementary Fig. S5), even if a general trend exists among most of the tests. No other relations are found to have a $V^{3/2}$ dependence, because of the trade-off between *V* and D_{min} (Supplementary Fig. S5). As the plastic displacement U_{res} is not an easily measurable parameter during an injection phase, such relationship might be difficult to use, except if a SIMFIP 3D strainmeter is set at the injection[39].

The relationship leading to the best fit, with a minimal number of unknowns, does not depend on the injected volume, but only on *Pc* and D_{min}:

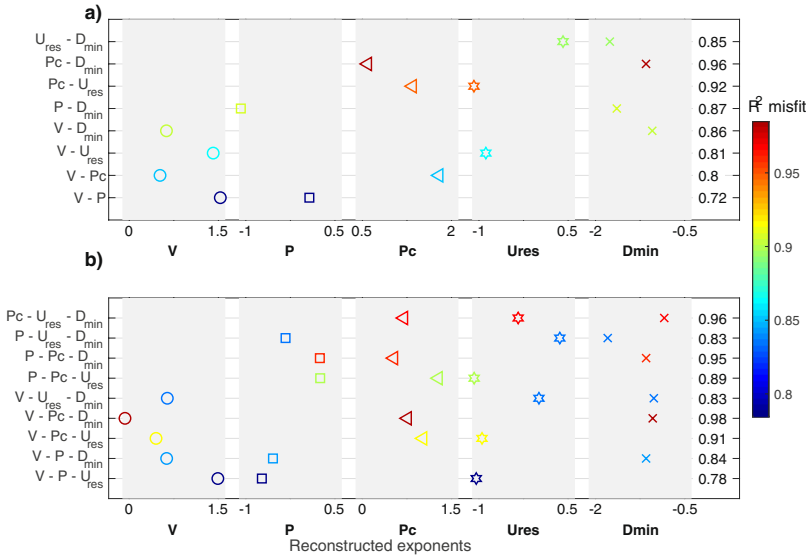

Figure 4. Multiparameters relationships for the released seismic moments. Exponents in the relationships (Eq. 1) between M_0^{tot} and (**a**) 2 parameters or (**b**) 3 parameters, among the volume V, the pressure P, the critical pressure Pc, the residual displacement U_{res} or the minimal hypocentral distance D_{inj}. The set of parameters that are jointly considered are given on the y-axis, left of the figures. The fit quality, expressed as R^2 coefficient is given by the color scale and by the number on the right of the figures.

$$M_0^{tot} = A\, D_{min}^{-1}\, Pc^{\frac{3}{4}} \tag{4}$$

with A very close to 1. This relationship, with only 2 parameters, leads to a near perfect fit ($R^2 = 0.99$). Therefore, the measurements of the critical pressure and of the minimal hypocentral distance from the injection allow a precise estimation of the induced seismic moments, at least in our experiments.

Discussion

In this study, we observed that the released seismic moment is linearly related to the hydraulic energy, and both scale as $V^{3/2}$, at first order. This result agrees with other recent results from Galis *et al.*[14] and van der Elst *et al.*[16], but not with the model brought by McGarr[13]. This discrepancy may come from the geometry of fluid pressure diffusion. Indeed, a 3D bulk diffusion will lead to a scaling with V, while a diffusion through a fault network, as observed in our experiments, will result in $M_0^{tot} \propto V^{3/2}$ [47]. In any cases, the injected volume is the main parameter that allows a quantification of the energy brought during the injection. However, moment predictions based only on a correlation with the volume overestimate the released moments, as they neglect that a large part of the deformation is aseismic[21,28]. In order to improve the prediction of the released seismic energy, the seismotectonic response of a reservoir (i.e., if the geological structures will respond either seismically or not) should be considered. We therefore explored the sensitivity of the induced seismic moment to the monitoring parameters during industrial fluid manipulations in reservoirs. The seismic moment does not depend on flowrate and permeability, but it scales with the volume, the maximum pressure, the plastic displacement at the injection, the minimal hypocenter distance to the injection, and the critical pressure. Other factors, such as the stress state, the depth of the injection or the thermal difference between the injected fluid and the rock, were not measured in the experiments considered in this study, but may also change the seismic moments.

To predict released seismic moments, the hydraulic energy, which is directly correlated to the injected volume, should be counterbalanced by considering the contribution of the aseismic motion. The easiest way is to consider the residual displacement (U_{res}), which is directly correlated to the aseismic motion, as it is the dominant deformation behavior compared with the much smaller seismic slips occurring far from the injection points[20,26]. The residual displacement depends on the seismotectonic properties of the reservoirs, as it is correlated with the orientation of the fracture network toward the stress field, and on their frictional and strength properties. Alternatively, the seismic moment can be predicted using the critical pressure (Pc) and the minimum hypocentral distance to the injection (D_{min}). The critical pressure Pc is related to the pressure required to reactivate faults. Therefore, it may also inform on the stress state, the orientation of the faults towards it, on the frictional parameters of the faults and on their interactions. D_{min} depends on the volume and allows a quantification of the injected energy (Supplementary Fig. S5). Besides, it is also a direct measurement of the aseismic motion at the injection, as it is the minimal size of the aseismic deforming zone and it strongly depends on the residual deformation U_{res} at the injection. This distance might be related to an earthquake nucleation length, but it is observed to be much larger than the seismic source size. As the aseismic slip is observed to be strongly dilatant at the injection, the fault walls might lose contact, which prevents seismic slips to occur. In this case, D_{min} might be a characteristic length for which the aseismic slip becomes predominant over the dilatancy. Therefore, D_{min} might carry information on

the shear stress versus pressure level at distance from the injection. This parameter might also be controlled by structural heterogeneities. Indeed, seismicity occurs on slip-weakening patches[26] belonging to structures where the perturbed effective stress state allows failures in shear. Such conditions on structures, frictional properties and stress state might not exist close to the injections. In this case, seismicity occurs on distant structures once they are sufficiently impacted by either the stress transferred from aseismic motion or the fluid diffusion[20,21,24].

Our analysis synthetizes results from[10] independent injection tests, which are representative of the contribution of seismic and aseismic behaviors at an intermediate scale between laboratory experiments and reservoir observations. At this scale, our results suggest new approaches to explore the physical processes of injection-induced seismicity. Because the scale of our experiments is much smaller than the scale of industrial injection, the upscaling remains an open question. However, at the reservoir scales, the deformation is also observed to be dominantly aseismic, as monitored seismic events are not large enough to explain observed deformation[6,25,27]. Moreover, the seismogenic index computed here are in the range of the ones observed at the reservoir scales, it therefore suggests that moment-volume relationships are similar, and that seismogenic context and processes might be similar. The relationships inferred here should be anyway properly tested at the reservoir scales. To do so, aseismic deformation monitoring, by either direct measurement[39] or through seismic velocity changes[22], should be improved to better characterize and anticipate the spectrum of reservoir seismogenic behaviors. Then, both relationships $M_0^{tot} = A\,V^{\frac{3}{2}}\,P^{-\frac{2}{3}}\,U_{res}^{-1}$ and/or $M_0^{tot} = AD_{min}^{-1}\,Pc^{\frac{3}{4}}$ can be easily tested, and might then be implemented to feed traffic-light warning systems of reservoir induced seismicity[1,11,30], in order to substitute the predictions based solely on the injected volume.

In our experiments, the injection times and volumes are small, with quite high injection pressure. Large-scale reactivation of faults are the dominant processes, while fluid diffusion is very limited in the intact rock or in the lower permeability fractures[6]. Similar high injection rates are performed in geothermal area and in reservoir exploitation through hydraulic fracturing, while wastewater disposals mainly induce poro-elastic diffusion. The inferred correlations between seismic moments and some parameters may vary according to the involved processes. For example, we do not observe a relationship between released moments and flowrate, while such relations were described for the Oklahoma seismicity[37]. Finally, we performed our experiments in rocks (limestone and shale) with very different frictional and hydromechanical properties. The seismic moments are well predicted by relationships that are not directly dependent on the rock properties. Therefore, once the upscaling to reservoir scale is verified, the relationships might be valid for any geological settings, as the seismotectonic context is indirectly considered through easily measurable parameters.

Our data set of injection-induced seismicity measured into fault zones within low- and high-permeability rocks allows for a better understanding of the relationship between seismic moment, injection parameters and induced deformation. The experiments clearly show that (1) only a small fraction of the injection energy and of the deformation is seismic, and (2) most of the deformation is aseismic at the injection and within the immediate volume that surrounds it.

When the contribution of the aseismic deformation is included in the energy budget, we find that the hydraulic and seismic energies are proportional to $V^{3/2}$ rather the conventional model that scales with V. Furthermore, control parameters for the seismic moments are the residual displacement in addition to the injection volume, or alternatively the critical fluid pressure for fault reactivation and the hypocentral distance relative to injection. Thus, the present study suggests that direct measurements of aseismic displacements, and estimation of minimal hypocentral distances relative to injection and of the critical pressures, should be considered to improve the prediction of the released seismic moment used in engineer-based risk assessment, traffic light warning system and mitigation strategies of injection-induced seismicity.

Methods: Computation of Moments and Energies

Moment predictions using the injected volume:

- McGarr[13,28]: $M_0^{tot} \leq 2\,\mu V$, with μ the shear modulus. This relationship quantifies the upper bound of the cumulative seismic moment, as it also includes the aseismic component of the deformation.
- Gallis *et al.*:[14] $M_0^{max} = \gamma V^{3/2}$, with $\gamma = \frac{0.4255}{\sqrt{d\tau_0}}\left(\frac{(K\,\mu_d}{h}\right)^{3/2}$.
- μ_d is the dynamic friction coefficient, $d\tau_0$ is the background stress drop, K is the bulk modulus, and h is the characteristic length of the intersection of the fault with the reservoir. h is arbitrarily set to 20 m, as the estimated size of the pressurized zone. Note that h = 80 km should be used for a good fit of our moment data.
- The Seismogenic index Σ was originally defined by Shapiro *et al.*[15] as $\sum = \log N + bM_w - \log V$. N is the number of events with magnitude greater than M_w and b is the Gutemberg Richter exponent. Reformulating this equation leads to $\sum = bM_w^{max} - \log V$, with M_w^{max} the magnitude of the largest event. van der Elst *et al.*[16]. Therefore used the relationship: $\log(M_0^{max}) = \left(\frac{3}{2b}\right)(\Sigma + \log V) + 9.2$.
- The moment of the event with the largest magnitude (M_0^{max}) is proportional to the cumulated moment (M_0^{tot}): $M_0^{tot} = \frac{B}{1-B}M_0^{max}$, where $B = 2b/3$[41]. Therefore, sensitivity to the injection and reservoir parameters should be similar for M_0^{max} and M_0^{tot}.

Hydraulic energy. This energy is computed as: $Eh = \int PQdt$, where P is the fluid pressure, Q is the injection flowrate, and t is the time.

Moment versus energy. The seismic moment can be converted to energy by the relationship: $M_0 = \frac{\mu}{\Delta\sigma}E$[48]. μ is the shear modulus, and $\Delta\sigma$ is the stress drop. The later was estimated to be about 100 kPa[20,26]. Therefore:

$$M_0 = 3e5E, \text{ or equivalently: } logE = \frac{3}{2}M_W + 3.6,$$

with M_W the seismic magnitude. This is consistent with the empirical relationship:[43] $logE = \frac{3}{2}M_W + 4.8$, which was derived for large earthquakes with stress drop of 1–5 MPa.

The seismic moments are directly computed, while hydraulic energy is first computed. Therefore, for sake the consistency between these measures, all the seismic moments could have been converted to energy, or conversely, we here choose to convert the hydraulic energy to an equivalent hydraulic moment.

Deformation moment M_0^{def}. For a shear motion u_s or a tensile motion u_n induced on a crack, the deformation moment can be expressed as[48]:

$$M_0^{def} = \mu \int u_s \, dS \text{ or } M_0^{def} = 3K \int u_n \, dS, \text{ respectively.}$$

μ is the shear modulus and K is the bulk modulus.

We can then assume that (1) the Lamé's parameters are equal ($\lambda = \mu$), which leads to $K = 5\mu/3$, and (2) that the displacements are maximal at the injection with a linear decrease with distance. Therefore, $M_0^{def} = \mu \, U_s \, S/2$ for shear motion and $M_0^{def} = 5 \, \mu \, U_n \, S/2$ for tensile displacement, with U_s and U_n the displacement measured at the injection, and S the rupture surface.

Separating the shear and tensile motions from the displacements measured at the injection required to project them on a fracture with known orientations and it is likely that several faults are playing during injections, with complex motions. Therefore, we prefer to keep a conservative approach, by computing the minimum and maximum values of the deformation moment.

The residual displacement contains only plastic, mainly shear, motion. The maximal displacement might be due to elastic and plastic behavior, with a large normal motion. Therefore, in order to find an uncertainty range for M_0^{def}:

$$\mu \, U_{res} \, S/2 < M_0^{def} < 5 \, \mu \, U_{max} \, S/2$$

Computing the surface area on which failures occurs is not trivial. We therefore assume that the seismic location can give extremum values for the surface S. Indeed, we can consider that all the seismicity is either (1) occurring on frictional patches within the deforming area, or (2) triggered by stress transfer outside the deforming area. Under this hypothesis, and assuming a circular surface, the surface S of the deforming area can be bounded by $S = \pi \, D_{\min}^2$ and $S = \pi \, D_{max}^2$, with D_{min} and D_{max} the minimal and maximal hypocentral distance to the injection well, respectively. Therefore, the deformation moment falls into the range:

$$\mu \, U_{res} \, \pi \, D_{min}^2/2 \leq M_0^{def} \leq 5 \, \mu \, U_{max} \, \pi D_{max}^2/2$$

These inequalities give the uncertainty range in Fig. 1.

Data Availability

The data used in this article are summarized in the Supplementary Table S6. Raw and unprocessed data are available upon request at debarros@geoazur.unice.fr.

References

1. Ellsworth, W. L. Injection-induced earthquakes. *Science* **341**(6142), 1225942 (2013).
2. Keranen, K. M., Weingarten, M., Abers, G. A., Bekins, B. A. & Ge, S. Sharp increase in central Oklahoma seismicity since 2008 induced by massive wastewater injection. *Science* **345**(6195), 448–451 (2014).
3. Bao, X. & Eaton, D. W. Fault activation by hydraulic fracturing in western Canada. *Science* **354**(6318), 1046–1409 (2016).
4. White, J. A. & Foxall, W. Assessing induced seismicity risk at CO2 storage projects: Recent progress and remaining challenges. *International Journal of Greenhouse Gas Control* **49**, 413–424 (2016).
5. Cesca, S. *et al*. The 2013 September–October seismic sequence offshore Spain: a case of seismicity triggered by gas injection? *Geophysical Journal International* **182**(2), 941–953 (2014).
6. Cornet, F. H. Seismic and aseismic motions generated by fluid injections. *Geomechanics for Energy and the Environment* **5**, 42–54 (2016).
7. Lengliné, O., Boubacar, M. & Schmittbuhl, J. Seismicity related to the hydraulic stimulation of GRT1, Rittershoffen, France. *Geophysical Journal International* **208**(3), 1704–1715 (2017).
8. Mukuhira, Y., Asanuma, H., Niitsuma, H. & Häring, M. O. Characteristics of large-magnitude microseismic events recorded during and after stimulation of a geothermal reservoir at Basel, Switzerland. *Geothermics* **45**, 1–17 (2013).
9. Grigoli, F. *et al*. The November 2017 Mw 5.5 Pohang earthquake: A possible case of induced seismicity in South Korea. *Science* **360**(6392), 1003–1006 (2018).
10. Kim, K. H. *et al*. Assessing whether the 2017 Mw 5.4 Pohang earthquake in South Korea was an induced event. Science (2018).
11. Bommer, J. J., Crowley, H. & Pinho, R. A risk-mitigation approach to the management of induced seismicity. *Journal of Seismology* **19**(2), 623–646 (2015).
12. McGarr, A. Seismic moments and volume changes. *Journal of geophysical research* **81**(8), 1487–1494 (1976).
13. McGarr, A. Maximum magnitude earthquakes induced by fluid injection. *Journal of Geophysical Research: solid earth* **119**(2), 1008–1019 (2014).
14. Galis, M., Ampuero, J. P., Mai, P. M. & Cappa, F. Induced seismicity provides insight into why earthquake ruptures stop. *Science advances* **3** (12) (2017).

15. Shapiro, S. A., Dinske, C., Langenbruch, C. & Wenzel, F. Seismogenic index and magnitude probability of earthquakes induced during reservoir fluid stimulations. *The Leading Edge* **29**(3), 304–309 (2010).
16. van der Elst, N. J., Page, M. T., Weiser, D. A., Goebel, T. H. W. & Hosseini, S. M. Induced earthquake magnitudes are as large as (statistically) expected. *Journal of geophysical Research: Solid Earth* **121**, 4575–4590 (2016).
17. Schultz, R., Atkinson, G., Eaton, D. W., Gu, Y. J. & Kao, H. Hydraulic fracturing volume is associated with induced earthquake productivity in the Duvernay play. *Science* **359**(6373), 304–308 (2018).
18. Eaton, D. W. & Igonin, N. What controls the maximum magnitude of injection-induced earthquakes? *The Leading Edge* **37**(2), 135–140 (2018).
19. Goodfellow, S. D., Nasseri, M. H. B., Maxwell, S. C. & Young, R. P. Hydraulic fracture energy budget: Insights from the laboratory. *Geophysical Research Letters* **42**(9), 3179–3187 (2015).
20. Duboeuf, L. *et al*. Aseismic motions drive a sparse seismicity during fluid injections into a fractured zone in a carbonate reservoir. *Journal of Geophysical Research: Solid Earth* **122**(10), 8285–8304 (2017).
21. De Barros, L., Guglielmi, Y., Rivet, D., Cappa, F. & Duboeuf, L. Seismicity and fault aseismic deformation caused by fluid injection in decametric *in-situ* experiments. *Comptes Rendus Geoscience* **350**(8), 464–475 (2018).
22. Rivet, D. *et al*. Seismic velocity changes associated with aseismic deformations of a fault stimulated by fluid injection. *Geophysical Research Letters* **43**(18), 9563–9572 (2016).
23. Rutledge, J. T., Phillips, W. S. & Mayerhofer, M. J. Faulting induced by forced fluid injection and fluid flow forced by faulting: An interpretation of hydraulic-fracture microseismicity, Carthage Cotton Valley gas field, Texas. *Bulletin of the Seismological Society of America* **94**(5), 1817–1830 (2004).
24. Guglielmi, Y., Cappa, F., Avouac, J. P., Henry, P. & Elsworth, D. Seismicity triggered by fluid injection–induced aseismic slip. *Science* **348**(6240), 1224–1226 (2015).
25. Wei, S. *et al*. The 2012 Brawley swarm triggered by injection-induced aseismic slip. *Earth and Planetary Science Letters* **122**, 115–125 (2015).
26. De Barros, L. *et al*. Fault structure, stress, or pressure control of the seismicity in shale? Insights from a controlled experiment of fluid-induced fault reactivation. *Journal of geophysical Research: Solid Earth* **121**(6), 4506–4522 (2016).
27. Cornet, F. H., Helm, J., Poitrenaud, H. & Etchecopar, A. Seismic and aseismic slips induced by large-scale fluid injections. In Seismicity associated with mines, reservoirs and fluid injections. Pageoph topical volumes., edited by S., T. (Birkhauser, Basel, 1997), pp. 563–583.
28. McGarr, A. & Barbour, A. J. Injection-induced moment release can also be aseismic. *Geophysical Research Letters* **45**(11), 5344–5351 (2018).
29. Langenbruch, C., Weingarten, M. & Zoback, M. D. Physics-based forecasting of man-made earthquake hazards in Oklahoma and Kansas. *Nature communications* **9**(1), 3946 (2018).
30. Langenbruch, C. & Zoback, M. D. How will induced seismicity in Oklahoma respond to decreased saltwater injection rates? *Science advances* **2**(11), e1601542 (2016).
31. Candela, T., Wassing, B., Ter Heege, J. & Buijze, L. How earthquakes are induced. *Science* **360**(6389), 598–600 (2018).
32. Magnani, M. B., Blanpied, M. L., DeShon, H. R. & Hornbach, M. J. Discriminating between natural versus induced seismicity from long-term deformation history of intraplate faults. *Science advances* **3**(11), e1701593 (2017).
33. Lund Snee, J. E. & Zoback, M. D. State of stress in Texas: Implications for induced seismicity. *Geophysical Research Letters* **43** (19) (2016).
34. Schoenball, M. & Ellsworth, W. L. A systematic assessment of the spatiotemporal evolution of fault activation through induced seismicity in Oklahoma and southern Kansas. *Journal of Geophysical Research: Solid Earth* **122**(12), 10189–10206 (2017).
35. Hincks, T., Aspinall, W., Cooke, R. & Gernon, T. Oklahoma's induced seismicity strongly linked to wastewater injection depth. *Science* **359**(6381), 1251–1255 (2018).
36. Pei, S., Peng, Z. & Chen, X. Locations of Injection-Induced Earthquakes in Oklahoma Controlled by Crustal Structures. *Journal of Geophysical Research: Solid Earth* **123**(3), 2332–2344 (2018).
37. Weingarten, M., Ge, S., Godt, J. W., Bekins, B. A. & Rubinstein, J. L. High-rate injection is associated with the increase in US mid-continent seismicity. *Science* **348**(6241), 1336–1340 (2015).
38. Hearn, E. H., Koltermann, C. & Rubinstein, J. L. Numerical models of pore pressure and stress changes along basement faults due to wastewater injection: Applications to the 2014 Milan, Kansas earthquake. *Geochemistry, Geophysics, Geosystems* **19**(4), 1178–1198 (2018).
39. Guglielmi, Y. *et al*. ISRM suggested method for step-rate injection method for fracture *in-situ* properties (SIMFIP): Using a 3-components borehole deformation sensor. In *The ISRM suggested methods for rock characterization, Testing and Monitoring*, edited by Ulusay, R., pp. 179–186 (Springer, Cham, 2013).
40. Guglielmi, Y. *et al*. *In situ* observations on the coupling between hydraulic diffusivity and displacements during fault reactivation in shales. *Journal of Geophysical Research: Solid Earth* **120**(11), 7729–7748 (2015).
41. Wyss, M. Towards a physical understanding of the earthquake frequency distribution. *Geophysical Journal International* **31**(4), 341–359 (1973).
42. Dinske, C. & Shapiro, S. A. Seismotectonic state of reservoirs inferred from magnitude distributions of fluid-induced seismicity. *Journal of seismology* **17**(1), 13–25 (2013).
43. Kanamori, H. Quantification of earthquakes. *Nature* **271**(5644), 411 (1978).
44. Jalali, M. *et al*. Transmissivity Changes and Microseismicity Induced by Small-Scale Hydraulic Fracturing Tests in Crystalline Rock. *Geophysical Research Letters* **45**(5), 2265–2273 (2018).
45. Jeanne, P., Guglielmi, Y., Rutqvist, J., Nussbaum, C. & Birkholzer, J. Permeability Variations Associated With Fault Reactivation in a Claystone Formation Investigated by Field Experiments and Numerical Simulations. *Journal of Geophysical Research: Solid Earth* **132**(2), 1694–1710 (2018).
46. Shapiro, S. A., Huenges, E. & Borm, G. Estimating the crust permeability from fluid-injection-induced seismic emission at the KTB site. *Geophysical Journal International* **131**(2), F15–F18 (1997).
47. Dieterich, J. H., Richards-Dinger, K. B. & Kroll, K. A. Modeling injection-induced seismicity with the physics-based earthquake simulator RSQSim. *Seismological Research Letters* **86**(4), 1102–1109 (2015).
48. Aki, K. & Richards, P. G. *Quantitative seismology*. (University Science Books, Sausalito, CA 2002).

Acknowledgements

We thank different funding agencies for supporting this work. The Tournemire experiment was funded by TOTAL SA through "Fluids and Faults" project (PIs: Claude Gout, and Raymi Castilla, Total, and P. Henry, CEREGE, CNRS). The Rustrel experiment was supported by the Agence Nationale de la Recherche (HYDROSEIS project, PI. F. Cappa, ANR-13-JS06-0004-01) and by Total SA (HPMS-Ca project, Albion, PI. G. Massonat). We thank the IRSN (French Institute of Radioprotection and Nuclear Safety) for their dedicated help and access to the IRSN Tournemire platform and the low noise underground laboratory (LSBB) of Rustrel for logistical help during the experiment. The SITES company (J. Durand, H. Caron, and Y. Zouhair) is acknowledged for installing

and maintaining the SIMFIP probe, sensors, and acquisition during the experiment. We thank the Magnitude Company (Sainte-Tulle, France office) for the Tournemire microseismic data processing. J.-R. G.'s contribution is partially supported by EPOS-IP (Anthropogenic Hazard), (EPOS IP. Project ID: 676564). and by SERA EC-H2020 (SERA: 730900) projects. Finally, we thank the associate editor (S. Falsaperla) and three anonymous reviewers for their constructive comments which improved our paper.

Author Contributions

L.D.B. wrote the manuscript. L.D.B., F.C., Y.G. and L.D. performed the experiments, and L.D.B., L.D., Y.G. and F.C. processed and analyzed the data. All authors (L.D.B., F.C., Y.G., L.D. and J.R.G.) discussed and reviewed the article.

Additional Information

Supplementary information accompanies this paper at https://doi.org/10.1038/s41598-019-41306-x.

Competing Interests: The authors declare no competing interests.

Publisher's note: Springer Nature remains neutral with regard to jurisdictional claims in published maps and institutional affiliations.

2.2. Suivi des fluides par imagerie sismique

Articles publiés dans ce thème

Rivet D., De Barros L., Guglielmi Y., Cappa F., Castilla R., Henry P.,(2016) Seismic velocity changes associated with aseismic deformations of a fault stimulated by fluid injection, *Geophys. Res. Lett.,* 43(18), 9563-9572.

De Barros L., Bean C. J., Zecevic+ M., Brenguier F., Peltier A. 2013. Eruptive fracture location forecasts from high-frequency events on Piton de la Fournaise Volcano, *Geophys. Res. Lett.,* 40, 1-5.

De Barros, L., F. Martini, C.J. Bean, A. Garcia-Yeguas , J. Ibanez. Magma storage below Teide volcano (Tenerife): evidence by scattered wavefields, Geophys. J. Int., 191 (2): 695-706

Martini, F., Lokmer, I., Jonsdottir, K., De Barros, L., Möllhoff, M., Bean, C. J., Hauser, F., Doherty, J., Ryan, C. and Mongan, J. (2012), A passive low-frequency seismic experiment in the Albertine Graben, Uganda. Geophysical Prospecting. doi: 10.1111/j.1365-2478.2012.01083.x

De Barros,L., B. Dupuy+, G. O'Brien, J. Virieux, S. Garambois, 2011. Using a poroelastic theory to reconstruct subsurface properties: numerical investigation, in *Seismic Waves, Research and Analysis*, ed. Dr K. Masaki, Intech

Dupuy+, B., L. De Barros, S. Garambois, J. Virieux, 2011. Wave propagation in heterogeneous porous media formulated in the frequency-space domain using a discontinuous Galerkin method, Geophysics, **76**, N13-N21

O'Brien, G. S., I. Lokmer, L. De Barros, C. J. Bean G. Saccorotti, J-P Métaxian and D. Patanè, 2011. Time Reverse Location of Seismic Long-Period events recorded on Mt Etna. *Geophys. J. Int.*, 184(1): 452-462

De Barros, L., M. Dietrich and B. Valette, 2010. Full waveform inversion of seismic waves reflected in a stratified porous medium. *Geophys. J. Int.*, 182(3):1543–1556.

De Barros, L., and M. Dietrich, 2008. Perturbations of the seismic reflectivity of a fluid-saturated depth-dependent poroelastic medium. *J. Acoust. Soc. Am.*, 123(3) :1409-1420.

De Barros, L., H. A. Pedersen, J.-P. Métaxian, C. Valdes-Gonzalez, and P. Lesage, 2008. Crustal structure below Popocatépetl Volcano (Mexico) from analysis of Rayleigh waves. *J. Volc. Geoth. Res.*, 170(1-2) :5-11.

Pour estimer le rôle des fluides dans la genèse des séismes, il est nécessaire de savoir où sont localisés les fluides en profondeur, et idéalement de pouvoir suivre leur diffusion. J'ai donc travaillé sur des techniques d'imagerie à partir des formes d'ondes complètes dans une théorie poro-élastique, pour découpler les phases fluide et solide (2.2.1). Il est cependant plus efficace de travailler sur les variations des propriétés, ce qui permet de suivre les perturbations (2.2.2). Enfin, je me suis aussi intéressé à l'imagerie des stockages magmatiques sous les volcans (2.2.3).

2.2.1. Imagerie en milieu poreux

Lors de mon doctorat et post-doctorat, je me suis intéressé à l'imagerie des milieux poreux, avec pour objectif de reconstruire à la fois les propriétés du squelette solide et du fluide le saturant. Alors qu'il est déjà délicat d'imager de manière robuste un milieu géologique solide, l'imagerie des phases fluides semblent utopiques. Il est donc nécessaire d'utiliser le maximum d'information présente dans le sismogramme, et donc d'utiliser les formes d'ondes complètes. Pour cela, les théories poro-élastiques (Biot, 1956; Carcione et al., 2010) mettent en équation le comportement dynamique des milieux polyphasiques. L'utilisation de telles théories nous a d'abord permis de modéliser le champ d'ondes complet (*Figure 12*) par des méthodes de volumes finis en 2D (**Dupuy et al., 2011**) et en milieu tabulaire par des matrices de réflexion/transmission généralisée **(De Barros and Dietrich, 2008**). L'influence des phases fluides sur les ondes sismiques a ainsi été explorée, notamment en reproduisant des cas de stockage de CO_2 dans des réservoirs profonds (**De Barros et al., 2012**). En particulier, il est important de noter que des différences significatives vont exister entre des modélisations effectuées avec une théorie élastique et poro-élastique. Par exemple, la Figure 12 montre l'apparition d'une deuxième onde P (onde de Biot), qui participe à l'atténuation du champ d'ondes en modifiant le partitionnement sismique aux interfaces (Pride et al., 2004).

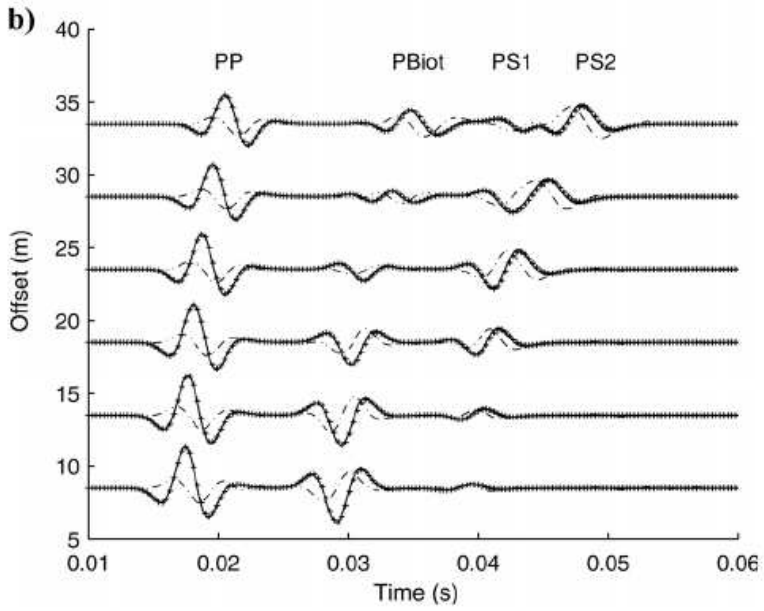

Figure 12: *Comparaison de sismogrammes synthétiques (déplacement vertical relatif fluide/solide) calculés en utilisant une méthode de volumes finies (Galerkin discontinu, trait plein,* ***Dupuy et al., 2011****) et de réflexion/transmission généralisés (croix,* ***De Barros et al., 2010****). La différence entre les deux, multipliée par un facteur 5, est indiquée en trait pointillé. Les ondes PP, Pbiot, PS1 et PS2 désignent les ondes P-directes et converties à l'interface en onde de Biot, conique S et S (figure modifiée de* ***Dupuy et al., 2011****). L'existence d'un déplacement relatif fluide/solide et d'une onde P lente (onde de Biot) sont les différences majeures avec les modèles élastiques, et participent efficacement à l'atténuation du champ d'ondes.*

L'étape suivante a consisté à calculer la sensibilité du champ d'ondes sismiques aux différents paramètres poro-élastiques (**De Barros and Dietrich, 2008**). J'ai donc calculé des expressions semi-

analytiques des dérivés de Fréchet, ce qui a permis d'explorer l'influence des propriétés du fluide et du solide sur le champ d'onde complet. Enfin, j'ai introduit ces expressions dans un algorithme d'inversion par moindres carrés généralisés dans lequel le modèle est optimisé par une méthode de gradients (Tarantola, 2005). L'objectif est de reconstruire simultanément les propriétés des phases solides et fluides du milieu poreux (**De Barros et al., 2010**; **De Barros et al., 2012**). Cependant, le nombre de paramètres à déterminer et leur fort couplage rend ce problème inverse trop mal posé pour être efficacement résolu. Il est donc nécessaire d'ajouter des contraintes extérieures afin de stabiliser la résolution de ce problème. Nous avons cependant montré que même si la reconstruction complète d'un milieu est très mal contrainte, le suivi des variations relatives d'un paramètre est toujours possible. Ainsi, une première inversion de tous les paramètres donnent un modèle inexact, mais le suivi de la saturation en fluide dans ce modèle est globalement correct (**De Barros et al., 2010**).

Article sélectionné

Le chapitre d'ouvrage suivant reprend et détaille les principaux résultats obtenus sur la modélisation et l'inversion des formes d'ondes sismiques dans une théorie poro-élastique :

De Barros, L., B. Dupuy+, G. O'Brien, J. Virieux, S. Garambois, 2011. Using a poroelastic theory to reconstruct subsurface properties: numerical investigation, in *Seismic Waves, Research and Analysis*, ed. Dr K. Masaki, Intech, p133-154

7

Using a Poroelastic Theory to Reconstruct Subsurface Properties: Numerical Investigation

Louis De Barros[1], Bastien Dupuy[2], Gareth S. O'Brien[1], Jean Virieux[2] and Stéphane Garambois[2]
[1] *School of Geological Sciences, University College Dublin*
[2] *ISTerre, CNRS - Université J. Fourier, Grenoble*
[1]*Ireland*
[2]*France*

1. Introduction

The quantitative imaging of the Earth subsurface is a major challenge in geophysics. In oil and gas exploration and production, aquifer management and other applications such as the underground storage of CO_2, seismic imaging techniques are implemented to provide as much information as possible on fluid-filled reservoir rocks. Biot theory (Biot, 1956) and its extensions provide a convenient framework to connect the various parameters characterizing a porous medium to the wave properties, namely, their amplitudes, velocities and frequency contents. The poroelastic model involves more parameters than the elastodynamic theory, but on the other hand, the wave attenuation and dispersion characteristics at the macroscopic scale are determined by the intrinsic properties of the medium without having to resort to empirical relationships. Attenuation mechanisms at microscopic and mesoscopic scales, which are not considered in the original Biot theory, can be introduced into alternative poroelastic theories (see e.g. Pride et al., 2004).

The inverse problem, that is, the retrieval of poroelastic parameters from the seismic waveforms, is much more challenging. Porosity, permeability and fluid saturation are the most important parameters for reservoir engineers. The estimation of poroelastic properties of reservoir rocks from seismic waves is however still in its infancy. The classical way of estimating these is to first solve the elastic problem and then interpret the velocities in terms of poroelastic parameters by using deterministic or stochastic rock physics modelling. However, unlike Full Waveform Inversion (FWI), these methods do not make full use of the seismograms.

In the poroelastic case, eight model parameters are required to describe the medium, compared with only one or two in the acoustic case, and three in the elastic case if wave attenuation is not considered. The advantages of using a poroelastic theory in FWI are (1) to directly relate seismic wave characteristics to porous media properties; (2) to use information that cannot be described by viscoelasticity or elasticity with the Gassmann (1951) formulae and (3) to open the possibility to use fluid displacement and force to determine permeability and fluid properties.

As an example of geological target, figure 1 presents the data recorded by a seismic survey on a seashore in the South of France. As water is pumped inland, saltwater is intruding into the coastal aquifer. This can affect the ground water and lead to severe problems with water supplies in the area. The monitoring of this phenomenon requires knowledge of the soil characteristics, including the permeability and porosity, and the properties of the fluid. A simple elastic approach cannot fully solve this problem, however the poroelastic theory may offer an alternative solution. In this example, the medium comprises alternating layers of sand, silt and clay with varying levels of compaction and a wide range of porosity and permeability. This layering produces strong reflected waves as shown in figure 1. The aim of the paper is to investigate how a poroelastic theory can be used to monitor water flow, and identify preferential pathways, using reflected waves. However, at this early stage, this chapter will only focus on numerical tests.

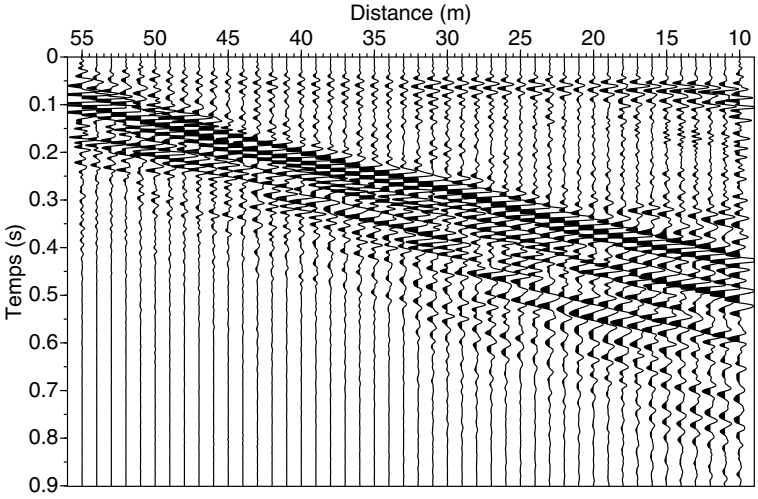

Fig. 1. Example of data for which a poroelastic-based interpretation may be useful. Data are recorded on a seashore in the South of France. Source is a hammer shot, and the 24 receivers are equally spaced between 10 and 55 m from the source. The medium is very soft and water saturated, with a direct P wave velocity of c. 1600m/s and a S wave velocity lower than 200 m/s.

We will investigate the gain and the feasibility of using a poroelastic approach, rather than the classical elastic one, in full waveform methods. The forward modelling is solved using different algorithms: a reflectivity approach, a 3D finite difference scheme and a 2D discontinuous Galerkin method. The comparison of synthetic data computed in the elastic and poroelastic cases shows that poroelastic modelling leads to some typical patterns that cannot be explained by elastic theory. This proves that the use of poroelastic theories may bring more insight to the model reconstruction, particularly, in relation to the fluid properties. Moreover, mesoscopic attenuation can be introduced in the poroelastic laws for double porosity medium, adding extra changes in the waveforms. This demonstrates the utility of using such theories to correctly reproduce measured seismic data.

Analytical formulae are then derived to compute the first-order effects produced by plane inhomogeneities on the point source seismic response of a fluid-filled stratified porous

medium. The derivation is achieved by a perturbation analysis of the poroelastic wave equations in the plane-wave domain using the Born approximation. The sensitivity of the wavefields to the different model parameters can be investigated: the porosity, consolidation parameter, solid density, and mineral shear modulus emerge as the most sensitive parameters in the forward and inverse modelling problems. However, the amplitude-versus-angle response of a thin layer shows strong coupling effects between several model parameters.

The inverse problem is then tackled using a generalized least-squares, quasi-Newton approach to determine the parameters of the porous medium. Simple models consisting of plane-layered, fluid-saturated and poro-elastic media are considered to demonstrate the concept and evaluate the performance of such a full waveform inversion scheme. Numerical experiments show that, when applied to synthetic data, the inversion procedure can accurately reconstruct the vertical distribution of a single model parameter, if all other parameters are perfectly known. However, the coupling between some of the model parameters does not permit the reconstruction of several model parameters at the same time. To get around this problem, we consider composite parameters defined from the original model properties and from *a priori* information, such as the fluid saturation rate or the lithology, to reduce the number of unknowns. We then apply this inversion algorithm to time-lapse surveys carried out for fluid substitution problems, such as CO_2 injection, since in this case only a few parameters may vary as a function of time. A two-step differential inversion approach allows the reconstruction of the fluid saturation in reservoir layers, even though the medium properties are mainly unknown.

2. Wave propagation in stratified porous media

The governing equations for the poroelastodynamic theory were first derived by Biot (1956), and are thus often referred to as "Biot's theory". The main hypothesis behind these equations is that the seismic wavelengths are longer than the pore size; the medium can then be described by homogeneised laws. Poroelastic theories have since been derived and improved by many authors (e.g. Auriault et al., 1985; Geertsma & Smith, 1961; Johnson et al., 1987).

2.1 Governing equations

Assuming a $e^{-i\omega t}$ dependence, Pride et al. (1992) rewrote Biot's (1956) equations of poro-elasticity in the frequency domain in the form

$$\begin{aligned} [\,(K_U + G/3)\,\nabla\nabla\, + (G\nabla^2 + \omega^2\rho)\,\boldsymbol{I}\,]\,.\,\mathbf{u} + [\,C\nabla\nabla + \omega^2\rho_f\boldsymbol{I}\,]\,.\,\mathbf{w} = 0 \\ [\,C\nabla\nabla + \omega^2\rho_f\boldsymbol{I}\,]\,.\,\mathbf{u} + [\,M\nabla\nabla + \omega^2\tilde{\rho}\boldsymbol{I}\,]\,.\,\mathbf{w} = 0\,, \end{aligned} \tag{1}$$

where $\mathbf{u}$ and $\mathbf{w}$ respectively denote the average solid displacement and the relative fluid-to-solid displacement, ω is the angular frequency, $\boldsymbol{I}$ the identity tensor, $\nabla\nabla$ the gradient of the divergence operator and ∇^2 the Laplacian operator. The other quantities appearing in equations (1) are properties of the medium.
The bulk density of the porous medium ρ is related to the fluid density ρ_f, solid density ρ_s and porosity ϕ:

$$\rho = (1-\phi)\rho_s + \phi\rho_f\,. \tag{2}$$

K_U is the undrained bulk modulus and G is the shear modulus. M (fluid storage coefficient) and C (C-modulus) are mechanical parameters. In the quasi-static limit, at low frequencies,

these parameters are real, frequency-independent and can be expressed in terms of the drained bulk modulus K_D, porosity ϕ, mineral bulk modulus K_s and fluid bulk modulus K_f (Gassmann, 1951):

$$\begin{aligned} K_U &= \frac{\phi K_D + \left[1 - (1+\phi)\frac{K_D}{K_s}\right] K_f}{\phi(1+\Delta)}, \\ C &= \frac{\left[1 - \frac{K_D}{K_s}\right] K_f}{\phi(1+\Delta)}, \quad M = \frac{K_f}{\phi(1+\Delta)} \\ \text{with} \quad \Delta &= \frac{1-\phi}{\phi}\frac{K_f}{K_s}\left[1 - \frac{K_D}{(1-\phi)K_s}\right]. \end{aligned} \tag{3}$$

It is also possible to link the frame properties K_D and G to the porosity and constitutive mineral properties (Korringa et al., 1979; Pride, 2005):

$$K_D = K_s \frac{1-\phi}{1+c_s\phi} \qquad \text{and} \qquad G = G_s \frac{1-\phi}{1+3c_s\phi/2}, \tag{4}$$

where G_s is the shear modulus of the grains. The consolidation parameter c_s appearing in these expressions is not necessarily the same for K_D and G (Korringa et al., 1979). However, to minimize the number of model parameters, and following the recommendation of Pride (2005), we consider only one consolidation parameter to describe the frame properties. c_s typically varies between 2 to 20 in a consolidated medium, but can be much greater than 20 in a soft soil.

Finally, the wave attenuation is explained by a generalized Darcy's law which uses a complex, frequency-dependent dynamic permeability $k(\omega)$ defined via the relationship (Johnson et al., 1994):

$$\tilde{\rho} = i\frac{\eta}{\omega\, k(\omega)} \quad \text{with} \quad k(\omega) = k_0 \Big/ \left[\sqrt{1 - i\,\frac{4}{n_J}\frac{\omega}{\omega_c}} - i\,\frac{\omega}{\omega_c}\right]. \tag{5}$$

In equation (5), η is the viscosity of the fluid and k_0 the hydraulic permeability. Parameter n_J is considered constant and equal to 8 to simplify the equations.

The relaxation frequency $\omega_c = \eta/(\rho_f F k_0)$, with F the electrical formation factor, separates the low frequency regime where viscous losses are dominant from the high frequency regime where inertial effects prevail. We refer the reader to the work of Pride (2005) for more information on the parameters used in this study.

The solution of equation (1) leads to classical fast P- and S-waves, and to an additional slow P-wave (often called Biot wave) . The fast P-wave has fluid and solid motion in phase, while the Biot wave has out-of-phase motions. At low frequency, the Biot wave has a diffusive pattern and can be seen as a fluid pressure diffusion wave. At high frequency, the inertial effects are predominant. This wave becomes propagative and can be seen in data, giving an experimental justification to the dynamic poroelasticity theory Plona (1980).

2.2 Mesoscopic attenuation and more complex theories

Although the slow P-wave does not appear on the seismograms at low frequency, it plays an important role in the attenuation process, as it produces loss of energy by wave-induced fluid-flow. However, the attenuation as described in the Biot theory is not strong enough to model the attenuation in geological media, especially at low (i.e. seismic) frequencies.

Attenuation processes can actually be separated into 3 different spatial scales, namely microscopic, mesoscopic and macroscopic (Pride et al., 2004). Within this classification, the Biot mechanism of attenuation takes place at macroscopic scale (on the order of the seismic wavelength). The microscopic attenuation is due to mechanisms that occur at the grain size, such as the squirt flow mechanism (Mavko & Jizba, 1991). This mechanism leads to wave attenuation mainly at high frequencies. The attenuation mechanism that prevails at low frequency comes from the mesoscopic scale (Pride et al., 2004), and it is due to fluid flow that occurs at boundaries between any medium heterogeneities whose sizes are between the grain sizes and the seismic wavelengths. This is particularly true for layered media (Gurevich et al., 1997; Pride et al., 2002) or when the medium contains 1) inclusions of different materials such as composite medium or double porosity medium (Berryman & Wang, 2000; Pride et al., 2004; Santos et al., 2006), or 2) different fluids (Santos et al., 1990) or patches of different saturation (Johnson, 2001).

Double porosity medium (DP in the text) refers to a porous medium which contains inclusions with different porosity and permeability (Pride et al., 2004; Santos et al., 2006). Assuming that the most compressible phase (patches, phase 2) is embedded into the least compressible one (host rock, phase1), the fluid flow inside the phase 2 can be eliminated from the homogenised equations. This assumption allowed Pride & Berryman (2003a, ,2003b) to write the DP equations under the form of the classical Biot theory (eq. 1). This involves the use of complex frequency dependent moduli K_U, C and M. Particularly, these parameters are functions of the respective volume of each phase and of the size of the patches (a denotes here the average radius of the inclusions in the host rock). Finally, as the patches are assumed to be spherical, the shear modulus of the medium is still real and not frequency dependent, and can be approximated by the geometrical mean of the modulus inside each phase. For the derivation and the detailed expressions of the parameters, please refer to the work of Pride et al. (2004) and Pride (2005).

To show how the mesoscopic attenuation due to DP media impacts the seismic properties, we look for the changes in the P-wave velocity and attenuation. The medium is composed of little patches of high permeable and high porosity in a less permeable host rock. Following the work of Liu et al. (2009), we consider a sandstone with 3% sand inclusions. The complex moduli K_U, C and M are computed using the DP effective theory of Pride et al. (2004), leading to the P-wave velocity and attenuation with respect to the frequency. The results are compared to the seismic properties of each single phase and to the response using an average single porosity medium, where moduli are computed by geometrical averages. Figure 2 shows the P-wave velocity and attenuation (via the inverse of the quality factor) for the double porosity medium (for the inclusion radius a equal to 1, 5 and 10 cm), for the average single porosity medium and for both single phase media.

The P-wave velocity is much more dispersive for the double porosity medium than for the equivalent single porosity medium. At high frequency, it is much higher in the double porosity medium than in the equivalent single porosity medium. It shows two main changes:

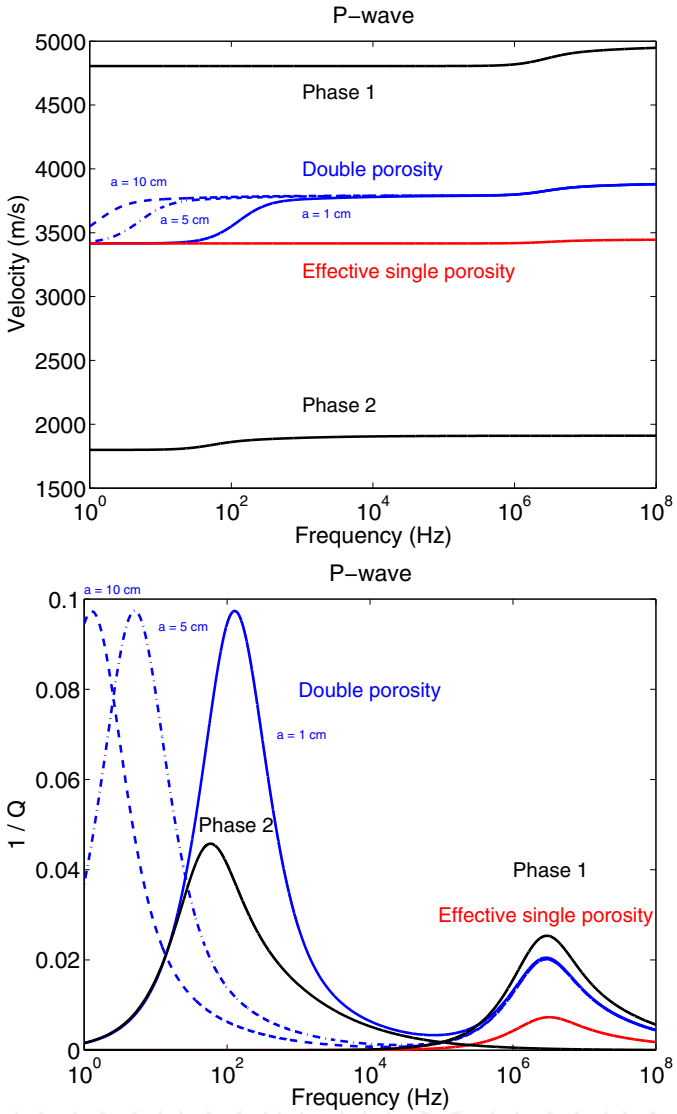

Fig. 2. P-wave velocities (top panel) and attenuations (bottom panel) with respect to the frequency (between 1 and 10^8 Hz). Blue lines are for the double porosity theory for inclusion sizes $a = 1$ cm (continuous lines), $a = 5$ cm (dotted-dashed lines) and $a = 10$ cm (dashed lines). Poroelastic responses of the individual phases are the black lines. The results for the average single porosity theory, computed using weighted average of each phase properties, are given by the red lines.

1) at the relaxation frequency of the host rock medium, which are at the transition between the diffusive and the propagative regime of the Biot wave, and 2) at low frequencies, around the relaxation frequency of the patches, with a strong dependance on a. It is worth noting that the size of inclusions, a, has an strong effect on the low frequency behaviour. We observe similar

patterns for the P-wave attenuation (inverse of the quality factor). In the double porosity medium, attenuation shows two main peaks, associated with the two phases, while the equivalent single poroelastic medium produces only one single peak at high frequency. At low frequency (seismic frequencies), the attenuation is very high for the double porosity medium, leading to quality factors that are in good agreement with quality factors in geological materials. This pattern strongly depends on the size of the inclusions. On the other hand, attenuation produced by single phase medium is too low to be realistic. This means that the fluid flow at the boundaries between heterogeneities plays a fundamental role in the attenuation process, that cannot be neglected. These P-wave characteristics will have a strong influence on the seismic waveforms (see section 3.2).

Using a poroelastic theory is much more complex than an equivalent visco-elastic theory. However, modelling seismic waves with poroelastic theories take into account the attenuation induced by fluid equilibration at layer interfaces or heterogeneity boundaries, whereas a viscoelastic approach neglects this attenuation process. As shown by Pride et al. (2004), this is the most important attenuation process at low frequency. As the shallow subsurface has strong lateral and vertical heterogeneities, one should solve the full poroelastic theory to deal with attenuation.

3. Numerical modelling of seismic waves in porous media

3.1 Forward modelling solution

The model properties $\mathbf{m}$, which are the material parameters introduced in the previous section, are nonlinearly related to the seismic data $\mathbf{d}$ via an operator f, i.e., $\mathbf{d} = f(\mathbf{m})$. The forward problem has been solved by many authors, using different methods. Analytical solutions have been derived for a homogeneous medium (Boutin et al., 1987; Philippacopoulos, 1997). The response of porous layered medium has been computed using reflectivity methods in the frequency-wavenumber domain, such as the Kennett (1983) approach (De Barros & Dietrich, 2008; Pride et al., 2002). This method was also used to solve the coupling between seismic and electromagnetic waves (Garambois & Dietrich, 2002; Haartsen & Pride, 1997). The poroelastic equations have been solved in 2D and 3D cases, mainly using finite difference schemes (Carcione, 1998; Dai et al., 1995; Masson & Pride, 2010; O'Brien, 2010) in the time-space domain. For discretisation issues, the equations (1) should be decomposed in propagative and diffusive parts, which have to be solved independently (Carcione, 1998). Other time domain numerical schemes have been used, such as finite elements (Morency & Tromp, 2008) or finite volume (de la Puente et al., 2008). Finally, Dupuy et al. (2011) solved this problem in the frequency domain using a discontinuous Galerkin approach. For a complete and precise review of the numerical modelling used to solve the poroelastic problem, we refer the reader to Carcione et al. (2010).

In this paper, we will use three different techniques to illustrate our points:

- a 3D Finite Difference scheme (FD; O'Brien, 2010): The solutions of Biot's equations are obtained by fourth-order in space and second-order in time staggered-grid and rotated-staggered-grid methods. Stability of the methods and accuracy of the solutions have been carefully checked in the low-frequency domain.
- a reflectivity approach (SKB; De Barros & Dietrich, 2008; De Barros et al., 2010): The 3D solution is obtained in the frequency-wavenumber domain for horizontally layered media

by using the generalized reflection and transmission method of Kennett (1983). The synthetic seismograms are finally transformed into the time-distance domain by using the 3D axisymmetric discrete wavenumber integration technique of Bouchon (1981).

- a Discontinuous Galerkin Method (DGM; Dupuy et al., 2011): For 2 dimension medium, the discrete linear system for the Biot theory has been deduced in the frequency domain for a discontinuous finite-element method, known as the nodal discontinuous Galerkin method. Solving this system in the frequency domain allows accurate modelling of the wave propagation for all frequencies.

The last two approaches are in the frequency domain, which has several advantages: 1) there is no need to decompose the problem into diffusive and propagative parts; 2) all frequencies, i.e., in the low- and high-frequency regimes, can be accuarately treated; 3) solving more complex theories, such as double porosity or poroviscoelastic theories is straighforward and does not require any modifications of the solver; and 4) frequency domain has been shown to be the most efficient way to solve the Full waveform inverse problem, as the solution has to be calculated only for a few frequencies (Pratt et al., 1998).

3.2 Seismic waveforms in poroelastic medium

As already stated, the main improvement of using poroelastic versus elastic theories is in the description of the attenuation from intrinsic medium parameters. Figure 3 gives an example of poroelastic and elastic data computed by equivalent finite difference codes (FD, O'Brien, 2010). The medium is a complex 200m thick reservoir embedded in a homogeneous half-space. The reservoir, modified from Manzocchi et al. (2008) is composed of 7 different facies, with different mineral and frame properties (see Fig. 3, top). In order to mimic a time lapse survey for CO_2 geological storage in a saline aquifer, a baseline is first computed for fully brine saturated medium. CO_2 is then injected in the center of the reservoir and spread out according to the permeability, leading to areas containing gas of roughly 500 m and 2000 m diameter.

Figure 3 presents the differential data (data with CO_2 in the reservoir minus baseline) for both gas extensions. The same models are run using equivalent elastic properties (computed through the Gassmann formulation). As the velocities are equal, arrival times of the elastic and poroelastic waves are the same. However, changes appear in amplitude, mainly in the multiple reflected waves and coda. The amplitude differences are up to 40% of the data. It stresses the importance of using attenuation in the forward modelling and inversion processes. Even if the Biot theory cannot explain the full range of attenuation, it leads to significant changes in the seismic waveforms.

Poroelastic attenuation is due to the fluid movement. In the poroelastic theories, evidence for this lies in the relative fluid-to-solid motion and in the existence of the slow P-wave. Figure 4 reproduces the experiment performed by Plona (1980). The models are made using the Discontinuous Galerking method (DGM) of Dupuy et al. (2011) and are checked against the reflectivity approach (SKB) used by De Barros & Dietrich (2008). The SKB synthetic data have been corrected from the 3D effects, using an infinite line of sources, in order to be directly comparable to the DGM solutions. A P-wave is generated with an explosive source (central frequency of 200 Hz) in an quasi-elastic layer (the Biot wave is entirely diffusive in this layer) and is transmitted and converted into S-wave and Biot wave at the interface with a porous layer. Receivers are set into the second layer and record the three waves.

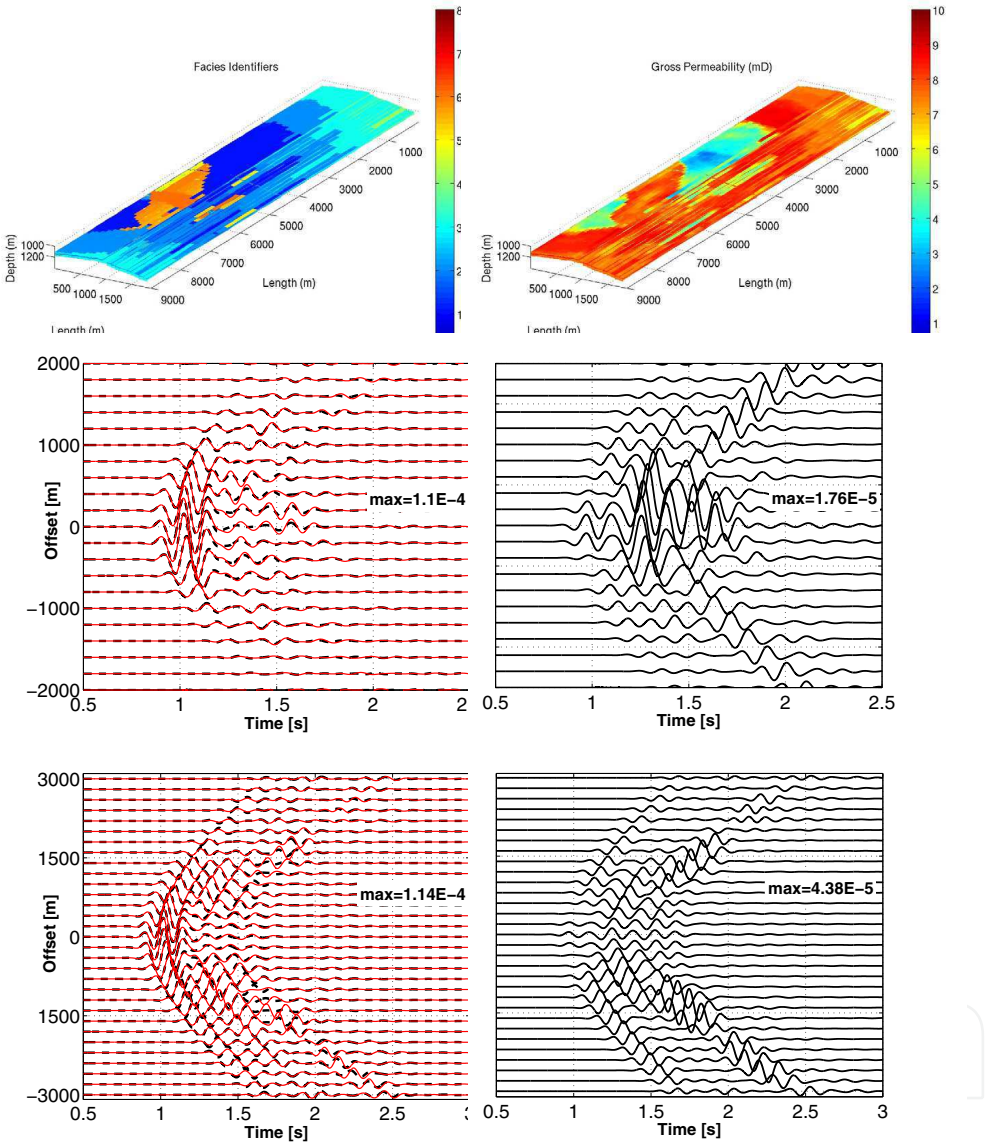

Fig. 3. Example of poroelastic and elastic numerical modelling to mimic differential data for CO_2 storage. Top) Resevoir models (left: Facies, right: Permeability) used in the modelling and modified from Manzocchi et al. (2008). Elastic properties are computed using the Gassmann relationships from the porous parameters. Middle) Left: Differential seismograms (model with CO_2 minus baseline) for elastic (red) and poroelastic data (black), and right: differences between the elastic and poroelastic differential data. Bottom) As the middle panels for a larger extension of CO_2. Receivers and source are located on the free surface. The explosive source has a 8Hz Ricker wavelet signature.

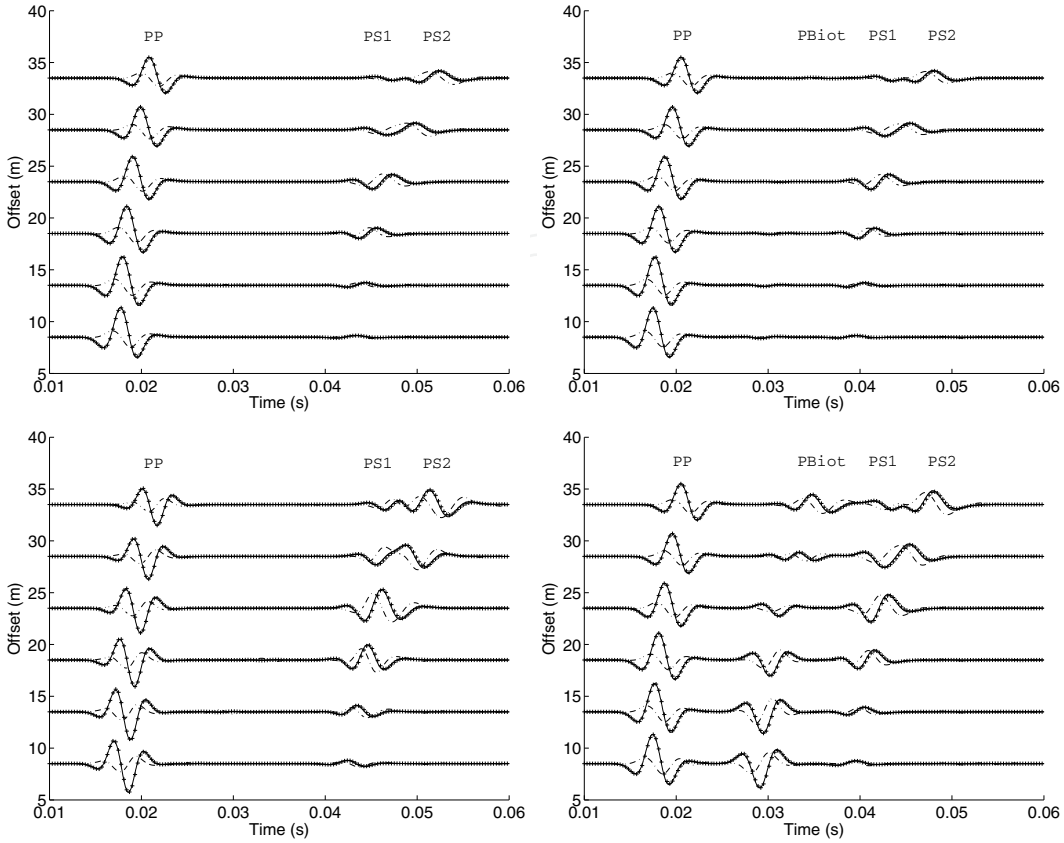

Fig. 4. Flat interface case: Left) Seismograms of (top) vertical solid u_z, and (bottom) relative fluid/solid displacement components w_z in the low-frequency regime; Right) As Left, but in the high-frequency domain. The SKB solution is indicated by a continuous line and the DGM by crosses; dashed-dotted lines indicate the differences between the two solutions (multiplied by a factor of 5). PP, PBiot and PS2 stand for the transmitted P and the converted Biot and S waves, respectively. PS1 stands for the conical wave associated with the direct P wave in the first layer. The explosive source is in a quasi-elastic layer, while receivers stand in a porous half space.

Two cases are studied: 1) a low frequency case, where the source frequency is smaller than the cut-off frequency (f_c = 6400 Hz). The Biot wave, in this case, is not propagative and cannot be seen; 2) a high frequency case, the source frequency is higher than the cut-off frequency (f_c = 0.64 Hz). This is obtained by decreasing the value of the fluid viscosity by 10000. The Biot wave becomes propagative, and can be observed, mainly in the fluid displacement data. In the seismograms of figure 4, the transmitted P-wave (PP), the conical wave associated with the P direct wave in the first layer (PS1), and the transmitted S-wave (PS2) are identified. These two S-waves (PS1 and PS2) will be uncoupled at further offsets. Finally, the very small differences between both modelling methods prove their accuracy.

A similar case is studied in a double porosity medium. Taking the same source/receiver layout with an explosive source in the first layer comprising a quasi-elastic sandstone and a line of receivers in the second layer comprising the double porosity medium described in the part 2.2 (sandstone with 3% of 1 *cm* spherical sand inclusions), we compute the seismograms and compare the double porosity results with the effective single porosity results. The seismograms of solid and relative fluid/solid displacements are given in figure 5. The influence of the double porosity homogeneization (via complex frequency dependent mechanic moduli) is clearly visible on the transmitted P-waves. Particularly, the waveforms are strongly distorted as the attenuation and dispersion are higher (see figure 2). As we are in the low frequency domain, the Biot waves are not visible in the seismograms, but they are responsible for the loss of seismic energy. As predicted by the theory, the converted S-waves are not impacted by the double porosity approach.

In these examples, we have demonstrated the importance of taking into account complex poroelastic theories in order to understand and reproduce real seismic signals whose waveforms are strongly impacted by the presence of fluid and medium heterogeneities.

4. Sensitivity analysis

In the next sections, we use the reflectivity algorithm SKB (De Barros & Dietrich, 2008) and focus on backscattered energy, i.e., we consider reflected seismic waves as in a seismic reflection experiment. We further assume that, whenever they exist, waves generated in the near surface (direct and head waves, surface and guided waves) are filtered out of the seismograms prior to the analysis. The assumption of plane-layered media is admittedly too simple to correctly describe the structural features of geological media, but it is nevertheless useful to explore the feasibility of an inversion process accounting for the rheology of porous media.

The sensitivity of the seismic waveforms to the model parameters is investigated for layered medium by computing the first-order derivatives of the seismic displacements with respect to the relevant poroelastic parameters. These operators, which are often referred to as the Fréchet derivatives, are expressed via semi-analytical formulae by using the Born approximation (De Barros & Dietrich, 2008). They can be readily and efficiently evaluated numerically because they are only functions of the Green's functions of the unperturbed medium. In each layer, we consider the eight following quantities as model parameters: 1) the porosity ϕ, 2) the mineral bulk modulus K_s, 3) the mineral density ρ_s, 4) the mineral shear modulus G_s, 5) the consolidation parameter c_s, 6) the fluid bulk modulus K_f, 7) the fluid density ρ_f and 8) the permeability k_0. This parameter set allows us to distinguish the parameters characterizing the solid phase from those describing the fluid phase. The fluid viscosity η is one of the input parameter but it is not considered in the inversion tests as its sensitivity is similar to the permeability.

Figure 6 (left) presents the sensitivity of the 8 parameters, for P and S waves. The sensitivity of the reflected wavefield varies drastically among the different parameters. We note that the reflected waves are especially sensitive to the mineral density ρ_s, porosity ϕ, shear modulus G_s and consolidation parameter cs. If we have some knowledge about the mineral properties (i.e., G_s, K_s and ρ_s are fixed), the porosity ϕ and consolidation factor cs are the most sensitive parameters and therefore the key parameters to consider in an inversion procedure. On the other hand, the viscosity η and permeability k_0 have only a weak influence (10^4 times smaller

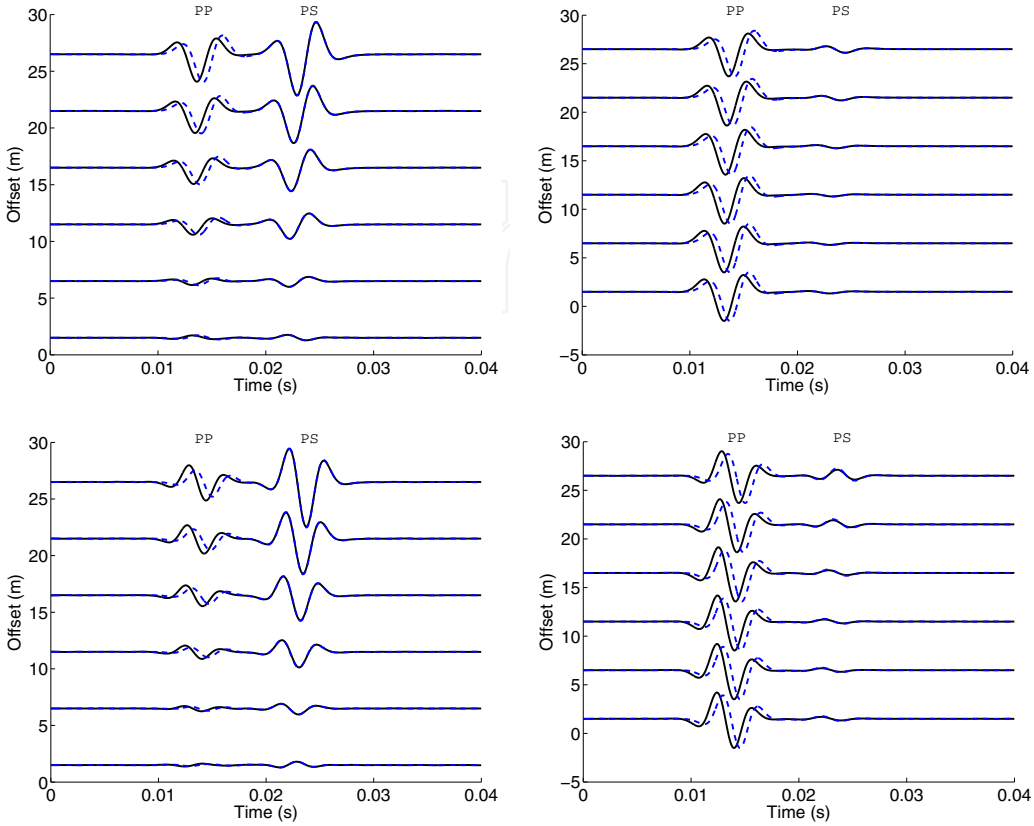

Fig. 5. Double porosity case: seismograms of top) solid displacement u_x (left) and u_z (right) and bottom) relative fluid/solid displacements w_x (left) and w_z (rigth). The setup is the same as for figure 4, the explosive source (Ricker with a 200Hz peak frequency) is in a quasi-elastic layer, while receivers stand in a double porosity half space. The double porosity solution is indicated by a continuous black line and the effective single porosity by a dashed blue line. PP and PS stand for the converted P and S waves, respectively.

than the porosity) on the wave amplitudes. The inversion for the parameters with such a low influence on the seismic waves will therefore be very delicate if other parameters are imperfectly known.

Figure 6 (right) shows the sensitivity of the P waves to the the fluid modulus K_f and the mineral solid modulus K_s. We note that the fluid modulus K_f has a stronger influence than the solid modulus K_s if the medium is poorly consolidated. The inverse is true for a consolidated medium. Similar patterns can be observed with the porosity: the higher the porosity, the stronger the influence of the fluid on the seismic waves. This means that it will be easier to determine fluid properties for an unconsolidated medium. For example, fluid substitution due to CO_2 injection leads to clear bright spot in Sleipner area (Norway, Arts et al., 2004), where the medium is poorly consolidated. The same set-up in stiff rocks does not produce such clear images, like in Weyburn field (Canada, White, 2009)

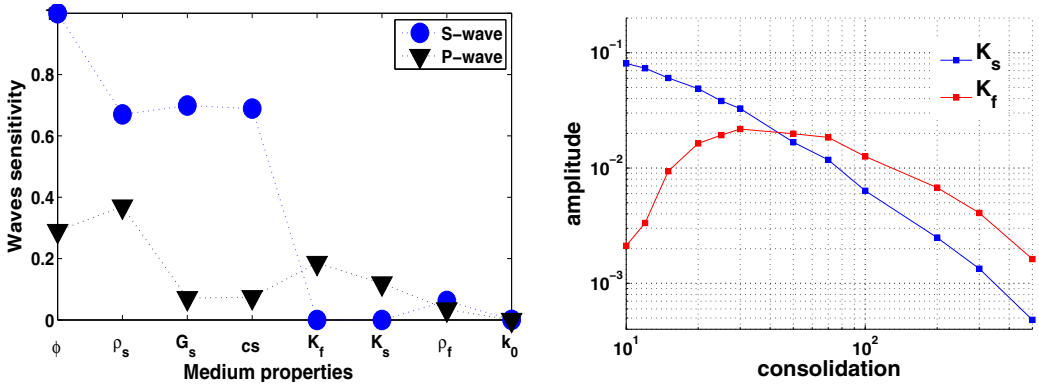

Fig. 6. Left) Sensitivity of the reflected waves to the porous parameters for the P (downward triangles) and S (circles) waves, i.e., maximum of the energy reflected back by a perturbation of the porous parameters. Right) Sensitivity of the reflected waves to the fluid K_f and the mineral bulk modulus K_s as a function of the consolidation parameter cs. Note that higher consolidation parameter cs corresponds to softer materials.

To evaluate the coupling between parameters, we look at the Amplitude Versus Angle (AVA) curves in figure 7 for the PP (left) and SS (right) reflected waves due to a small and localized perturbation of a model parameter. We note that for some parameters, the model perturbations lead to similar modifications of the seismic response. For example, perturbations in densities and permeability show identical AVA responses. The same is true for the bulk moduli. This strong coupling between parameters will prevent simultaneous reconstruction of these parameters in an inversion process.

Morency et al. (2009) also investigated the sensitivity of the seismic waves in porous media. They determined finite-frequency kernels based upon adjoint methods and investigated different parameter sets, in order to find the set that leads to the minimal coupling between parameters. They concluded that decomposing the input parameters into seismic velocities is the most stable approach in an inversion code.

5. Full waveform inversion

Full waveform inversion has shown to be an efficient and accurate tool to study the subsurface in the acoustic and elastic wave theory (Brossier et al., 2009). Historically, most of the FWI methods (Lailly, 1983; Tarantola, 1984) have been implemented under the acoustic approximation, for 2D model reconstruction (e.g. Gauthier et al., 1986; Pratt et al., 1998) or 3D structures (for instance, Ben-Hadj-Ali et al., 2008; Sirgue et al., 2008). Applications to real data are even more recent (Hicks & Pratt, 2001; Operto et al., 2006; Pratt & Shipp, 1999). The elastic case is more challenging, as the coupling between P and S waves leads to ill-conditioned problems. Since the early works of Mora (1987) and Kormendi & Dietrich (1991), the elastic problem has been addressed several times over the last years with methodological developments (Brossier et al., 2009; Choi et al., 2008; Gélis et al., 2007).

Using a poroelastic theory makes the problem even more difficult, especially because it adds much more unknowns. To the best of our knowledge, the first attempt to solve this

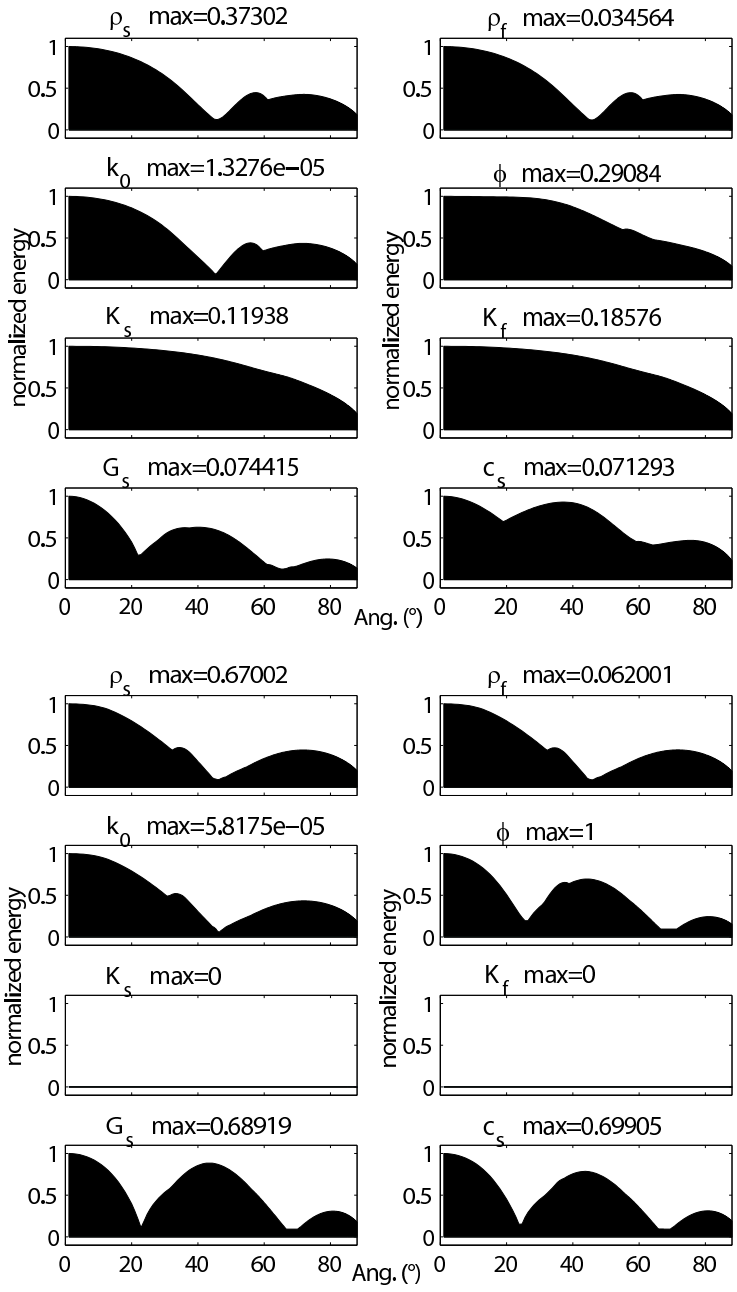

Fig. 7. Energy of plane waves reflected from perturbations in ρ_s, ρ_f, k_0, ϕ, K_s, K_f , G_s, and cs, as a function of incidence angle. The eight upper panels and eight lower panels correspond to PP and SS reflections, respectively. The curves are normalized with respect to the maximum value indicated above each panel.

problem was made by De Barros & Dietrich (2008) and De Barros et al. (2010) for stratified media and by Morency et al. (2009) and Morency et al. (2011) in 3-dimensional media. In the following sections, we will describe the main results obtained by De Barros & Dietrich (2008) and De Barros et al. (2010).

5.1 Inversion algorithm

Our method to determine the intrinsic properties of porous media is based on a full waveform iterative inversion procedure. It is carried out with a gradient technique to infer an optimum model which minimizes a misfit function. The latter is defined by a sample-to-sample comparison of the observed data $\boldsymbol{d_{obs}}$ with a synthetic wavefield $\boldsymbol{d} = f(\boldsymbol{m})$ in the time-space domain, and by an equivalent term describing the deviations of the current model $\boldsymbol{m}$ with respect to an *a priori* model $\boldsymbol{m_0}$, i.e.,

$$S(m) = \frac{1}{2} \, ||\boldsymbol{d} - \boldsymbol{d_{obs}}||_D + ||\boldsymbol{m} - \boldsymbol{m_0}||_M, \tag{6}$$

where the L2-norms $||\ .\ ||_D$ and $||\ .\ ||_M$ are defined in terms of a data covariance matrix $\boldsymbol{C_D}$ and an *a priori* model covariance matrix $\boldsymbol{C_M}$ Tarantola (1987). The model $\boldsymbol{m}$ contains the description of one or several parameters in layers whose thicknesses are defined by the peak content of the data (Kormendi & Dietrich, 1991). The model is updated using a quasi-Newton algorithm Tarantola (1987), which involves the Fréchet derivatives obtained earlier. As this problem is strongly non-linear, several iterations are necessary to converge toward an optimum model $\boldsymbol{m}$, i.e, a model whose response $\boldsymbol{d}$ satisfactorily fits the observed data $\boldsymbol{d_{obs}}$.

5.2 Numerical results

In order to determine the accuracy of the inversion procedure for the different model parameters considered, we first invert for a single parameter, in this case the mineral density ρ_s, and keep the others constant. The true model to reconstruct and the initial model used to initialize the iterative inversion procedure (which is also the *a priori* model) are displayed in figure 8. The other parameters are assumed to be perfectly known. Their vertical distributions consist of four 250 m thick homogeneous layers. Parameters ϕ, c_s and k_0 decrease with depth while parameters ρ_f, K_s, K_f and G_s are kept strictly constant.

Vertical-component seismic data (labelled DATA, fig 9) are then computed from the true model for an array of 50 receivers spaced 20 metres apart at offsets ranging from 20 to 1000 metres from the source. The latter is a vertical point force whose signature is a perfectly known Ricker wavelet with a central frequency of 25 Hz. Source and receivers are located at the free surface. As mentioned previously, direct and surface waves are not included in our computations to avoid complications associated with their contributions. Figure 9 also shows the seismogram (labelled INIT) at the beginning of the inversion, i.e., the seismogram computed from the starting model. Figure 8 shows that the true model, which consists in 10 metre thick layers from the surface to 1000 metre depth, is very accurately reconstructed by inversion. As there are no major reflectors in the deeper part of the model, very little energy is reflected toward the surface, which leads to some minor reconstruction problems at depth. In figure 9, we note that the final synthetic seismograms (SYNT) almost perfectly fit the input data (DATA) as shown by the data residuals (RES) which are very small.

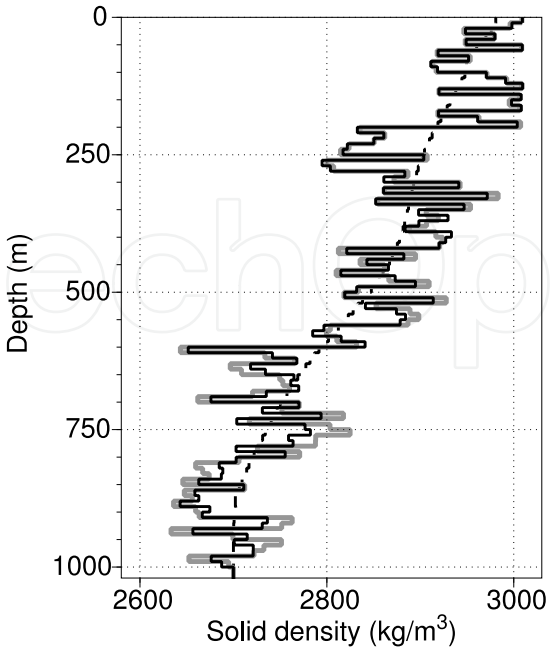

Fig. 8. Models corresponding to the inversion for the mineral density ρ_s: initial model, which is also the *a priori* model (dashed line), true model (thick grey line), and reconstructed model (black line). The corresponding seismograms are shown in figure 9.

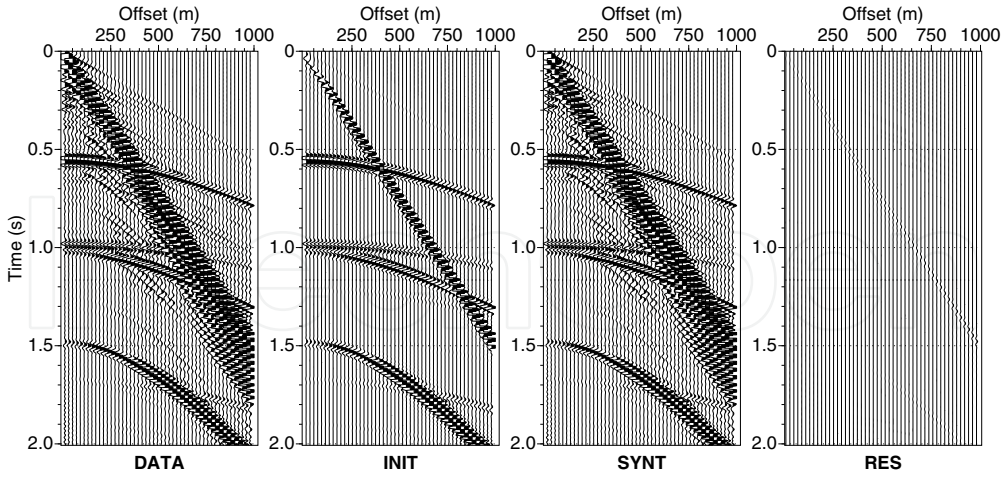

Fig. 9. Seismograms corresponding to the inversion for the mineral density ρ_s: synthetic data used as input (DATA), seismograms associated with the initial model (INIT), seismograms obtained at the last iteration (SYNT), and data residuals (RES) computed from the difference between the DATA and SYNT sections for the models depicted in figure 8. For convenience, all sections are displayed with the same scale, but the most energetic signals are clipped.

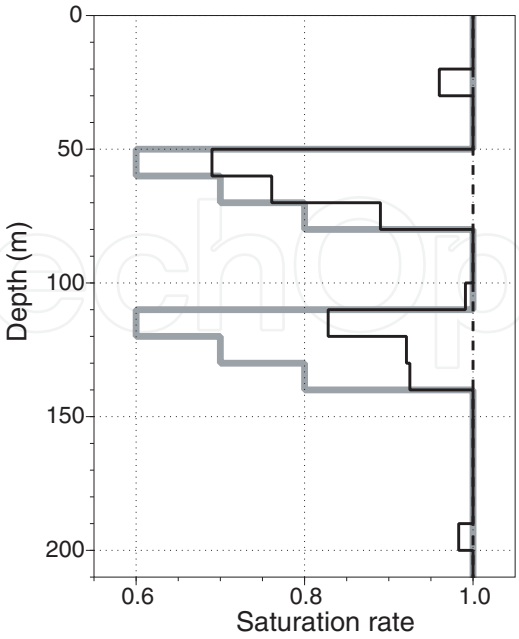

Fig. 10. Models corresponding to the differential inversion for the water saturation S_r : Initial model (dashed line), true model (thick grey line), and reconstructed model (black line).

The inversions carried out for the ϕ, ρ_f, K_s, K_f, G_s and c_s parameters (not shown) exhibit the same level of accuracy. However, as predicted by De Barros & Dietrich (2008) and Morency et al. (2009) with two different approaches, the weak sensitivity of the reflected waves to the permeability does not allow us to reconstruct the variations of this parameter. Being related to seismic wave attenuation and fluid flow, permeability appears as not only the most difficult parameter to estimate but also the one which would have the greatest benefits to the characterization of porous formations, notably in the oil industry (Pride et al., 2003). One possibility to estimate it is to measure the fluid motion, or, by reciprocity, to use fluid pressure sources.

As observed in the sensitivity study, parameters are strongly coupled. Multiparameter inversion is thus an ill-posed problem, which is, in most of the cases, not reliable, as errors on one parameter will map into the reconstruction of the other parameters. The use of analytical expressions for the sensitivity kernels allows an easy rearrangement of the parameter set, in order to invert for the most pertinent parameters. Using some *a priori* information, it is then possible to efficiently decrease the number of unknown parameters. For example, there is no reason to invert for both fluid parameters ρ_f and K_f, if we know that pores are filled by either gas or water. It is much more efficient to invert only for the saturation rate.

5.3 Differential inversion

To reduce the ambiguities of multiparameter inversion, a differential inversion has been considered and implemented (De Barros et al., 2010). Instead of dealing with the full complexity of the medium, we concentrate on small changes in the subsurface properties such

as those occurring over time in underground fluid-filled reservoirs. This approach may be particularly useful for time-lapse studies to follow the extension of fluid plumes or to assess the fluid saturation as a function of time.

For example, the monitoring of CO_2 underground storage sites mainly aims at mapping the CO_2 extension. Time lapse studies performed over the Sleipner CO_2 injection site in the North Sea (see e.g. Arts et al., 2004) highlight the variations of fluid content as seen in the seismic data after imaging and inversion. In this fluid substitution issue, the parameter of interest is the carbon dioxide/saline water relative saturation. A differential inversion process will allow us to free ourselves from the unknown model parameters. This approach is valid for any type of fluid substitution monitoring problem, such as water-table variation, gas and oil extraction or hydrothermal activity.

The first step in this approach is to perform a base or reference survey to estimate the solid properties before the fluid substitution occurs. When performing a multiparameter inversion, the model properties are poorly reconstructed in general. However, the seismic data are reasonably well recovered. Thus, in spite of its defects, the reconstructed model respects the wave kinematics of the input data. In other words, the inverted model provides a description of the solid earth properties which can be used as a starting model for subsequent inversions. The latter would be used to estimate the fluid variations within the subsurface from a series of monitor surveys (second step).

To test this concept, we perform an inversion for two strongly coupled parameters, namely the porosity and the consolidation parameter. The resulting models are then used as starting models. We perturb the fluid properties of the true model to simulate a fluid variation over time. Two 30-metre thick layers located between 50 and 80 metres depth and between 110 and 140 metres depth are water depleted due to gas injection. The water saturation then varies between 60 and 80% in these two layers (figure 10). Our goal is to estimate the fluid properties by inverting the seismic data for the water saturation.

The model obtained is displayed in figure 10. We see that the location and extension of the gas-filled layers are correctly estimated. The magnitude of the water saturation curve, which defines the amount of gas as a function of depth, is somewhat underestimated in the top gas layer but is nevertheless reasonably well estimated. In the bottom gas layer, the inversion procedure only provides a qualitative estimate of the water saturation. These computations show that the differential inversion approach is capable of estimating, with reasonably good quality, the variations of fluid content in the subsurface without actually knowing all properties of the medium.

6. Conclusion

Using a poroelastic theory is much more complex than an elastic or a visco-elastic theory. However, poroelastic theories are an attempt to quantitatively describe the attenuation processes from the physical properties of the geological material. Furthermore, at seismic frequencies, attenuation is dominated by the mesoscopic scale mechanism, involving fluid flow at the boundaries of any heterogeneities. Poroelastic theories intrinsically take into account this loss of energy, while the equivalent visco-elastic approach neglects it. As the near surface media are stronly heterogeneous, with strong lateral and vertical contrasts, and different fluids involved, one has to deal with full poroelastic theories to accurately consider attenuation and fluid-solid motions.

The sensitivity to the different parameters varies hugely among parameters, and parameters are strongly coupled. Using a poroelastic theory to reconstruct model properties is in its nature an ill-conditioned problem. It shows however very promising possibility for differential inversion, and for certain issues where the problems can be reduced to the determination of only few parameters.

Poroelastic theories are, of course, not perfect yet, as they fail to give an universal law to explain seismic wave attenuation and propagation. They are however the direction to go if one wants to use full waveform inversion to make quantitative imagery of the rock physics and subsurface fluids. In particular, the permeability is a key parameter for exploration; the reconstruction of such a parameter from seismic waves will necessitate the use of complex poroelastic theories. Development in this direction still has to be continued. In particular, for imagery problems, data have to be improved to get around the problems of coupling between parameters. This can be done by using the information carried by fluid motions, which can give new insights into the permeability and the fluid properties, or by exploring in deeper details the coupling between seismic and electromagnetic waves.

7. Acknowledgements

L. De Barros and G. S. O'Brien were partly funded by the department of Communications, Energy and Natural Resources (Ireland) under the National Geosciences programme 2007-2013. B. Dupuy, S. Garambois and J. Virieux are supported by the National Research Agency (ANR) "Captage et Stockage de CO_2" program (ANR-07-PCO2-002). The numerical computations were performed by using the computational facilities from SFI/HEA ICHEC (Ireland), the HPC national computer centers (France, CINES and IDRIS under the allocation 2010-046091 GENCI) and the HPC center of the Grenoble observatory (OSUG).

8. References

Arts, R., Eiken, O., Chadwick, A., Zweigel, P., des Meer, L. V. & Zinszner, B. (2004). Monitoring of CO_2 injected at Sleipner using time-laps seismic data., *Energy* 29: 1323–1392.

Auriault, J.-L., Borne, L. & Chambon, R. (1985). Dynamics of porous saturated media, checking of the generalized law of Darcy, *J. Acoust. Soc. Am.* 77(5): 1641–1650.

Ben-Hadj-Ali, H., Operto, S. & Virieux, J. (2008). Velocity model-building by 3-D frequency-domain, full waveform inversion of wide aperture seismic data, *Geophysics* 73(5): 101–117.

Berryman, J. & Wang, H. (2000). Elastic wave propagation and attenuation in a double-porosity dual permeability medium, *Int. J. Rock Mech.* 37: 63–78.

Biot, M. (1956). Theory of propagation of elastic waves in a fluid-saturated porous solid. I. Low-frequency range, II. Higher frequency range, *J. Acoust. Soc. Am.* 28: 168–191.

Bouchon, M. (1981). A simple method to calculate Green's functions for elastic layered media, *Bull. Seism. Soc. Am.* 71(4): 959–971.

Boutin, C., Bonnet, G. & Bard, P. (1987). Green functions and associated sources in infinite and stratified poroelastic media, *Geophys. J. Roy. Astr. Soc.* pp. 521–550.

Brossier, R., Operto, S. & Virieux, J. (2009). Seismic imaging of complex onshore structures by 2D elastic frequency-domain full-waveform inversion, *Geophysics* 74(6): 63–76.

Carcione, J. (1998). Viscoelastic effective rheologies for modelling wave propagation in porous media, *Geophysical Prospecting* 46: 249–270.

Carcione, J. M., Morency, C. & Santos, J. E. (2010). Computational poroelasticity - a review, *Geophysics* 75: A229–A243.

Choi, Y., Min, D.-J. & Shin, C. (2008). Two-dimensional waveform inversion of multi-component data in acoustic-elastic coupled media, *Geophysical Prospecting* 56(19): 863–881.

Dai, N., Vafidis, A. & Kanasewich, E. (1995). Wave propagation in heteregeneous porous media: A velocity-stress, finite-difference method, *Geophysics* 60(2): 327–340.

De Barros, L. & Dietrich, M. (2008). Perturbations of the seismic reflectivity of a fluid-saturated depth-dependent poroelastic medium, *J. Acoust. Soc. Am.* 123(3): 1409–1420.

De Barros, L., Dietrich, M. & Valette, B. (2010). Full waveform inversion of seismic waves reflected in a stratified porous medium, *Geophy. J. Int.* 182(3): 1543–1556.

de la Puente, J., Dumbser, M., Käser, M. & Igel, H. (2008). Discontinuous galerkin methods for wave propagation in poroelastic media., *Geophysics* 73(5): 77–97.

Dupuy, B., De Barros, L., Garambois, S. & Virieux, J. (2011). Wave propagation in heterogeneous porous media formulated in the frequency-space domain using a discontinuous galerkin method, *Geophysics* 76: N13–N21.

Garambois, S. & Dietrich, M. (2002). Full waveform numerical simulations of seismoelectromagnetic wave conversions in fluid-saturated stratified porous media, *J. Geophys. Res.* 107(B7): 2148–2165.

Gassmann, F. (1951). Über die elastizität poröser medien, *Vierteljahrsschrift der Naturforschenden Gesellschaft in Zürich* 96: 1–23.

Gauthier, O., Virieux, J. & Tarantola, A. (1986). Two dimensionnal nonlinear inversion of seismic waveforms: numerical results, *Geophysics* 51: 1387–1403.

Geertsma, J. & Smith, D. (1961). Some aspects of elastic wave propagation in fluid-saturated porous solid, *Soc. Pet. Eng. J.* 26: 235–248.

Gélis, C., Virieux, J. & Grandjean, G. (2007). Two-dimensional elastic full waveform inversion using Born and Rytov formulations in the frequency domain, *Geophy. J. Int.* 168(2): 605–633.

Gurevich, B., Zyrianov, V. & Lopatnikov, S. (1997). Seismic attenuation in finely layered porous rocks: Effects of fluid flow and scattering, *Geophysics* 62(1): 319–324.

Haartsen, M. & Pride, S. (1997). Electroseismic waves from point sources in layered media, *J. Geophys. Res.* 102(B11): 745–769.

Hicks, G. & Pratt, R. (2001). Reflection waveform inversion using local descent methods: Estimating attenuation and velocity over a gas-sand deposit, *Geophysics* 66: 598–612.

Johnson, D. (2001). Theory of frequency dependent acoustics in patchy-saturated porous media, *J. Acoust. Soc. Am.* 110(2): 682–694.

Johnson, D., Koplik, J. & Dashen, R. (1987). Theory of dynamic permeability and tortuosity in fluid-saturated porous media, *Journal of Fluid Mechanics.* 176: 379–402.

Johnson, D., Plona, T. & Kojima, H. (1994). Probing porous media with first and second sound. I. dynamic permeability., *Journal of Applied Physics* 76(1): 104–125.

Kennett, B. (1983). *Seismic Wave Propagation in Stratified Media*, 342 p, Cambridge University Press, Cambridge.

Kormendi, F. & Dietrich, M. (1991). Nonlinear waveform inversion of plane-wave seismograms in stratified elastic media, *Geophysics* 56(5): 664–674.

Korringa, J., Brown, R., Thompson, D. & Runge, R. (1979). Self-consistent imbedding and the ellipsoidal model for porous rocks, *J. Geophys. Res.* 84: 5591–5598.

Lailly, P. (1983). The seismic inverse problem as a sequence of before stack migrations, *in* J. B. Bednar, R. Redner, E. Robinson & A. Weglein (eds), *Conference on Inverse Scattering: Theory and Application*, Soc. Industr. Appl. Math.

Liu, X., Greenhalgh, S. & Zhou, B. (2009). Transient solution for poro-viscoacoustic wave propagation in double porosity media and its limitations, *Geophy. J. Int.* 178: 375–393.

Manzocchi, T., Carter, J. N., Skorstad, A., Fjellvoll, B., Stephen, K. D., Howell, J., Matthews, J. D., Walsh, J. J., Nepveu, M., Bos, C., Cole, J., Egberts, P., Flint, S., Hern, C., Holden, L., Hovland, H., Jackson, H., Kolbjornsen, O., MacDonald, A., Nell, P., Onyeagoro, K., Strand, J., Syversveen, A. R., Tchistiakov, A., Yang, C., Yielding, G. & Zimmerman, R. (2008). Sensitivity of the impact of geological uncertainty on production from faulted and unfaulted shallow marine oil reservoirs - objectives and methods, *Petroleum Geoscience* 14: 3–15.

Masson, Y. & Pride, S. (2010). Finite-difference modeling of Biot's poroelastic equations across all frequencies, *Geophysics* 75(2): 33–41.

Mavko, G. & Jizba, D. (1991). Estimating grain-scale fluid effects on velocity dispersion in rocks, *Geophysics* 56: 1940–1949.

Mora, P. (1987). Nonlinear two-dimensional elastic inversion of multioffset seismic data, *Geophysics* 52: 1211–1228.

Morency, C., Luo, Y. & Tromp, J. (2009). Finite-frequency kernels for wave propagation in porous media based upon adjoint methods, *Geophy. J. Int.* 179(2): 1148–1168.

Morency, C., Luo, Y. & Tromp, J. (2011). Acoustic, elastic and poroelastic simulations of co2 sequestration crosswell monitoring based on spectral-element and adjoint methods, *Geophy. J. Int.* 185(2): 955–966.

Morency, C. & Tromp, J. (2008). Spectral-element simulations of wave propagation in porous media, *Geophy. J. Int.* 175(1): 301–345.

O'Brien, G. (2010). 3D rotated and standard staggered finite-difference solutions to Biot's poroelastic wave equations: Stability condition and dispersion analysis, *Geophysics* 75(4): T111–T119.

Operto, S., Virieux, J., Dessa, J. X. & Pascal, G. (2006). Crustal-scale seismic imaging from multifold ocean bottom seismometer data by frequency- domain full-waveform tomography: application to the eastern nankai trough, *J. Geophys. Res.* 111: B09306.

Philippacopoulos, A. (1997). Buried point source in a poroelastic half-space, *J. Engineering Mechanics* 123(8): 860–869.

Plona, T. (1980). Observation of a second bulk compressional wave in a porous medium at ultrasonic frequencies, *Appl. Phys. Lett.* 36(4): 259–261.

Pratt, R., Shin, C. & Hicks, G. (1998). Gauss-Newton and full Newton methods in frequency-space seismic waveform inversion, *Geophy. J. Int.* 133(22): 341–362.

Pratt, R. & Shipp, R. (1999). Seismic waveform inversion in the frequency domain, part II: Fault delineation in sediments using crosshole data, *Geophysics* 64(3): 902–914.

Pride, S. (2005). Relationships between seismic and hydrological properties, in *Hydrogeophysics*, Water Science and Technology Library, Springer, chapter 8, pp. 253–284.

Pride, S. & Berryman, J. (2003a). Linear dynamics of double-porosity dual-permeability materials, i. governing equations and acoustic attenuation, *Physical Review E* 68: 1–211.

Pride, S. & Berryman, J. (2003b). Linear dynamics of double-porosity dual-permeability materials, ii. fluid transport equations, *Physical Review E* 68: 1–211.

Pride, S., Berryman, J. & Harris, J. (2004). Seismic attenuation due to wave-induced flow, *J. Geophys. Res.* 109: B01201.

Pride, S., Gangi, A. & Morgan, F. (1992). Deriving the equations of motion for porous isotropic media, *J. Acoust. Soc. Am.* 92(6): 3278–3290.

Pride, S., Harris, J., Johnson, D., Mateeva, A., Nihei, K., Nowack, R., Rector, J., Spetzler, H., Wu, R., Yamamoto, T., Berryman, J. & Fehler, M. (2003). Permeability dependence of seismic amplitudes, *The Leading Edge* 22: 518–525.

Pride, S., Tromeur, E. & Berryman, J. (2002). Biot slow-wave effects in stratified rock, *Geophysics* 67: 201–211.

Santos, J. E., Douglas, J., Corbero, J. & Lovera, O. M. (1990). A model for wave propagation in a porous medium saturated by a two-phase fluid, *J. Acoust. Soc. Am.* 87(4): 1439–1448.

Santos, J. E., Ravazzoli, C. L. & Geiser, J. (2006). On the static and dynamic behavior of fluid saturated composite porous solids: A homogenization approach, *International Journal of Solids and Structures* 43(5): 1224–1238.

Sirgue, L., Etgen, J. & Albertin, U. (2008). 3D frequency domain waveform inversion using time domain finite difference methods, *Extended Abstracts, 70th EAGE Conference & Exhibition, Rome*, number F022.

Tarantola, A. (1984). The seismic reflection inverse problem, in *Inverse Problems of Acoustic and Elastic Waves*, SIAM, Philadelphia, pp. 104–181.

Tarantola, A. (1987). *Inverse Problem Theory: Methods for data fitting and model parameter estimation*, Elsevier, Amsterdam.

White, D. (2009). Monitoring CO2 storage during EOR at the Weyburn-Midale Field, *The Leading Edge* 28(7): 838–842.

2.2.2. Suivi des variations du milieu

Pour suivre les variations du milieu, des techniques d'interférométrie, appliquées soit sur la coda de multiplets, soit sur les fonctions de Green reconstruites par corrélation, permettent de reconstruire des variations de vitesses sismiques extrêmement fines, de l'ordre de 0.1%. De telles approches ont permis d'imager des variations du milieu associées à des séismes (Froment et al., 2013), des éruptions volcaniques (Brenguier et al., 2008), des glissements lents (Rivet et al., 2011), des modifications du contenu en fluide (Hillers et al., 2014), etc. En se basant sur la coda des signaux, ces analyses sont surtout sensibles aux ondes S, ce qui ne permet pas une relation directe et non ambiguë avec les fluides.

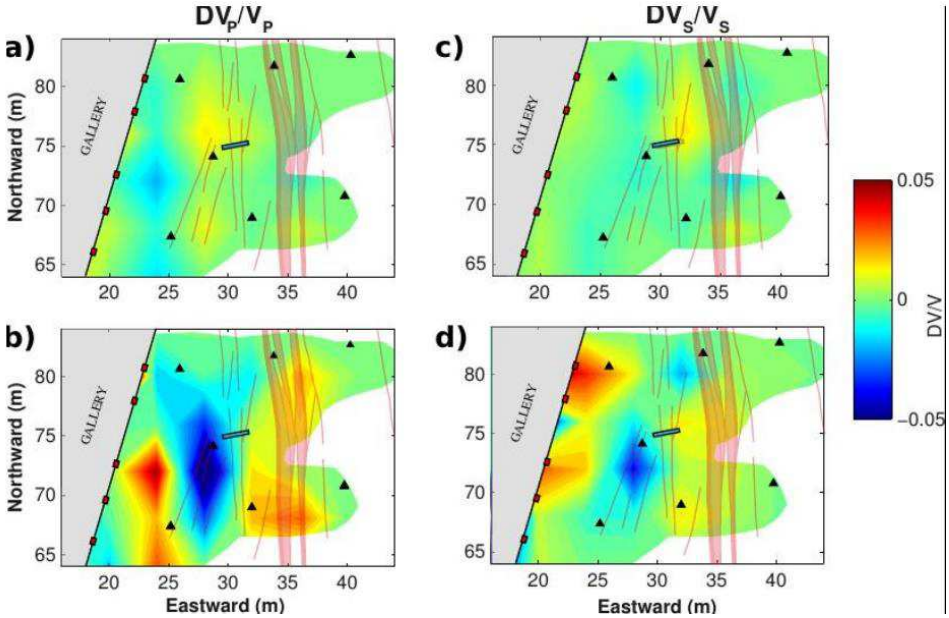

***Figure 13**: Carte de variations des vitesses des ondes P (a et b) et des ondes S (c et d), associées à une injection de fluide (rectangle bleue), à basse pression (a et c) et à haute pression (b et d). La zone bleue (b et d) est reliée à la réactivation asismique des failles, tandis que les variations positives autour sont dues à des augmentations des contraintes de confinement (**Rivet et al., 2017**)*

Lors des expériences de réactivation de faille dans les argilites de Tournemire, nous avons utilisé des sources actives et répétitives. Nous avons pu ainsi mesurer simultanément les variations des vitesses des trajets directs des ondes P et S, et ainsi imager les variations en fluide et du milieu. Nous avons montré (**Rivet et al., 2016**) que les variations de vitesse sismique obtenues par interférométrie permettait de suivre les modifications autour d'une faille en glissement (*Figure 13*). Comme les vitesses d'ondes P et d'ondes S sont impactées de manière similaire, nous avons principalement attribué ces perturbations à des ouvertures/fermeture de micro-fractures lors d'épisodes de transferts de contraintes. Ainsi, différentes phases ont été vues :

1) Avant la rupture, les augmentations de vitesses suggèrent une fermeture des microfractures par augmentation de la pression de confinement autour de l'injection ;
2) Lors de la rupture, une zone de d'une dizaine de mètres de long montre de très fortes chutes de vitesses, associées au glissement dilatant des failles secondaires dans lesquelles

l'injection est réalisée (Guglielmi et al., 2015b). Cette zone est entourée par des augmentations de vitesses dues aux transferts de contraintes

3) Après la fin des injections, le milieu retrouve les vitesses initiales en quelques heures.

L'interprétation de ces variations a ensuite été validée par modélisations numériques. Comme ce glissement ne s'accompagne pas de sismicité, les variations de vitesse ont ainsi permis de montrer les modifications de contraintes associées à un glissement lent. En particulier, la résolution obtenue ici suggère que les faibles chutes de vitesse observées lors des glissements sismiques (Froment et al., 2013) peuvent être en réalité une moyenne de fortes chutes au niveau de la faille et d'augmentation par transfert de contraintes autour.

2.2.3. Imagerie des réservoirs magmatiques

Je me suis aussi intéressé, durant mon master et mon postdoctorat aux zones de stockages magmatiques sous les volcans. L'existence de chambres magmatiques continues, et surtout leur géométrie et volume, sont toujours en question. En effet, de tels réservoirs ont été imagés sous les dorsales océaniques (Singh et al., 2006), mais leur reconstruction sous les volcans restent difficile, souvent basée sur des observations indirectes ou sur des tomographie faiblement contrainte (Aloisi et al., 2002; Auger et al., 2001; García-Yeguas et al., 2012; Lees, 2007) . L'imagerie de telle structures est en effet rendue délicate par 1) un environnement bruité, avec une subsurface très hétérogène et une topographie fortement accidentée ; 2) un contraste de vitesse entre le magma et l'encaissant pouvant être positif, négatif ou nul, selon le contenu en gaz (Lees, 2007) ; et 3) une géométrie de stockage inconnue, qui peut être sous forme d'un réseaux de fractures, (« sills », « dikes »,…) plutôt que d'un volume continu.

Durant mon master, nous avons recherché si il existait une anomalie des vitesses en ondes S sous le volcan Popocatépetl (Mexique), à partir de l'analyse par des méthodes d'antennes des ondes de surfaces de séismes régionaux et lointains (**De Barros et al., 2008**). Pas d'anomalies nettes ont été observées, sauf une importante diffraction des ondes de surface entre 6 et 12s. Ces observations peuvent suggérer la présence d'un stockage diffractant à des profondeurs de 5 à 10 km.

En suivant cette idée, j'ai ensuite travaillé sur des données de sismiques actives acquises sur le volcan Teide (Canaries). Des tirs en mer (« airgun ») tout autour de l'ile de Tenerife ont été enregistrés par 137 stations sismologiques installées sur le volcan (Ibáñez et al., 2008). García-Yeguas et al. (2012) ont réalisé un modèle tomographique 3D sous le volcan, qui ne révèle pas d'anomalies clairement reliées à un stockage magmatique. En prenant l'hypothèse que l'information à utiliser est portée par les ondes diffractées, j'ai utilisé une méthode de double formation de voies pour faire une imagerie en points diffractants. Des tests numériques m'ont permis d'améliorer et tester la méthode. J'ai ainsi pu montrer que deux zones, l'une superficielle sous le cratère et une autre plus profonde au nord de l'édifice, diffractent les ondes (Figure 14**, De Barros et al., 2012**). Elles peuvent correspondre à des stockages magmatiques, en accord avec d'autres observations sur ce volcan (Martí et al., 2008).

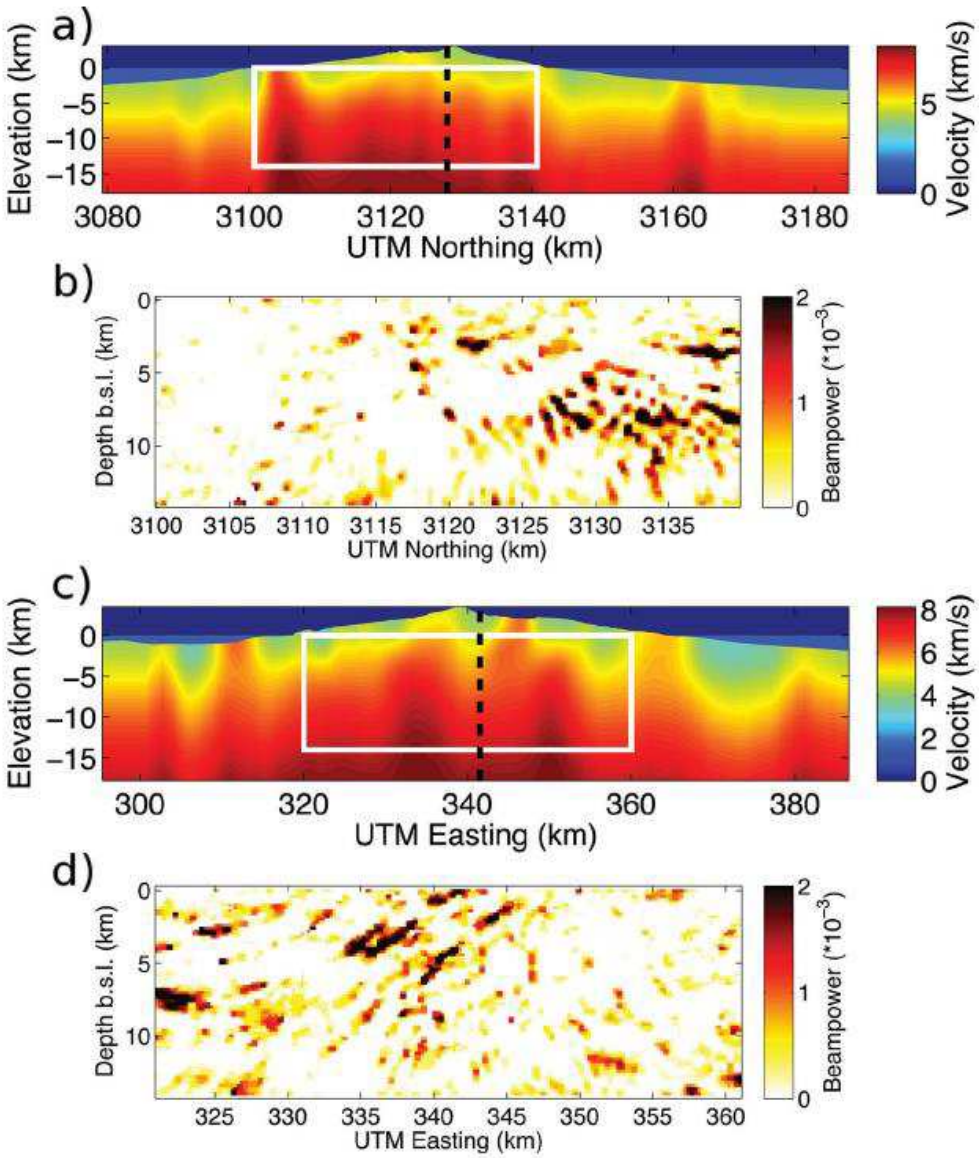

***Figure 14**: a) et c) Modèles tomographiques dans des coupes nord-sud (a) et est-ouest (c), (Garcia-Yeguas et al., 2012). Résultat de l'analyse par double formation de voies dans les directions nord-sud (b) et est-ouest (d), au niveau des zones encadrées en blanc dans les coupes tomographiques. Les couleurs sombres indiquent une forte diffraction des ondes. Deux anomalies apparaissent: une zone entre 5 et 10 km au nord du volcan, et une zone plus superficielle (3-5 km) sous le cratère (**De Barros et al., 2012**).*

2.3. Signatures sismiques non conventionnelles

Articles publiés dans ce thème

Zecevic+ M., De Barros L., Eyre+ T. S., Lokmer I., Bean C. (2016) Relocation of Long Period (LP) seismic events reveals en echelon fractures in the upper edifice of Turrialba volcano, Costa Rica, *Geophysical Research Letters*, vol.43 (19), pp.10,105-10,114.

Derode+, B., Guglielmi, Y., De Barros, L., & Cappa, F. (2015). Seismic responses to fluid pressure perturbations in a slipping fault. *Geophysical Research Letters*, *42*(9), 3197-3203.

Bean C. J., De Barros L., Lokmer I., Métaxian J.-P., O'Brien G., Murphy S., 2014, Long-period seismicity in the shallow volcanic edifice formed from slow-rupture earthquakes, Nature Geoscience, vol.7, pp.71-75, 2014

Eyre+ T.S., C. J. Bean, L. De Barros, F. Martini, I. Lokmer, M. M. Mora, J. F. Pacheco, G. J. Soto. A brittle failure model for long-period seismic events recorded at Turrialba volcano, Costa Rica, *Journal of Geophysical Research: Solid Earth*, *120*(3), 1452-1472.

De Barros L., Lokmer I., Bean C. J., 2013. Origin of spurious single forces in the source mechanism of volcanic seismicity, *J. Volc. Geotherm. Res.* (262), pp.1-6

Eyre+, T.S., C.J. Bean, L. De Barros, G.S. O'Brien, F. Martini, I. Lokmer, M.M. Mora, J.F. Pacheco, G.J. Soto, 2013, Moment tensor inversion for the source location and mechanism of long period (LP) seismic events from 2009 at Turrialba volcano, Costa Rica, *J. Volc. Geotherm. Res.,* doi :10.1016/j.jvolgeores.2013.04.016.

Zecevic+, M., L. De Barros, C. J. Bean, G. S. O'Brien, F., Brenguier, 2013, Investigating the source characteristics of long-period (LP) seismic events recorded on Piton de la Fournaise volcano, La Réunion. *J. Volc. Geotherm. Res.*, Vol. 258, pp 1–11, doi :10.1016/j.jvolgeores.2013.04.009

Davi+, R., G. O'Brien, L. De Barros, I. Lokmer, C. Bean, P. Lesage, M. Mora. 2011. Seismic source mechanisms of tremor events recorded on Arenal vocano, Costa Rica. *J. Volc. Geotherm. Res*. (213-214), pp 1-13

De Barros, L., I. Lokmer, C. Bean, G. O'Brien, G. Saccorotti, J.-P. Métaxian, L. Zuccarello, and D. Patanè, 2011. Source Mechanism of Long Period events recorded by a high density seismic network during the 2008 eruption on Mt Etna, J. Geophys. Res.,116, B01304, doi:10.1029/2010JB007629.

O'Brien, G. S., I. Lokmer, L. De Barros, C. J. Bean G. Saccorotti, J-P Métaxian and D. Patanè, 2011. Time Reverse Location of Seismic Long-Period events recorded on Mt Etna. *Geophys. J. Int.*, 184(1): 452-462

De Barros, L., C.J. Bean, I. Lokmer, G. Saccorotti, L. Zuccarello, G. O'Brien, J.-P. Métaxian, and D. Patanè, 2009. Source geometry from exceptionally high resolution long period event observations at Mt Etna during the 2008 eruption. *Geophys. Res. Lett.*, 36. doi : 10.1029/2009GL041273.

Des signatures sismiques avec des formes d'ondes différentes de celles de la sismicité classique sont observées dans différents environnements géologiques. Alors que les sources des séismes « conventionnels » sont associées à des glissements instables sur des failles, les processus à l'origine de la sismicité dite non conventionnelle restent débattus, mais peuvent être reliés aux fluides et/ou aux déformations lentes. Il est donc nécessaire de comprendre l'origine de ces signaux pour 1) mieux comprendre les processus hydro-mécanique en profondeur et 2) les utiliser de manière optimale dans la surveillance des risques et des réservoirs. Dans ce but, j'ai en particulier travaillé sur les évènements volcaniques Longues Périodes, pour lesquels nous avons suggéré une origine liée à du glissement lent (2.3.1), et sur les signatures sismiques « étranges » observées dans les expériences in-situ (0).

2.3.1. Signatures volcaniques longues Périodes

Les signaux volcaniques « Longues Périodes » sont des signaux émergents, avec un contenu fréquentiel étroit, centré autour de 0.1 à 1Hz. Ils accompagnent les phases pré-éruptives, et sont donc utilisés pour l'anticipation des éruptions (Chouet, 1996). Comme ces signaux sont répétitifs et basses fréquences, un mécanisme de glissement sur des failles a été écarté, et des modèles de résonnance de cavités saturées en fluide sont utilisées depuis 30 ans pour interpréter les processus des sources (Aki et al., 1977; Chouet, 1988). Cependant, l'aspect résonant de certains signaux peut être attribués à des effets de propagation, et le manque de contraintes sur ces modèles les rendent discutables.

Pour mieux comprendre les processus à l'origine de ces signaux, j'ai travaillé avec des données acquises sur différents volcans :

- L'Etna, où plus de 30 stations large-bande ont été installées pendant 3 semaines en 2008, durant une phase éruptive. La très forte densité de stations de stations a permis de tester de nouvelles méthodes et d'avoir des résultats fins sur les processus des signaux longues Périodes **(Bean et al., 2014; De Barros et al., 2011, 2009; O'Brien et al., 2011**).
- Le Piton de la Fournaise où l'ANR Undervolc (PI F. Brenguier) a permis l'installation de plus de 15 stations sismologiques (Brenguier et al., 2012). Accompagnant les 6 phases éruptives de 2009-2010, seuls 15 événements Longues périodes ont été détectés et analysés, ce qui reste cependant une première observation sur ce volcan (**Zecevic et al., 2013**).
- Le Turrialba (Costa Rica), où nous avons installé en 2009 et 2011 un réseau temporaire dense de stations, incluant des stations sur les bords du cratère éruptif **(Eyre et al., 2015, 2013; Zecevic et al., 2016b**).

Pour analyser ces formes d'ondes particulières et déterminer leurs processus de source, les outils classiques de sismologie tectonique ne sont pas adaptés. J'ai donc développé, amélioré ou adapté différentes techniques, et testé celles-ci sur des données synthétiques calculées dans des modèles 3D avec des topographies complexes. En particulier, j'ai travaillé sur des méthodes de :

- Relocalisation par corrélation et doubles-différences de familles d'évènements (**De Barros et al., 2009; Zecevic et al., 2016a**)
- Localisation par retournement temporel : l'énergie sismique des signaux retournés en temps et propagés numériquement à partir des capteurs va se refocaliser au foyer (**O'Brien et al., 2011**)
- Reconstruction du tenseur complet (6 moments et 3 forces) des moments sismiques par inversion des formes d'ondes dans le domaine fréquentiel (**De Barros et al., 2013b, 2011**)
- Détermination conjointe des localisations et du tenseur des moments (**Eyre et al., 2013**).

Lors de ces études, nous avons en particulier montré que :

- Les signaux Longues Périodes ont une origine superficielle, dans l'édifice volcanique **(De Barros et al., 2009; O'Brien et al., 2011; Zecevic et al., 2013**) ;

- Leur mécanisme de sources est un mécanisme en mode 1 (ouverture/fermeture), avec une forte composante cisaillante (**De Barros et al., 2011; Eyre et al., 2015**)
- Les forces simples communément reconstruites lors des inversions de sources sont des artéfacts, dus en particulier à un modèle de vitesse incorrect (**De Barros et al., 2013b**).
- Ces signaux s'organisent sur des structures « en échelon », compatibles avec des bandes de cisaillement (**De Barros et al., 2011; Zecevic et al., 2016b**), et ne sont donc pas forcément des signaux répétitifs.
- La taille des sources de ces signaux suit une relation classique avec le moment sismique (**Bean et al., 2014**), alors que leur distribution de magnitude ne suit pas une loi de Gutemberg-Richter **(Eyre et al., 2015**).
- L'aspect résonnant de la forme d'onde est principalement dû à l'effet de la topographie et de la couche déconsolidée à la surface du cône volcanique (Bean et al., 2008; **De Barros et al., 2011)**.

Tous ces résultats nous ont permis de proposer un nouveau modèle pour les sources à l'origine de ces signatures sismiques particulières. Nous avons ainsi montré que ces signaux sont produits par des ruptures, et non par des résonnances de fractures (**Bean et al., 2014**). Comme les vitesses d'ondes S dans la partie supérieure de l'édifice volcanique sont faibles, les vitesses de rupture n'atteignent que quelques centaines de m/s. La lenteur des ruptures est accentuée par la présence d'une déformation en ouverture/fermeture qui accompagne le cisaillement sur les failles (Broberg, 2006). Cette composante normale est permise par les pressions fluides dans un environnement superficiel où les contraintes sont faibles. Cette rupture lente conduit donc à des signaux au contenu plus basses fréquences comparé aux séismes classiques. Les formes d'ondes sont ensuite fortement modifiées par l'environnement volcanique, incluant 1) un contenu en champ proche et intermédiaire, 2) une structure très hétérogène dans l'édifice, avec notamment une couche non consolidée en surface, et 3) une topographie abrupte et diffractante et 4) un milieu fortement atténuant. Contrairement, aux modèles basés sur la résonnance de structures géologiques, ce modèle offre des similarités avec la sismologie tectonique. Il change fortement notre compréhension du fonctionnement volcanique : de telles signatures sont révélatrices de déformations de l'édifice, et non de la présence et circulation de fluide.

De la même manière, j'ai aussi travaillé sur la localisation et les mécanismes des trémors monochromatiques typique du volcan Arenal (Costa Rica). Nous avons déterminé que leur mécanisme est associé à des ouvertures de fractures. Cependant, cette inversion n'est pas suffisamment solide pour proposer une interprétation robuste. De plus, la distribution fréquentielle de l'énergie sur certaines bandes très nettes peut suggérer un mécanisme de résonnances **(Davi et al., 2012**).

Article sélectionné

L'article suivant présente les observations permettant de proposer un nouveau modèle pour la source des signaux longues Périodes. Une rupture sur une faille dans la partie superficielle de l'édifice volcanique apparait en effet capable de produire des signatures basses fréquences, de manière plus simple que les modèles basés sur des résonances de fractures saturées en fluide.

Bean C. J., De Barros L., Lokmer I., Métaxian J.-P., O'Brien G., Murphy S., 2014, Long-period seismicity in the shallow volcanic edifice formed from slow-rupture earthquakes, Nature Geoscience, vol.7, pp.71-75, 2014

nature geoscience

ARTICLES

PUBLISHED ONLINE: 15 DECEMBER 2013 | DOI: 10.1038/NGEO2027

Long-period seismicity in the shallow volcanic edifice formed from slow-rupture earthquakes

Christopher J. Bean[1]*, Louis De Barros[1†], Ivan Lokmer[1], Jean-Philippe Métaxian[2], Gareth O' Brien[3] and Shane Murphy[4]

Forecasting of volcanic eruptions is still inadequate, despite technological advances in volcano monitoring. Improved forecasting requires a deeper understanding of when unrest will lead to an actual eruption. Shallow, long-period seismic events often precede volcanic eruptions and are used in forecasting. They are thought to be generated by resonance in fluid-filled cracks or conduits, indicating the presence of near-surface magmatic fluids. Here we analyse very-high-resolution seismic data from three active volcanoes—Mount Etna in Italy, Turrialba Volcano in Costa Rica and Ubinas Volcano in Peru—measured between 2004 and 2009. We find that seismic resonance is dependent on the wave propagation path and that the sources for the long-period seismic waves are composed of short pulses. We use a numerical model to show that slow-rupture failure in unconsolidated volcanic materials can reproduce all key aspects of these observations. Therefore, contrary to current interpretations, we suggest that short-duration long-period events are not direct indicators of fluid presence and migration, but rather are markers of deformation in the upper volcanic edifice. We suggest that long-period volcano seismicity forms part of the spectrum between slow-slip earthquakes and fast dynamic rupture, as has been observed in non-volcanic environments.

A primary goal in volcano seismology is to find reliable precursory signals to volcanic eruptions. Hence it is of paramount importance to understand the physical processes that underlie the diverse range of seismic events supported by volcano edifices. Broadly these events can be divided into four groups: volcano tectonic earthquakes; long-period events; very-long-period events; and seismic tremor[1]. Although volcano tectonics events resemble tectonic earthquakes in signal character and are thought to be caused by brittle failure of the edifice[2], long-period, very long-period and tremor events are usually interpreted in terms of fluid-driven processes. In particular, the present universally applied models for long-period events require that they are necessarily associated with either fluid-filled crack[3,4] or conduit[5,6] resonance, triggered by rapid disturbance of the fluid-filled structure (for example, a fluid pressure fluctuation in a subsurface conduit or dynamic excitation by a local volcano tectonic earthquake). As fluids are thought to participate actively in the source process, mechanistically this sets all long-period events apart from both volcano tectonic and tectonic earthquakes, forming a distinct earthquake class that is viewed with considerable interest in terms of our understanding of the shallow volcano plumbing system[7–10]. Their increased frequency of occurrence is regularly used as a key component in eruption forecasting[2].

Seismic source versus path effects

Long-period seismicity has lower seismic frequencies than volcano tectonics, typically 0.3–2 Hz central frequency, and are usually of narrow spectral band and of long duration (5–40 s). Recently, full wavefield numerical seismic simulations in realistic volcano velocity models designed to constrain long-period source inversions[11] demonstrated a surprisingly strong influence of path effects. Short-duration low-frequency-input source pulses present as artificial long duration resonating long period-like signals when recorded more than a few hundred metres from the source. The effect is very pronounced for shallow sources (<1 km depth) in low-velocity near-surface layers. Sensitivity kernel[12] analysis demonstrates that these effects are global (that is, not local to individual recording stations, but seen throughout the numerical model) implying that they could be misinterpreted as seismic source effects. As such proximal field observations above the sources (for example, stations <∼500 m from the epicentre) are very rare in field studies, these numerical results motivated an uniquely high-resolution field experiment on Mount Etna in 2008, in which two families (similar waveforms) of long-period events were detected[13]. The wavefield distribution for long-period events from that experiment (Fig. 1a) shows extreme spatial variability, with pulse-like low-frequency signals at the summit stations that appear as classical resonating long-period signals at off-summit stations, in excellent agreement with numerical predictions[11]. This unequivocally demonstrates that the apparent resonance in these low-frequency seismic events is caused by wavefield distortions as a consequence of wave propagation effects and is not source-related. Similar pulse-like long-period events can be seen at other time periods at Mount Etna and other volcanoes, when short-range observations are available (Fig. 1b and Supplementary Fig. 1). In fact, we were unable to identify long-duration long-period events at summit stations in these data sets among many thousands of pulse-like long periods. Hence, on several volcanoes, we have identified short duration pulse-like long-period populations that masquerade as classical long-duration long-period events if recorded >∼500–800 m from the epicentre. We conclude that the long seismogram durations in these data are purely path related. Based on waveform

[1]Seismology Laboratory, School of Geological Sciences, University College Dublin, Belfield, Dublin 4, Ireland, [2]ISTerre, IRD, CNRS, Université de Savoie, F-73376 Le Bourget du Lac, France, [3]Geophysical Technology Group, Tullow Oil plc, Leopardstown, Dublin 18, Ireland, [4]Geophysics Research Group, Environmental Sciences Research Institute, University of Ulster, Coleraine BT52 1SA, UK. †Present address: Géoazur, Université de Nice Sophia-Antipolis, CNRS, Observatoire de la Côte d'Azur, 250 rue Albert Einstein, Sophia Antipolis 06560, Valbonne, France. *e-mail: chris.bean@ucd.ie

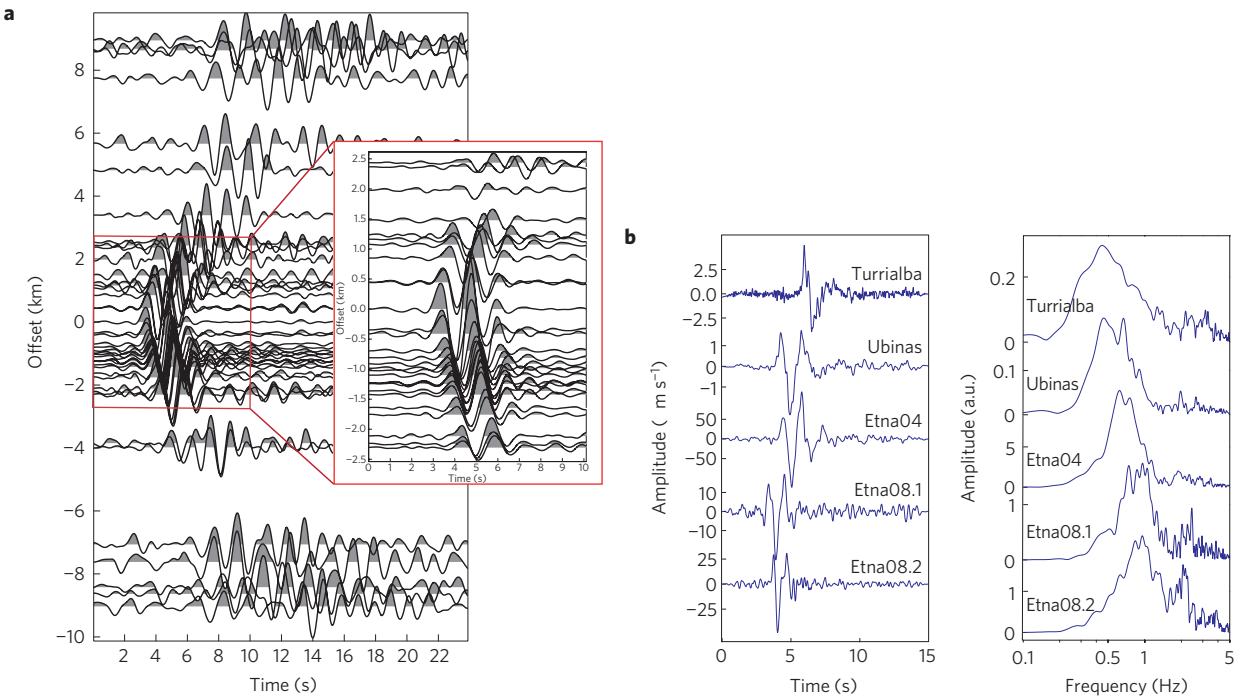

Figure 1 | Illustration of short-duration long-period events and strong propagation path effects. a, Spatial distribution of the long-period wavefield for family 1, 2008 Mount Etna field data. Each seismic trace is a stack of ~60 events in the family. Events are located beneath the summit at depths < 800 m. Normalized vertical component traces are plotted as a function of the station's distance from the volcano summit. **b**, Left panel, shallow pulse-like long-period events (vertical component) detected on near-summit stations at Turrialba Costa Rica (2009); Ubinas, Peru (2009) and two different time periods on Mount Etna (2004 and 2008, family 1 and 2); right panel, amplitude spectra for the data shown in the left panel.

analysis, a previous study[14] arrived at the same conclusion for some hybrid volcano seismic events. A literature search reveals that shallow long-period seismicity is almost universally recorded at epicentral distances > 500 m on standard volcano networks, which usually lack summit stations for operational reasons. Hence non-resonating long-period sources could be commonplace but further specific field experiments will be needed to detect them. Three location methods applied to the 2008 Mount Etna data[15] show that these long-period events are shallow: <800 m and <600 m depth beneath the summit for families 1 and 2, respectively. Moment tensor solutions for both 2008 long-period families favour a predominantly tensile crack mechanism[16] with the possibility of a shear component. Both long-period families occur on cracks with very similar strikes (approximately westsouthwest–eastnortheast) however the failure planes for both families are orthogonal in conjugate sets of fractures, which is why their seismograms differ leading to two distinct families (Supplementary Fig. 2). We cannot unequivocally distinguish between crack opening and closing, although displacement seismograms favour an opening mechanism.

Dry failure of the edifice?

The pulse-like nature of the long-period signals is difficult to reconcile in terms of a fluid-driven crack model. It would require specifically tuned choices of crack stiffness and/or seismic wave attenuation, to dampen resonance. This difficulty is compounded by independent results from laboratory experiments, which demonstrate that the presence of fluids in the source process leads to long-duration monochromatic signals[17,18], which, as demonstrated, we do not see as a source signature in these short-duration pulse-like field data. Specifically, wet and dry laboratory experiments designed to determine unequivocal seismological discriminators between fluid-driven long-period seismicity and brittle (volcano tectonic) events reveal that wet experiments generate long-duration resonating classical long-period-type signals whereas the dry experiments produce volcano-tectonic-like brittle failure events[17]. Notably, the source corner frequency (f_c) for the dry experiments scales with event size as $1/f_c^3$ (ref. 19), consistent with brittle failure theory[20]. In contrast, the fluid-driven laboratory events do not show any clear f_c scaling with event size[19], consistent with present applications of a fluid-driven crack model, where frequencies for a crack of a fixed size are controlled by the crack's geometry and stiffness, not seismic moment. If the crack size was allowed to vary in these models, scaling would be observed. Figure 2 shows an equivalent analysis for 2004 field long-period data from Mount Etna. A clear scaling of f_c with seismic moment is visible, strongly indicating that these shallow Mount Etna long periods are caused by dry mechanical failure, consistent with laboratory observations. Given the body of observations above, it is prudent to seek an alternative explanation for long-period events observed here. We investigate stress-driven edifice deformation as a possible cause of long-period activity.

Active volcanoes have relatively high deformation rates. On Mount Etna, flank instability in the form of east–west spreading is by far the predominant type of deformation[21,22]. Rheological mechanisms for accommodating this deformation in the near surface (top ~1 km) have not been addressed in the literature. In general, volcano tectonic and long-period events on volcanoes separate spatially, with volcano tectonic events located approximately >1–2 km below the edifice surface and long-period events located at depths of <1 km (refs 2,23–25). Brittle failure volcano tectonic earthquakes are markers for edifice fracturing. Hence the absence of near-surface fracturing (that is, very shallow volcano tectonic events) seems to imply that deformation is almost entirely silent (aseismic) in the top 1 km or that seismic events other than brittle volcano tectonics are related to near-surface deformation. As demonstrated here, long-period events develop on populations of primarily tensile cracks (depths < 800 m) at

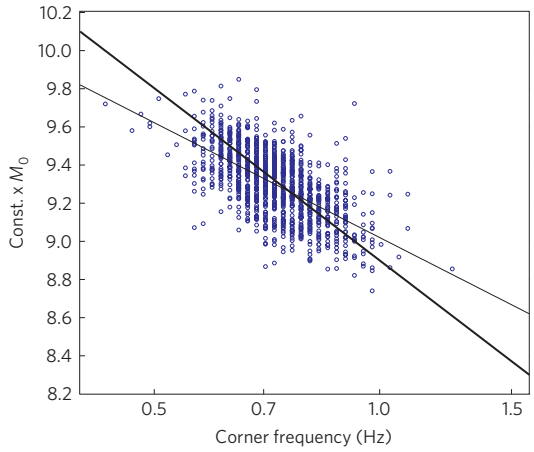

Figure 2 | Scaling of long-period seismic moment magnitude versus corner frequency. The amplitude spectra of 1,150 long-period events, recorded in March 2004 at Mount Etna near-summit station (ECPN) are fitted with an ω^{-2} source model, to determine the corner frequency. The *y* axis is proportional to the seismic moment. The thin line is best fitting with slope −2.2; the thick line has slope −3 and is broadly consistent with the data. Note: we use 2004 data as the signal-to-noise ratio is not high enough in the 2008 Mount Etna data to carry out this analysis.

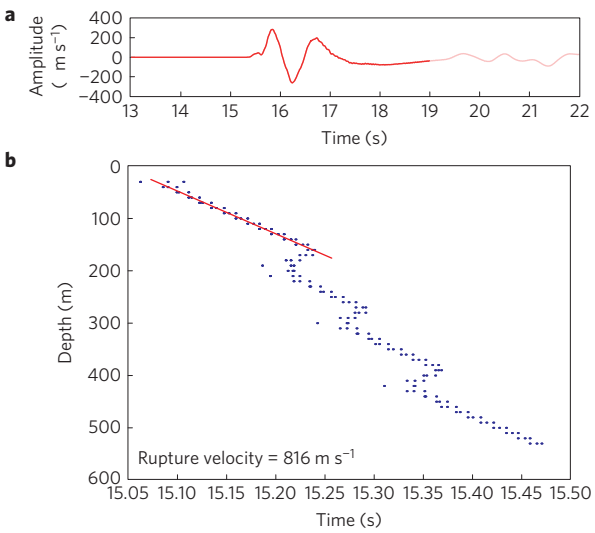

Figure 3 | 2D molecular dynamic simulations of rupture propagation. **a**, Illustrative example of slow rupture seismograms. Vertical component seismic trace caused by rupture on a 500-m-long vertical tensile crack. The crack's top is 20 m below the surface. The seismic station is on the free surface, 500 m laterally displaced from a surface projection of the crack. Faded parts of traces represent edge effects from model boundaries/surface. **b**, Rupture velocity plot for simulated data in **a**. Blue dots represent failed bonds. The estimated (red line) sub-Rayleigh rupture velocity is ~816 m s^{-1}.

westsouthwest–eastnortheast orientations, consistent with known east–west spreading and sliding of the eastern flank of Etna volcano. A key question is: do they play a role in accommodating some near-surface deformation in the form of slow seismic rupture? That is, are long-period events a weak brittle signal in a largely ductile deformation field? The top 800 m on many volcanoes contain poorly consolidated material with very low seismic velocities[26–29]. A previous study[13] determined a mean P-wave velocity of 1.8 km s^{-1} in the top 800 m of Mount Etna's edifice, giving a Rayleigh wave velocity (V_R) of ~855 m s^{-1} (for a Poisson's ratio of 0.3; ref. 16). Source inversions constrain the 2008 long periods to have a predominantly tensile (mode I) crack mechanism[16]. It has been demonstrated[30] that mode I brittle failure cracks are theoretically forbidden to rupture at speeds $> V_R$ and in practice rupture at speeds $\ll V_R$ in low-stress environments. Hence rupture speed can be controlled by both the failure mechanism and the stress environment. We carried out two-dimensional (2D) molecular dynamic rupture simulations[31], using codes from ref. 32, for mode I cracks in a model with an upper edifice (top 800 m) $V_R = 855$ m s^{-1} (Fig. 3a,b). As our model fault is idealized and smooth, to achieve sub-shear-wave rupture speeds in the molecular dynamic model we approximate the real structure as a shallow vertical tensile crack (5% weaker than the host material). The model is prestressed with vertical stress $\sigma_1 = 0$ and horizontal stress $\sigma_3 = -0.0065$ MPa (that is, in tension, up to the approximate tensile strength of near-surface volcanic materials[33]). It is then allowed to equilibrate and failure is achieved by subsequent incremental increases in the horizontal extensional stresses until rupture initiates. Consistent with theoretical predictions[30], we observe sub-V_R rupture speeds. These dynamic simulations demonstrate that slow rupture speeds (relative to failure in stiff materials with higher Rayleigh wave speeds) of ~816 m s^{-1} on a 500-m-long crack lead to 2-s-long pulse-like long-period seismograms, similar to those recorded at the summit stations on several volcanoes (compare Fig. 1b with Fig. 3a). Our kinematic simulations (not shown) produce equivalent pulse-like synthetic seismograms, for crack dips from ref. 16. Even though the true stress regime is unknown and highly stylized in the 2D molecular dynamic model, seismogram velocity amplitudes are of the same order of magnitude as our largest long-period field observations.

Volcano seismicity and other slow-rupture observations

Crack dimensions for field data can be estimated using an expression for the radius of an expanding circular tensile crack[34] $r = 1.99 \times V_s/(2\pi \times f_c)$. Taking S-wave velocity (V_s) = 950 m s^{-1} and $f_c = 0.72$ (Fig. 2) gives a circular crack diameter of ~800 m. This estimate is broadly consistent with the dynamic rupture simulation results (Fig. 3) and the vertical dimension of the near-surface low-velocity zone (<1 km), which we argue herein limits rupture speeds and stress accumulation in quasi-brittle failure events leading to low-frequency seismic radiation even for small faults. The past decade has seen the discovery of a wide range of slow-earthquake phenomena in a wide variety of environments from subduction zone interfaces to landslides to glaciers[35]. The controlling mechanism for rupture and/or slip rate (fast classical earthquakes to slow or even creeping) seems to relate to the local stress state and/or frictional properties of the material, with brittle failure as the underlying cause of seismic radiation. Ref. 35 developed an integrated perspective on the continuum between classical earthquakes, slow-rupture and slow-slip phenomena. Within their framework we propose that volcano tectonic earthquakes morph into long-period events in the shallow edifice. This volcano tectonic to long-period transition occurs because weak low-stiffness materials promote slower rupture speeds, leading to low-frequency seismic radiation. This implies that at least some populations of long periods (but almost certainly not tornillo[7] events, which do seem fluid-driven) are part of the same mechanical/dynamical class as volcano tectonic events, in that they are caused directly by brittle failure. Hence, like volcano tectonic events, these long periods are stress driven and do not require a fluid-driven source model. As slip rate ≈ ((stress drop × rupture velocity)/shear modulus; ref. 36), the interplay between local stress conditions and local material properties controls failure details. Our estimated stress drops from waveform analysis[37] of the Mount Etna long-period seismicity of ~0.01 MPa are two to three orders of magnitude smaller than expected for tectonic seismicity. Possible causes of such low stress drops are discussed below. In Mount

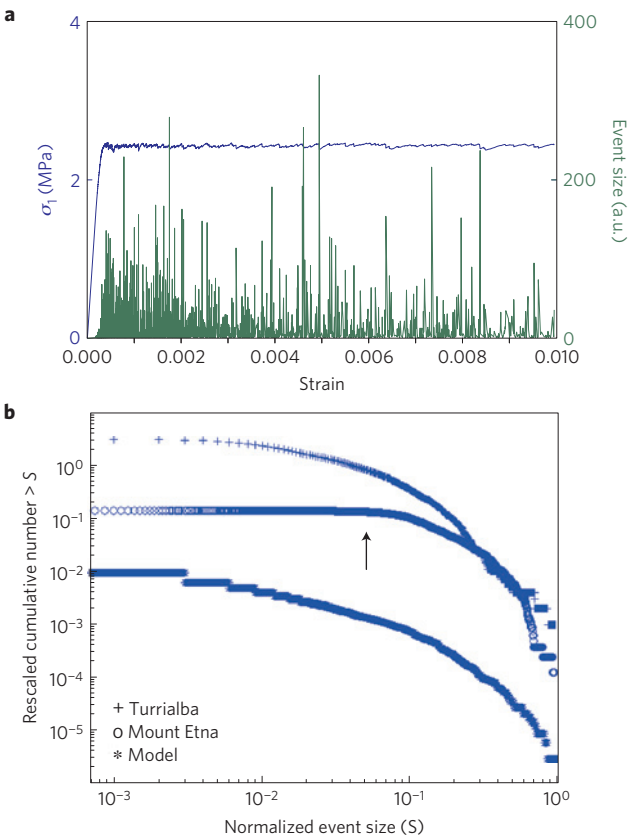

Figure 4 | Simulated seismicity in a weak volcanic upper edifice. **a**, Stress–strain (stress on left *y* axis and blue data) and seismicity (seismic event sizes on right *y* axis and green data) output from a simulated uni-axial deformation experiment using the damage mechanics model of ref. 38 and material properties for shallow volcano deposits[33]. Model parameters: modulus of elasticity 0.8 GPa; Poisson's ratio 0.3; apparent cohesion 0.6–1.1 MPa; angle of internal friction 20°. **b**, Seismic *b*-value plots for model data from **a** (asteriks), for long-period events from Mount Etna (open circle) and for long-period data from Turrialba in 2009 (plus symbol). Data are normalized, and all catalogues have >1,100 events. Mount Etna magnitude of completeness is indicated by black arrow.

Etna's case, we propose that east–west extension leads to slow-tear predominantly tensile failure. It should be noted that we cannot definitively rule out the presence of possible double-couple components in moment tensor inversions for small long-period events. Crack apertures are poorly constrained, estimates vary from ~2 mm using $\Delta u = (24/7\pi)(\Delta\sigma/\mu)r$ (ref. 34) to 0.5 mm taking the shear failure analogy of slip $= M_0/(r^2\pi\mu)$, where Δu, crack maximum aperture; $\Delta\sigma$, stress drop; μ, shear modulus; M_0, seismic moment. Hence these displacements are probably below the present detection threshold of earthquake-related deformation studies.

The authors of a previous study[33] undertook comprehensive field studies and laboratory experiments to determine the physical and mechanical properties of near-surface deposits at Stromboli Volcano, Italy. Their key finding is that bulk deposits are both compliant and weak. Using the damage mechanics model of ref. 38 we simulate seismicity in an equivalent material (Fig. 4a). A surprising result is the emergence of swarms of very low stress-drop events rather than discrete higher stress-drop individual failures, very similar in character to our low stress-drop long-period families (swarms). We also see diffuse damage in these seismicity simulations, consistent with the observed spread in long-period hypocentres, which are not localized on an individual structure[13,15]—but are sufficiently close to display similar waveforms, when they share the same focal mechanism. Unexpectedly, model failure-size distributions (seismic *b*-values) show non-power-law scaling, with a deficit of larger events, which we determine is primarily controlled by the low internal friction angle of the material. Although the stress–strain relationship in Fig. 4a has the characteristics of ductile behaviour, it is accompanied by seismicity, which demonstrates that the material sits at the brittle–ductile transition and seems to be unable to sustain the high stresses required for larger seismic events. Seismic *b*-values for long-period seismicity at Mount Etna and Turrialba, Costa Rica (data collected during a summit deployment in 2009), exhibit similar behaviour (Fig. 4b) suggesting that the swarms (often forming families) of low stress-drop pulse-like long-period events are a consequence of failure in material close to the brittle–ductile transition. Here, as in weakly cemented sand[39], we suggest that quasi-ductility in shallow (<1 km depth) volcanic materials is primarily controlled by low internal friction angles of the volcanic deposits, not by high temperature and pressure. Numerical simulation tests demonstrate that model seismicity data show power-law scaling for internal friction angles $>\sim 35°$. Drilling at Unzen Volcano, Japan[40], where borehole washout and accidental side tracking occurred to several hundred metres depth, testifies to the unconsolidated nature of subsurface volcanic materials at depth—demonstrating that the physical properties determined by ref. 33 and used in our simulations are not merely superficial. Consistent with our numerical seismicity results (Fig. 4a), laboratory experiments in gypsum at the brittle–ductile transition show swarms of low-frequency acoustic emissions associated with the dynamic propagation of shear bands[41], showing that brittle–ductile materials can support both dynamic rupture and low-frequency seismicity.

Eruption forecasting: reassessing the upper edifice

We propose a new model for a class of long-period volcano seismicity, where long-period swarms are caused by slow, quasi-brittle, low stress-drop failure driven by transient upper-edifice deformation. This model is not appropriate for tornillo-type long-period events. Underlying stress fluctuations can be driven by gravity, gas influx or magma migration, while the consequent material failure is dry mechanical, where fluids are not directly involved in the seismic signature of the source process. The absence of resonance in the source, non-power-law *b*-value observations, swarms of very low stress-drop long-period events, long-period source crack orientations consistent with known east–west spreading on Mount Etna, the lack of upper-edifice volcano tectonic earthquakes, $1/f_c$ (ref. 19) scaling of long-period corner frequencies, dynamic rupture simulations and numerical modelling of upper-edifice material failure all call for a new paradigm that is consistent with this broad range of new observations. We hypothesize that long periods here represent a weak slow-rupture brittle signature in an otherwise ductile failure field. The proposed model predicts the temporal evolution of pre-eruptive seismicity as summarized in ref. 42, particularly the relative timing of volcano tectonic and long-period events and the relative seismic quiescence often seen before eruptions, when magma- or gas-driven stress perturbations are concentrated in the uppermost part of the edifice. More broadly, this slow-rupture model is consistent with an emerging framework[35] for failure in Earth materials, from slow-slip phenomena to full dynamic rupture, across a wide range of geo-environments. In our proposed model, high spectral frequency volcano tectonic seismic events morph into low spectral frequency long-period events as they attempt to initiate in very weak near-surface volcanic materials. In this model (non-tornillo) long-period and volcano tectonic seismicity are unified, forming part of the same stress-driven mechanical class—simplifying our understanding of these event types and

integrating aspects of volcano seismology with wider seismological developments over the past decade. Finally, improved forecasting requires a deeper understanding of when unrest will lead to an actual eruption or when potential eruptions stall[43]. The model presented here offers a new perspective on the workings of the uppermost edifice on volcanoes. Consequently it has significant implications for the way in which we apply seismology to forecasting and hazard estimation. Additional very near-summit observations of long-period seismicity and high-resolution surface deformation are required, at a variety of volcanoes, to further test this model.

Received 5 September 2012; accepted 7 November 2013; published online 15 December 2013

References

1. McNutt, S. R. Volcanic seismology. *Annu. Rev. Earth Planet. Sci.* **32,** 461–491 (2005).
2. Wassermann, J. in *IASPEI New Manual of Seismological Observatory Practice (NMSOP)* Vol. 1 (ed. Bormann, P.) (GeoForschungsZentrum Potsdam, 2002).
3. Chouet, B. & Julian, B. R. Dynamic of an expanding fluid-filled crack. *J. Geophys. Res.* **90,** 11187–11198 (1985).
4. Chouet, B. A. in *Volcanic Seismology* (eds Gasparini, P., Scarpa, R. & Aki, K.) 133–156 (Springer, 1992).
5. Neuberg, J., Luckett, R., Baptie, V. & Olsen, K. Models of tremor and low-frequency earthquake swarms on Montserrat. *J. Volcanol. Geotherm. Res.* **101,** 83–104 (2000).
6. Jousset, P., Neuberg, J. & Sturton, S. Modelling the time-dependent frequency content of low-frequency volcanic earthquakes. *J. Volcanol. Geotherm. Res.* **128,** 201–223 (2003).
7. Chouet, B. A. Long-period volcano seismicity: Its source and use in eruption forecasting. *Nature* **380,** 309–316 (1996).
8. Nakano, M., Kumagai, H. & Chouet, B. A. Source mechanism of long-period events at Kusatsu-Shirane Volcano, Japan, inferred from waveform inversion of the effective excitation functions. *J. Volcanol. Geotherm. Res.* **122,** 149–164 (2003).
9. Matsubara, W. *et al.* Distribution and characteristics in waveforms and spectrum of seismic events associated with the 2000 eruption of Mt. Usu. *Earth Planet. Sci. Lett.* **136,** 141–158 (2004).
10. Lokmer, I., Saccorotti, G., Di Lieto, B. & Bean, C. J. Temporal evolution of long-period seismicity at Etna Volcano, Italy, and its relationships with the 2004–2005 eruption. *Earth Planet. Sci. Lett.* **266,** 141–158 (2008).
11. Bean, C. J., Lokmer, I. & O'Brien, G. S. Influence of near-surface volcanic structure on long-period seismic signals and on moment tensor inversions: Simulated examples from Mount Etna. *J. Geophys. Res.* **113,** B08308 (2008).
12. Tromp, J., Tape, C. & Liu, Q. Seismic tomography, adjoint methods, time reversal and banana-doughnut kernels. *Geophys. J. Int.* **160,** 195–216 (2005).
13. De Barros, L. *et al.* Source geometry from exceptionally high resolution long period event observations at Mt. Etna during the 2008 eruption. *Geophys. J. Int.* **36,** L24305 (2009).
14. Harrington, R. M. & Brodsky, E. E. Volcanic hybrid earthquakes that are brittle-failure events. *Geophys. Res. Lett.* **34,** L06308 (2007).
15. O'Brien, G. S. *et al.* Time reverse location of seismic long-period events recorded on Mt Etna. *Geophys. J. Int.* **184,** 452–462 (2011).
16. De Barros, L. *et al.* Source Mechanism of Long Period events recorded by a high density seismic network during the 2008 eruption on Mt Etna. *J. Geophys. Res.* **116,** B01304 (2011).
17. Benson, P. M., Vinciguerra, S., Meredith, P. G. & Young, R. P. Laboratory simulation of volcano seismicity. *Science* **322,** 249–252 (2008).
18. Burlini, L. *et al.* Seismicity preceding volcanic eruptions: New experimental insights. *Geology* **35,** 183–186 (2007).
19. Harrington, R. M. & Benson, P. M. Analysis of lab simulations of volcanic hybrid earthquakes using empirical Green's functions. *J. Geophys. Res.* **116,** B11303 (2011).
20. Kanamori, H. & Rivera, L. Static and dynamic scaling relations for earthquakes and their implications for rupture speed and stress drop. *Bull. Seismol. Soc. Am.* **94,** 314–319 (2004).
21. Solaro, G. *et al.* Anatomy of an unstable volcano from InSAR: Multiple processes affecting flank instability at Mt. Etna. *J. Geophys. Res.* **115,** B10405 (2010).
22. Neri, M. *et al.* The changing face of Mount Etna's summit area documented with Lidar technology. *Geophys. Res. Lett.* **35,** L09305 (2008).
23. Gil-Cruz, F. & Chouet, B. A. Long-period events, the most characteristic seismicity accompanying the emplacement and extrusion of a lava dome in Galeras Volcano, Colombia, in 1991. *J. Volcanol. Geotherm. Res.* **77,** 121–158 (1997).
24. Arciniega-Ceballos, A., Valdes-Gonzalez, C. & Dawson, P. Temporal and spectral characteristics of seismicity observed at Popocatepetl volcano, central Mexico. *J. Volcanol. Geotherm. Res.* **102,** 207–216 (2000).
25. Saccorotti, G. *et al.* Seismicity associated with the 2004–2006 renewed ground uplift at Campi Flegrei Caldera, Italy. *Phys. Earth Planet. Int.* **165,** 14–24 (2007).
26. De Luca, G., Scarpa, R., Del Pezzo, E. & Simini, M. Shallow structure of Mt. Vesuvius Volcano, Italy, from seismic array analysis. *Geophys. Res. Lett.* **24,** 481–484 (1997).
27. Chouet, B. A. *et al.* Shallow velocity structure of Stromboli volcano, Italy, derived from small-aperture array measurements of Strombolian tremor. *Bull. Seismol. Soc. Am.* **88,** 653–666 (1998).
28. Ferrazzini, V., Aki, K. & Chouet, B. A. Characteristics of seismic waves composing hawaiian volcanic tremor and gas-piston events observed by a near-source array. *J. Geophys. Res.* **96,** 6199–6209 (1991).
29. Mora, M. M. *et al.* Shallow velocity structure and seismic site effects at Arenal volcano, Costa Rica. *J. Volcanol. Geotherm. Res.* **152,** 121–139 (2006).
30. Broberg, K. B. Differences between Mode I and Mode II crack propagation. *Pure Appl. Geophys.* **163,** 1867–1879 (2006).
31. Abraham, F. F. & Gao, H. How fast can cracks propagate? *Phys. Rev. Lett.* **84,** 3113–3116 (2000).
32. O'Brien, G. S. & Bean, C. J. A 3D discrete numerical elastic lattice method for seismic wave propagation in heterogeneous media with topography. *Geophys. Res. Lett.* **31,** L14608 (2004).
33. Apuani, T., Corazzato, C., Cancelli, A. & Tibaldi, A. Physical and mechanical properties of rock masses at Stromboli: A dataset for volcano instability evaluation. *Bull. Eng. Geol. Environ.* **64,** 419–431 (2005).
34. Sato, T. A note on body wave radiation for expanding tension crack. *Sci. Rep. Tohoku Univ. Ser. 5, Geophys.* **25,** 1–10 (1978).
35. Peng, Z. & Gomberg, J. An integrated perspective of the continuum between earthquakes and slow-slip phenomena. *Nature Geosci.* **3,** 599–607 (2010).
36. Rubin, A. Episodic slow slip events and rate-and-state friction. *J. Geophys. Res.* **113,** B11414 (2008).
37. Madariaga, R. Dynamics of an expanding circular fault. *Bull. Seismol. Soc. Am.* **3,** 639–666 (1976).
38. Amitrano, D. Brittle-ductile transition and associated seismicity: Experimental and numerical studies and relationships with the *b* value. *J. Geophys. Res.* **108,** 2044–2059 (2003).
39. Collins, B. D. & Sitar, N. Geotechnical Properties of Cemented Sands in Steep Slopes. *J. Geotech. Geoenviron. Eng.* **135,** 43–51 (2009).
40. Sakuma, S., Kajiwara, T., Nakada, S., Uto, K. & Shimizu, H. Drilling and logging results of USDP-4—Penetration into the volcanic conduit of Unzen Volcano, Japan. *J. Volcanol. Geotherm. Res.* **175,** 1–12 (2009).
41. Brantut, N., Schubnel, A. & Guéguen, Y. Damage and rupture dynamics at the brittle-ductile transition: The case of gypsum. *J. Geophys. Res.* **116,** B01404 (2011).
42. McNutt, S. R. in *Encyclopedia of Volcanoes* (eds Sigurdsson, H. *et al.*) 1095–1119 (Academic, 2000).
43. Sparks, R. S. J., Biggs, J. & Neuberg, J. W. Montoring volcanoes. *Science* **335,** 1310–1311 (2012).

Acknowledgements

Financial support from Science Foundation Ireland (SFI) and the European Commission, and computational support from the Irish Centre for High End Computing (ICHEC), are acknowledged. We are grateful to M. Mora, J. Pacheco, F. Martini and G. Soto (Costa Rica), O. Macedo and A. Inza (IGP-Peru). M. Möllhoff, D. Patanè (D.P.) and INGV staff (Italy) for field campaign support and D.P. for feedback on an early manuscript. D. Amitrano is gratefully acknowledged for application of his damage mechanics code and A. Braiden for assistance with drafting the manuscript. T. Eyre is thanked for Supplementary Fig. 1.

Author contributions

C.J.B. initiated the concepts, analysed synthetic seismicity data and wrote the manuscript. L.d.B. analysed the seismic data and, with I.L., helped develop the concepts. J-P.M. provided data and intellectual input. G.O'B. carried out rupture modelling and S.M. made contributions on source modelling.

Additional information

Supplementary information is available in the online version of the paper. Reprints and permissions information is available online at www.nature.com/reprints. Correspondence and requests for materials should be addressed to C.J.B.

Competing financial interests

The authors declare no competing financial interests.

2.3.2. Signatures non conventionnelles dans les réservoirs

Des signatures non conventionnelles sont aussi observées lors de l'exploitation des réservoirs d'hydrocarbures, et en particulier lors de la fracturation hydraulique dans des argilites (Das and Zoback, 2013; Hu et al., 2017; Kumar et al., 2017b). Cependant, les mécanismes générant ce type de signaux ne sont pas clairement établis. Ces événements peuvent en effet être reliés à la résonnance des fractures ouvertes par la fracturation hydraulique (Hu et al., 2017) ou au glissement lent de certaines fractures mal orientées par rapport aux contraintes (Kumar et al., 2017b) . De plus, il a été montré que certaines signatures (Das and Zoback, 2013) n'étaient en fait que des séismes régionaux, dont la forme a été modifiée par le contexte géologique et l'instrumentation en forage (Zecevic et al., 2016a). Enfin, d'autres signatures de ce type peuvent être reliées à des résonnances des forages (Tary et al., 2014).

Un des objectifs initiaux des expériences décamétriques de réactivation de failles était l'observation et la caractérisation de tels événements. En effet, lors de l'expérience préliminaire faite à Rustrel en 2010, nous avons pu observer une grande variété de signaux sismiques (**Derode et al., 2015**). En particulier, des signaux ressemblant à des trémors tectoniques sont enregistrés pendant une phase de glissement lent, avant l'accélération de celui-ci et l'occurrence d'évènements micro-sismiques (*Figure 15*). Cependant, le nombre limité et le type de capteurs sismiques n'ont pas permis d'analyser en détails ces signatures, et de conclure sur leur lien réel avec le glissement de la faille. Des signatures basses fréquences, centrées entre 200 et 400 Hz, ont aussi été observées lors des expériences de Tournemire. Cependant, des tests sur site, leur temps d'occurrence et leur localisation montrent que ces signaux sont générés par des résonnances des forages d'injection et d'instrumentation (Tary et al., 2014) .

Enfin, à la fin des années 2000, des articles ont débattu l'existence de micro-trémors générés par les réservoirs de gaz (Holzner et al., 2005; Steiner et al., 2008). L'observation principale suggérant l'existence de ces signaux est l'amplification des composantes horizontales sur les stations positionnées au-dessus des réservoirs. Des mécanismes possibles pour expliquer ces signatures sont liés à des interactions fluide-solide dans le réservoir, à des propriétés d'atténuation particulières, ou à la résonnance de la couche saturée en hydrocarbure. Pour vérifier l'origine de telles signatures, nous avons déployé des antennes de capteurs au-dessus d'un réservoir de gaz situé dans une vallée de l'Ouganda. Nous avons identifié des anomalies dans le bruit sismique, compatibles avec de tels micro-trémors. Cependant, nous avons montré que ces anomalies étaient liées à la structure du bassin, et non à la présence d'un réservoir d'hydrocarbures (**Martini et al., 2013**).

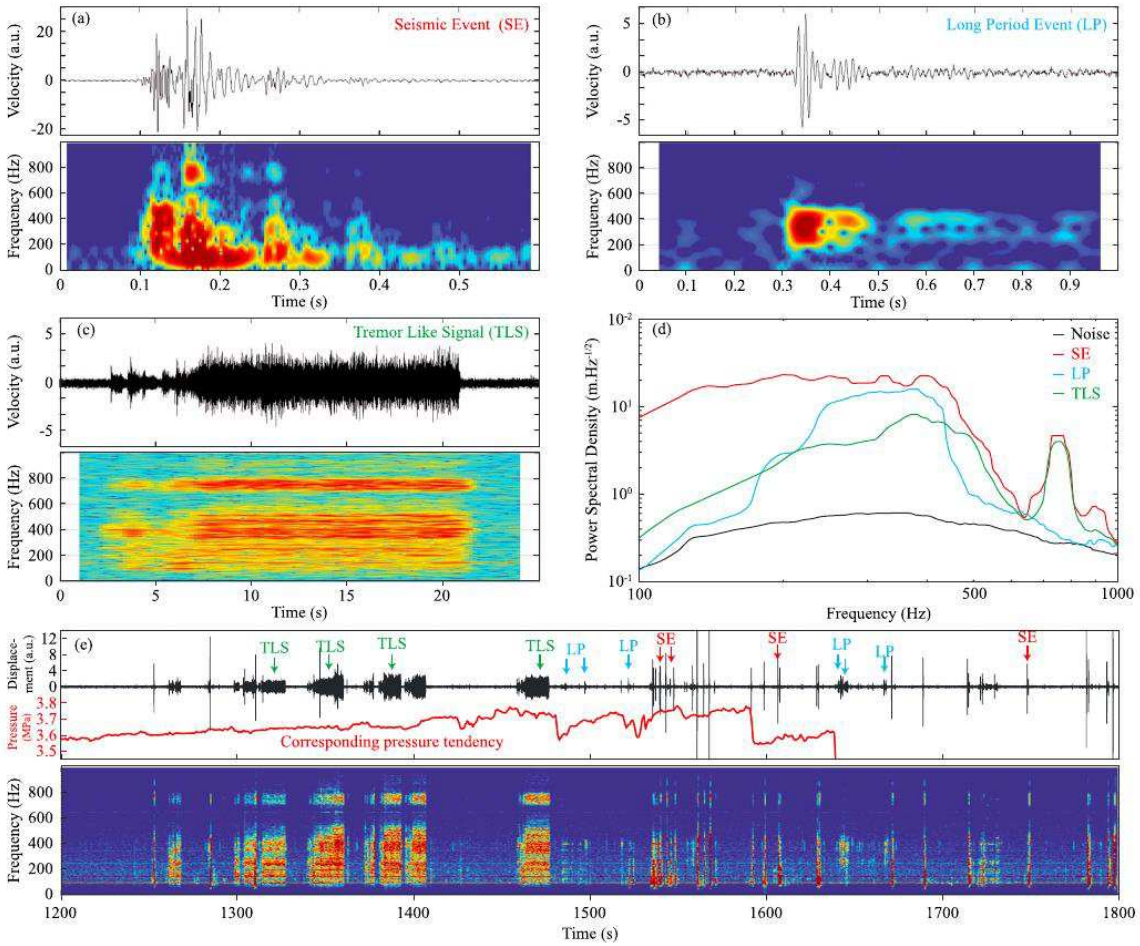

Figure 15 *: Signatures sismiques enregistrées durant le test de réactivation de faille fait à Rustrel en 2010. a) forme d'onde et spectrogramme d'un évènement micro-sismique ; b) forme d'onde et spectrogramme d'un signal « longues périodes » ; c) forme d'onde et spectrogramme d'un trémor; d) spectre en déplacement des ces 3 signaux et du bruit sismique ; e) données sismiques, pression et spectrogramme des 600 secondes de l'expérience pendant lesquelles de la sismicité est observée (**Derode et al., 2015**).*

2.4. Crises sismiques associées aux fluides

Articles publiés dans ce thème

De Barros, L., M. Baques, M. Godano, A. Helmstteter, A. Deschamps, C. Larroque, F. Courboulex (2019) Fluid-Induced Swarms and Coseismic Stress Transfer: a Dual Process Highlighted in the Aftershock Sequence of the 7 April 2014 Earthquake (Ml 4.8, Ubaye, France), *Journal of Geophysical Research: Solid Earth*, doi:2018JB017226

Duboeuf, L., De Barros, L., Cappa, F., Guglielmi, Y., Deschamps, A., & Seguy, S. (2017). Aseismic motions drive a sparse seismicity during fluid injections into a fractured zone in a carbonate reservoir. Journal of Geophysical Research: Solid Earth, 122(10), 8285-8304.

De Barros, L., Deschamps, A., Sladen, A., Lyon-Caen, H., & Voulgaris, N. (2017). Investigating dynamic triggering of seismicity by regional earthquakes: the case of the Corinth Rift (Greece). *Geophysical Research Letters*, 44(21).

De Barros, L., G Daniel, Y Guglielmi, D Rivet, H Caron, X Payre, et al. (2016), Fault structure, stress, or pressure control of the seismicity in shale? Insights from a controlled experiment of fluid-induced fault reactivation, J. Geophys. Res. Solid Earth, 121, 4506–4522, doi:10.1002/2015JB012633

Derode, B., Guglielmi, Y., De Barros, L., & Cappa, F. (2015). Seismic responses to fluid pressure perturbations in a slipping fault. *Geophysical Research Letters*, *42*(9), 3197-3203.

De Barros L., Bean C. J., Zecevic+ M., Brenguier F., Peltier A. 2013. Eruptive fracture location forecasts from high-frequency events on Piton de la Fournaise Volcano, Geophysical Research Letters, vol.40, pp.1-5.

Les perturbations des pressions fluides en profondeur génèrent de la sismicité. Son organisation spatiale et temporelle peut renseigner sur les migrations de fluides, la présence de glissement lent, l'état des contraintes, etc. Ce chapitre présente donc des résultats sur l'organisation des crises sismiques, et sur les forçages les générant. En particulier, les zones tectoniques peuvent être frappées soit par des chocs principaux soit par des essaims sismiques. Il est donc souhaitable de comprendre comment les fluides et autres processus influent sur le comportement sismique (2.4.1). De même, les éruptions volcaniques sont précédées par une crise sismique, qu'il est nécessaire de comprendre pour améliorer la prédiction de l'éruption (2.4.2). Dans tous les cas, la migration de la sismicité est une observation riche pour caractériser les forçages (2.4.3).

2.4.1. Crise sismique induites par des fluides

L'activité sismique des zones tectoniques actives est généralement caractérisée par des périodes intersismiques calmes séparant l'occurrence de séismes forts et de leurs répliques. Un comportement opposé est celui de l'essaim sismique, dans lequel une zone subit pendant des jours ou des semaines de nombreux évènements sismiques de faible magnitude. Une perturbation de l'état de contraintes par des déformations lentes (Lohman and McGuire, 2007) ou des pressions fluides (Chen et al., 2012; Duverger et al., 2015) est nécessaire pour maintenir une telle activité. Les zones de Barcelonnette ou du golfe de Corinthe sont des zones dans lesquelles s'expriment ces deux comportements, avec des alternances de chocs principaux/répliques et d'essaims sismiques. Les processus en jeux sont donc complexes. Les forts taux de sismicité et la dense instrumentation (au moins temporaires) de ces deux zones en font des laboratoires naturels appropriés pour l'étude des processus sismiques.

Le golfe de Corinthe est un rift d'arrière-arc avec un fort taux d'extension (>cm/an), et une sismicité riche et dense. La distribution spatio-temporelle de certains essaims sismiques suggère l'influence de migration fluide dans sa genèse (Duverger et al., 2015; Pacchiani and Lyon-Caen, 2010). Des glissements lents sur un détachement repris en extension semble aussi jouer un rôle important dans ce double comportement sismique (Bernard et al., 2006; Duverger et al., 2018). En travaillant sur la détection des évènements par l'analyse d'une antenne de 7 capteurs, je me suis aperçu d'une augmentation du nombre d'évènements après les séismes régionaux. Nous avons ainsi pu montrer la présence de déclenchement dynamique de sismicité par le passage des ondes générées par des tremblements de terre de magnitude modérée (4.5 à 6) situés à moins de 500 km du golfe. Ce déclenchement semble contrôlé par l'azimut d'incidence de la perturbation, avec un déclenchement uniquement par des ondes de Rayleigh, et non par des ondes de Love. De manière indirecte, cette observation suggère la présence de failles dans lesquelles la pression de fluide est sub-critique (**De Barros et al., 2017**).

La région de l'Ubaye, près de la ville de Barcelonnette subit régulièrement des essaims sismiques, avec plus de 16000 évènements de magnitude inférieure à 3 en 2003-2004 (Jenatton et al., 2007), mais aussi des séismes de magnitudes proches de 5 produisant de faibles dégâts (Thouvenot et al., 2016). Ce comportement dual est unique dans le sud des Alpes, et semble être relié à la présence de fluide (Leclère et al., 2013). Suite au séisme du 07/04/2014 (magnitude Mw=4.8), un réseau temporaire de stations a été installé pour surveiller les répliques. L'analyse fine de cette sismicité nous a permis de mettre en évidence un comportement complexe des répliques. Les événements ne se produisent pas sur la faille principale, mais sur une arborescence de structures annexes, décrivant la zone endommagée de la faille principale. De plus, les évènements se séparent spatialement en fonction du processus qui les déclenche. Les sources à proximité du choc principal sont associées à un transfert de contraintes statiques. Les essaims sismiques situés au-dessus ou à distance du choc principal montrent une interaction avec des migrations de fluide. Cette dualité de processus explique le nombre anormalement élevé de répliques observées (**De Barros et al., 2019a**).

Article sélectionné

L'article suivant décrit l'analyse des répliques du séisme de Barcelonnette du 07/04/2014, en se basant en partie sur le stage de Master 2 de M. Baques. Il décrit notamment la ségrégation spatiale et les différences de comportement entre différents groupes de séismes, ce qui illustre le double processus à l'origine des anomalies sismiques observées dans cette région.

De Barros, L., M. Baques, M. Godano, A. Helmstteter, A. Deschamps, C. Larroque, F. Courboulex (2019) Fluid-Induced Swarms and Coseismic Stress Transfer: a Dual Process Highlighted in the Aftershock Sequence of the 7 April 2014 Earthquake (Ml 4.8, Ubaye, France), *Journal of Geophysical Research: Solid Earth*, doi:2018JB017226

JGR Solid Earth

RESEARCH ARTICLE
10.1029/2018JB017226

Key Points:
- Improved detection, classification, and location of the aftershock sequence following the Ml 4.8 earthquake in the French Alps
- Event sources align consistently along the mainshock fault, but on structures of its damaged zone or to small faults further away
- Spatial separation of two different processes: coseismic stress transfer close to the mainshock and fluid-pressure diffusion further away

Supporting Information:
- Supporting Information S1
- Movie S1

Correspondence to:
L. De Barros,
debarros@geoazur.unice.fr

Citation:
De Barros, L., Baques, M., Godano, M., Helmstetter, A., Deschamps, A., Larroque, C., & Courboulex, F. (2019). Fluid-induced swarms and coseismic stress transfer: A dual process highlighted in the aftershock sequence of the 7 April 2014 earthquake (Ml 4.8, Ubaye, France). *Journal of Geophysical Research: Solid Earth*, *124*, 3918–3932. https://doi.org/10.1029/2018JB017226

Received 20 DEC 2018
Accepted 17 MAR 2019
Accepted article online 21 MAR 2019
Published online 11 APR 2019

Fluid-Induced Swarms and Coseismic Stress Transfer: A Dual Process Highlighted in the Aftershock Sequence of the 7 April 2014 Earthquake (Ml 4.8, Ubaye, France)

Louis De Barros[1], Marion Baques[1], Maxime Godano[1], Agnès Helmstetter[2], Anne Deschamps[1], Christophe Larroque[1], and Francoise Courboulex[1]

[1]Université Côte d'Azur, CNRS, OCA, IRD, Géoazur, Sophia Antipolis, Valbonne, France, [2]Université Grenoble Alpes, Université Savoie Mont Blanc, CNRS, IRD, IFSTTAR, ISTerre, Grenoble, France

Abstract The upper part of the Ubaye Valley (French Alps) is characterized by alternating mainshock-aftershock sequences and swarms. Particularly, during the 2012–2015 crisis, four mainshocks with Ml > 3.5 occurred. We here focus on the aftershocks of the largest one (Ml = 4.8, 7 April 2014), in order to better understand the involved processes behind this peculiar seismic behavior. We use template matching detection, waveform classification, and double-difference relocations to analyze this seismicity, on average and at the scale of the clusters that compose it. Most event sources are aligned along a plane consistent with the mainshock fault (N165, 65°W), but occurred on conjugate structures. A few clusters of seismicity are also observed far from the mainshock source. Our analysis shows that distinct, spatially separated processes are at play. While coseismic stress transfer explains the seismicity close to the mainshock source, fluid-pressure diffusion and distant stress triggering are required to generate events farther away. The overall distributions in time and magnitude followed a slow Omori's decay and a Gutenberg-Richter relationship, respectively. However, these classical responses arise from the superposition of very different behaviors, associated with different processes at depth.

Plain Language Summary Earthquakes have regularly shaken the upper part of the Ubaye valley, near the town of Barcelonnette in the Southwestern French Alps, for nearly 20 years. The earthquake behavior is peculiar, as swarms of numerous low magnitude events alternate with larger earthquakes, such as the Ml 4.8 one occurring on 7 April 2014. To understand this dual behavior, we performed an in-depth analysis of the aftershock of this event. The seismicity mainly aligns on a plane consistent with the mainshock fault (N165, 65°W). However, most of the events occurred on branching structures, belonging to the damaged zone of this fault, or on some other small faults far away. While the average behavior of this aftershock sequence is close to a standard one, we show that two different processes occurred at depth. Events occurring close to the mainshock are triggered by coseismic stress transfer, while fluid-pressure diffusion are likely required to explain the seismicity further away. Such dual process should be considered for seismic hazard assessment.

1. Introduction

Earthquakes commonly occur either as mainshock-aftershock sequences or as seismic swarms. Mainshock-aftershock sequences are characterized by the occurrence of a large magnitude event, followed by a decaying series of smaller events. The latter are primarily related to the coseismic static stress transfer (Stein, 1999), but also to dynamic stress changes (Felzer & Brodsky, 2006), coseismic fluid pressurization (Miller et al., 2004), or aseismic afterslip (Perfettini & Avouac, 2004). A swarm activity is characterized by a localized cluster of seismicity, without a clear onset, as the largest event occurs in the middle of the sequence. In space, the size of the swarm is much larger than the rupture length of the largest event (Vidale & Shearer, 2006), so that Coulomb static stress changes cannot explain the triggering of the sequence. An additional forcing is thus required to explain the triggering at large distances and the long duration. It can be associated to fluids from meteoric origin (e.g., West Bohemian swarm, Hainzl et al., 2012), pervasive in the faulted crusts (e.g., Corinth Gulf, Duverger et al., 2015), or linked to anthropic activities (e.g., waste water disposal in Oklahoma, Keranen et al., 2014). Seismic swarms are also observed driven by slow, aseismic slips, on

creeping faults, such as on parts of the San Andreas fault (Waldhauser et al., 2004), in subduction areas (Vallée et al., 2013), and in central Italy (Collettini & Barchi, 2002).

Therefore, aftershock sequences and swarms may share common driving processes, related to fluids or to aseismic slip. These processes may be intertwined, as fluid flow, aseismic slip, and stress transfer may be simultaneously at play. For example, aseismic creep might induce fault dilatancies, which perturb the fluid distribution at depth, sustaining the aseismic motion and leading to seismicity by stress transfer (De Barros et al., 2018; Guglielmi et al., 2015). Therefore, the driving mechanisms of both swarms and aftershocks are still questionable, especially if a full continuum of behaviors exists between these two end-members. This question is particularly relevant for areas that are alternatively struck by mainshocks and seismic swarms, as the latter may evolve to the first one. For example, the seismicity in the Gulf of Corinth is mainly characterized by swarms (Duverger et al., 2015), with large and damaging earthquakes occasionally (e.g., M~6 Aigion earthquake, Bernard et al., 1997). The l'Aquila earthquake (Mw = 6.2, 2009, central Italy) occurred after a 2-month-long swarm-like crisis, interpreted as driven by a slow-slip event (Borghi et al., 2016). Therefore, in order to understand the overall behavior of a seismic area, it is of crucial importance to understand what the driving processes are and how they interact. Such processes, which are still under debate, may be inferred by the analysis of either seismic swarms or aftershock sequences, as both share similarities.

We focus on the peculiar aftershock sequences following the 7 April 2014 earthquake (Ml = 4.8) in the Ubaye Valley. This area is the most active one in the French Alps. It has been frequently struck both by mainshocks with magnitude close to 5 (Thouvenot et al., 2016) and by several swarms, attributed to fluid migration (Jenatton et al., 2007; Leclère et al., 2013). The alternating swarms and mainshock/aftershock sequences make this area of scientific interest. Particularly, it was seismically active between 2012 and 2017, with more than 13,000 events of magnitude greater than 0.5, including four mainshocks with Ml > 3.5. As (1) the seismicity rate never came back to the pre-2012 rate, and (2) the largest event occurred in the middle of the sequence, the overall distribution of this crisis suggests a swarm behavior. After the 2014 mainshock, a dense network of postseismic temporary stations was installed at less than 10 km around the epicenter (see Figure 1). This aftershock sequence is of particular interest as the decay in the number of event is slower than expected by an Omori's law. By studying in details this sequence, we aim at identifying the driving process of the seismicity in this area, in order to understand the reason of such a peculiar behavior. Using a template matching detection and accurate relocation, we will zoom inside the seismic cluster and focus on the different families that compose it. Doing so, we will isolate the aftershocks, driven by coseismic stress transfer, from the swarm-like events, and we will separately analyze their spatiotemporal behavior.

2. Seismotectonic Context

The Ubaye valley is located in the southwestern Alps, close to the suture between Europe and the colliding Adriatic microplate (e.g., Dewey et al., 1989). The Paleozoic crystalline rocks of the Argentera massif are there overlapped by a 2-km-thick sedimentary cover made of the autochtonous Mesozoic and Cenozoic sediments of the Dauphinois domain and by the allochtonous unit of the Embrunais-Ubaye nappes which was thrusted onto the autochtonous during the Oligo-Miocene times (Corsini et al., 2004; Fry, 1989). Therefore, the crust displays numerous faults inherited from the Hercynian and Alpine orogenies and from the ongoing deformation in the Pliocene (Bigot-Cormier et al., 2000; Bogdanoff et al., 2000; Sue & Tricart, 2003). In Argentera-Ubaye, the major faults belong to a NW-SE system of subvertical right-lateral faults mainly activated during the Oligocene-Miocene times and whose current activity is being discussed (Larroque et al., 2001; Sanchez et al., 2010). From 2002 to 2016, the seismicity is mainly aligned N130°E and occurs at 3–8 km depth in the crystalline basement (Daniel et al., 2011; Jenatton et al., 2007; Thouvenot et al., 2016). Unfortunately, no coseismic surface rupture has been identified in the field to confirm this assumption.

At the scale of the western Alps, continuous GPS measurements since 16 years point out a complex deformation pattern with uplift of the axial part of the belt, decreasing from 2 mm/year in the north to 0.3 mm/year in the south. This uplift is combined with low East-West extensional deformation (in the range of 10 nanostrain per year) in the center of the belt, including the Ubaye area, while no active shortening is detected between each side of the Alps (Nocquet et al., 2016; Walpersdorf et al., 2018). Therefore, the present-day dynamic of the western Alps is under discussion and results certainly of a combination of processes such

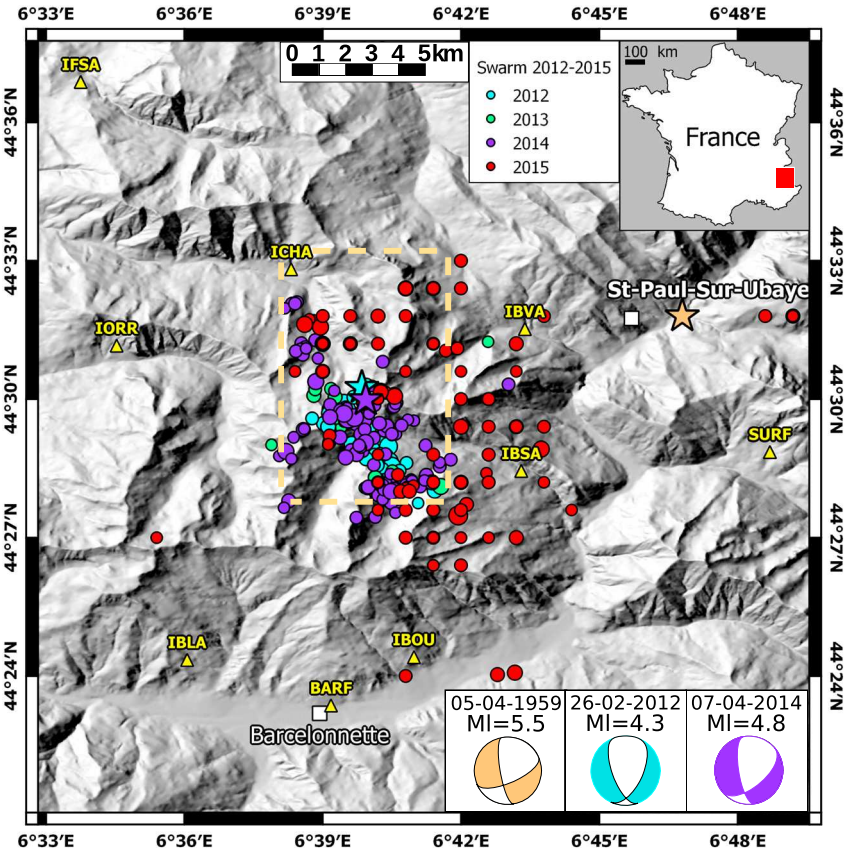

Figure 1. Map of the upper Ubaye valley in the French Alps and general overview of the seismicity. Top right inset shows the location in France. Topography is shown as gray shaded area, with main towns represented as white squares. The largest events (Ml $\geq$ 1.5) of the 2012–2016 swarms are colored by year, with size related to magnitudes (Sismalp catalog, Thouvenot et al., 2016). The main earthquakes in the area (1959, 2012, and 2014) are shown as stars, with their mechanisms given in the bottom right insets. Yellow triangles show the nine seismic stations used in this study. The dashed orange rectangles indicate the studied area.

as buoyancy effects (Larroque et al., 2009), deep asthenospheric processes (Zhao et al., 2015), erosional unloading (Vernant et al., 2013), and/or postglacial rebound (Nocquet et al., 2016). Whatever, in Ubaye, the extensional deformation highlighted by the geodetic measurements is consistent with the observed earthquake mechanisms.

Nowadays, the Ubaye valley is the most active seismic zone in the French Alps. This area is indeed regularly struck either by seismic swarms of small magnitude events or by classical mainshock/aftershock sequences. Historically, one of the largest earthquakes in the French Alps (Ml ~5.5) occurred on 5 April 1959 (Nicolas et al., 1990). Seismic swarms occurred then in 1978, 1989, and 2003–2004 (Fréchet & Pavoni, 1979). The latter, with more than 16,000 detected events, clustered on a 9 km long normal/strike-slip fault (Jenatton et al., 2007). Despite this large number of events, no large earthquake occurred currently, as the magnitudes stayed below Ml 2.7. The unfavorable orientation of the faults toward the stress state (Leclère et al., 2012) and the spatiotemporal migration (Daniel et al., 2011) suggest a fluid-induced seismicity. More recently, an intense seismic activity started with a Ml 4.3 earthquake on the 26 February 2012 (22h37 UTC). This event, located a few kilometers NW of the 2003–2004 cluster, occurred beneath the Parpaillon massif, belonging to the Ubaye-Embrunais nappes which peaks at 3,046 m. It was felt by the population, particularly toward the south because of a strong source directivity effect (Courboulex et al., 2013) and caused some structural damages in the epicentral zone. On 7 April 2014 (19h26 UTC), another earthquake occurred at a similar location (0.3 km southward and 1 km downward), with a local magnitude Ml between 4.8 (Thouvenot et al., 2016) and 5.2 (Sira et al., 2014) and a moment magnitude Mw = 4.8. This event was the strongest since 1959 in this area, but also in the French Alps in the last 20 years. Once again, this event

was a source of concern for the surrounding population, and few damages were noticed on close buildings (maximal EMS98 intensity of VI, Sira et al., 2014). It occurred at about 9 km depth below sea level, on a ~N160, 55°SW fault (Thouvenot et al., 2016). Its focal mechanism, similarly as the 2012 event, show a dominant normal motion, with a right-lateral strike-slip component. Two other mainshocks occurred in 2015 in the same area, with magnitudes of Ml 3.4 (11 April 2015) and 4.2 (6 November 2015). After all those mainshocks, the seismicity decreased (see Figure 2), at rate that can be slower than expected by an Omori's law. Interestingly, the decrease is much slower after the 26 February 2012 event than after the 6 November 2015 event, despite similar magnitudes. It suggests that the aftershock sequences, at least for the 2012 and 2015 events, are not solely driven by coseismic stress transfer. In total, in the 2012–2015 years, more than 13,000 events, with a cut-off magnitude of ~0.5, were detected and analyzed by Thouvenot et al. (2016). After the 2012 event, but not the 2014 one, a general spatiotemporal migration of the aftershocks toward the South-East is interpreted as due to fluid-pressure diffusion (Thouvenot et al., 2016). The behavior of the 2012 crisis is therefore peculiar: While a mainshock started the crisis, the aftershock sequences share common features with seismic swarms, in the large number of events or in migration patterns (Thouvenot et al., 2016). Furthermore, numerous focal mechanisms are now well constrained and reveal a complex normal-transtensional tectonic regime which strike as the high relief of the western Alps (Delacou et al., 2004; Larroque et al., 2009). As the current ruptures were blind, the active fault extensions and geometry are partly unknown in this area. Therefore, the complex seismological behavior and tectonic context make that the possibility of a large, damaging earthquakes is still an open question.

3. Data and Methods

The aftershock sequence of the 7 April 2014 (19h26 UTC) earthquake was initially analyzed by Thouvenot et al. (2016) using the Sismalp network. This network was mainly composed of triggered stations equipped with 1 Hz seismometers. Apart from four stations, most stations are located a few tens of kilometers away from the swarm area, and up to 150 km. In order to improve (1) the detection capability and (2) the accuracy of the analysis, seven short-period stations, with continuous recordings, were installed after the 2014 mainshock. These seven stations, plus two permanent stations (SURF belonging to the French RESIF network, RESIF, 1995, and BARF belonging to the French Sismo à L'Ecole network) were located at distances smaller than 10 km from the epicenter area (Figure 1). This network was fully running for 2 months, since 10 April until 15 June 2014.

Events from the 2012–2016 Sismalp catalog (Thouvenot et al., 2016) were used as templates to improve the detection level. We used data from station SURF, the permanent station located closer from the swarm area. Earthquakes were first correlated with each other to group events into families with similar waveforms. An earthquake was associated with a family if the correlation with at least one event from this family was larger than 0.8. Then we stacked all waveforms inside each family to obtain the template waveforms. We used these templates to look for similar signals in the continuous records of station SURF using a template-matching filter with a minimum correlation of 0.5 (Gibbons & Ringdal, 2006). Between the 10 April and the 15 June 2014, the Sismalp catalog contains 846 events. We have extended this catalog up to 10,895 events, which have been classified into families with similar waveforms. Within each family, we therefore expect to find events that share similar locations and mechanisms, that is, that originate from the same structure, or to subparallel ones. We then focus on the largest 31 families, containing between 52 and 1,757 events, for a total of 9,027 events.

Fifty events, which are either the largest events of each family or events with magnitude larger than 2 in the Sismalp catalog, were then manually picked on 12 stations and relocated using the double-difference HYPODD software (Waldhauser & Ellsworth, 2000). These master-events are then used as first guesses for the location of the family centroid. Similarly to Thouvenot et al. (2016), the location is performed using an eight-layer crustal model proposed by Sellami et al. (1995) for the western-part of the Alps.

Inside each family, the travel time differences between pairs of events are then computed using cross-correlation on short windows around *P* and *S* wave arrivals. A pair of events is composed of one event and one among the ~15% of the events that share the mean highest correlation coefficients with the other. Within each family, as the detection makes the events roughly aligned, *P* and *S* waves are manually picked for a single event on all stations, in order to define the position of the windows used for correlation. The

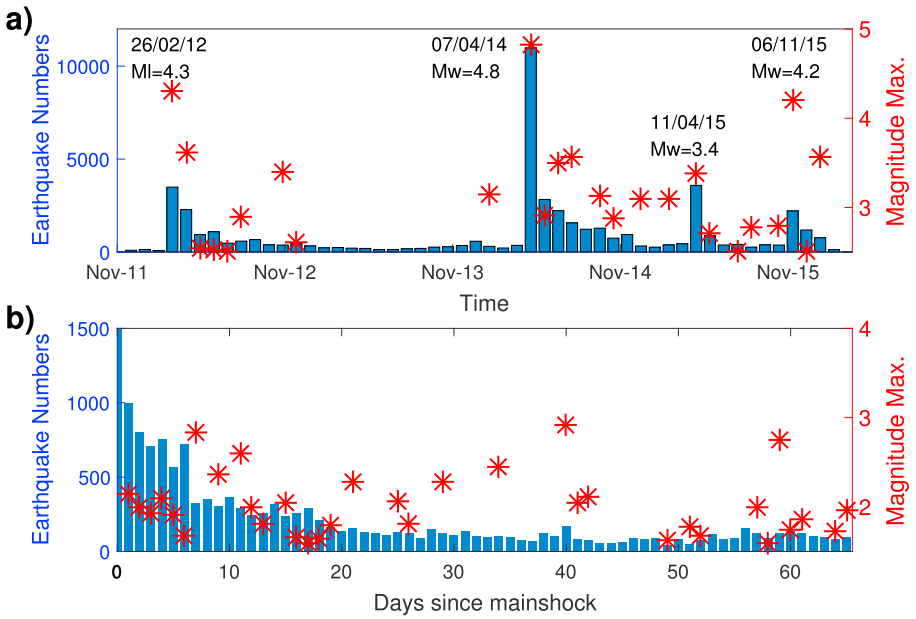

Figure 2. Time distribution of earthquakes and their magnitudes. (a) Monthly rates and maximum magnitude (Ml > 2.5) from November 2011 to March 2016 and (b) daily rates and maximum magnitudes (Ml > 1.5) after the Ml 4.8 mainshock occurring on 7 April 2014.

correlation between events is then made on 2 s long windows (0.4 s before and 1.6 s after the picked times, with a 3–15 Hz filtering). Only the travel-time differences with a cross-correlation coefficient higher than 70% are kept, leading to a total of 161,090 and 688,895 travel-times for *P* and *S* waves, respectively. Note that the number of P-travel times is smaller because of its low amplitude on most of the stations. Events inside every family are then relocated separately with the HYPODD software. Finally, the locations of all events are corrected to replace the master-events at their location determined in the first inversion step. In total, 5,947 events were relocated. It represents only 55% of the detected events, but 700% of the initial Sismalp catalog.

We then compute location errors. The locations of the family cluster, obtained through the first relative location step, have an uncertainty lower than 30 m horizontally and 70 m vertically. Inside a family, the relative errors (second relocation) are found to be less than 10 m in all directions (see supporting information Figure S1). Despite a very similar cluster shape, the seismicity is observed to be more sharply clustered, with clearer location structures, in our location compared to the ones from Thouvenot et al. (2016). Our locations are, on average, shifted by ~600 m toward the South-East, and 300 m shallower. As the same velocity model is used, this discrepancy may come from the station distribution, as our network has stations with well-distributed azimuths and at short distance around the epicenter area. The 7 April 2014 mainshock was not recorded by the temporary stations. We therefore correct the location found by Thouvenot et al. (2016) by these average shifts, which may lead to location uncertainties that might reach several hundred of meters.

We then analyze the geometry of every family cluster by means of two different methods. The 3-point method from Fehler et al. (1987) allows the statistical determination of the most likely poles of the planar structures. This method assumes planar structures, and therefore fails in case of elongated structure. It is however robust when several parallel planes are present. The second method (Michelini & Bolt, 1986) is based on the eigenvalue decomposition of the covariance matrix, which allows inferring the axis orientation and length of the best fitting ellipsoid, which characterizes the geometry of the structures. Both method results are carefully checked against each other and by visual inspection.

For the events with a magnitude already computed by Sismalp (Thouvenot et al., 2016), we invert the *S* wave amplitudes and the hypocentral distance to the stations to build a local magnitude law. The errors on this reconstruction are lower than 0.2, which is then assumed to be the uncertainty on the computed

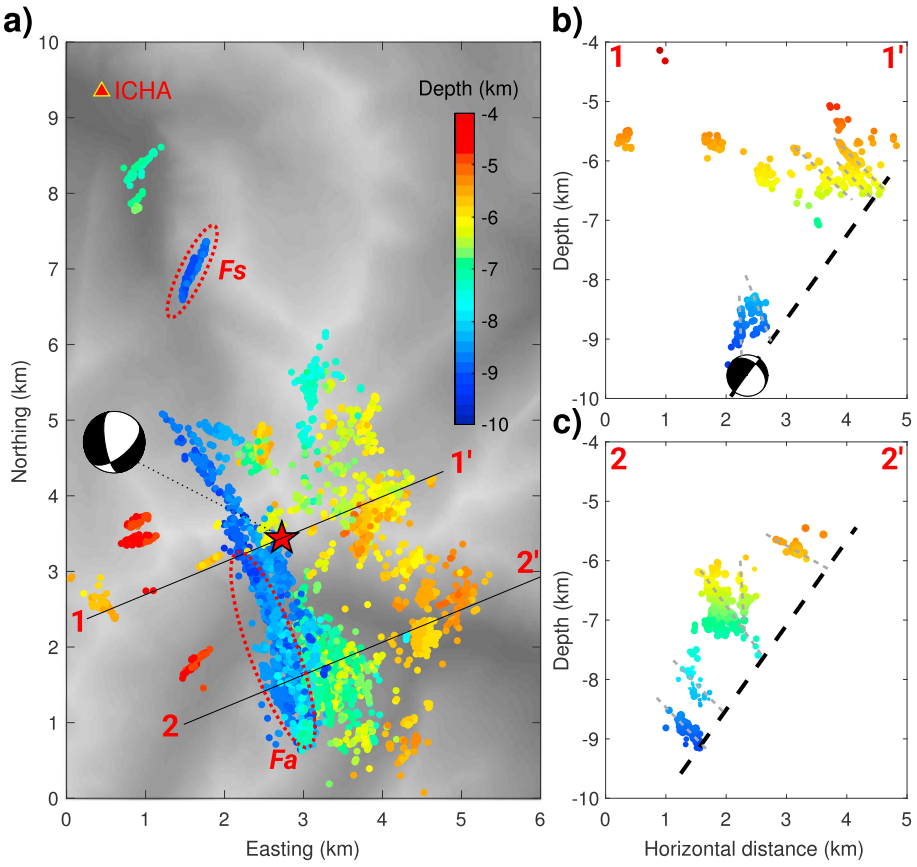

Figure 3. Event locations, colored by depth below sea level. (a) Map view of the seismicity. The star shows the mainshock location. The latitude and longitude reference are $N = 44°27'46''$ and $E = 6°38'12''$, respectively. Events at horizontal distances smaller than 200 m from the vertical planes 1–1′ and 2–2′ are projected onto those planes, to build the cross-sections given in (b) and (c), respectively. On each panel, the size of the location dots refers to the event magnitude. The mainshock mechanism is given on panels (a) and (b), with its fault plane extrapolated in (b) and (c). On panel (a), red ellipses identify the families Fa and Fs used as examples in this study. On panels (b) and (c), light gray dashed lines schematically show the event alignments. The evolution of the locations with time is shown in the Movie S1.

magnitudes. This law then allows for the extrapolation of the magnitude computation to every event, down to magnitude Ml ≈ −1.5. The cut-off magnitude in the Gutenberg-Richter relationships is Ml ≈ −0.5, with a maximal magnitude of 3.2. The inferred properties of all families are gathered in auxiliary materials (Table S1).

4. Results

4.1. Location Geometry

Between 10 April and 14 June 2014 (days 3 to 68 after the mainshock), 5,947 events, belonging to 31 different families, have been relocated (see Figure 3 and Movie S1). The depth sources lie between −4 and −10 km. At these depths, all events occurred in the crystalline basement of the Argentera massif, without any seismicity in the sedimentary layers at shallower depths.

The main alignment of seismicity describes a 5 km long, 4 km wide plane, striking N160. With event depths lying between 5 and 9.5 km, this plane is dipping ~60 W. This dip is confirmed by the 3-points method applied on all events. This plane orientation is compatible with the N160, 55°W fault plane inferred from the focal mechanism of the mainshock (Thouvenot et al., 2016), with the mainshock hypocenter located in its deeper part. At first order, the plane on which seismicity aligns (later refereed as main structure) might be the mainshock fault.

When looking in more details at the seismicity distribution on and around this main plane, the geometry is quite complex (see Figure 3):

- Deep events (7.5–9.5 km): In the lowest part of the main structure, both 3-point or covariance analysis show that families of events align on planes that are striking as the main structure (N160), but dipping either ~70°E or ~65°W (see Table S1 and Figure S2). The planes dipping west might be either on the main plane or parallel to it, while the ones dipping East might be conjugate structures. For example, the family denoted *Fa* on Figure 3 and composed of 1,250 located events aligns on a ~N160, 60°E planar structure which is 2.5 km long and ~1 km wide.
- Intermediate depth events (6.5–8 km): A smaller density of events characterizes the middle part of the main structure.
- Shallow events (5–6.5 km): In the upper part of the main structure, the seismicity aligns on planes which are striking N20-to-60° and dipping ~65°E or °W or on elongated structures, oriented normal to the main structure (N~60°, ~60°E). Therefore, the seismicity on those structures do not belong to the main structure either.

Therefore, on average, the seismicity is drawing a broad alignment compatible with the fault plane of the mainshock. In details, the 3-points and the covariance analysis show that most of the seismic sources gather on planes with dip and/or azimuth strongly different from the main structure. Therefore, this shows that a large part of the seismicity did not occur on the main fault plane. Even if the mainshock location was erroneous by more than 1 km vertically, most of the seismicity would have occurred above the mainshock plane, in the hanging wall. Deep and shallow events are also aligned on planes with very different dips and azimuths. It suggests either that the stress field changes between depths of 9 and 5 km, or that different mechanical processes are at play.

Finally, there are a few clusters of seismic events that do not belong to the main structure (later referred to as outer families). These clusters can be either shallow or deep (from 4 to 10 km depth), above the main structure or up to 3 km far away from it. They do not show any consistent strikes and dips, even if some of them are striking N0-to-50°. These clusters do not seem to have active connection with the main structure, as there are seismic gaps between them and the main structure. For example, the cluster denoted *Fs* on Figure 3 is composed of 279 events, whose sources align on a N10°, subvertically dipping plane at ~10 km depth. It occurred 2 km away from the main structure (3.5 km from the mainshock), without any seismic event located in between.

4.2. Space, Time, and Magnitude Behavior

Figure 4 shows the temporal distribution and the spatiotemporal behavior of the seismicity, on average for all events, and for two selected families (*Fa* and *Fs*, see Figure 3). When looking at the average behavior of all events together, the number of events decays with time. The same pattern is observed for the deeper families, such as *Fa*, while family *Fs* and the outer families show a swarm-like behavior, with a delayed increase and decrease of seismicity. Most of the shallow families, in the upper part of the main structure, also behave like a swarm. For example, family *Fs* is mainly active from 55 to 65 days after the mainshock, with nearly no event before.

To refine the time distributions, we can fit a modified Omori's law (Utsu, 1961) of the form $N(t) = K/(c + t)^p$, where N is the number of events; t is the time; and K, c, and p are constants to determine. This fit is performed for the period in which events have been relocated (days 4 to 62, see Figure 5) using a maximum likelihood method (Ogata, 1999). From day 4, the relocated events show a decay with an exponent of $p = 0.77$, that is, lower than 1. We checked that this value does not come from a bias of the catalog, as (1) all detected events, (2) all relocated events, and (3) relocated events with magnitude above the completeness magnitude (Ml = −0.5) lead to similar values. Note that the detection catalog shows a smaller exponent in the first 4 days, leading to an average $p = 0.65$ exponent when looking at all the aftershock period. This change in the decay rate may be due either to a bias in the catalog in the first few days, or to a change in the seismic behavior. The families that behave as aftershocks, such as *Fa*, strongly differ from the classical Omori's law, as they decay much faster, with a $p = 1.41$ exponent. On the other hand, the swarm families decay very slowly, with an exponent $p = 0.18$. Therefore, while the overall seismic response is decaying more slowly than what is commonly

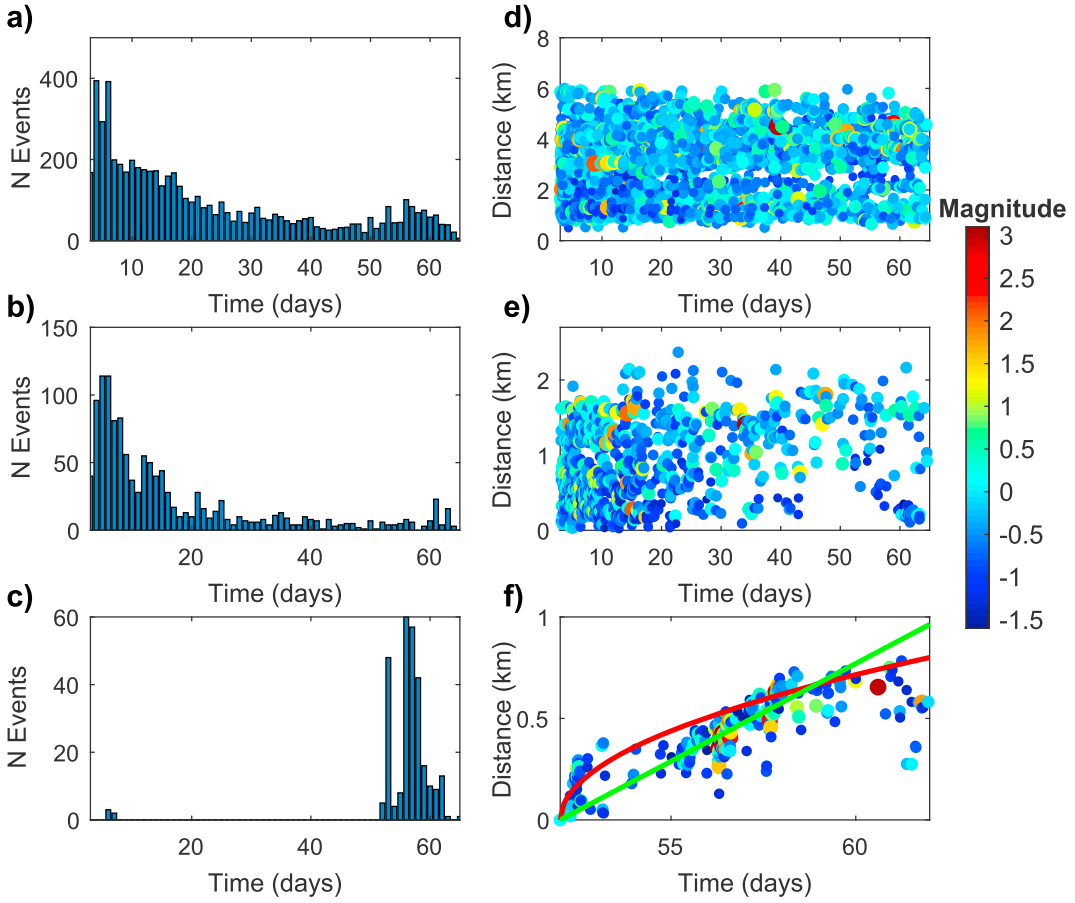

Figure 4. Temporal (left columns) and spatiotemporal (right column) distributions of the seismicity, for (a) and (d) all located events; (b) and (e) the Fs family; and (c) and (f) for the Fa family (see Figure 3). For the spatiotemporal distributions (d–f), the colors show the magnitude of events. In all panels, time is in days from the mainshock. In (d), distances are computed from the mainshock hypocenter; in (e) and (f), they are computed from the first event in families Fs and Fa, respectively. In panel (f), the green and red lines are the best fit for a constant velocity migration (V = 0.1 km/day) and for a diffusion law fit (D = 0.05 m^2/s), respectively.

observed, the families that compose it show either a faster-than-usual decay after the mainshock perturbation, or a delayed swarm behavior.

There is no overall clear migration of the seismicity after the mainshock. The events occurred at up to 6 km from the mainshock hypocenter 3 days after it, and this distance did not grow with time (see Figure 4). As already stated by Thouvenot et al. (2016), the mainshock reactivates the entire area quasi-instantaneously. Similar behaviors are observed for families with decaying number of events, for example, *Fa*. However, when looking in deeper details inside the swarm families, clear migrations can be observed. Therefore, while no spatiotemporal variations are observed within the deep families of the main structure, most of the clusters that are either outside or shallow show a seismic migration (see Table S1). Assuming a constant migration velocity, the seismic front grows with a speed varying between 6 and 85 m/day depending on the clusters. Such velocity is too slow to be attributed to slow-slip (Lohman & McGuire, 2007), but may be related to fluid-pressure diffusion. If the seismicity occurred at the fluid-pressure front, the distance-time (so-called R-t diagram) distribution envelops can be fitted by a diffusion law, such as $R = \sqrt{(\pi\ D\ t)}$ (Shapiro et al., 1997). The diffusion coefficient *D* is found to vary between 2e-3 and 6e-2 m/s^2, which leads to permeability estimation in the range 1e-16 to 5e-14 m^2.

The magnitude distribution also differs among families (Figure 6). Fitting a Gutenberg-Richter law (maximum likelihood fit; Ogata & Katsura, 1993) to the full set of events gives a b-value slightly lower than 1 ($b = 0.95 \pm 0.01$), where the uncertainty is computed as $b/\sqrt{N}$, with N the number of events (Aki, 1965).

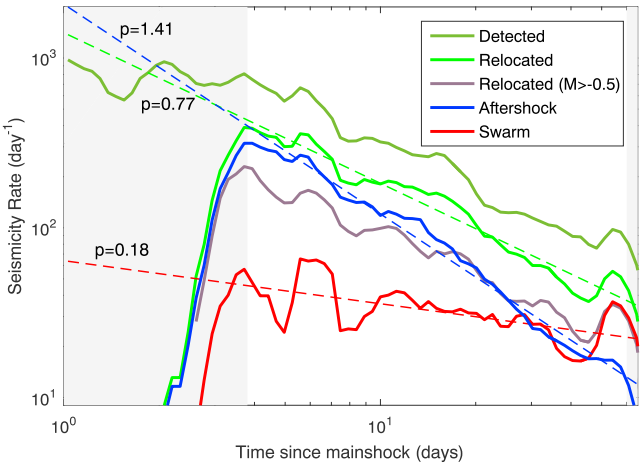

Figure 5. Seismicity rate for all detected events, relocated events, relocated events with magnitude greater than the magnitude of completeness ($M > -0.5$), relocated events belonging to aftershock families and relocated events belonging to swarm-like families. The dashed lines indicate the best fit for a modified Omori's law, with a slope of $p = 1.41$ (aftershocks), $p = 0.77$ (relocated and detected events), and $p = 0.18$ (swarms).

The aftershock-like families are characterized by a slightly higher value of $b = 0.99 \pm 0.02$. However, a lower exponent is found for the swarm-like families, with a mean b-value of 0.85 ± 0.02. The same observations can be made on individual families, despite a variability in the b-values and the magnitude completeness (see Figure 6 and Table S1). For example, the family *Fa*, at the bottom of the main structure, has a b-value of 1.01 ± 0.03 while the swarm cluster *Fs* shows $b = 0.81 \pm 0.05$.

5. Discussion

5.1. Complex Spatial Distribution of Seismicity

The aftershocks of the 7 April 2014 Ubaye earthquake mainly align on a large plane, whose dips and azimuths are consistent with the fault plane of the mainshock. This fault plane is shown in Figure 3 as an oversimplified straight line and is more likely to be more complex, with some curvatures. However, improbable changes in dips between subvertical to less than 30° are required for this structure to pass through the aftershock cluster. Furthermore, most of the family structures show strikes and dips that are not compatible with the main fault plane. Therefore, the seismicity seems to occur on conjugate structures or on subparallel planes, mainly around the deeper and shallower ends of the main fault plane. The crust around the main fault should be highly fractured, inherited from its complex tectonic history. The structures highlighted by the event alignments could also correspond to the fault damaged zone, as a splay network developing at the tips of the main fault (Perrin et al., 2016). The occurrence of aftershocks on different structures than the mainshock one is not exceptional. The aftershock sequence of the 1996 Pyrenees earthquake (Ml 5.2) also distributes on structures with various orientations (Pauchet et al., 1999). The Mogul swarm (Nevada, United States) locations highlighted a main fault and its damaged zone (Ruhl et al., 2016). On the San Jacinto fault, most aftershocks of the Mw 5.2 Borrego Springs earthquake do not occur on the main plane, but on branches orthogonal to it (Ross, Hauksson, et al., 2017). Therefore, the aftershock location highlights the complex interaction between the stress perturbations and the damaged zone of the fault.

Most of the seismicity is not located on the assumed mainshock fault, but above it. The coseismic stress changes might have been negative on the main fault plane and in its footwall, leading to a lack of seismicity in these zones. Alternatively, it could be a consequence of the previous 2012 mainshock, which share similar location and mechanisms with the 2014 one (Thouvenot et al., 2016). It may have discharged the stress on this fault plane, except on its bottom end where the 2014 earthquake occurred. Such an asymmetric distribution was also observed for aftershocks on large faults in California (Zaliapin & Ben-Zion, 2011) and interpreted as due to the difference in materials properties between both sides of the faults (Rubin & Ampuero, 2007). The damaged zone might also be strongly asymmetric, due to a preferential rupture directivity. However, even if the 2012 earthquake showed a clear rupture directivity toward the south-east (Courboulex et al., 2013), rupture propagation was not observed directional for the 2014 earthquake. Alternatively, the mainshock slip might have changed the permeability of the fault, leading to new fluid paths and upward migration of the fluids, which then induced the swarm behaviors observed in the upper part of the main structure.

Finally, the structures at depth (7.5–9.5 km), with a ~N160° azimuth, show a very different orientation from the shallower structures (5–6.5 km), striking N20-to-50°. The seismic clusters outside the main structure occurred on structures with various azimuths. By inverting focal mechanisms for the 2003–2004 crisis (Leclère et al., 2013) and the 2012–2015 crisis (Fojtíková & Vavryčuk, 2018), the stress field shows a subhorizontal minor component σ3 oriented ~N100° and a N11 to 29° σ1 component, with a plunge between 12° and 61° depending on the authors. Such stress field is compatible with slip on N160° structures, such as the deep ones. However, shallow structures and outer ones are badly oriented toward the stress state. For example, the *Fs* structure is subvertically dipping with an N20° azimuth which is aligned with the major stress component. As shown by Leclère et al. (2013) for the 2004–2005 crisis, such heterogeneous

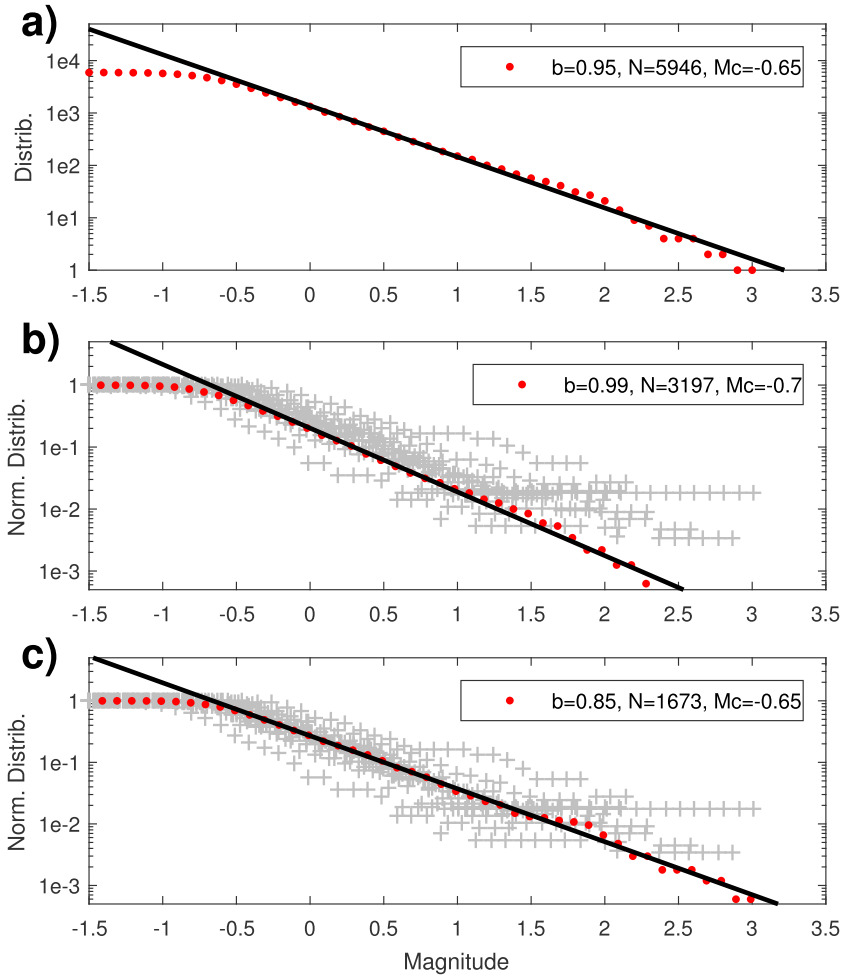

Figure 6. Cumulative magnitude distribution (red dots) for (a) all events, (b) events belonging to aftershock-like families, and (c) events belonging to swarm-behaving families. Black lines are their best fitting trend, with the computed b-value and completeness magnitude in the legend box. In panels (b) and (c), gray crosses show the normalized distributions for every families.

structures, and therefore mechanisms, are not compatible with a unique, static, stress state. Fojtíková and Vavryčuk (2018) also found that a very low friction coefficient of 0.2–0.3 is required. Therefore, either high fluid-pressure or heterogeneous stress state are required to induce slips on badly oriented structures. A detailed analysis of the mechanisms is however required to study in details the link between the seismicity and the stress state.

5.2. Two Processes: Fluid-Pressure and Stress Transfer

Among families, the spatial, temporal, and magnitude distributions reveal two clearly distinct behaviors. On one side, 53.7% of the located events belong to families that exhibit classical patterns of aftershock sequences: Their rates show a power law decay in the rate of events with time, without any migration patterns, their magnitudes follow a Gutenberg-Richter law with b ≈ 1, and they are located close to the mainshock. Such events are mostly located in the surroundings of the deeper part of the main fault. Only one area in the upper part and none of the outside clusters shows such behavior (Figure 7). They are mainly located at less than 3 km from the mainshock hypocenter, that is, at less than a typical fault length for a magnitude 5 earthquake. This is a classical observation for aftershocks, which are mainly on or around the rupture area, with a fast decay away from it (e.g., Harris, 1998). Therefore, these events are likely to be triggered by the static stress transferred from the mainshock (Stein, 1999), and they participate to rebalance the stress after the earthquake perturbation.

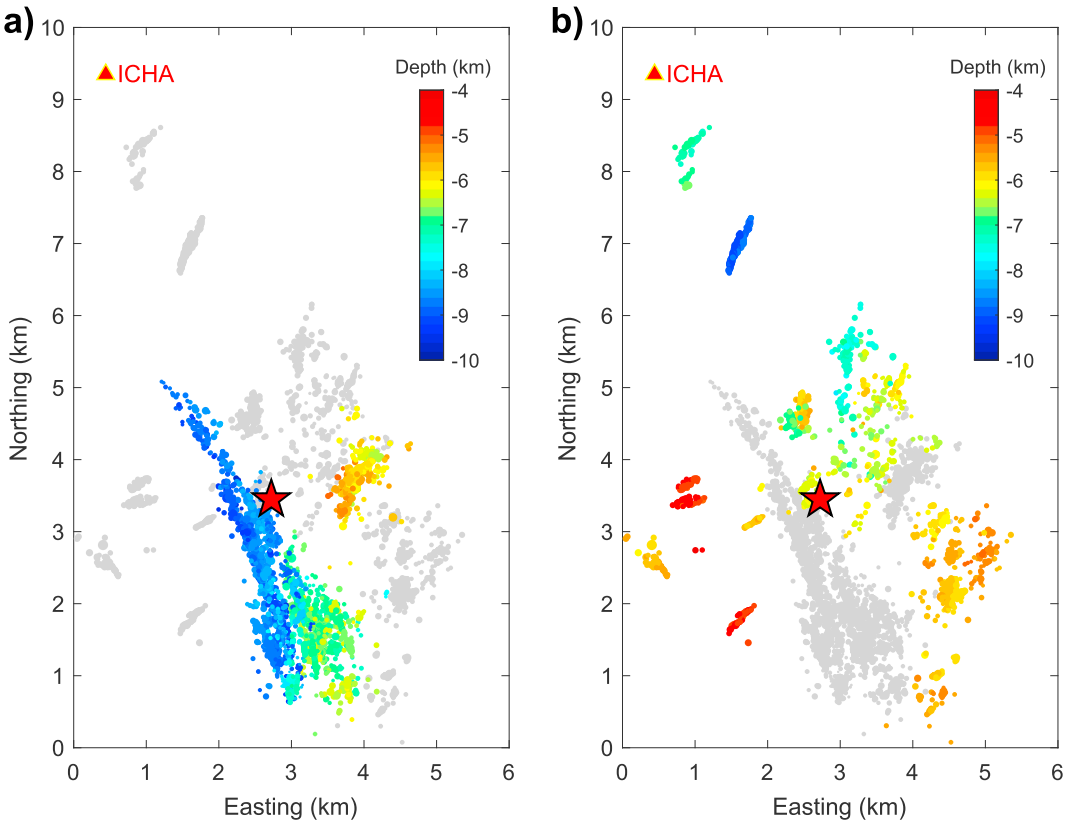

Figure 7. Location map with colorscale indicating the depth for events that belong to (a) aftershock-like families and (b) swarm-like and uncertain families.

On the other side, more than 28% of the events belongs to families with a swarm-like behavior. (1) Their maximum rate is reached days to months after the mainshock, with the largest event in the middle of the sequence; (2) they occurred at larger distances from the mainshock hypocenter (mainly between 3 and 6 km); (3) the rate of events shows an emergent increase and a slow decrease. Most of the outer families and of the shallow ones, but none of the deep ones, share this behavior (Figure 7). Among these families, most of them show a spatiotemporal migration of seismicity. Assuming a constant-rate migration leads to a mean velocity of about 0.1 km/day. Such slow velocities are not consistent with slow-slip processes, for which observed speeds are about 0.1 to 1.0 km/hr (Roland & McGuire, 2009). With a linear fluid diffusion process (Shapiro et al., 1997), diffusivity ranges from 0.002 to 0.06 m^2/s. Similar values were observed in Southern California (Chen et al., 2012), Corinth Rift (Duverger et al., 2015), or geothermal areas (Shapiro et al., 1997). Therefore, these events are likely induced by fluid-pressure diffusion. These families are also characterized by a low b-values in the magnitude distribution (Gutenberg-Richter law), with b-value ranging between 0.75 and 0.9. Fluid-induced seismicity usually shows b-values larger than 1, but also lower than 1 in extensional context such as in this study (Ibs-von Seht et al., 2008). Finally, the remaining 18% of events belong to families with a mix behavior, that is, with a power law temporal decay at the beginning, and a swarm activity later on. This latter number is quite small, meaning that on nearly 80% of the structures, the seismicity is controlled by a single process, and not by a mix of processes.

The differences between these two behaviors may also be increased by structural differences. While the aftershock sequences occurred on large (up to 3 km long) and planar NW-SE structures as evidenced in the geology, the swarm-like clusters describe structures that are smaller than 1 km long, with various orientation and shapes. Particularly, the seismicity highlights several elongated structures that can be related to the intersection of two faults. Therefore, a lack of large faults in the upper part of the main plane, with a suitable orientation for slip, might explain the swarm-like behaviors. However, this does not explain the slower-than-usual decay of the event rates or the delay in the seismicity onset for the swarm-like clusters.

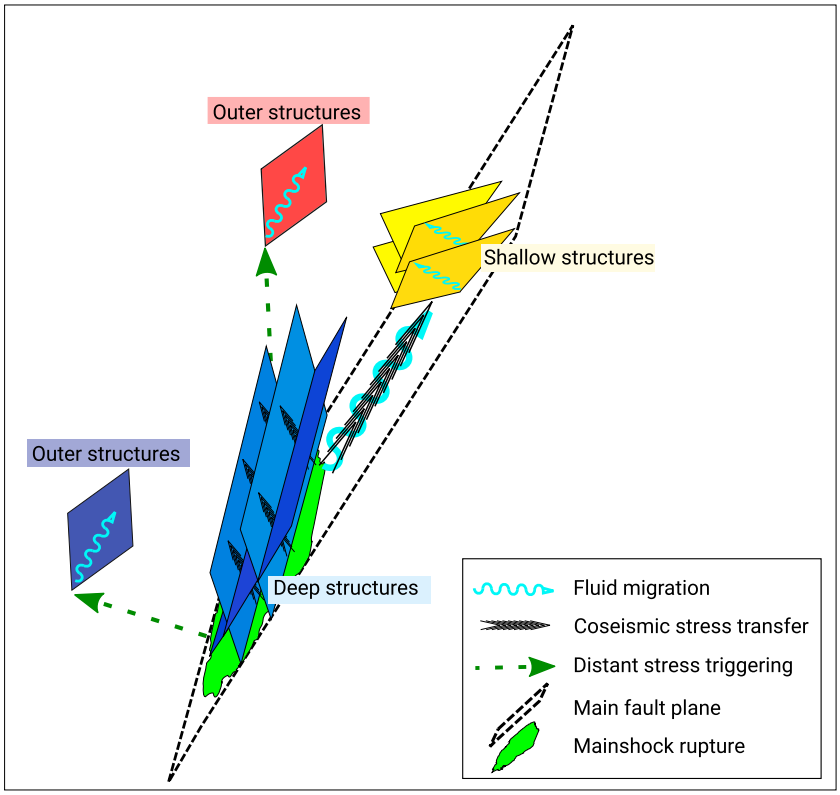

Figure 8. Conceptual model for the processes driving the aftershock sequence.

Therefore, we suggest that two different processes, which are spatially segregated, occurred. Close to the mainshock hypocenter, seismicity follows an aftershock-like behavior, in response to the coseismic Coulomb stress transfer. At larger distances, seismicity is dominated by swarm behaviors, likely induced by fluid-driven processes. On average, the aftershock sequence nearly decays as predicted by an Omori's law (though with a smaller than 1 exponent), and follows a Gutenberg-Richter law with a $b \approx 0.95$ value. However, this classical response masks the sum of two different behaviors: the 1/t decay originates from the sum of very fast ($p \approx 1.4$) decays and swarm-like distributions. The b-value is an average of a $b \approx 1$ value for the aftershocks and a $b \approx 0.85$ for the fluid-induced events. Therefore, it is likely that these two classical laws, commonly observed after mainshocks, originate from the regional average of different processes (Ben-Zion, 2008), that we were here able to separate.

5.3. Conceptual Model

Several processes, linked to fluid-pressure and stress transfer, are therefore required to explain the relationships between the mainshock and its aftershock sequence. Ross, Rollins, et al. (2017) reached a similar conclusion, with the observations of fluid-induced and stress-driven aftershocks after the 2010 M7.2 El Mayor-Cucapah earthquake in the Yuha Desert (United States). Miller et al. (2004) also involved CO_2 degassing to explain the aftershocks in the 1997 Umbria–Marche sequence (Italy). Interestingly, using a waveform-based classification, we are here able to isolate the processes because of their spatial segregation and to summarize them into a conceptual model (Figure 8).

First, at close distance from the mainshock and large depths, the seismicity is directly triggered by the coseismic stress transfer in the damaged zone of the hanging wall of the fault. Therefore, it highlights the complex interaction between the coseismic stress perturbation and the damaged zone. The shallower activity required fluid, as it is dominated by swarm behavior on structures badly oriented with the stress field. Fluid pressurization may directly originate from the coseismic stress perturbation. As shown by Bosl and Nur (2002) after the Landers earthquake (1992), the region of coseismic positive Coulomb stress correlates

with areas with pore pressure increased in response to the mainshock perturbation. Alternatively, the mainshock slip, through dilatancy processes, may have open new fluid paths, following the fault-valve behavior of Sibson (1990). Overpressurized fluids then migrated upward, inducing the seismicity of the shallow families.

Finally, some swarms occurred far from the mainshock, with areas devoid of events between them. If a fluid diffusion process started from the mainshock or the aftershock sequence on the main structure, it would be likely that seismic events would highlight the fluid paths. Furthermore, some swarms are at similar depths as the mainshock: A 3-to-6 km purely horizontal fluid migration is not likely. Therefore, a distant triggering is required. It might be due to coseismic or postseismic stress change, or to some dynamic triggering by the seismic waves of the mainshock or large aftershocks. Dynamic triggering has been shown to be efficient in areas with fluids (Brodsky et al., 2003; De Barros et al., 2017; Hill & Prejean, 2015). These transient perturbations might then open some fluid paths within the outer structures, leading to a fluid-pressure diffusion and inducing seismicity with a spatiotemporal migration.

Such dual behaviors, both in the seismicity and in the processes, are specific to the areas of Barcelonnette. Around this area, and despite similar tectonic context, the inner part of the Alpine chain do not behave like that and shows a more diffuse seismicity. Therefore, such behavior is related to an anomaly, likely related to fluids. Other localized areas, for example, the area of Vallorcine, in the northern part of the French Alps, also show similar anomalies, with alternating mainshocks (such as the 8 September 2005 Ml 4.5; Fréchet et al., 2011) and seismic swarms. These small and localized areas, gather much higher rate of seismicity than the rests of the Alps, and should have therefore a specific response in terms of earthquake hazard mitigation.

6. Conclusion

Since 2012, earthquakes have struck the Ubaye valley continuously, making this area the most active one in the French Alps. In 2014, a Ml 4.8 earthquake was a source of concern for the population. The aftershock sequence broadly aligns on a large plane, consistent with the mainshock fault. However, families individually align on distinct planes. Therefore, a majority of the seismic sources do not occur on the main fault plane, but on conjugate structures belonging or damage zone of the main fault. About 50% of the seismic events originate from coseismic stress transfer, at short distance from the mainshock. The remaining seismicity is further away, and requires fluid-pressure diffusion and distant, maybe dynamic, triggering. Such different processes required a highly fractured medium with pervasive fluids at depths. This area is therefore peculiar as deep fluid processes in addition to stress perturbations control the alternating swarms and mainshock/aftershock sequences. Such an aftershock sequence has therefore an intermediate behavior between the two end-members that are the fluid-induced seismicity and the tectonic-driven earthquakes. On average, the seismicity rate decay is slower than expected by an Omori's law, and the Gutenberg-Richer b-value is close to 1. This average behavior is however resulting from two strongly different patterns and processes. Therefore, it is likely that such dual behaviors are more common than expected, and hidden behind classical responses.

Acknowledgments
We thank SISMOB, the French seismic mobile pool and Géoazur for providing us with the seismological instrumentation for the temporary deployment, David Ambrois, Jerôme Chèze, and Xavier Martin from Géoazur and Cécile Cornou and Christophe Voisin from Isterre for the deployment itself. Continuous seismic data are available online through the RESIF portal (http://seismology.resif.fr/). RESIF is a national Research Infrastructure, recognized as such by the French Ministry of Higher Education and Research. It is managed by the RESIF Consortium, composed of 18 Research Institutions and Universities in France and it is additionally supported by a public grant overseen by the French National Research Agency (ANR) as part of the "Investissements d'Avenir" program (reference: ANR-11-EQPX-0040) and the French Ministry of Ecology, Sustainable Development and Energy. SURF data are from the permanent French Network FR (https://doi.org/10.15778/RESIF.FR), the other data are distributed as XG_2014 temporary network (https://doi.org/10.15778/RESIF.XG2014). Deployment and processing has been supported by Interreg-Alcotra France-Italy projects CASSAT (N° 181, 2007–2013) and RISVAL (N° 1510, 2014–2020) funded on European Regional Development Fund (ERDF). The catalog of relocated events is available upon request at L. De Barros (debarros@geoazur.unice.fr). We thank the associate editor (Y. Ben Zion), G. De Landro, and an anonymous reviewer for their useful comments.

References

Aki, K. (1965). Maximum likelihood estimate of b in the formula log N = a-bM and its confidence limits. *Bulletin of the Earthquake Research Institute, University of Tokyo*, *43*, 237–239.

Ben-Zion, Y. (2008). Collective behavior of earthquakes and faults: Continuum-discrete transitions, progressive evolutionary changes, and different dynamic regimes. *Reviews of Geophysics*, *46*, RG4006. https://doi.org/10.1029/2008RG000260

Bernard, P., Briole, P., Meyer, B., Lyon-Caen, H., Gomez, J. M., Tiberi, C., et al. (1997). The M s = 6.2, June 15, 1995 Aigion earthquake (Greece): Evidence for low angle normal faulting in the Corinth rift. *Journal of Seismology*, *1*(2), 131–150. https://doi.org/10.1023/A:1009795618839

Bigot-Cormier, F., Poupeau, G., & Sosson, M. (2000). Differential denudations of the Argentera Alpine external crystalline massif (SE France) revealed by fission track thermochronology (zircons, apatites). *Comptes Rendus de l'Académie des Sciences. Série II, Sciences de la Terre et des Planètes*, *330*, 363–370.

Bogdanoff, S., Michard, A., Mansour, M., & Poupeau, G. (2000). Apatite fission track analysis in the Argentera massif: Evidence of contrasting denudation rates in the external crystalline massifs of the Western Alps. *TerraNova*, *12*(3), 117–125. https://doi.org/10.1046/j.1365-3121.2000.123281.x

Borghi, A., Aoudia, A., Javed, F., & Barzaghi, R. (2016). Precursory slow-slip loaded the 2009 L'Aquila earthquake sequence. *Geophysical Journal International*, *205*(2), 776–784.

Bosl, W. J., & Nur, A. (2002). Aftershocks and pore fluid diffusion following the 1992 Landers earthquake. *Journal of Geophysical Research*, *107*(B12), 2366. https://doi.org/10.1029/2001JB000155

Brodsky, E. E., Roeloffs, E., Woodcock, D., Gall, I., & Manga, M. (2003). A mechanism for sustained groundwater pressure changes induced by distant earthquakes. *Journal of Geophysical Research*, *108*(5), 2390. https://doi.org/10.1029/2002JB002321

Chen, X., Shearer, P. M., & Abercrombie, R. E. (2012). Spatial migration of earthquakes within seismic clusters in Southern California: Evidence for fluid diffusion. *Journal of Geophysical Research*, *117*, B04301. https://doi.org/10.1029/2011JB008973

Collettini, C., & Barchi, M. R. (2002). A low-angle normal fault in the Umbria region (Central Italy): A mechanical model for the related microseismicity. *Tectonophysics*, *359*(1–2), 97–115. https://doi.org/10.1016/S0040-1951(02)00441-9

Corsini, M., Ruffet, G., & Caby, R. (2004). Alpine and late-Hercynian geochronological constraints in the Argentera massif (Western Alps). *Eclogae Geologicae Helvetiae*, *97*, 3–15. https://doi.org/10.1007/s00015-004-1107-8

Courboulex, F., Dujardin, A., Vallée, M., Delouis, B., Sira, C., Deschamps, A., et al. (2013). High-frequency directivity effect for an Mw 4.1 earthquake, widely felt by the population in southeastern France. *Bulletin of the Seismological Society of America*, *103*(6), 3347–3353. https://doi.org/10.1785/0120130073

Daniel, G., Prono, E., Renard, F., Thouvenot, F., Hainzl, S., Marsan, D., et al. (2011). Changes in effective stress during the 2003–2004 Ubaye seismic swarm, France. *Journal of Geophysical Research*, *116*, B01309. https://doi.org/10.1029/2010JB007551

De Barros, L., Deschamps, A., Sladen, A., Lyon-Caen, H., & Voulgaris, N. (2017). Investigating dynamic triggering of seismicity by regional earthquakes: The case of the Corinth Rift (Greece). *Geophysical Research Letters*, *44*, 10,921–10,929. https://doi.org/10.1002/2017GL075460

De Barros, L., Guglielmi, Y., Rivet, D., Cappa, F., & Duboeuf, L. (2018). Seismicity and fault aseismic deformation caused by fluid injection in decametric in-situ experiments. *Comptes Rendus Geoscience*, *350*, 464–475. https://doi.org/10.1016/j.crte.2018.08.002

Delacou, B., Sue, C., Champagnac, J.-D., & Burkhard, M. (2004). Present-day geodynamics in the bend of the western and central Alps as constrained by earthquake analysis. *Geophysical Journal International*, *158*(2), 753–774. https://doi.org/10.1111/j.1365-246X.2004.02320.x

Dewey, J., Helman, M., Turco, E., Hutton, D., & Knott, S. (1989). Kinematics of the western Mediterranean. In: Alpine tectonics, M. Coward, D. Dietrich and G.G. Parks. *Geological Society of London, Special Publication*, *45*, 265–283. https://doi.org/10.1144/GSL.SP.1989.045.01.15

Duverger, C., Godano, M., Bernard, P., Lyon-Caen, H., & Lambotte, S. (2015). The 2003–2004 seismic swarm in the western Corinth rift: Evidence for a multiscale pore pressure diffusion process along a permeable fault system. *Geophysical Research Letters*, *42*, 7374–7382. https://doi.org/10.1002/2015GL065298

Fehler, M., House, L., & Kaieda, H. (1987). Determining planes along which earthquakes occur: Method and application to earthquakes accompanying hydraulic fracturing. *Journal of Geophysical Research*, *92*(B9), 9407–9414. https://doi.org/10.1029/JB092iB09p09407

Felzer, K. R., & Brodsky, E. E. (2006). Decay of aftershock density with distance indicates triggering by dynamic stress. *Nature*, *441*(7094), 735–738. https://doi.org/10.1038/nature04799

Fojtíková, L., & Vavryčuk, V. (2018). Tectonic stress regime in the 2003–2004 and 2012–2015 earthquake swarms in the Ubaye Valley, French Alps. *Pure and Applied Geophysics*, *175*(6), 1997–2008. https://doi.org/10.1007/s00024-018-1792-2

Fréchet, J., & Pavoni, N. (1979). Etude de la sismicité de la zone briançonnaise entre Pelvoux et Argentera (Alpes Orientales) à l'aide d'un réseau de stations portables. *Eclogae Geologicae Helvetiae*, *118*(8), 4461–4476. https://doi.org/10.1002/jgrb.50297

Fréchet, J., Thouvenot, F., Frogneux, M., Deichmann, N., & Cara, M. (2011). The M w 4.5 Vallorcine (French Alps) earthquake of 8 September 2005 and its complex aftershock sequence. *Journal of Seismology*, *15*(1), 43–58. https://doi.org/10.1007/s10950-010-9205-8

Fry, N. (1989). Southwestward thrusting and tectonics of the Western Alps. *Geological Society of London, Special Publication*, *45*(1), 83–109. https://doi.org/10.1144/GSL.SP.1989.045.01.05

Gibbons, S. J., & Ringdal, F. (2006). The detection of low magnitude seismic events using array-based waveform correlation. *Geophysical Journal International*, *165*(1), 149–166. https://doi.org/10.1111/j.1365-246X.2006.02865.x

Guglielmi, Y., Cappa, F., Avouac, J. P., Henry, P., & Elsworth, D. (2015). Seismicity triggered by fluid injection–induced aseismic slip. *Science*, *348*(6240), 1224–1226. https://doi.org/10.1126/science.aab0476

Hainzl, S., Fischer, T., & Dahm, T. (2012). Seismicity-based estimation of the driving fluid pressure in the case of swarm activity in Western Bohemia. *Geophysical Journal International*, *191*(1), 271–281. https://doi.org/10.1111/j.1365-246X.2012.05610.x

Harris, R. A. (1998). Introduction to special section: Stress triggers, stress shadows, and implications for seismic hazard. *Journal of Geophysical Research*, *103*(B10), 24,347–24,358. https://doi.org/10.1029/98JB01576

Hill, D. P., & Prejean, S. (2015). Dynamic triggering. In G. Schubert (Ed.), *Earthquake seismology, treatise on geophysics* (2nd ed., Vol. 4, pp. 273–304). Oxford: Elsevier. https://doi.org/10.1016/B978-0-444-53802-4.00078-6

Ibs-von Seht, M., Plenefisch, T., & Klinge, K. (2008). Earthquake swarms in continental rifts—A comparison of selected cases in America, Africa and Europe. *Tectonophysics*, *452*(1–4), 66–77. https://doi.org/10.1016/j.tecto.2008.02.008

Jenatton, L., Guiguet, R., Thouvenot, F., & Daix, N. (2007). The 16,000-event 2003–2004 earthquake swarm in Ubaye (French Alps). *Journal of Geophysical Research*, *112*(B11). https://doi.org/10.1029/2006JB004878

Keranen, K. M., Weingarten, M., Abers, G. A., Bekins, B. A., & Ge, S. (2014). Sharp increase in central Oklahoma seismicity since 2008 induced by massive wastewater injection. *Science*, *345*(6195), 448–451. https://doi.org/10.1126/science.1255802

Larroque, C., Béthoux, N., Calais, E., Courboulex, F., Deschamps, A., Déverchère, J., et al. (2001). Active and recent deformation at the Southern Alps-Ligurian basin junction. *Geologie en Mijnbouw*, *80*(3/4), 255–272.

Larroque, C., Delouis, B., Godel, B., & Nocquet, J. M. (2009). Active deformation at the southwestern Alps–Ligurian basin junction (France-Italy boundary): Evidence for recent change from compression to extension in the Argentera massif. *Tectonophysics*, *467*(1–4), 22–34. https://doi.org/10.1016/j.tecto.2008.12.013

Leclère, H., Fabbri, O., Daniel, G., & Cappa, F. (2012). Reactivation of a strike-slip fault by fluid overpressuring in the southwestern French-Italian Alps. *Geophysical Journal International*, *189*(1), 29–37.

Leclère, H., Daniel, G., Fabbri, O., Cappa, F., & Thouvenot, F. (2013). Tracking fluid pressure buildup from focal mechanisms during the 2003–2004 Ubaye seismic swarm, France. *Journal of Geophysical Research: Solid Earth*, *118*, 4461–4476. https://doi.org/10.1002/jgrb.50297

Lohman, R. B., & McGuire, J. J. (2007). Earthquake swarms driven by aseismic creep in the Salton Trough, California. *Journal of Geophysical Research*, *112*, B04405. https://doi.org/10.1029/2006JB004596

Michelini, A., & Bolt, B. A. (1986). Application of the principal parameters method to the 1983 Coalinga, California, aftershock sequence. *Bulletin of the Seismological Society of America*, *76*(2), 409–420.

Miller, S. A., Collettini, C., Chiaraluce, L., Cocco, M., Barchi, M., & Kaus, B. J. (2004). Aftershocks driven by a high-pressure CO_2 source at depth. *Nature*, *427*(6976), 724–727. https://doi.org/10.1038/nature02251

Nicolas, M., Santoire, J.-P., & Delpech, P.-Y. (1990). Intraplate seismicity: New seismotectonic data in Western Europe. *Tectonophysics*, *179*, 27–53. https://doi.org/10.1016/0040-1951(90)90354-B

Nocquet, J. M., Sue, C., Walpersdorf, A., Tran, T., Lenôtre, N., Vernant, P., et al. (2016). Present-day uplift of the western Alps. *Scientific Reports*, *6*, 28404. https://doi.org/10.1038/srep28404

Ogata, Y. (1999). Seismicity analysis through point-process modeling: A review. In M. Wyss, K. Shimazaki, & A. Ito (Eds.), *Seismicity patterns, their statistical significance and physical meaning* (Vol 155, pp. 471–507). Basel: Pageoph Topical Volumes. Birkhäuser. https://doi.org/10.1007/978-3-0348-8677-2_14

Ogata, Y., & Katsura, K. (1993). Analysis of temporal and spatial heterogeneity of magnitude frequency distribution inferred from earthquake catalogues. *Geophysical Journal International*, *113*(3), 727–738. https://doi.org/10.1111/j.1365-246X.1993.tb04663.x

Pauchet, H., Rigo, A., Rivera, L., & Souriau, A. (1999). A detailed analysis of the February 1996 aftershock sequence in the eastern Pyrenees, France. *Geophysical Journal International*, *137*(1), 107–127. https://doi.org/10.1046/j.1365-246x.1999.00776.x

Perfettini, H., & Avouac, J. P. (2004). Postseismic relaxation driven by brittle creep: A possible mechanism to reconcile geodetic measurements and the decay rate of aftershocks, application to the Chi-Chi earthquake, Taiwan. *Journal of Geophysical Research*, *109*, B02304. https://doi.org/10.1029/2003JB002488

Perrin, C., Manighetti, I., & Gaudemer, Y. (2016). Off-fault tip splay networks: A genetic and generic property of faults indicative of their long-term propagation. *Comptes Rendus Geoscience*, *348*(1), 52–60. https://doi.org/10.1016/j.crte.2015.05.002

RESIF (1995). RESIF-RLBP French Broad-band network, RESIF-RAP strong motion network and other seismic stations in metropolitan France. RESIF - Réseau Sismologique et géodésique Français. Seismic Network. doi:10.15778/RESIF.FR

Roland, E., & McGuire, J. J. (2009). Earthquake swarms on transform faults. *Geophysical Journal International*, *178*(3), 1677–1690. https://doi.org/10.1111/j.1365-246X.2009.04214.x

Ross, Z. E., Hauksson, E., & Ben-Zion, Y. (2017). Abundant off-fault seismicity and orthogonal structures in the San Jacinto fault zone. *Science Advances*, *3*(3), e1601946. https://doi.org/10.1126/sciadv.1601946

Ross, Z. E., Rollins, C., Cochran, E. S., Hauksson, E., Avouac, J. P., & Ben-Zion, Y. (2017). Aftershocks driven by afterslip and fluid pressure sweeping through a fault-fracture mesh. *Geophysical Research Letters*, *44*, 8260–8267. https://doi.org/10.1002/2017GL074634

Rubin, A. M., & Ampuero, J. P. (2007). Aftershock asymmetry on a bimaterial interface. *Journal of Geophysical Research*, *112*, B05307. https://doi.org/10.1029/2006JB004337

Ruhl, C. J., Abercrombie, R. E., Smith, K. D., & Zaliapin, I. (2016). Complex spatiotemporal evolution of the 2008 Mw 4.9 Mogul earthquake swarm (Reno, Nevada): Interplay of fluid and faulting. *Journal of Geophysical Research: Solid Earth*, *121*, 8196–8216. https://doi.org/10.1002/2016JB013399

Sanchez, G., Rolland, Y., Corsini, M., Braucher, R., Bourlès, D., Arnold, M., & Aumaître, G. (2010). Relationships between tectonics, slope instability and climate change: Cosmic ray exposure dating of active faults, landslides and glacial surfaces in the SW Alps. *Geomorphology*, *117*, 1–13. https://doi.org/10.1016/j.geomorph.2009.10.019

Sellami, S., Kissling, E., Thouvenot, F., & Fréchet, J. (1995). Initial reference velocity model for seismic tomography in the western Alps, 20th Gen. Ass. Europ. Geophys. Soc., Hamburg.

Shapiro, S. A., Huenges, E., & Borm, G. (1997). Estimating the crust permeability from fluid-injection-induced seismic emission at the KTB site. *Geophysical Journal International*, *131*(2), F15–F18. https://doi.org/10.1111/j.1365-246X.1997.tb01215.x

Sibson, R. H. (1990). Conditions for fault-valve behaviour. *Geological Society, London, Special Publications*, *54*(1), 15–28.

Sira, C., Schlupp, A., Schaming, M., Chesnais, C., Cornou, C., Dechamp, A., et al. (2014). Séisme de Barcelonnette du 7 avril 2014, Rapport du BCSF, BCSF2014-R1, 76p.

Stein, R. S. (1999). The role of stress transfer in earthquake occurrence. *Nature*, *402*(6762), 605–609. https://doi.org/10.1038/45144

Sue, C., & Tricart, P. (2003). Neogene to ongoing normal faulting in the inner Western Alps: A major evolution of the late alpine tectonics. *Tectonics*, *22*(5), 1050. https://doi.org/10.1029/2002TC001426

Thouvenot, F., Jenatton, L., Scafidi, D., Turino, C., Potin, B., & Ferretti, G. (2016). Encore Ubaye: Earthquake swarms, foreshocks, and aftershocks in the southern French Alps. *Bulletin of the Seismological Society of America*, *106*(5), 2244–2257. https://doi.org/10.1785/0120150249

Utsu, T. (1961). A statistical study on the occurrence of aftershocks. *Geophysical Magazine*, *30*, 521–605.

Vallée, M., Nocquet, J. M., Battaglia, J., Font, Y., Segovia, M., Regnier, M., et al. (2013). Intense interface seismicity triggered by a shallow slow slip event in the Central Ecuador subduction zone. *Journal of Geophysical Research: Solid Earth*, *118*, 2965–2981. https://doi.org/10.1002/jgrb.50216

Vernant, P., Hivert, F., Chery, J., Steer, P., Cattin, R., & Rigo, A. (2013). Erosion-induced isostatic rebound triggers extension in low convergent mountain ranges. *Geology*, *41*(4), 467–470. https://doi.org/10.1130/G33942.1

Vidale, J. E., & Shearer, P. M. (2006). A survey of 71 earthquake bursts across southern California: Exploring the role of pore fluid pressure fluctuations and aseismic slip as drivers. *Journal of Geophysical Research*, *111*, B05312. https://doi.org/10.1029/2005JB004034

Waldhauser, F., & Ellsworth, W. L. (2000). A double-difference earthquake location algorithm: Method and application to the northern Hayward fault, California. *Bulletin of the Seismological Society of America*, *90*(6), 1353–1368. https://doi.org/10.1785/0120000006

Waldhauser, F., Ellsworth, W. L., Schaff, D. P., & Cole, A. (2004). Streaks, multiplets, and holes: High-resolution spatio-temporal behavior of Parkfield seismicity. *Geophysical Research Letters*, *31*, L18608. https://doi.org/10.1029/2004GL020649

Walpersdorf, A., Pinget, L., Vernant, P., Sue, C., Deprez, A., & RENAG team (2018). Does long-term GPS in the Western Alps finally confirm earthquake mechanisms? *Tectonics*, *37*(10), 3721–3737. https://doi.org/10.1029/2018TC005054

Zaliapin, I., & Ben-Zion, Y. (2011). Asymmetric distribution of aftershocks on large faults in California. *Geophysical Journal International*, *185*(3), 1288–1304. https://doi.org/10.1111/j.1365-246X.2011.04995.x

Zhao, L., Paul, A., Guillot, S., Solarino, S., Malusà, M. G., & Zheng, T. (2015). First seismic evidence for continental subduction beneath the western Alps. *Geology*, *43*(9), 815–818. https://doi.org/10.1130/G36833.1

2.4.2. Sismicité pré-éruptive

La sismicité pré-éruptive sur les volcans est associée à la remontée de magma, et aux perturbations des contraintes et de pression fluide qu'elle génère. De manière surprenante, cette sismicité s'organise schématiquement de la même manière, quel que soit le type de volcan (McNutt, 2005). La crise pré-éruptive commence en effet par un essaim volcano-tectonique qui migre vers la surface, suivi d'une phase de quiescence dans laquelle sont enregistrés signaux à basses fréquences et trémors, avant le début de l'éruption (*Figure 16*). Une telle crise peut durer de quelques heures à quelques années selon la viscosité de la lave. La présence sur tous les volcans de cette même séquence suggère une universalité des processus en jeu.

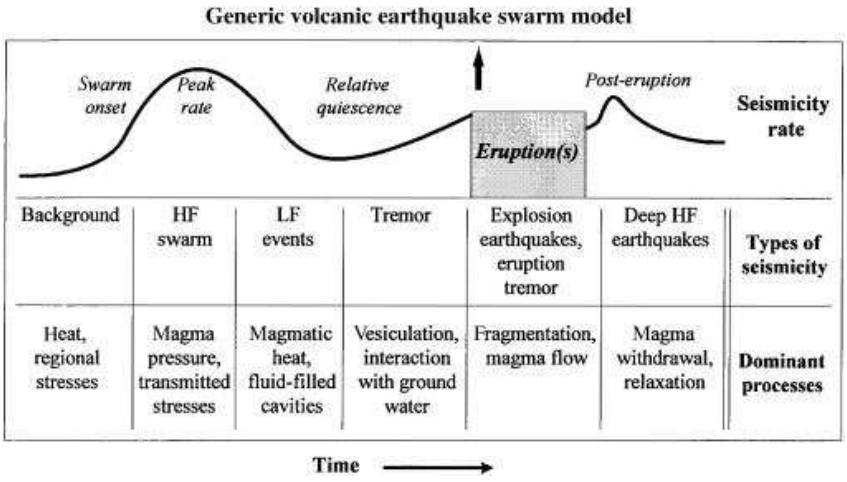

***Figure 16**: Taux et type de sismicité volcanique précédant et accompagnant les éruptions volcaniques, ainsi que les processus associés (McNutt, 2015) . Une telle crise sismique peut durer de quelques heures (Piton de la Fournaise) à plusieurs années sur des volcans à lave très visqueuse.*

Sur le Piton de la Fournaise, cette même séquence sismique est observée. Après un essaim dense de sismicité qui migre du niveau de la mer vers la surface, seuls quelques signaux Longues Périodes sont observés pendant une phase de quiescence (**Zecevic et al., 2013**). En utilisant le réseau dense de stations déployées pour le projet ANR UNDERVOLC (Brenguier et al., 2012), nous avons observé l'occurrence d'essaim de sismicité de très faible amplitude pendant la période de quiescence lors de plusieurs éruptions en 2010-2011 (**De Barros et al., 2013a**). Cette sismicité est de trop faible amplitude pour être détectée par un réseau lâche, mais est localisée au niveau de la future sortie de lave quelques heures après. Par conséquent, elle peut être utilisée pour l'anticipation du lieu de l'éruption. De plus, le décalage temporel entre la sismicité et l'arrivée de la lave en surface montre que la sismicité a lieu loin devant le front de magma dans l'édifice volcanique.

Ces observations, et le nouveau modèle que nous proposons pour les signaux Longues Périodes, permettent de discuter les processus de la séquence sismique pré-éruptive. L'universalité de cette séquence (*Figure 16*) suggère que ces processus doivent être reliés au contexte général des volcans. En profondeur, le milieu est sismogène. Les perturbations de contraintes associées à la migration du magma génèrent donc de nombreux glissements sismiques. Le cône volcanique est lui très hétérogène, avec des contraintes de confinement faible. Les déformations de l'édifice sont donc accommodées par des glissements avec des vitesses faibles (LP, **Bean et al., 2014**). Localement, il peut y avoir des zones plus compactes, permettant une sismicité peu nombreuse et de faible amplitude. Ces deux comportements sismiques (nombreux séismes en profondeur, sismicité rare et longues Périodes dans le cône volcanique) viennent donc tous deux de la perturbation de contraintes dus à la remontée du magma, mais s'exprime différemment à cause du contexte (états de contraintes, raideur et homogénéité des matériaux).

Article sélectionné

L'article suivant présente les observations d'une sismicité de faible amplitude dans la phase de quiescence pré-éruptive, qui 1) démontre que le chemin emprunté par le magma est créé bien en amont du magma par transfert de contraintes, et 2) ouvre la possibilité d'anticiper la localisation des sorties de lave.

De Barros L., Bean C. J., Zecevic+ M., Brenguier F., Peltier A. 2013. Eruptive fracture location forecasts from high-frequency events on Piton de la Fournaise Volcano, Geophysical Research Letters, vol.40, pp.1-5.

Eruptive fracture location forecasts from high-frequency events on Piton de la Fournaise Volcano

Louis De Barros,[1,2] Christopher J. Bean,[1] Megan Zecevic,[1] Florent Brenguier,[3] and Aline Peltier[4]

Received 27 June 2013; revised 20 August 2013; accepted 20 August 2013.

[1] Piton de la Fournaise (La Réunion island) is a very active basaltic volcano, with five eruptions between Nov 2009 and Dec 2010. Pre-eruptive seismic crises usually last for a few hours and mainly consist of a volcano-tectonic swarm. During the quiescent period between the volcano-tectonic swarm and the eruptive tremor, we identify another swarm of events with a very high frequency content. These events are shallow and are located close to the future eruption site. They seem associated with the opening of the path for the magma propagating laterally at shallow depth. As these events start to occur while the magma is still in a vertical propagation phase, this seismicity seems to be related with the generic response of the volcano to the stress perturbation and not directly induced by the magma pressure. This new observation brings new insights to short-term forecasting of the eruption location. **Citation:** De Barros, L., C. J. Bean, M. Zecevic, F. Brenguier, and A. Peltier (2013), Eruptive fracture location forecasts from high-frequency events on Piton de la Fournaise Volcano, *Geophys. Res. Lett.*, *40*, doi:10.1002/grl.50890.

1. Introduction

[2] Piton de la Fournaise (PdF) volcano is a hot-spot shield volcano located on La Réunion island in the Indian Ocean. This very active volcano erupted more than 30 times between 2000 and 2010 [*Roult et al.*, 2012]. The eruptions are usually of short duration, lasting from a few hours to a few months and emit basaltic lava. Eruptions are either summital in the Dolomieu crater, proximal (on the flank of the central cone) or distal at more than 4 km from the summit [*Peltier et al.*, 2009]. Since the end of 2009, the volcano is monitored by 21 broadband seismic stations (UNDERVOLC project; *Brenguier et al.* [2012]), which have recorded five eruptions (5 Nov 2009, 14 Dec 2009, 2 Jan 2010, 14 Oct 2010, and 9 Dec 2010).

[3] The pre-eruptive seismicity on Piton de la Fournaise is characterized by a dense swarm of volcano-tectonic (VT) events [*Battaglia et al*., 2005; *Massin et al*., 2011; *Brenguier et al*., 2012]. These events are mainly located around sea level, i.e., at about 2500 m below the summit. Several long-period events sometimes occur toward the end of the seismic crisis, but only for proximal and distal eruptions [*Aki and Ferrazzini*, 2000; *Zecevic et al.*, 2013]. These VT crises are followed by a period of pre-eruption quiescence, with a duration of several minutes or hours, which in turn are followed by the eruptive tremor accompanying the flow of lava. This simple and repetitive sequence of events exactly follows the general pre-eruptive pattern of seismicity described by *McNutt* [2005].

[4] The high resolution network of seismic stations, the frequent recurrence and the short time duration of eruptions, and the simplicity of the pre-eruptive patterns make this volcano an exceptional laboratory for developing new forecasting observations [e.g., *Schmid et al.*, 2012]. We mainly focus here on the seismicity occurring before the proximal eruption on 14 Oct 2010. Interestingly, after the main seismic swarm of VT events, we identify a second swarm of events with a higher frequency content during the quiescence time at the stations, the closest to the eruptive vents. This paper aims to investigate the origin of these events and their potential for short-term forecasting of the location of lava extrusion.

2. The 14 October 2010 Eruption

[5] Since the end of 2009, the volcano has been monitored by 21 broadband seismic stations, including six 60 s Guralp CMG-3ESPC sensors and fifteen 30 s Guralp CMG-40T sensors (UNDERVOLC project; *Brenguier et al.* [2012]). All data used in this paper have been corrected for instrument response. The station distribution is exceptionally good with stations on the ridge of the main crater and an average distance of 1 to 2 km between stations.

[6] Figure 1 shows the seismic crisis recorded by two stations (U05 near the summit and FOR in the South, see Figure 2c). The main swarm of VT events started at 10:00 and lasted for less than 2 h, after which a quiescence period of 3 h commenced. At 15:20, lava started to flow from a 150 m long fissure which opened South of the Dolomieu crater in the "Enclos Fouqué" (see Figure 2c and *Roult et al.* [2012]). The activity decreased after 17 Oct, and stopped on 31 Oct. This eruption is the first proximal eruption since the major eruption and crater collapse of 2007.

[7] For both stations, the seismic energy is very strong during the main VT swarm and the eruptive tremor episode. This energy is mainly present in a low-frequency range

Additional supporting information may be found in the online version of this article.

[1]School of Geological Sciences, University College Dublin, Dublin, Ireland.
[2]Géoazur, Université Nice Sophia Antipolis, CNRS, Observatoire de la Côte d'Azur, Sophia Antipolis, France.
[3]ISTerre, Université J. Fourier, CNRS, OSUG, Grenoble, France.
[4]Institut de Physique du Globe de Paris-Sorbonne Paris Cité, Université Paris Diderot, CNRS, Paris, France.

Corresponding author: L. De Barros, Géoazur, Université Nice Sophia Antipolis, CNRS, Observatoire de la Côte d'Azur, 250 rue Albert Einstein, Sophia Antipolis 06560, Valbonne, France. (debarros@geoazur.unice.fr)

0094-8276/13/10.1002/grl.50890

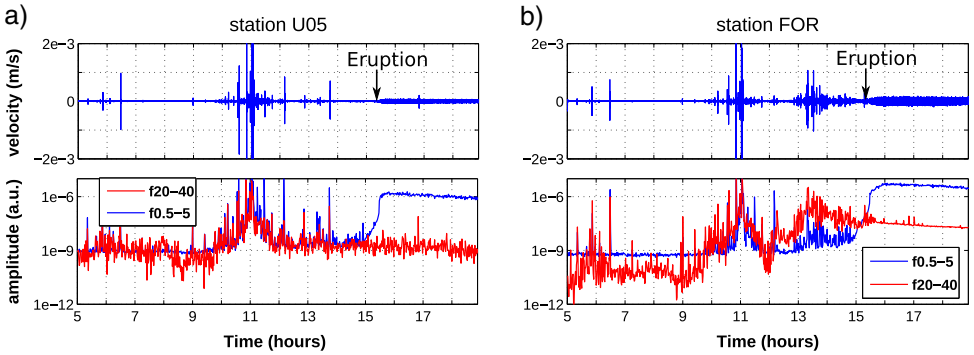

Figure 1. Vertical component of the pre-eruptive and initial eruption seismicity recorded on 14 Oct 2010 by stations (a) U05 and (b) FOR. The bottom panels show the seismic energy in two frequency bands (0.5–5 Hz and 20–40 Hz) for both stations. The vertical arrows show the beginning of the eruption.

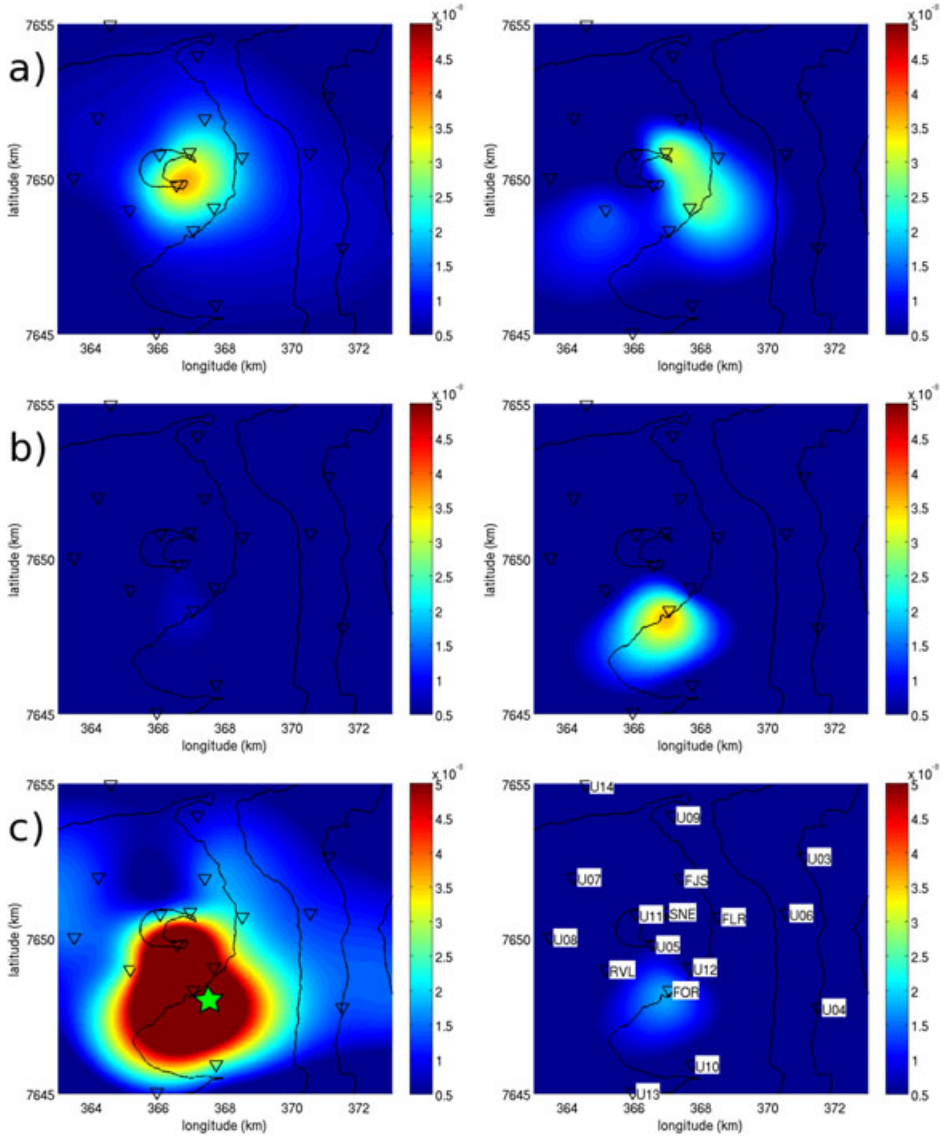

Figure 2. Five minutes root mean square amplitude interpolated between stations on the surface of the volcano in a (left) low-frequency band (0.5–5 Hz) and (right) high-frequency band (20–40 Hz) at three different periods: (a) Main seismic swarm (10:55), (b) high-frequency event swarm (13:49), and (c) beginning of the eruptive tremor (15:36). Elevation between contour lines is 500 m. Triangles show the stations and the star indicate the eruptive vent location. Color scale (root mean square amplitude) is common for all the panels. See also Animation S2 in the supporting information.

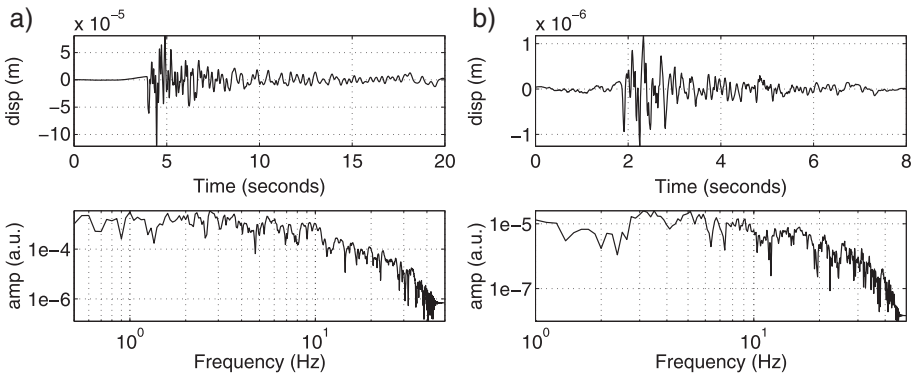

Figure 3. Seismic waveforms and spectra of (a) a VT event recorded during the main seismic crisis (11:02) and (b) a High-Frequency event (14:32). Both events are recorded at FOR station.

(i.e., less than 10 Hz). While the quiescence period is almost free of visible events in the U05 data, a swarm of events can be seen at FOR station between 13:00 and 15:00. This swarm of events has a higher frequency content than the VT swarm. The energy of the signal filtered between 20 and 40 Hz clearly shows these events (see Figure 1). Herein we refer to the events forming this swarm as High-Frequency (HF) events.

3. High-Frequency Events

[8] Figure 3 shows a close-up of two events, one VT event recorded during the main seismic crisis and one HF event. They differ in their amplitudes (2 orders of magnitude) and their frequency content. The spectra of the VT and HF events show a classical earthquake pattern, with a corner frequency of 6 Hz and 14 Hz, respectively. The HF events also seem to be volcano-tectonic (i.e., with a shear, brittle mechanism), but occur on smaller faults or smaller patches of faults.

[9] When looking at the waveforms recorded by different stations, the HF events can be seen at only four stations. Due to their low amplitude, the lowest frequencies of the signals are masked by noise at all stations. The high-frequency content, which is clearly visible in FOR data, is strongly scattered and attenuated, and subsequently cannot propagate very far from the source. It is therefore not possible to perform a quantitative location for these sources. In order to estimate the location qualitatively and to link the HF event with the other seismic signals, we interpolate the RMS amplitude onto the surface of PdF volcano [*Battaglia and Aki*, 2003]. This is achieved using a cubic interpolation of the cumulative RMS amplitude measured in 5 min windows filtered in a low-frequency band (0.5–5 Hz) and in a high-frequency band (20–40 Hz). Three snapshots are shown in Figure 2, corresponding to (1) the main VT swarm, (2) the HF swarm, and (3) the eruptive tremor periods. The Animation S2 (supporting information) shows the continuous distribution of the RMS amplitude in both frequency bands along the entire pre-eruptive sequence. The VT crisis is associated with high energy at both frequency bands, located at depth below the summit. High-frequency energy starts to appear south of the Dolomieu crater, and becomes progressively more visible during the quiescence period, which is dominated by the HF swarm. The eruptive tremor mainly contains low frequencies and also occurs in the south of the volcano around the eruptive vent. Unlike the VT seismicity, the HF events yield information on the future eruptive fracture location (see Figure 2) as their energy strongly decays with the offset from this area, where their epicenter seems to be located. Moreover, a deep source (i.e., at a depth greater than the interstation distance) would produce similar amplitudes on different stations. Hence, the sources of these events have to be shallow. This is supported by the b-value in the Gutenberg-Richter law: a value of 0.9 and 1.55 is obtained for the VT swarm and HF swarm, respectively. This high value is a distinctive feature of events occurring in a low-stress environment [*Schorlemmer et al.*, 2005], such as in the shallow subsurface of the volcano.

4. Pre-eruptive Behavior

[10] The HF swarm mainly differs from the VT swarm through its higher frequency content. Therefore, the ratio between the high-frequency and the low-frequency contents can be used to indicate the presence of HF events. Figure 4b shows the cumulative ratio for all stations, computed on 5 min-long windows. As expected, this ratio is the highest in the stations for which high-frequency events can be seen and which surround the eruptive fracture. For those stations, this ratio starts to increase significantly at 10:00, i.e., during the main VT crisis and more than 5 h before the eruption onset. For the other eruptions in 2010 and 2011, the highest ratio is always observed at the stations that are the closest to the area where the eruption will occur a few hours later (see supporting Figure S1). This method can therefore be employed to forecast the location of the impending eruption.

[11] The average depth of the seismicity is derived using the seismic intensity ratio method described by *Taisne et al.* [2011]. In order to use waves propagating throughout the network and to consider the different types of events, we focus on the 5–15 Hz frequency band. We assume a *S* wave velocity of 2 km/s (consistent with *Brenguier et al.* [2007]). The seismicity first has deep and scattered source locations (around sea level), and then migrates toward the surface between 11:00 and 12:00, i.e., at the end of the VT crisis (Figure 4c). As usually observed on PdF [*Peltier et al.*, 2009], the GPS data indicate a two-phase deformation, and GPS stations close to UV5 and FOR (Figure 2c) show different deformation patterns (Figure 4d). The dike first propagates vertically, leading to high deformation of the

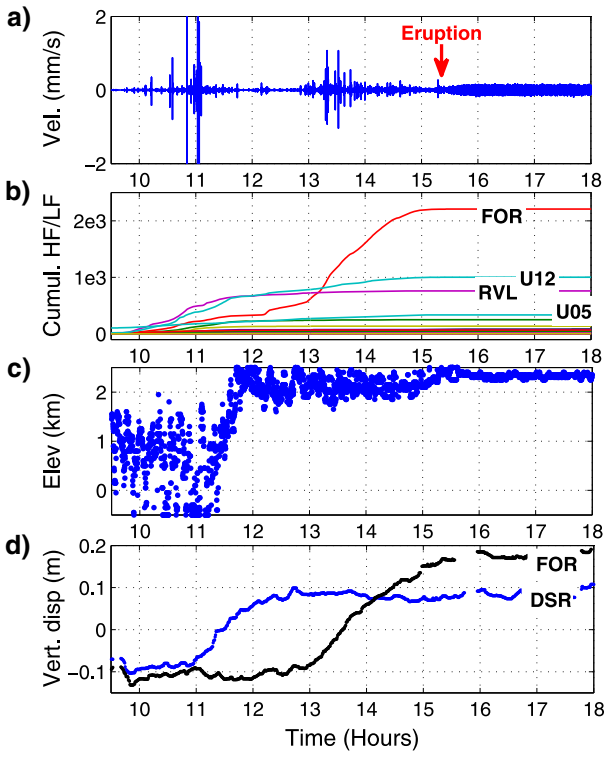

Figure 4. (a) Seismic activity before and during the beginning of the eruption on 14 Oct 2010 recorded by the FOR station. (b) Cumulative High Frequency (20–40Hz)/Low Frequency (0.5–5 Hz) ratio for all stations. The four highest ratios are labeled with the corresponding station names. (c) Elevation of the seismicity sources using radiated seismic intensity. (d) Vertical deformation recorded by the GPS station DSR (close to U05) and FOR.

volcano summit between 10:55 and 12:00. From 11:30, the magma starts its lateral propagation toward the south, the deformation is localized only in the south of the volcano after 13:00.

[12] The different observations summarized in Figure 4 show the following: (1) The VT swarm occurred at the beginning of the vertical propagation of the magma. The vertical migration of the seismicity is associated with deformation localized on the summit; (2) During the lateral propagation of the dike, deformation and seismicity (HF events) are only recorded in the south of the volcano; (3) The HF/LF ratio starts to increase in the south of the volcano toward the end of the VT swarm, i.e., when the dike is still in its vertical migration phase.

5. Discussion and Conclusion

[13] During the quiescence period occurring between the main seismic crisis and the eruption, we observe a second swarm of high-frequency events at some stations. This observation is rendered possible thanks to the highly dense seismic network deployed on the volcano. These events seem to be generated at very shallow depths compared to the classical VT events, which usually occur at depths greater than 1 km [*Battaglia et al.*, 2005; *Massin et al.*, 2011]. Using energy mapping, we determine that the HF events are located in the area of the eruptive fracture. As they have a high-frequency content, which is lacking in the VT events, high-to-low-frequency ratios allow us to track their evolution. Their high-frequency contents indicate failure on small faults (or small patches), with a diameter no greater than 60 m [*Madariaga*, 1976]. This is consistent with a shallow seismicity, as the near-surface cannot support large faults because of the topography and/or weak material properties. Therefore, the VT and HF in this study share a similar mechanism and belong to the same group of events.

[14] These HF events may have significant implications for monitoring purposes: monitoring the high-to-low-frequency energy ratio during the main seismic crisis (i.e., a few hours before the eruption onset) allows for a forecast of the eruption location. This is confirmed here by computing this ratio for another proximal eruption (Dec 2010) and for summit eruptions (Nov 2009 and Jan 2010, see supporting information Figure S1). In every case, the largest frequency ratio before the eruption onset is obtained at the stations closest to the upcoming eruptions. This information can be coupled with the occurrence of Long-Period events, which is an indication of an eruption outside of the summit area on PdF [*Aki and Ferrazzini*, 2000; *Zecevic et al.*, 2013].

[15] The VT and HF swarms are related to the vertical and lateral migration of the magma, respectively. However, the HF seismicity seems to start to occur during the VT swarm, i.e., when the magma is still in its vertically migrating phase at depth (c. 2 km below sea level) beneath the summit. The HF seismicity is therefore likely a generic response of the shallow part of the edifice to the stress changes due to the dike propagation [*Traversa et al.*, 2010]. These failures are triggered indirectly by the stress induced by the magma movement, and not by the magma itself. As these shallow failures occur in the area of the eruption, they play a role in the process of dike propagation by creating the pathway along which the magma later propagates. The eruptive fissure might be exploiting a structural weakness which can be monitored through HF events. The shallow magma path and the eruption area are therefore already defined when the magma is still in its vertically migrating phase. Hence, the location of lava output can be forecast up to 3 h prior to the eruption.

[16] On Piton de la Fournaise, the pre-eruptive seismicity has a short time duration and is rather simple compared to other volcanoes. However, it follows the generic swarm pattern of *McNutt* [2005]. The observations made herein might therefore be reproduced on other volcanoes where the station distribution is sufficiently dense.

[17] **Acknowledgments.** The data used for the analysis were collected by the Institut de Physique du Globe de Paris, Observatoire Volcanologique du Piton de la Fournaise (IPGP/OVPF), and the Institut des Sciences de la Terre (ISTerre) within the framework of ANR_08_RISK_011/UnderVolc project. The sensors are property of the French transportable seismic network, Sismob (INSU-CNRS). We are grateful to V. Ferrazzini, T. Staudacher, and A. Di Muro for instructive discussions.

[18] The editor thanks an anonymous reviewer for his assistance in evaluating this paper.

References

Aki, K., and V. Ferrazzini (2000), Seismic monitoring and modeling of an active volcano for prediction, *J. Geophys. Res.*, *105*(B7), 16,617–16,640.

Battaglia, J., and K. Aki (2003), Location of seismic events and eruptive fissures on the Piton de la Fournaise volcano using seismic amplitudes, *J. Geophys. Res.*, *108*(B8), 2364, doi:10.1029/2002JB002193.

Battaglia, J., V. Ferrazzini, T. Staudacher, K. Aki, and J.-L. Cheminée (2005), Pre-eruptive migration of earthquakes at the Piton de la Fournaise volcano (Réunion island), *Geophys. J. Int.*, *161*(2), 549–558.

Brenguier, F., N. M. Shapiro, M. Campillo, A. Nercessian, and V. Ferrazzini (2007), 3-D surface wave tomography of the Piton de la Fournaise volcano using seismic noise correlations, *Geophys. Res. Lett.*, *34*, L02305, doi:10.1029/2006GL028586.

Brenguier, F., et al. (2012), First results from the UnderVolc high resolution seismic and GPS network deployed on Piton de la Fournaise volcano, *Seismol. Res. Lett.*, *83*(1), 97–102.

Madariaga, R. (1976), Dynamics of an expanding circular fault, *Bull. Seismol. Soc. Am.*, *66*(3), 639–666.

Massin, F., V. Ferrazzini, P. Bachlery, A. Nercessian, Z. Duputel, and T. Staudacher (2011), Structures and evolution of the plumbing system of Piton de la Fournaise volcano inferred from clustering of 2007 eruptive cycle seismicity, *J. Volcanol. Geotherm. Res.*, *202*(1-2), 96–106.

McNutt, S. R. (2005), Volcanic seismology, *Annu. Rev. Earth Planet. Sci.*, *33*(1), 461–491.

Peltier, A., P. Bachlery, and T. Staudacher (2009), Magma transport and storage at Piton de La Fournaise (la Réunion) between 1972 and 2007: A review of geophysical and geochemical data, *J. Volcanol. Geotherm. Res.*, *184*(1-2), 93–108.

Roult, G., A. Peltier, B. Taisne, T. Staudacher, V. Ferrazzini, and A. Di Muro (2012), A new comprehensive classification of the Piton de la Fournaise activity spanning the 1985–2010 period. Search and analysis of short-term precursors from a broad-band seismological station, *J. Volcanol. Geotherm. Res.*, *241-242*, 78–104.

Schmid, A., J. R. Grasso, D. Clarke, V. Ferrazzini, P. Bachlery, and T. Staudacher (2012), Eruption forerunners from multiparameter monitoring and application for eruptions time predictability (Piton de la Fournaise), *J. Geophys. Res.*, *117*, B11203, doi:10.1029/2012JB009167.

Schorlemmer, D., S. Wiemer, and M. Wyss (2005), Variations in earthquake-size distribution across different stress regimes, *Nature*, *437*(7058), 539–542.

Taisne, B., F. Brenguier, N. M. Shapiro, and V. Ferrazzini (2011), Imaging the dynamics of magma propagation using radiated seismic intensity, *Geophys. Res. Lett.*, *38*, L04304, doi:10.1029/2010GL046068.

Traversa, P., V. Pinel, and J. R. Grasso (2010), A constant influx model for dike propagation: Implications for magma reservoir dynamics, *J. Geophys. Res.*, *115*, B01201, doi:10.1029/2009JB006559.

Zecevic, M., L. De Barros, C. J. Bean, G. O'Brien, and F. Brenguier (2013), Investigating the source characteristics of long-period (LP) seismic events recorded on Piton de la Fournaise volcano, La Réunion, *J. Volcanol. Geotherm. Res.*, *258*, 1–11.

2.4.3. Fluide et migration de la sismicité

La migration de la sismicité est un des arguments majeurs utilisés pour impliquer des fluides dans les processus de genèse sismique. Cependant, la sismicité suit le font de pression fluide (Shapiro et al., 1997b) dans les réservoirs ou zone tectonique, alors que la sismicité volcanique est devant le fluide. Cette dichotomie peut suggérer deux processus distincts, mais surtout une interprétation à affiner.

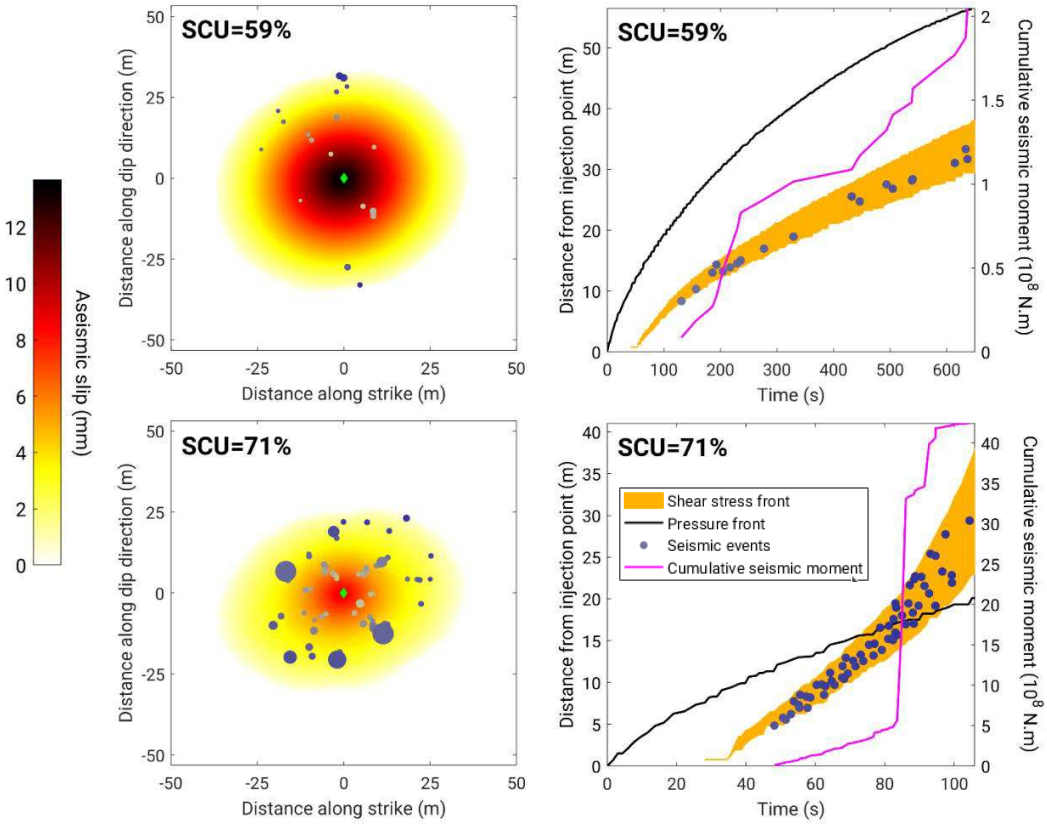

***Figure 17**: Réponse d'une faille soumise à une injection de fluide dans deux états de contraintes différents. La criticalité (SCU) c'est-à-dire la proximité de la faille à la rupture, est faible en haut, forte en bas. La colonne de gauche montre la distribution du glissement asismique et de la sismicité, à la fin des tests numériques. Plus la criticalité est forte, plus le ratio de déformation sismique/asismique augmente. La colonne de droite représente la migration du front de pression, du front de contrainte cisaillante (qui est aussi le front de rupture), la distribution des évènements sismiques, ainsi que les moments sismiques relâchés. Pour des criticalités faibles, les fronts de sismicité et de rupture sont derrière le front de pression, mais vont doubler celui-ci pour des criticalités fortes (figure modifiée de **Wynants-Morel et al., submitted**).*

Le modèle classiquement utilisé dans les réservoirs suggère que la sismicité est induite par augmentation de la pression interstitielle uniquement. Par conséquent, la sismicité est derrière le front de pression. Cependant, les expériences in-situ n'ont pas montré ce type de comportement (**De Barros et al., 2018**; **Duboeuf et al., 2017**). Sur certains tests, la sismicité semble diffusive, tandis qu'elle apparait quasi-simultanément à de grandes distances de l'injection sur d'autres tests, ce qui suggère un rôle important des transferts de contraintes. Nous avons donc émis l'idée que la sismicité était déclenchée en réponse aux déformations asismiques, et pas directement par la pression fluide (**De Barros et al., 2018**). Dans ce cas, le front de sismicité suit donc le front de perturbation de contraintes.

Pour confirmer ces hypothèses, nous avons utilisé des modélisations numériques. En collaboration avec F. Cappa, la thèse de N. Wynants consiste en l'implémentation de lois de frictions complexes et de pas de temps adaptatifs pour permettre des ruptures sismiques dans un code de modélisation hydro-mécanique (éléments distincts, 3DEC, Itasca). Des tests d'injection dans une faille perméable montrent que la déformation induite est principalement asismique. La réponse de la faille dépend de sa criticalité, c'est-à-dire de sa proximité à la rupture en termes de contraintes (**Wynants-Morel et al., submitted**). Dans tous les cas, la sismicité est déclenchée au front de rupture, par les transferts de contraintes de la déformation asismique, et ne suit donc pas le front de pression. Pour de faibles criticalités, la rupture asismique et la sismicité restent confinées dans la zone pressurisée. Au contraire, pour des criticalités plus fortes, le front de rupture accélère pour se propager au-delà de la zone pressurisée (*Figure 17*). Le comportement spatio-temporel de la sismicité ne suit donc plus une loi de diffusion (Shapiro et al., 1997a), mais montre une accélération. La rupture, et la sismicité qu'elle produit, ne sont donc pas directement induites par les fluides, mais par la réorganisation des contraintes au front du glissement asismique. Le front de sismicité n'apporte donc pas d'information sur les propriétés de diffusion hydraulique, mais sur la distribution du glissement asismique et sur la diffusion des contraintes.

Une même conclusion peut être atteinte à partir de la sismicité volcanique. Sur l'étude de la sismicité pré-éruptive du Piton de la Fournaise, la sismicité précède spatialement la migration du magma en profondeur (**De Barros et al., 2013a**). La sismicité est donc générée devant le front fluide, et est induite par les perturbations de contraintes devant celui-ci. Et le magma ne créé pas directement son trajet : le chemin qu'il emprunte par est donc créé par les perturbations de contraintes et les ruptures associées, en amont du front magmatique.

2.5. Bilan

En résumé, mes principaux résultats scientifiques concernent :

- **des développements méthodologiques**. J'ai en particulier travaillé sur l'inversion des formes d'ondes complètes en milieu poreux, sur les techniques de relocalisation et de calcul de mécanismes de la sismicité volcaniques, etc.
- **l'importance des déformations asismiques, et des transferts de contraintes associées, dans les réponses des failles aux injections de fluides**. Les injections de fluide semblent en effet générer une déformation majoritairement asismique. La sismicité, déclenchée par les transferts de contraintes n'est donc qu'une réponse indirecte aux fluides. Ces résultats ont des conséquences fortes, la sismicité n'étant pas un marqueur des fluides, mais de la déformation induite dans un contexte de contraintes et de structures géologiques.
- **une remise en question des processus de la sismicité non conventionnelle**. En particulier, nous avons montré que les signatures Longues Périodes sur les volcans n'étaient pas attribuées à des résonnances de fractures, mais à des déformations lentes. Cette sismicité est donc plus un marqueur de déformation que de perturbations de pression.
- **l'identification de nouveaux observables** pour suivre les processus d'interaction entre fluide et solide.

3. PROSPECTIVES : NOUVELLES IDEES ET PROJETS

Echelles et objets géologiques différents, ….

Les fluides jouent donc un rôle important dans la genèse des séismes et leur distribution spatio-temporelle, sur différents objets géologiques et à différentes échelles. La sismicité volcanique, les essaims sismiques des zones tectoniques et la micro-sismicité associée aux activités anthropiques dans et autour des réservoirs rocheux sont toutes induites par les fluides. Les conditions de contraintes, de température et les fluides peuvent cependant varier très fortement entre objets géologiques. Par exemple, la sismicité volcanique est associée à de très fortes températures et pression, ainsi qu'à de larges déformations. Ce n'est pas le cas par exemple pour la sismicité de l'Oklahoma, où les surpressions dues aux injections sont très faibles (Goebel et al., 2017). Cependant, dans tous ces cas, il est nécessaire de suivre et interpréter la migration de la sismicité et de comprendre les processus qui la génèrent pour anticiper (où ?, quand ?, quelle magnitude ?) tremblements de terre majeurs ou éruptions volcaniques. Les questions à résoudre sont donc similaires.

… des questions en suspens, …

En particulier, on peut se demander :

- Pourquoi une déformation asismique ou sismique ? Comment voir et quantifier une déformation asismique ?
- Pourquoi une rupture s'exprime-t-elle sous forme d'un essaim sismique et non comme un choc principal ? Quelles sont les conditions nécessaires pour qu'un tremblement de terre de grande magnitude s'initie ?
- Quel est le lien entre la magnitude d'un évènement et la perturbation de fluides (volume, pression, …) ?

… mais processus similaires ?

Pour répondre à ces questions similaires, les analyses sismologiques sont souvent faites de manière cloisonnée entre ces différents objets. A titre d'exemple, la corrélation entre le volume de fluide et la magnitude des séismes, relation utilisée mais débattue depuis plus de 40 ans pour les réservoirs (McGarr, 1976), n'a été appliquée sur les volcans qu'en 2016 (White et al., 2016). Les réponses sismologiques peuvent cependant être très similaires (*Figure 18*). On peut donc se demander si les processus qui accompagnent et génèrent ces séismes sont identiques (Traversa and Grasso, 2010), et si la comparaison entre objets peut apporter des contraintes sur ceux-ci. Ayant travaillé sur différents objets géologiques, et à une échelle décamétrique sur des expériences contrôlées, je souhaite maintenant mettre l'accent sur la comparaison multi-échelles et multi-objets des réponses sismiques aux perturbations fluides. Mes prospectives scientifiques sont donc :

- Améliorer les observations sismologiques des glissements lents et asismiques

- Améliorer la compréhension du lien entre fluide, déformation et sismicité par de nouvelles observations, expériences in-situ, et modélisations couplées sismo-hydro-mécaniques.
- Faire le lien d'échelles entre les expériences en laboratoire et les réservoirs en utilisant les expériences aux échelles décamétriques.
- Confronter les lois d'échelles, les distributions spatio-temporelles et de magnitudes observées sur différents objets géologiques**.**

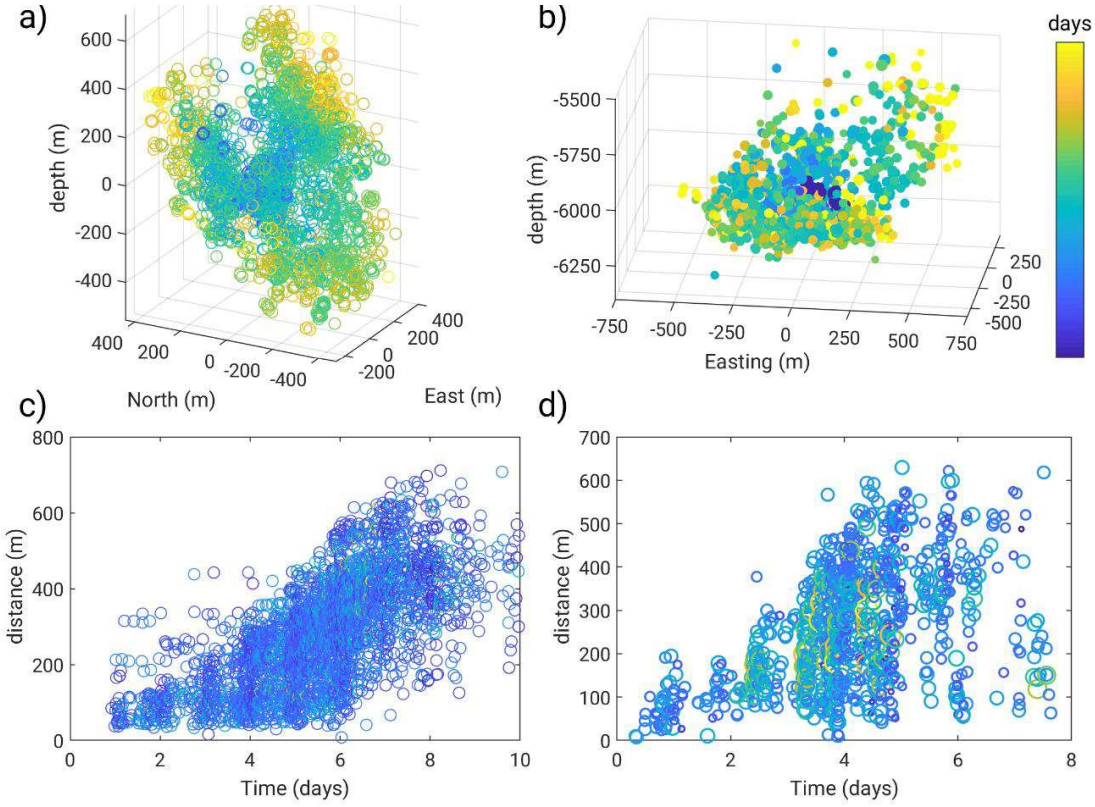

Figure 18: *Similitudes entre sismicité induite et essaim sismique. a) distribution spatiale et c) diagramme distance-temps de la sismicité induite par les injections de fluide pour l'exploitation géothermique en 2006 à Bale, Suisse (Herrmann et al., 2019). c) et d) idem pour la un essaim sismique enregistrée en 2015 dans le golfe de Corinthe (**De Barros et al., submitted**).*

3.1. Améliorer les observations sismologiques

Les mesures et observations des déformations lentes sont rares et indirectes lorsque non percevables en surface. De plus, il existe souvent une ambiguïté dans les interprétations des données sismologiques entre des processus reliés aux fluides, à des glissements lents, ou à une interaction entre les deux. Pour améliorer notre compréhension des processus en profondeur, il est donc nécessaire d'améliorer nos observations, en particulier des glissements lents. Cela peut se faire par une recherche d'observations dans le bruit sismique ou GPS (3.1.1), par une étude plus systématique des évènements répétitifs (3.1.2), par le développement de nouveaux instruments de mesures (fibre optique, 3.1.3) ou en creusant le lien séismes/failles/états de contraintes (3.1.4).

3.1.1. Déformations lentes dans le bruit ?

La déformation associée aux essaims sismiques, aux glissement lents ou à la sismicité induite est en général trop faible pour être mesurable en surface (GPS, INSAR). Les mesures in-situ de déformation donnent des informations précieuses, mais ponctuelles et nécessitant des forages au plus près des sources. Pour compenser ces lacunes dans les données, il est possible de cumuler les déformations mesurées lors de plusieurs crises sismiques. Ainsi, en séparant les données GPS des périodes d'occurrence de LFEs ou de trémors au niveau des subductions du Mexique et des Cascades, Frank et al. (2018) ont pu identifier les périodes où le glissement lent est caché dans le bruit des signaux GPS (*Figure 19*). Une telle approche serait intéressante à appliquer sur les essaims sismiques, pour faire un bilan global du partitionnement sismique/asismique lors d'essaims sismiques, par exemple sur le rift de Corinthe.

L'occurrence de déformations asismiques peut se voir dans les signatures sismiques non conventionnelles. Les LFE et les trémors, observés dans les zones de subduction (Mexique, Cascades, Japon) ou sur les zones en fluage de la faille de San Andreas sont associés à des glissements lents vus par GPS. Ces observations sont cependant rares sur des failles de plus petites dimensions et/ou moins bien instrumentés. Cette absence d'observations ne signifie pas une absence de signaux, mais révèle une difficulté à les voir. Il est en effet probable que de telles signatures soient cachées dans le bruit sismique. La caractérisation de l'amplitude du bruit et de ses variations temporelles peuvent permettre de détecter ces signaux. De telles méthodes (RSAM ou SSAM principalement) sont communément utilisées pour surveiller les phases pré-éruptives des volcans (Cornelius and Voight, 1994), mais pas les zones tectoniques. En utilisant des techniques de localisation par amplitude développées pour les trémors volcaniques (Battaglia et al., 2005; Taisne et al., 2011), l'origine spatiale de ces anomalies pourrait ensuite être déterminée. En particulier, il serait intéressant de caractériser le bruit 1) précédant les tremblements de terre, pour identifier les phases de préparation de la rupture, et 2) accompagnant les essaims sismiques, pour mieux contraindre leur processus. Une telle approche pourrait donc être développée autour des zones de subduction où des glissements lents et la nucléation de la rupture sont observés (subduction Sud-Américaine), ce qui permettra une calibration de la méthode. L'application d'une telle approche pourrait permettre

de répondre à la question des glissements lents dans des zones bien instrumentées, telles les Apennins ou le golfe de Corinthe, dans lesquelles des déformations asismiques sont suspectées.

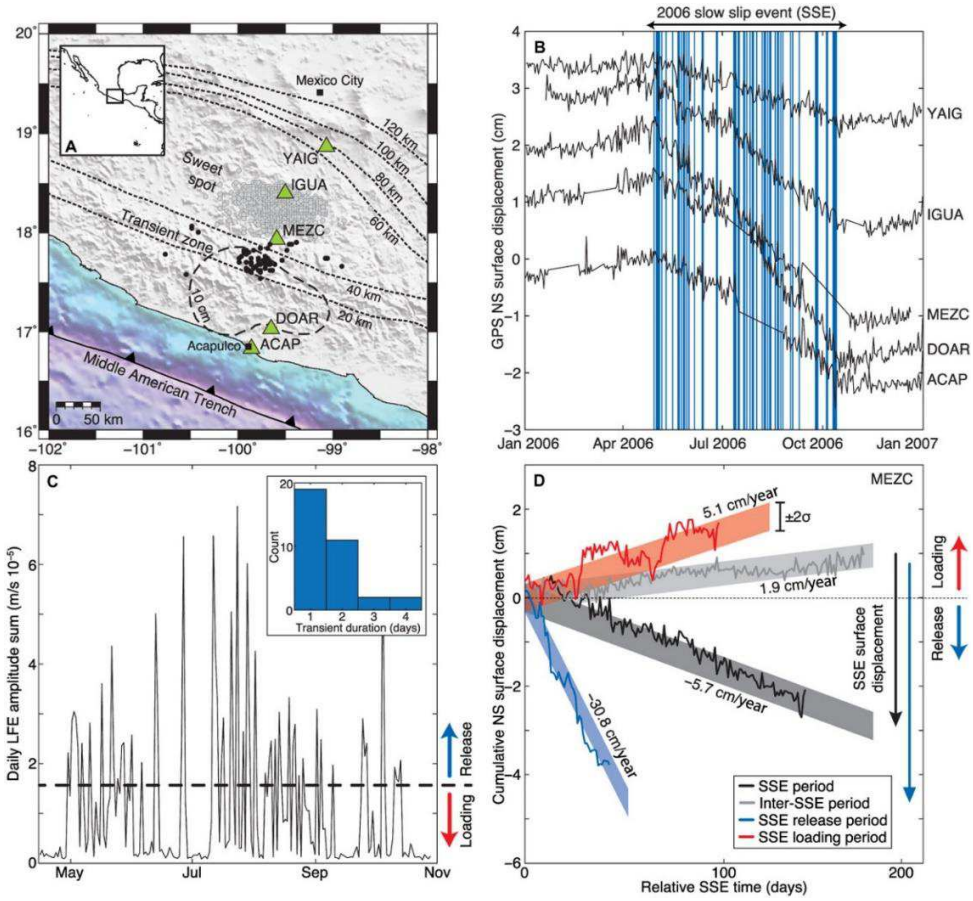

***Figure 19**: A) Contexte tectonique de la zone de subduction sous Guerrero, Mexico, où un glissement lent a été enregistré par GPS en 2006 (traits pointillés épais) ; B) Déplacement GPS en 2006. Les traits bleus montrent les périodes de signatures transitoires, c'est-à-dire les périodes où le taux quotidien de signaux Longues Périodes (C) excèdent un seuil prédéfini. D) déplacement GPS cumulé sur les périodes séparant les glissements lents (gris clair) et de glissements lents (gris foncé). Cette dernière est décomposée en 2 périodes : avec (bleu) et sans (rouge) signatures transitoires (bleu). Cette décomposition permet d'isoler la déformation associée aux périodes transitoires, qui était sinon noyée dans le bruit du GPS.*

3.1.2. Evènements répétitifs ?

Les signaux répétitifs sont aussi un moyen d'avoir des informations sur les glissements lents. En effet, pour avoir des formes d'ondes exactement similaires (*Figure 20*), il faut qu'une même aspérité casse plusieurs fois. Il est donc nécessaire que l'état de contraintes sur cette aspérité soit rechargé entre chaque rupture, ce qui a lieu lorsque cette aspérité est coincée dans un glissement asismique. Les

glissements asismiques permettent ainsi de quantifier le taux de glissement lent, et de suivre leurs variations (Chen et al., 2010; Uchida and Bürgmann, 2019) .

Les signaux répétitifs sont principalement observés dans les zones de subduction (Igarashi et al., 2003) et sur les parties en fluage de la faille de San-Andreas (Nadeau and McEvilly, 1999). J'ai commencé à travailler sur de telles signatures dans les répliques du séisme de Pedernales (Equateur), qui permettent notamment de détailler le glissement post-sismique (suivi de thèse de C. Chalumeau, dir. Ph. Charvis).

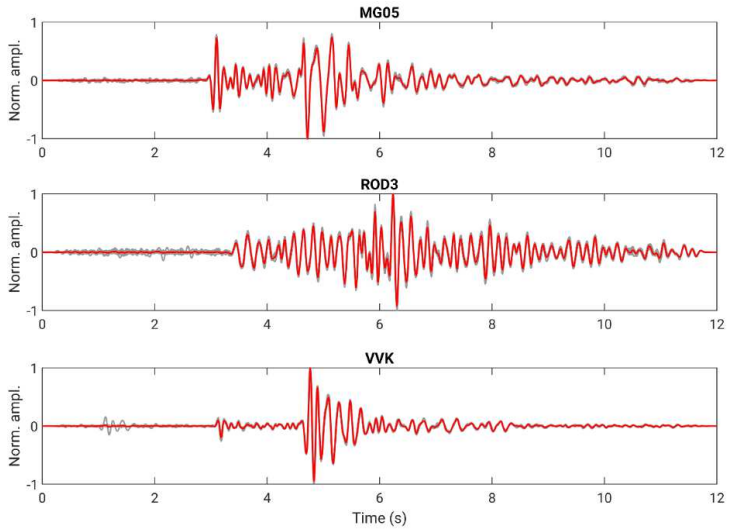

Figure 20: *Exemple d'une famille de 10 évènements répétitifs enregistrés en 2015 lors d'un essaim du golfe de Corinthe par 3 stations (MG05, ROD3, et VVK). Les 10 signaux, normalisés, sont en gris, leur moyenne en rouge. Les magnitudes de ces évènements varient entre 1.4 et 2.5, indiquant une variation d'un facteur 10 en amplitude (**De Barros et al., soumis**).*

Des ruptures se recouvrant au moins partiellement ont aussi été observées lors d'essaims sismiques, naturels ou liés aux activités anthropiques (Lengliné et al., 2014). On peut se demander si les processus à l'origine de ces signaux sont les mêmes que dans les zones de subduction, c'est-à-dire s'ils indiquent aussi des glissements lents, ou s'ils sont associés à des relâchements partiels de contraintes, à des augmentations progressives des pressions fluides ou à des rechargements par transfert de contraintes. Dit autrement, on peut se demander si le taux d'évènements répétitifs quantifie la déformation ou les variations de l'état de contrainte. La compréhension de telles signatures peut donc apporter des informations précises et quantifiées sur le fonctionnement de la sismicité induite. J'ai donc commencé à regarder de telles signatures lors d'essaims sismiques à Corinthe, qui semblent permettre de déchiffrer l'interaction fluide/glissement lent à l'origine des essaims de sismicité (**De Barros et al., soumis**). Cette étude mérite d'être approfondie, notamment par des modélisations numériques (Coll. P. Dublanchet), et généralisée à la sismicité induite dans les réservoirs.

Les chutes de contraintes observées sur les multiplets ou événements répétitifs sont aussi riches d'enseignement. En effet, des signaux exactement similaires ont des fréquences coins, et donc des tailles de source, identiques. Cependant, on observe des différences de 1 à 2 dans leur magnitude, indiquant des variations des chutes de contraintes de 1 à 2 ordres de grandeurs. De telles observations ont été faites dans des réservoirs (Lengliné et al., 2014) et des zones tectoniques (Abercrombie, 2014), et notamment dans les essaims de Corinthe. Elles peuvent indiquer des variations 1) dans les vitesses de rupture, 2) dans l'état de contraintes et de pression, ou 3) dans les propriétés frictionnelles. En collaboration avec Y. Huang (U. Michigan), nous envisageons de travailler sur ce problème, pour relier variations de chutes de contraintes et physique de rupture.

3.1.3. Fibres optiques : un champ de nouvelles observations ?

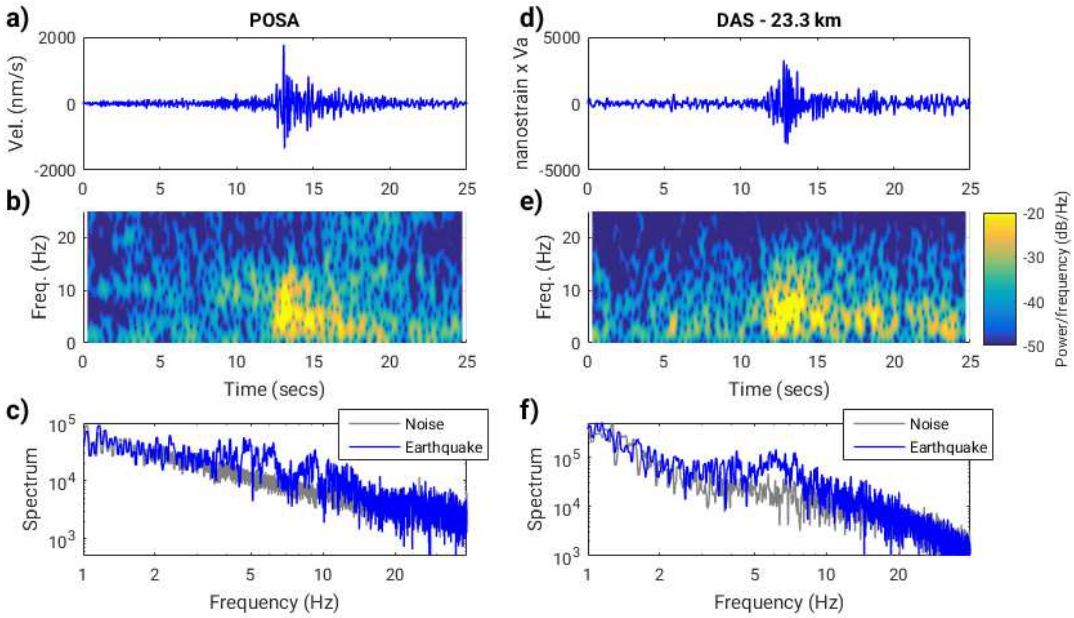

***Figure 21**: Formes d'ondes, spectrogramme et spectre d'un séisme de magnitude M1.9, enregistré par une station large-bande (POSA) et par une fibre optique sous-marine au large de Toulon. La distance entre le séisme et les acquisitions est supérieure à 100 km (**Sladen et al., 2019**).*

Une meilleure compréhension des processus passe par de meilleures observations. Les fibres optiques nous ont permis des mesures de déformations localisées (réseau de Bragg) lors des expériences décamétriques (sonde SIMFIP, Guglielmi et al., 2014). Cependant, la diffraction de la lumière permet aussi la mesure distribuée de la déformation, de la température, et surtout des signaux acoustiques (Distributed Acoustic Sensing, DAS). Cette technique émergente a ainsi montré qu'il était possible d'enregistrer des séismes, d'imager des zones de failles, etc., avec une qualité comparable à celle des capteurs classiques (Jousset et al., 2018; Lindsey et al., 2017). En particulier, il est possible de transformer les réseaux de fibres optiques déployés pour les télécommunications en lignes denses de capteurs sismiques. Dans le projet SEAFOOD (PI. A. Sladen), nous avons ainsi pu enregistrer les bruits océaniques et des séismes locaux de très faible amplitude (*Figure 21*) à partir

d'une fibre sous-marine de télécommunications installée au large de Toulon (**Sladen et al., 2019**). De tels résultats restent exploratoires, avec une technologie de mesures qui progresse extrêmement vite. Ces techniques ouvrent un large champ de possibilité d'observations, pouvant permettre une instrumentation dense dans des environnements difficiles (volcans), voire inaccessibles (environnement marin profond). Un autre intérêt de cette technique réside aussi dans la possibilité d'avoir des mesures conjointes de déformation et de sismicité.

3.1.4. Lien séismes et contexte sismo-tectonique ?

Comprendre le lien séisme/fluide/déformation nécessite de replacer la sismicité dans son contexte tectonique, et donc de caractériser les failles et surtout leur état de contraintes. En effet, la réponse sismique/asismique d'une faille à une perturbation varie selon son état de criticalité par rapport à la rupture (Bhattacharya and Viesca, 2019; **Wynants-Morel et al., soumis**). Les mesures de contraintes, difficiles en profondeur, sont accessibles par les mécanismes au foyer. En effet, ceux-ci permettent d'identifier les structures en jeux et d'estimer les états de contraintes par inversion de leur plans nodaux (Michael, 1987). L'orientation des plans de failles dans cet état de contrainte peut ensuite être interprété pour déterminer les pressions de fluide et/ou les propriétés frictionnelles des failles (Leclère et al., 2013; Sibson, 1985). On peut cependant se poser la question de la signification de cet état de contraintes : il n'est peut-être pas régional, car les hétérogénéités, et en particulier les zones de failles, peuvent induire variations et rotations des contraintes (Faulkner et al., 2006). Il n'est sans doute pas statique non plus, car il est modifié par les glissements asismiques et les interactions entre séismes. Comprendre pourquoi ces états de contraintes sont perturbés peut donc permettre d'avoir des observations sur les processus en jeux.

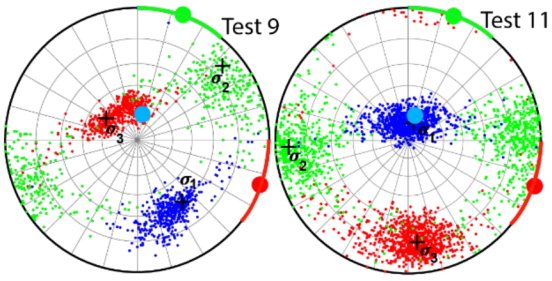

Figure 22: *Comparaison des états de contraintes déterminés par inversion des mécanismes au foyer (nuages de points et croix) et par inversion des données hydromécaniques (larges cercles) lors de 2 tests d'injection à Rustrel (σ1, σ2 et σ3 respectivement en bleu, vert et rouge).*

A partir des expériences in-situ de Rustrel, je souhaite travailler sur ces interprétations en comparant les états de contraintes statiques mesurés par la sonde hydro-mécanique et déduits de la sismologie. La connaissance de l'état de contrainte statique et des orientations des principales structures géologiques permet d'évaluer les pressions de fluide ou les perturbations de contraintes nécessaires pour réactiver sismiquement les fractures mal-orientées. Ces perturbations peuvent ensuite être comparées aux mesures de pression et de déformation à l'injection, pour évaluer leur rôle respectif,

et ainsi évaluer pourquoi les états de contraintes estimées par les mécanismes diffèrent des états de contraintes statiques (*Figure 22*).

Dans le cadre de la thèse de M. Baques (2019-), nous aimerions généraliser les travaux de Leclère et al. (2013) pour relier comportement sismologique, failles et états de contraintes. Le calcul des mécanismes des répliques du séisme de Barcelonnette (2014) nous permettra d'évaluer dans une zone naturelle les variations spatiales et temporelles de l'état de contraintes, en lien avec des processus connus (**De Barros et al., 2019a**), et ainsi de comprendre comment ces variations nous renseignent sur les processus en jeux.

3.2. Comparaison multi-échelles et multi-objets

Les observations multi-paramètres, au plus près des sources, sont primordiales pour appréhender la physique de la rupture, et comprendre les couplages entre processus. Pour améliorer les interprétations de ces observations, je souhaite confronter différentes échelles, et différents objets. En effet, la mise en parallèle des observations et de leurs contextes peut aider à discriminer parmi les différentes interprétations, et ainsi identifier des similarités et des différences dans les processus. En particulier, les expériences in-situ, à une échelle intermédiaire entre laboratoire et réservoirs, peuvent permettre d'extrapoler les lois d'échelle classiquement utilisées en sismologie (3.2.1). Je souhaite aussi comparer les distributions spatio-temporelles de la sismicité, observation commune sur différents objets (3.2.2). Un autre analogue intéressant à étudier pourrait être les glissements de terrains, où la micro-sismicité permet de suivre une rupture souvent contrôlée par les fluides (3.2.3). Enfin, les modélisations numériques permettent de coupler fluide, déformation et rupture sismique à différentes échelles de temps. Elles permettent ainsi de tester et comparer des scenarii construits à partir des données d'expériences ou d'observations sur une zone tectonique ou un volcan (3.2.4).

3.2.1. Expériences in situ : lien entre laboratoire et réservoirs ?

Les expériences de sismicité à une échelle décamétrique ont permis de repenser le lien entre sismicité et fluide, publiée dans plusieurs articles. Des questions restent en suspens et de nouvelles expériences sont en cours d'analyse, ou prévues (coll. Y. Guglielmi et M. Schoenball, Berkeley) :

- Une expérience de stimulation hydraulique a été conduite en 2018 dans les granodiorites d'une mine dans l'état du Dakota (Schoenball et al., 2019). La création de fractures a été soulignée par une sismicité dense.
- Une nouvelle expérience est en cours dans les argilites du Mont Terri (PI. Y. Guglielmi). L'idée de cette expérience est 1) de tester la réponse long terme et les propriétés de cicatrisation d'une faille argileuse et 2) d'imager avec précision la déformation asismique. Pour cela, un réseau dense de surveillance est mis en place, incluant accéléromètres, hydrophones et géophones, capteurs de déformations et de pression, ainsi qu'un réseau de fibres optiques en forages pour des mesures acoustiques et de déformation.

Ces nouveaux jeux de données vont permettre de compléter les jeux de données existants (Tournemire, Rustrel et Mont Terri), qui n'ont pas été encore totalement exploités. En particulier, l'originalité de cette échelle, entre laboratoires et réservoirs, n'a été que partiellement exploitée. Ces données peuvent en effet permettre de relier ces deux échelles d'observations. Je souhaite donc travailler sur le changement et l'extrapolation d'échelles entre réservoirs et laboratoires.

La majorité des lois d'échelles (Gutenberg-Richter par exemple, relations volume-magnitude pour les réservoirs, relations magnitude-durée (Ide et al., 2007), etc) a été définie à partir de « forts » séismes (M>4). Les expériences décamétriques, avec des séismes de M~-2.5 à -4, complètent le spectre de magnitude, entre les mesures acoustiques en laboratoire et les données de réservoirs ou

tectoniques. Prolonger les lois d'échelles vers les plus basses valeurs permettra d'évaluer l'universalité (ou les différences) des processus en jeux. Par exemple, la dichotomie entre séismes lents et glissements rapides s'observe dans les relations empiriques moment – durée de sources (Ide et al., 2007; Peng and Gomberg, 2010), mais ces relations posent un problème pour les petites magnitudes (Mo=10^{11} N.m, soit Mw~1), pour lesquelles les courbes se croisent (*Figure 23*). Compléter un tel graphe avec des magnitudes faibles pourrait permettre d'extrapoler les observations et éventuellement de répondre à la question d'un continuum entre glissements lents et tremblements de terre.

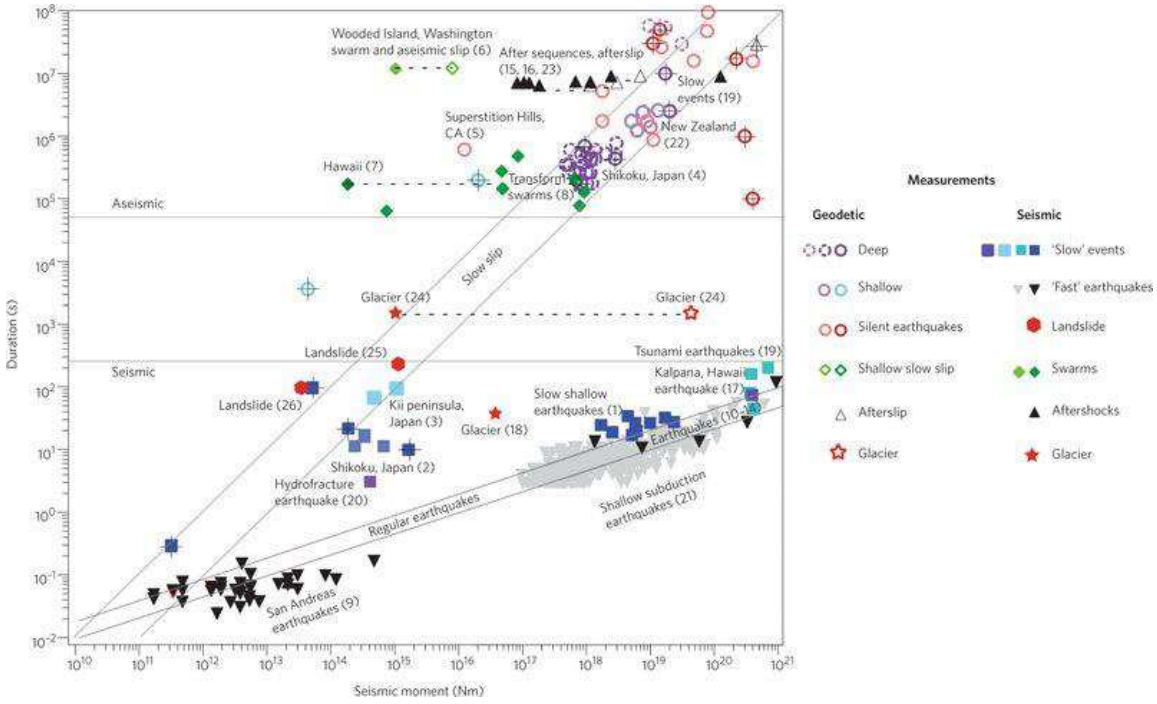

***Figure 23**: Relation entre la durée de source et le moment sismique pour différentes observations de glissements, incluant zones tectoniques, glissements de terrains et glaciers (Peng and Gomberg, 2010). Les glissements lents et glissements rapides s'alignent sur deux droites différentes, suggérant deux processus mécaniques différents et distincts. Cette dichotomie est toujours débattue (Gomberg et al., 2016; Ide et al., 2007; Peng and Gomberg, 2010).*

3.2.2. Comportement spatio-temporel de la sismicité ?

Quel que soit l'objet géologique, la sismicité présente souvent une migration. Cette migration est expliquée par les perturbations de contraintes au front du magma dans les volcans (Carrier et al., 2018; **De Barros et al., 2013a**), par la diffusion des pressions fluides (Shapiro et al., 1997b) dans les réservoirs et les essaims sismiques (Duverger et al., 2015), ou par l'occurrence de glissement lents et asismiques dans les zones de subduction (**Agurto-Detzel et al., 2019**; Vallée et al., 2013). Les migrations peuvent donc être modélisées par des lois linéaires, semi-logarithmiques (Perfettini et al., 2018) ou paraboliques. Il y a donc des observations pouvant renseigner sur les processus, mais des ambiguïtés d'interprétations. On peut donc légitimement s'interroger sur les similitudes et

différences dans les migrations entre les différents objets géologiques. En particulier, il est très certainement nécessaire de revoir les contributions des fluides et des transferts de contraintes, (Bhattacharya and Viesca, 2019) par des approches théoriques, numériques et observationnelles.

De plus, seul le front de sismicité est considéré dans l'analyse de la migration. Cependant, la distribution de la sismicité dans les diagrammes distance-temps montre généralement des phases discontinues, avec des phases de quiescences alternant avec des phases de migrations rapides (*Figure 18*). L'analyse détaillée de ces phases d'accélération et de la distribution discontinue de la sismicité peut renseigner sur les processus des essaims de sismicité. Enfin, je souhaite regarder ces migrations, non seulement à partir du nombre ou de l'occurrence des évènements, mais aussi en fonction de la distribution de leur énergie (moment sismique) et des volumes injectés lorsqu'ils sont connus. Cette étude peut se faire par la comparaison de différents catalogues de crises sismiques pour lesquels les forçages sont relativement connus (sismicité induite) ou encore débattus (essaims sismiques). Dans un deuxième temps, cette approche pourra être généralisée à des objets complexes (volcans, glissement de terrains, …).

3.2.3. Glissement de terrains: un autre analogue ?

J'ai travaillé et souhaite donc comparer la sismicité observée sur les volcans, les zones tectoniquement actives et les réservoirs. Une analogie pourrait aussi être faite avec la sismicité enregistrée sur les glissements de terrains. En effet, les processus fluides jouent un rôle prépondérant sur le glissement qui se produit sur une surface de rupture, analogue à une faille. Les glissements peuvent présenter des phases de mouvements lents, avec des accélérations brutales, qui sont souvent corrélées avec des apports d'eau par les précipitations (Helmstetter and Garambois, 2010). On retrouve donc une dualité glissement lent/rapide, contrôlée par les pressions fluides.

Tout comme sur les volcans, une grande variété de signatures sismiques a été enregistrée sur les glissements de terrains. Ainsi, des trémors et des signaux avec des contenus fréquentiels à longues périodes ont été observés. Une classification de ces signatures est proposée par Provost et al. (2018). Tout comme sur les volcans, certains de ces signaux ont une origine connue, mais d'autres restent incertaines et débattues (*Figure 24*). Une mise en parallèle des signaux observés sur des volcans et les glissements de terrains permettra certainement de mieux comprendre leurs mécanismes, en s'appuyant sur les similitudes et différences de contexte.

Comme les glissements de terrains sont des objets superficiels avec des déformations rapides, le déplacement peut être mesuré. De même, les arrivées de fluide peuvent être connues en première approximation par les données météorologiques. Le contexte peut donc permettre de renseigner sur les processus en profondeur, le type de sismicité, les phénomènes de migration, etc. En contrepartie, les glissements de terrains sont des objets extrêmement hétérogènes avec une fracturation intense, et des structures en jeux complexes et souvent peu connues.

Au sein de Géoazur, le glissement de terrain de La Clapière, dans la vallée de la Tinée, est un objet d'études depuis de nombreuses années. Il s'agit d'un des plus grands glissements actifs d'Europe, avec une hauteur de 700 m sur 1100 m de large, et un volume instable estimé à plus de 50 millions de m^3 (Jomard et al., 2007). Les conditions hydrologiques et mécaniques ont été étudiées et modélisées (Cappa et al., 2004), ce qui permet de comprendre l'effet des fluides sur la déstabilisation gravitaire. Dans le cadre d'OMIV (Observatoire des Mouvements et Instabilités de Versants), ce glissement est instrumenté par des capteurs sismiques. La sismicité de ce glissement, dans un contexte hydrologique et de déformation lui aussi surveillé, pourrait être riche d'enseignement sur les processus en jeux.

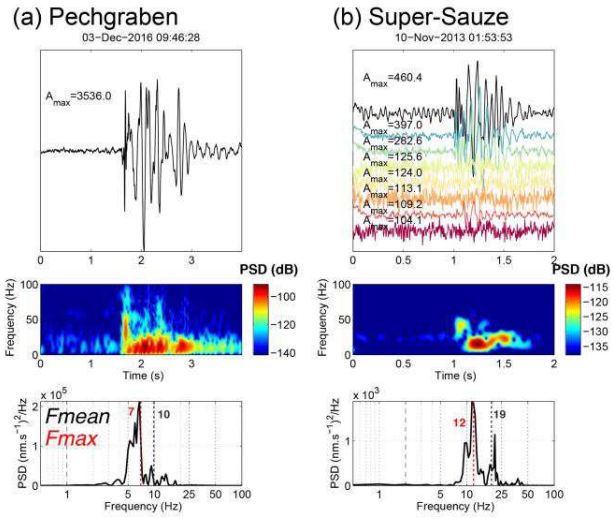

***Figure 24**: Exemple de signaux enregistrés sur des glissements de terrains (Provost et al., 2018), avec un mécanisme incertain. Ces signaux hybrides commencent par une phase impulsive, suivie par des signatures monochromatiques. Ils peuvent être dus à une rupture fragile induisant une résonnance de fractures (Chouet, 1988). De telles signatures sont aussi observées sur les volcans (White et al., 1998).*

3.2.4. Modélisation sismo-hydro-mécanique : une validation des scénarios ?

Le changement d'échelles des observations et résultats obtenus lors des expériences décamétriques peut aussi se faire à travers des modélisations numériques, qui permettent un couplage sismo-hydro-mécanique. A travers la collaboration développée avec F. Cappa, nous avons ainsi pu tester la réponse sismologique d'une faille soumise à une injection de fluide (travail de thèse de N. Wynants). Ce travail mérite d'être poursuivi, en utilisant des géométries plus complexes et réalistes.

Premièrement, de telles simulations peuvent être effectuées dans des milieux découpés par des centaines de failles, ce qui générerait de nombreux évènements sismiques synthétiques. Alternativement, il est aussi possible de regarder la réponse de failles très hétérogènes (Almakari et al., 2019). L'analyse de ces catalogues de sismicité synthétique permettrait d'affiner la compréhension des anomalies visibles dans les lois d'échelles ou dans les distributions de mécanismes.

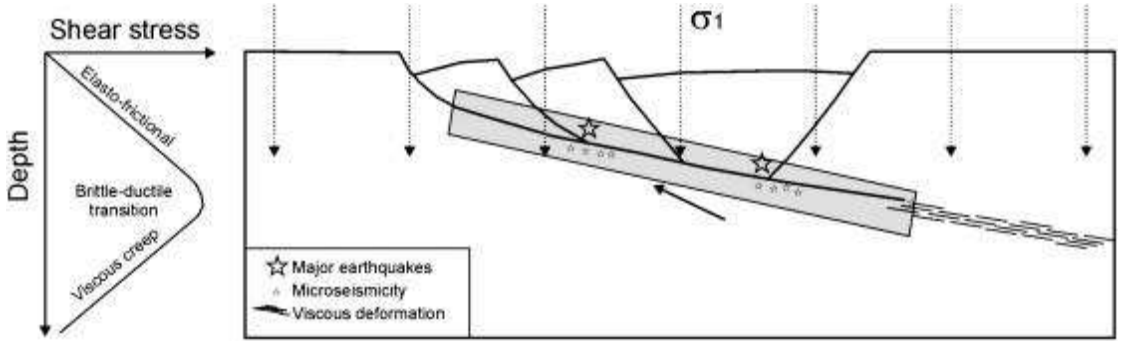

Figure 25: *représentation schématique (Collettini, 2011) d'une faille normale à faible pendage, dans laquelle viennent s'enraciner des failles à pendage plus élevée. Un telle géométrie est suspectée par exemple dans les Apennins ou dans le golfe de Corinthe. Du glissement lent, accompagné de micro-sismicité, a lieu sur le détachement, alors que les failles normales inclinées peuvent porter des séismes majeurs (ex. Aquila, 2009).*

En plus de cette approche statistique, je souhaiterai tester des scénarios développés à partir des observations, que ce soit dans les expériences in-situ, les zones tectoniques ou les réservoirs. Cette approche permettrait ainsi de valider (ou infirmer) ces scénarios, de compléter leur compréhension, et de rapprocher différentes échelles. Par exemple, le test 11 à Rustrel montre la réactivation d'un plan faiblement penté. Ce glissement n'est accompagné d'aucun évènement sismique, les séismes ayant lieu sur des structures à forts pendages qui viennent se raccorder à ce plan. Les tremblements de terre semblent donc être générés par transfert de contraintes du glissement asismique vers des structures annexes (**Huang et al., 2019**). Cette géométrie, et cette distribution de la sismicité, se retrouve dans la sismicité du golfe de Corinthe ou dans les Appenins *(Figure 25*). Dans ces deux cas, une partie des évènements a lieu sur des failles normales à fort pendage, bien qu'une déformation asismique est suspectée sur le détachement à leur racine (Collettini, 2011). Cette géométrie peut aussi rappeler celle des glissements de terrains, où une part importante de la sismicité a lieu dans le volume, et non sur le plan de glissement principal. La modélisation numérique d'une telle géométrie permettra de tester l'influence des fluides sur le partitionnement sismique/asismique du glissement, et d'estimer comment les différentes structures en jeux interagissent par transferts de contraintes.

4. CONCLUSION

Dans ce document, j'ai présenté des résultats et perspectives de mes activités de recherche. Je me suis attaché à montrer comment les fluides influent sur la rupture sismique, et inversement comment les formes d'ondes et la distribution de la sismicité permettent de renseigner sur les processus en profondeur. En particulier, j'ai voulu insister sur l'importance des déformations asismiques et des glissements lents dans l'interaction complexe entre fluide et séismes. Ces interdépendances génèrent des ambiguïtés dans les interprétations entre des processus reliés à la pression fluide et ou aux déformations lentes.

Dans mon cursus, j'ai eu la chance de travailler sur différents objets géologiques, à différentes échelles. Les observations jouent maintenant un rôle central dans mon approche, et orientent mon travail. J'estime donc qu'il est indispensable de consacrer du temps à regarder les données, pour pouvoir exploiter toutes les richesses qu'elles renferment. L'augmentation exponentielle des volumes de données rend cette tâche longue et délicate, mais exploiter et valoriser des données existantes est indispensable. Même si l'observation tient une position centrale, modélisations théoriques, numériques ou expérimentales sont indispensables pour conforter et généraliser les résultats. Des collaborations scientifiques sont donc nécessaires et toujours positives.

Contrairement à l'organisation de ce document, mes activités de recherche n'ont pas été planifiées à l'avance. Au contraire, elles se sont faites surtout par opportunité et par chance : opportunité d'emplois, de collaborations, de discussions scientifiques, et surtout opportunité de découvertes. En effet, il n'est pas possible de planifier que telles observations dans tels jeux de données vont pouvoir aboutir à des résultats intéressants. Cette liberté dans la recherche et dans la découverte est ce qui rend notre travail aussi intéressant. Une telle vision n'est pas compatible avec une recherche court terme, sur projets, où il est nécessaire de définir à l'avance quels vont être les résultats que l'on va obtenir. Bien sûr, il est nécessaire d'avoir des sources de financement pour pouvoir développer expériences et observations innovantes. Mais en aucun cas l'obtention ou non de projets de financement ne devrait être un critère d'évaluation de la recherche.

Je n'ai pas abordé dans ce document les activités d'enseignement. J'apprécie l'enseignement, car il oblige à vulgariser des connaissances souvent trop complexes et à essayer de transmettre une passion qui peut manquer à certains étudiants. J'apprécie aussi les relations avec les étudiants et le retour immédiat qu'ils renvoient. Bien que très enrichissante, cette activité demande énormément de temps. Les responsabilités de filière (ou autres) sont des taches lourdes au sein d'une université où le changement est perpétuel. De plus, jongler avec deux métiers aussi différents que la recherche et l'enseignement n'est pas toujours facile. Cela oblige donc à faire de la recherche par intermittence, et des choix sélectifs dans les missions qui me sont confiées, avec un sentiment de devoir tout faire dans l'urgence. Malgré ces difficultés, ce métier est passionnant, et je m'amuse dans la recherche et joue dans l'enseignement.

REFERENCES

Abercrombie, R.E., 2014. Stress drops of repeating earthquakes on the San Andreas Fault at Parkfield. Geophysical Research Letters 41, 8784–8791. https://doi.org/10.1002/2014GL062079

Agurto-Detzel, H., Font, Y., Charvis, P., Régnier, M., Rietbrock, A., Ambrois, D., Paulatto, M., Alvarado, A., Beck, S., Courboulex, F., De Barros, L., Deschamps, A., Hernandez, M.J., Hernandez, S., Hoskins, M., León-Ríos, S., Lynner, C., Meltzer, A., Mercerat, E.D., Michaud, F., Nocquet, J.M., Rolandone, F., Ruiz, M., Soto-Cordero, L., 2019. Ridge subduction and afterslip control aftershock distribution of the 2016 Mw 7.8 Ecuador earthquake. Earth and Planetary Science Letters 520, 63–76. https://doi.org/10.1016/j.epsl.2019.05.029

Aki, K., Fehler, M., Das, S., 1977. Source mechanism of volcanic tremor: Fluid-driven crack models and their application to the 1963 Kilauea eruption. Journal of volcanology and geothermal research 2, 259–287.

Almakari, M., Dublanchet, P., Chauris, H., Pellet, F., 2019. Effect of the injection scenario on the rate and magnitude content of injection-induced seismicity: Case of a heterogeneous fault. Journal of Geophysical Research: Solid Earth.

Aloisi, M., Cocina, O., Neri, G., Orecchio, B., Privitera, E., 2002. Seismic tomography of the crust underneath the Etna volcano, Sicily. Physics of the Earth and Planetary Interiors 134, 139–155.

Auger, E., Gasparini, P., Virieux, J., Zollo, A., 2001. Seismic evidence of an extended magmatic sill under Mt. Vesuvius. Science 294, 1510–1512.

Bao, X., Eaton, D.W., 2016. Fault activation by hydraulic fracturing in western Canada. Science 354, 1406–1409. https://doi.org/10.1126/science.aag2583

Bardainne, T., Dubos-Sallée, N., Sénéchal, G., Gaillot, P., Perroud, H., 2008. Analysis of the induced seismicity of the Lacq gas field (Southwestern France) and model of deformation. Geophys J Int 172, 1151–1162. https://doi.org/10.1111/j.1365-246X.2007.03705.x

Battaglia, J., Aki, K., Ferrazzini, V., 2005. Location of tremor sources and estimation of lava output using tremor source amplitude on the Piton de la Fournaise volcano: 1. Location of tremor sources. Journal of volcanology and geothermal research 147, 268–290.

Bean, C., Lokmer, I., O'Brien, G., 2008. Influence of near-surface volcanic structure on long-period seismic signals and on moment tensor inversions: Simulated examples from Mount Etna. Journal of Geophysical Research: Solid Earth 113.

Bean, C.J., De Barros, L., Lokmer, I., Métaxian, J.-P., O' Brien, G., Murphy, S., 2014. Long-period seismicity in the shallow volcanic edifice formed from slow-rupture earthquakes. Nature Geoscience 7, 71–75. https://doi.org/10.1038/ngeo2027

Bernard, P., Lyon-Caen, H., Briole, P., Deschamps, A., Boudin, F., Makropoulos, K., Papadimitriou, P., Lemeille, F., Patau, G., Billiris, H., 2006. Seismicity, deformation and seismic hazard in the western rift of Corinth: New insights from the Corinth Rift Laboratory (CRL). Tectonophysics 426, 7–30.

Bhattacharya, P., Viesca, R.C., 2019. Fluid-induced aseismic fault slip outpaces pore-fluid migration. Science 364, 464–468. https://doi.org/10.1126/science.aaw7354

Biot, M.A., 1956. Theory of propagation of elastic waves in a fluid-saturated porous solid. II. Higher frequency range. The Journal of the acoustical Society of america 28, 179–191.

Bourouis, S., Bernard, P., 2007. Evidence for coupled seismic and aseismic fault slip during water injection in the geothermal site of Soultz (France), and implications for seismogenic transients. Geophysical Journal International 169, 723–732.

Bräuer, K., Kämpf, H., Strauch, G., 2009. Earthquake swarms in non-volcanic regions: What fluids have to say. Geophysical Research Letters 36. https://doi.org/10.1029/2009GL039615

Brenguier, F., Kowalski, P., Staudacher, T., Ferrazzini, V., Lauret, F., Boissier, P., Catherine, P., Lemarchand, A., Pequegnat, C., Meric, O., 2012. First results from the UnderVolc high resolution seismic and GPS network deployed on Piton de la Fournaise volcano. Seismological Research Letters 83, 97–102.

Brenguier, F., Shapiro, N.M., Campillo, M., Ferrazzini, V., Duputel, Z., Coutant, O., Nercessian, A., 2008. Towards forecasting volcanic eruptions using seismic noise. Nature Geoscience 1, 126.

Broberg, K.B., 2006. Differences Between Mode I and Mode II Crack Propagation. Pure appl. geophys. 163, 1867–1879. https://doi.org/10.1007/s00024-006-0101-7

Cappa, F., Guglielmi, Y., Soukatchoff, V.M., Mudry, J., Bertrand, C., Charmoille, A., 2004. Hydromechanical modeling of a large moving rock slope inferred from slope levelling coupled to spring long-term hydrochemical monitoring: example of the La Clapiere landslide (Southern Alps, France). Journal of Hydrology 291, 67–90.

Cappa, F., Scuderi, M.M., Collettini, C., Guglielmi, Y., Avouac, J.-P., 2019. Stabilization of fault slip by fluid injection in the laboratory and in situ. Science Advances 5, eaau4065. https://doi.org/10.1126/sciadv.aau4065

Carcione, J.M., Morency, C., Santos, J.E., 2010. Computational poroelasticity—A review. Geophysics 75, 75A229-75A243.

Carrier, A., Got, J.-L., Peltier, A., Ferrazzini, V., Staudacher, T., Kowalski, P., Boissier, P., 2018. A damage model for volcanic edifices: Implications for edifice strength, magma pressure, and eruptive processes. Journal of Geophysical Research: Solid Earth 567–583. https://doi.org/10.1002/2014JB011485@10.1002/(ISSN)2169-9356.SSMCV1

Cervelli, P., Segall, P., Johnson, K., Lisowski, M., Miklius, A., 2002. Sudden aseismic fault slip on the south flank of Kilauea volcano. Nature 415, 1014.

Chang, K.W., Segall, P., 2016. Injection-induced seismicity on basement faults including poroelastic stressing. Journal of Geophysical Research: Solid Earth 121, 2708–2726.

Chen, K.H., Bürgmann, R., Nadeau, R.M., Chen, T., Lapusta, N., 2010. Postseismic variations in seismic moment and recurrence interval of repeating earthquakes. Earth and Planetary Science Letters 299, 118–125.

Chen, X., Shearer, P.M., Abercrombie, R.E., 2012. Spatial migration of earthquakes within seismic clusters in Southern California: Evidence for fluid diffusion. Journal of Geophysical Research: Solid Earth 117. https://doi.org/10.1029/2011JB008973

Chiaraluce, L., Valoroso, L., Piccinini, D., Di Stefano, R., De Gori, P., 2011. The anatomy of the 2009 L'Aquila normal fault system (central Italy) imaged by high resolution foreshock and aftershock locations. Journal of Geophysical Research: Solid Earth 116.

Chouet, B., 1988. Resonance of a fluid-driven crack: Radiation properties and implications for the source of long-period events and harmonic tremor. Journal of Geophysical Research: Solid Earth 93, 4375–4400. https://doi.org/10.1029/JB093iB05p04375

Chouet, B.A., 1996. Long-period volcano seismicity: its source and use in eruption forecasting. Nature 380, 309–316. https://doi.org/10.1038/380309a0

Collettini, C., 2011. The mechanical paradox of low-angle normal faults: Current understanding and open questions. Tectonophysics 510, 253–268. https://doi.org/10.1016/j.tecto.2011.07.015

Cornelius, R.R., Voight, B., 1994. Seismological aspects of the 1989–1990 eruption at Redoubt Volcano, Alaska: The Materials Failure Forecast Method (FFM) with RSAM and SSAM seismic data. Journal of Volcanology and Geothermal Research 62, 469–498.

Cornet, F.H., 2016. Seismic and aseismic motions generated by fluid injections. Geomechanics for Energy and the Environment 5, 42–54. https://doi.org/10.1016/j.gete.2015.12.003

Cornet, F.H., Helm, J., Poitrenaud, H., Etchecopar, A., 1998. Seismic and Aseismic Slips Induced by Large-scale Fluid Injections, in: Talebi, S. (Ed.), Seismicity Associated with Mines, Reservoirs and Fluid Injections, Pageoph Topical Volumes. Birkhäuser Basel, pp. 563–583.

Crawford, B.R., Faulkner, D.R., Rutter, E.H., 2008. Strength, porosity, and permeability development during hydrostatic and shear loading of synthetic quartz-clay fault gouge. Journal of Geophysical Research: Solid Earth 113.

Das, I., Zoback, M.D., 2013. Long-period, long-duration seismic events during hydraulic stimulation of shale and tight-gas reservoirs—Part 1: Waveform characteristicsLPLD events: Waveform characteristics. Geophysics 78, KS107–KS118.

Davi, R., O'Brien, G.S., De Barros, L., Lokmer, I., Bean, C.J., Lesage, P., Mora, M.M., Soto, G.J., 2012. Seismic source mechanisms of tremor recorded on Arenal volcano, Costa Rica, retrieved by waveform inversion. Journal of Volcanology and Geothermal Research 213–214, 1–13. https://doi.org/10.1016/j.jvolgeores.2011.10.008

De Barros, L., Baques, M., Godano, M., Helmstetter, A., Deschamps, A., Larroque, C., Courboulex, F., 2019a. Fluid-Induced Swarms and Coseismic Stress Transfer: A Dual Process Highlighted in the Aftershock Sequence of the 7 April 2014 Earthquake (Ml 4.8, Ubaye, France). Journal of Geophysical Research: Solid Earth 124, 3918–3932. https://doi.org/10.1029/2018JB017226

De Barros, L., Bean, C.J., Lokmer, I., Saccorotti, G., Zuccarello, L., O'Brien, G.S., Métaxian, J.-P., Patanè, D., 2009. Source geometry from exceptionally high resolution long period event observations at Mt Etna during the 2008 eruption. Geophysical Research Letters 36. https://doi.org/10.1029/2009GL041273

De Barros, L., Bean, C.J., Zecevic, M., Brenguier, F., Peltier, A., 2013a. Eruptive fracture location forecasts from high-frequency events on Piton de la Fournaise Volcano. Geophysical Research Letters 40, 4599–4603. https://doi.org/10.1002/grl.50890

De Barros, L., Cappa, F., Guglielmi, Y., Duboeuf, L., Grasso, J.-R., 2019b. Energy of injection-induced seismicity predicted from in-situ experiments. Scientific Reports 9, 4999. https://doi.org/10.1038/s41598-019-41306-x

De Barros, L., Daniel, G., Guglielmi, Y., Rivet, D., Caron, H., Payre, X., Bergery, G., Henry, P., Castilla, R., Dick, P., 2016. Fault structure, stress, or pressure control of the seismicity in shale? Insights from a controlled experiment of fluid-induced fault reactivation. Journal of Geophysical Research: Solid Earth 121, 4506–4522.

De Barros, L., Deschamps, A., Sladen, A., Lyon-Caen, H., Voulgaris, N., 2017. Investigating Dynamic Triggering of Seismicity by Regional Earthquakes: The Case of the Corinth Rift (Greece). Geophysical Research Letters 44, 10,921-10,929. https://doi.org/10.1002/2017GL075460

De Barros, L., Dietrich, M., 2008. Perturbations of the seismic reflectivity of a fluid-saturated depth-dependent poroelastic medium. The Journal of the Acoustical Society of America 123, 1409–1420. https://doi.org/10.1121/1.2835419

De Barros, L., Dietrich, M., Valette, B., 2010. Full waveform inversion of seismic waves reflected in a stratified porous medium. Geophys J Int 182, 1543–1556. https://doi.org/10.1111/j.1365-246X.2010.04696.x

De Barros, L., Dupuy, B., O'Brien, G., Virieux, J., Garambois, S., 2012a. Using a poroelastic theory to reconstruct subsurface properties: Numerical investigation, in: Seismic Waves: Research and Analysis. Intech, pp. 133–154.

De Barros, L., Guglielmi, Y., Rivet, D., Cappa, F., Duboeuf, L., 2018. Seismicity and fault aseismic deformation caused by fluid injection in decametric in-situ experiments. Comptes Rendus Geoscience, Invited contributions by 2016–2017 geoscience laureates of the French Academy of Sciences 350, 464–475. https://doi.org/10.1016/j.crte.2018.08.002

De Barros, L., Lokmer, I., Bean, C.J., 2013b. Origin of spurious single forces in the source mechanism of volcanic seismicity. Journal of Volcanology and Geothermal Research 262, 1–6.

De Barros, L., Lokmer, I., Bean, C.J., O'Brien, G.S., Saccorotti, G., Métaxian, J.-P., Zuccarello, L., Patanè, D., 2011. Source mechanism of long-period events recorded by a high-density seismic network during the 2008 eruption on Mount Etna. Journal of Geophysical Research: Solid Earth 116. https://doi.org/10.1029/2010JB007629

De Barros, L., Martini, F., Bean, C.J., Garcia-Yeguas, A., Ibáñez, J., 2012b. Imaging magma storage below Teide volcano (Tenerife) using scattered seismic wavefields. Geophys J Int 191, 695–706. https://doi.org/10.1111/j.1365-246X.2012.05637.x

De Barros, L., Pedersen, H.A., Métaxian, J.-P., Valdés-Gonzalez, C., Lesage, P., 2008. Crustal structure below Popocatépetl Volcano (Mexico) from analysis of Rayleigh waves. Journal of Volcanology and Geothermal Research, The 1994-Present eruption of Popocatépetl: Background, current activity, and impacts 170, 5–11. https://doi.org/10.1016/j.jvolgeores.2007.09.001

Deichmann, N., Giardini, D., 2009. Earthquakes induced by the stimulation of an enhanced geothermal system below Basel (Switzerland). Seismological Research Letters 80, 784–798.

Derode, B., Guglielmi, Y., De Barros, L., Cappa, F., 2015. Seismic responses to fluid pressure perturbations in a slipping fault. Geophysical Research Letters 42, 3197–3203.

Dieterich, J.H., 1992. Earthquake nucleation on faults with rate-and state-dependent strength. Tectonophysics 211, 115–134.

Dmitrieva, K., Hotovec-Ellis, A.J., Prejean, S., Dunham, E.M., 2013. Frictional-faulting model for harmonic tremor before Redoubt Volcano eruptions. Nature Geoscience 6, 652.

Duboeuf, L., 2018. Injections de fluide dans une zone de faille (LSBB, Rustrel): sismicité induite et déformation asismique.

Duboeuf, L., De Barros, L., Cappa, F., Guglielmi, Y., Deschamps, A., Seguy, S., 2017. Aseismic motions drive a sparse seismicity during fluid injections into a fractured zone in a carbonate reservoir. Journal of Geophysical Research: Solid Earth 122, 8285–8304.

Dupuy, B., De Barros, L., Garambois, S., Virieux, J., 2011. Wave propagation in heterogeneous porous media formulated in the frequency-space domain using a discontinuous Galerkin method. GEOPHYSICS 76, N13–N28. https://doi.org/10.1190/1.3581361

Duverger, C., Godano, M., Bernard, P., Lyon-Caen, H., Lambotte, S., 2015. The 2003–2004 seismic swarm in the western Corinth rift: Evidence for a multiscale pore pressure diffusion process along a permeable fault system. Geophysical Research Letters 42, 7374–7382.

Duverger, C., Lambotte, S., Bernard, P., Lyon-Caen, H., Deschamps, A., Nercessian, A., 2018. Dynamics of microseismicity and its relationship with the active structures in the western Corinth Rift (Greece). Geophysical Journal International 215, 196–221.

Eaton, D.W., Igonin, N., 2018. What controls the maximum magnitude of injection-induced earthquakes? The Leading Edge 37, 135–140.

Ellsworth, W.L., 2013. Injection-induced earthquakes. Science 341, 1225942.

Eyre, T.S., Bean, C.J., De Barros, L., Martini, F., Lokmer, I., Mora, M.M., Pacheco, J.F., Soto, G.J., 2015. A brittle failure model for long-period seismic events recorded at Turrialba Volcano, Costa Rica. Journal of Geophysical Research: Solid Earth 120, 1452–1472. https://doi.org/10.1002/2014JB011108

Eyre, T.S., Bean, C.J., De Barros, L., O'Brien, G.S., Martini, F., Lokmer, I., Mora, M.M., Pacheco, J.F., Soto, G.J., 2013. Moment tensor inversion for the source location and mechanism of long period (LP) seismic events from 2009 at Turrialba volcano, Costa Rica. Journal of Volcanology and Geothermal Research 258, 215–223. https://doi.org/10.1016/j.jvolgeores.2013.04.016

Eyre, T.S., Eaton, D.W., Garagash, D.I., Zecevic, M., Venieri, M., Weir, R., Lawton, D.C., 2019. The role of aseismic slip in hydraulic fracturing–induced seismicity. Science Advances 5, eaav7172. https://doi.org/10.1126/sciadv.aav7172

Faulkner, D.R., Mitchell, T.M., Healy, D., Heap, M.J., 2006. Slip on "weak" faults by the rotation of regional stress in the fracture damage zone. Nature 444, 922–925.

Frank, W.B., Rousset, B., Lasserre, C., Campillo, M., 2018. Revealing the cluster of slow transients behind a large slow slip event. Science Advances 4, eaat0661. https://doi.org/10.1126/sciadv.aat0661

Froment, B., Campillo, M., Chen, J.H., Liu, Q.Y., 2013. Deformation at depth associated with the 12 May 2008 Mw 7.9 Wenchuan earthquake from seismic ambient noise monitoring. Geophysical Research Letters 40, 78–82.

Galis, M., Ampuero, J.P., Mai, P.M., Cappa, F., 2017. Induced seismicity provides insight into why earthquake ruptures stop. Sci. Adv. 3, eaap7528. https://doi.org/10.1126/sciadv.aap7528

Garagash, D.I., Germanovich, L.N., 2012. Nucleation and arrest of dynamic slip on a pressurized fault. Journal of Geophysical Research: Solid Earth 117.

García-Yeguas, A., Koulakov, I., Ibáñez, J.M., Rietbrock, A., 2012. High resolution 3D P wave velocity structure beneath Tenerife Island (Canary Islands, Spain) based on tomographic inversion of active-source data. Journal of Geophysical Research: Solid Earth 117.
Ge, S., Liu, M., Lu, N., Godt, J.W., Luo, G., 2009. Did the Zipingpu reservoir trigger the 2008 Wenchuan earthquake? Geophysical Research Letters 36.
Goebel, T.H.W., Weingarten, M., Chen, X., Haffener, J., Brodsky, E.E., 2017. The 2016 Mw5. 1 Fairview, Oklahoma earthquakes: Evidence for long-range poroelastic triggering at> 40 km from fluid disposal wells. Earth and Planetary Science Letters 472, 50–61.
Gomberg, J., Wech, A., Creager, K., Obara, K., Agnew, D., 2016. Reconsidering earthquake scaling. Geophysical Research Letters 43, 6243–6251.
Grasso, J.-R., Karimov, A., Amorese, D., Sue, C., Voisin, C., 2018. Patterns of Reservoir-Triggered Seismicity in a Low-Seismicity Region of France. Bulletin of the Seismological Society of America 108, 2967–2982.
Grasso, J.R., Wittlinger, G., 1990. Ten years of seismic monitoring over a gas field. Bulletin of the Seismological Society of America 80, 450–473.
Grigoli, F., Cesca, S., Rinaldi, A.P., Manconi, A., López-Comino, J.A., Clinton, J.F., Westaway, R., Cauzzi, C., Dahm, T., Wiemer, S., 2018. The November 2017 Mw 5.5 Pohang earthquake: A possible case of induced seismicity in South Korea. Science 360, 1003–1006. https://doi.org/10.1126/science.aat2010
Guglielmi, Y., Birkholzer, J., Rutqvist, J., Jeanne, P., Nussbaum, C., 2017. Can Fault Leakage Occur Before or Without Reactivation? Results from an in Situ Fault Reactivation Experiment at Mont Terri. Energy Procedia, 13th International Conference on Greenhouse Gas Control Technologies, GHGT-13, 14-18 November 2016, Lausanne, Switzerland 114, 3167–3174. https://doi.org/10.1016/j.egypro.2017.03.1445
Guglielmi, Y., Cappa, F., Avouac, J.-P., Henry, P., Elsworth, D., 2015a. Seismicity triggered by fluid injection–induced aseismic slip. Science 348, 1224–1226. https://doi.org/10.1126/science.aab0476
Guglielmi, Y., Cappa, F., Lançon, H., Janowczyk, J.B., Rutqvist, J., Tsang, C.F., Wang, J.S.Y., 2014. ISRM Suggested Method for Step-Rate Injection Method for Fracture In-Situ Properties (SIMFIP): Using a 3-Components Borehole Deformation Sensor. Rock Mech Rock Eng 47, 303–311. https://doi.org/10.1007/s00603-013-0517-1
Guglielmi, Y., Elsworth, D., Cappa, F., Henry, P., Gout, C., Dick, P., Durand, J., 2015b. In situ observations on the coupling between hydraulic diffusivity and displacements during fault reactivation in shales. Journal of Geophysical Research: Solid Earth 120, 7729–7748. https://doi.org/10.1002/2015JB012158
Gupta, H.K., 2002. A review of recent studies of triggered earthquakes by artificial water reservoirs with special emphasis on earthquakes in Koyna, India. Earth-Science Reviews 58, 279–310.
Hainzl, S., Ogata, Y., 2005. Detecting fluid signals in seismicity data through statistical earthquake modeling. Journal of Geophysical Research: Solid Earth 110.
Healy, J.H., Rubey, W.W., Griggs, D.T., Raleigh, C.B., 1968. The denver earthquakes. Science 161, 1301–1310.
Helmstetter, A., Garambois, S., 2010. Seismic monitoring of Séchilienne rockslide (French Alps): Analysis of seismic signals and their correlation with rainfalls. Journal of Geophysical Research: Earth Surface 115.
Herrmann, M., Kraft, T., Tormann, T., Scarabello, L., Wiemer, S., 2019. A Consistent High-Resolution Catalog of Induced Seismicity in Basel Based on Matched Filter Detection and Tailored Post-Processing. Journal of Geophysical Research: Solid Earth 124, 8449–8477. https://doi.org/10.1029/2019JB017468
Hill, D.P., Prejean, S., 2015. Dynamic triggering 4, 273–304. https://doi.org/10.1016/B978-0-444-53802-4.00078-6
Hillers, G., Campillo, M., Ma, K.-F., 2014. Seismic velocity variations at TCDP are controlled by MJO driven precipitation pattern and high fluid discharge properties. Earth and Planetary Science Letters 391, 121–127.
Holzner, R., Eschle, P., Zürcher, H., Lambert, M., Graf, R., Dangel, S., Meier, P.F., 2005. Applying microtremor analysis to identify hydrocarbon reservoirs. First Break 23.
Hu, H., Li, A., Zavala-Torres, R., 2017. Long-period long-duration seismic events during hydraulic fracturing: Implications for tensile fracture development. Geophysical Research Letters 44, 4814–4819.
Huang, Y., De Barros, L., Cappa, F., 2019. Illuminating the rupturing of microseismic sources in an injection-induced earthquake experiment. Geophysical Research Letters.
Ibáñez, J.M., Rietbock, A., García-Yeguas, A., 2008. Imaging an active volcano edifice at Tenerife Island, Spain. Eos, Transactions American Geophysical Union 89, 289–290.
Ide, S., Beroza, G.C., Shelly, D.R., Uchide, T., 2007. A scaling law for slow earthquakes. Nature 447, 76.
Igarashi, T., Matsuzawa, T., Hasegawa, A., 2003. Repeating earthquakes and interplate aseismic slip in the northeastern Japan subduction zone. Journal of Geophysical Research: Solid Earth 108.
Jenatton, L., Guiguet, R., Thouvenot, F., Daix, N., 2007. The 16,000-event 2003–2004 earthquake swarm in Ubaye (French Alps). Journal of Geophysical Research: Solid Earth 112.
Jomard, H., Lebourg, T., Tric, E., 2007. Identification of the gravitational boundary in weathered gneiss by geophysical survey: La Clapière landslide (France). Journal of Applied Geophysics 62, 47–57.

Jousset, P., Reinsch, T., Ryberg, T., Blanck, H., Clarke, A., Aghayev, R., Hersir, G.P., Henninges, J., Weber, M., Krawczyk, C.M., 2018. Dynamic strain determination using fibre-optic cables allows imaging of seismological and structural features. Nature Communications 9, 1–11. https://doi.org/10.1038/s41467-018-04860-y

Keranen, K.M., Weingarten, M., Abers, G.A., Bekins, B.A., Ge, S., 2014. Sharp increase in central Oklahoma seismicity since 2008 induced by massive wastewater injection. Science 345, 448–451. https://doi.org/10.1126/science.1255802

Kumar, A., Zorn, E., Hammack, R., Harbert, W., 2017a. Long-period, long-duration seismicity observed during hydraulic fracturing of the Marcellus Shale in Greene County, Pennsylvania. The Leading Edge 36, 580–587.

Kumar, A., Zorn, E., Hammack, R., Harbert, W., 2017b. Long-period, long-duration seismicity observed during hydraulic fracturing of the Marcellus Shale in Greene County, Pennsylvania. The Leading Edge 36, 580–587.

Leclère, H., Daniel, G., Fabbri, O., Cappa, F., Thouvenot, F., 2013. Tracking fluid pressure buildup from focal mechanisms during the 2003–2004 Ubaye seismic swarm, France. Journal of Geophysical Research: Solid Earth 118, 4461–4476.

Lees, J.M., 2007. Seismic tomography of magmatic systems. Journal of Volcanology and Geothermal Research 167, 37–56.

Lengliné, O., Lamourette, L., Vivin, L., Cuenot, N., Schmittbuhl, J., 2014. Fluid-induced earthquakes with variable stress drop. Journal of Geophysical Research: Solid Earth 119, 8900–8913.

Linde, A.T., Gladwin, M.T., Johnston, M.J., Gwyther, R.L., Bilham, R.G., 1996. A slow earthquake sequence on the San Andreas fault. Nature 383, 65.

Lindsey, N.J., Martin, E.R., Dreger, D.S., Freifeld, B., Cole, S., James, S.R., Biondi, B.L., Ajo-Franklin, J.B., 2017. Fiber-optic network observations of earthquake wavefields. Geophysical Research Letters 44, 11,792-11,799.

Liu, Y., Rice, J.R., 2007. Spontaneous and triggered aseismic deformation transients in a subduction fault model. Journal of Geophysical Research: Solid Earth 112.

Lohman, R.B., McGuire, J.J., 2007. Earthquake swarms driven by aseismic creep in the Salton Trough, California. Journal of Geophysical Research: Solid Earth 112.

Marsan, D., Lengliné, O., 2008. Extending Earthquakes' Reach Through Cascading. Science 319, 1076–1079. https://doi.org/10.1126/science.1148783

Martí, J., Geyer, A., Andujar, J., Teixidó, F., Costa, F., 2008. Assessing the potential for future explosive activity from Teide–Pico Viejo stratovolcanoes (Tenerife, Canary Islands). Journal of Volcanology and Geothermal Research 178, 529–542.

Martini, F., Lokmer, I., Jonsdottir, K., De Barros, L., Möllhoff, M., Bean, C.J., Hauser, F., Doherty, J., Ryan, C., Mongan, J., 2013. A passive low-frequency seismic experiment in the Albertine Graben, Uganda. Geophysical Prospecting 61, 39–61.

McClure, M.W., Horne, R.N., 2014. Correlations between formation properties and induced seismicity during high pressure injection into granitic rock. Engineering geology 175, 74–80.

McGarr, A., 1976. Seismic moments and volume changes. Journal of geophysical research 81, 1487–1494.

McGarr, A., Barbour, A.J., 2018. Injection-induced moment release can also be aseismic. Geophysical Research Letters 45, 5344–5351.

McNutt, S.R., 2005. Volcanic seismology. Annu. Rev. Earth Planet. Sci. 32, 461–491.

Michael, A.J., 1987. Use of focal mechanisms to determine stress: A control study. Journal of Geophysical Research: Solid Earth 92, 357–368. https://doi.org/10.1029/JB092iB01p00357

Miller, S.A., Collettini, C., Chiaraluce, L., Cocco, M., Barchi, M., Kaus, B.J.P., 2004. Aftershocks driven by a high-pressure CO 2 source at depth. Nature 427, 724–727. https://doi.org/10.1038/nature02251

Nadeau, R.M., McEvilly, T.V., 1999. Fault slip rates at depth from recurrence intervals of repeating microearthquakes. Science 285, 718–721.

Nur, A., Booker, J.R., 1972. Aftershocks caused by pore fluid flow? Science 175, 885–887.

Nussbaum, C., Guglielmi, Y., De Barros, L., Birkholzer, J., 2017. Imaging the Long-term Loss of Faulted Caprock Integrity-In-situ Experiments in the Mont Terri Rock Laboratory, Switzerland, in: EAGE/SEG Research Workshop 2017.

Obara, K., Hirose, H., Yamamizu, F., Kasahara, K., 2004. Episodic slow slip events accompanied by non-volcanic tremors in southwest Japan subduction zone. Geophysical Research Letters 31.

O'Brien, G.S., Lokmer, I., De Barros, L., Bean, C.J., Saccorotti, G., Metaxian, J.-P., Patane, D., 2011. Time reverse location of seismic long-period events recorded on Mt Etna. Geophys J Int 184, 452–462. https://doi.org/10.1111/j.1365-246X.2010.04851.x

Pacchiani, F., Lyon-Caen, H., 2010. Geometry and spatio-temporal evolution of the 2001 Agios Ioanis earthquake swarm (Corinth Rift, Greece). Geophysical Journal International 180, 59–72.

Parotidis, M., Rothert, E., Shapiro, S.A., 2003. Pore-pressure diffusion: A possible triggering mechanism for the earthquake swarms 2000 in Vogtland/NW-Bohemia, central Europe. Geophysical Research Letters 30. https://doi.org/10.1029/2003GL018110

Payre, X., Maisons, C., Marblé, A., Thibeau, S., 2014. Analysis of the Passive Seismic Monitoring Performance at the Rousse CO2 Storage Demonstration Pilot. Energy Procedia, 12th International Conference on Greenhouse Gas Control Technologies, GHGT-12 63, 4339–4357. https://doi.org/10.1016/j.egypro.2014.11.469

Pei, S., Peng, Z., Chen, X., 2018. Locations of injection-induced earthquakes in Oklahoma controlled by crustal structures. Journal of Geophysical Research: Solid Earth 123, 2332–2344.
Peng, Z., Gomberg, J., 2010. An integrated perspective of the continuum between earthquakes and slow-slip phenomena. Nature geoscience 3, 599.
Perfettini, H., Avouac, J.-P., Tavera, H., Kositsky, A., Nocquet, J.-M., Bondoux, F., Chlieh, M., Sladen, A., Audin, L., Farber, D.L., 2010. Seismic and aseismic slip on the Central Peru megathrust. Nature 465, 78.
Perfettini, H., Frank, W.B., Marsan, D., Bouchon, M., 2018. A model of aftershock migration driven by afterslip. Geophysical Research Letters 45, 2283–2293.
Pride, S.R., Berryman, J.G., Harris, J.M., 2004. Seismic attenuation due to wave-induced flow. Journal of Geophysical Research: Solid Earth 109.
Provost, F., Malet, J.-P., Hibert, C., Abanco Martínez de Arenzana, C., Hurlimann Ziegler, M., 2018. Towards a standard typology of endogenous landslide seismic sources. Earth surface dynamics 6, 1059–1088.
Rivet, D., Campillo, M., Shapiro, N.M., Cruz-Atienza, V., Radiguet, M., Cotte, N., Kostoglodov, V., 2011. Seismic evidence of nonlinear crustal deformation during a large slow slip event in Mexico. Geophysical Research Letters 38.
Rivet, D., De Barros, L., Guglielmi, Y., Cappa, F., Castilla, R., Henry, P., 2016. Seismic velocity changes associated with aseismic deformations of a fault stimulated by fluid injection. Geophysical Research Letters 43, 9563–9572. https://doi.org/10.1002/2016GL070410
Rolandone, F., Nocquet, J.-M., Mothes, P.A., Jarrin, P., Vallée, M., Cubas, N., Hernandez, S., Plain, M., Vaca, S., Font, Y., 2018. Areas prone to slow slip events impede earthquake rupture propagation and promote afterslip. Science advances 4, eaao6596.
Schmittbuhl, J., Lengliné, O., Cornet, F., Cuenot, N., Genter, A., 2014. Induced seismicity in EGS reservoir: the creep route. Geothermal Energy 2, 14. https://doi.org/10.1186/s40517-014-0014-0
Schoenball, M., Ajo-Franklin, J., Blankenship, D., Cook, P., Dobson, P., Guglielmi, Y., Fu, P., Kneafsey, T., Knox, H., Petrov, P., 2019. Microseismic monitoring of meso-scale stimulations for the DOE EGS Collab project at the Sanford Underground Research Facility, in: Proceedings: 44th Workshop on Geothermal Reservoir Engineering, Stanford University, Stanford, CA.
Schoenball, M., Davatzes, N.C., Glen, J.M., 2015. Differentiating induced and natural seismicity using space-time-magnitude statistics applied to the Coso Geothermal field. Geophysical Research Letters 42, 6221–6228.
Schubnel, A., Thompson, B.D., Fortin, J., Guéguen, Y., Young, R.P., 2007. Fluid-induced rupture experiment on Fontainebleau sandstone: Premonitory activity, rupture propagation, and aftershocks. Geophysical research letters 34.
Schultz, R., Atkinson, G., Eaton, D.W., Gu, Y.J., Kao, H., 2018. Hydraulic fracturing volume is associated with induced earthquake productivity in the Duvernay play. Science 359, 304–308. https://doi.org/10.1126/science.aao0159
Schwartz, S.Y., Rokosky, J.M., 2007. Slow slip events and seismic tremor at circum-Pacific subduction zones. Reviews of Geophysics 45.
Scotti, O., Cornet, F.H., 1994. In situ evidence for fluid-induced aseismic slip events along fault zones, in: International Journal of Rock Mechanics and Mining Sciences & Geomechanics Abstracts. Elsevier, pp. 347–358.
Scuderi, M.M., Collettini, C., 2016. The role of fluid pressure in induced vs. triggered seismicity: insights from rock deformation experiments on carbonates, in: Scientific Reports. https://doi.org/10.1038/srep24852
Segall, P., Rubin, A.M., Bradley, A.M., Rice, J.R., 2010. Dilatant strengthening as a mechanism for slow slip events. Journal of Geophysical Research: Solid Earth 115. https://doi.org/10.1029/2010JB007449
Shapiro, N.M., Campillo, M., Kaminski, E., Vilotte, J.-P., Jaupart, C., 2018. Low-Frequency Earthquakes and Pore Pressure Transients in Subduction Zones. Geophysical Research Letters 45, 11,083-11,094.
Shapiro, S.A., Huenges, E., Borm, G., 1997a. Estimating the crust permeability from fluid-injection-induced seismic emission at the KTB site. Geophysical Journal International 131, F15–F18.
Shapiro, S.A., Huenges, E., Borm, G., 1997b. Estimating the crust permeability from fluid-injection-induced seismic emission at the KTB site. Geophysical Journal International 131, F15–F18.
Shelly, D.R., Beroza, G.C., Ide, S., 2007. Non-volcanic tremor and low-frequency earthquake swarms. Nature 446, 305.
Sibson, R.H., 1990. Conditions for fault-valve behaviour. Geological Society, London, Special Publications 54, 15–28. https://doi.org/10.1144/GSL.SP.1990.054.01.02
Sibson, R.H., 1985. A note on fault reactivation. Journal of Structural Geology 7, 751–754.
Singh, S.C., Crawford, W.C., Carton, H., Seher, T., Combier, V., Cannat, M., Canales, J.P., Düsünür, D., Escartin, J., Miranda, J.M., 2006. Discovery of a magma chamber and faults beneath a Mid-Atlantic Ridge hydrothermal field. Nature 442, 1029.
Sintubin, M., 2018. The Groningen Case: When Science Becomes Part of the Problem, Not the Solution. Seismological Research Letters 89, 2001–2007. https://doi.org/10.1785/0220180203
Sladen, A., Rivet, D., Ampuero, J.-P., De Barros, L., Hello, Y., Calbris, G., Lamare, P., 2019. Distributed sensing of earthquakes and ocean-solid Earth interactions on seafloor telecom cables. Nature Communications 10, 1–8.

Snee, J.-E.L., Zoback, M.D., 2016. State of stress in Texas: Implications for induced seismicity. Geophysical Research Letters 43, 10,208-10,214.
Stearns, H.T., 1925. The explosive phase of Kilauea Volcano, Hawaii, in 1924. Bulletin volcanologique 2, 193–208.
Stein, R.S., 1999. The role of stress transfer in earthquake occurrence. Nature 402, 605.
Steiner, B., Saenger, E.H., Schmalholz, S.M., 2008. Time reverse modeling of low-frequency microtremors: Application to hydrocarbon reservoir localization. Geophysical Research Letters 35.
Taisne, B., Brenguier, F., Shapiro, N.M., Ferrazzini, V., 2011. Imaging the dynamics of magma propagation using radiated seismic intensity. Geophysical Research Letters 38. https://doi.org/10.1029/2010GL046068
Tarantola, A., 2005. Inverse problem theory and methods for model parameter estimation. siam.
Tary, J.-B., Van der Baan, M., Eaton, D.W., 2014. Interpretation of resonance frequencies recorded during hydraulic fracturing treatments. Journal of Geophysical Research: Solid Earth 119, 1295–1315.
Terakawa, T., Zoporowski, A., Galvan, B., Miller, S.A., 2010. High-pressure fluid at hypocentral depths in the L'Aquila region inferred from earthquake focal mechanisms. Geology 38, 995–998.
Thouvenot, F., Jenatton, L., Scafidi, D., Turino, C., Potin, B., Ferretti, G., 2016. Encore ubaye: earthquake swarms, foreshocks, and aftershocks in the Southern French Alps. Bulletin of the Seismological Society of America 106, 2244–2257.
Tokarev, P.I., 1963. On a possibility of forecasting of Bezymianny volcano eruptions according to seismic data. Bulletin of volcanology 26, 379–386.
Traversa, P., Grasso, J.-R., 2010. How is Volcano Seismicity Different from Tectonic Seismicity?How is Volcano Seismicity Different from Tectonic Seismicity? Bulletin of the Seismological Society of America 100, 1755–1769. https://doi.org/10.1785/0120090214
Uchida, N., Bürgmann, R., 2019. Repeating earthquakes. Annual Review of Earth and Planetary Sciences 47, 305–332.
Utsu, T., Ogata, Y., 1995. The centenary of the Omori formula for a decay law of aftershock activity. Journal of Physics of the Earth 43, 1–33.
Vallée, M., Nocquet, J.-M., Battaglia, J., Font, Y., Segovia, M., Regnier, M., Mothes, P., Jarrin, P., Cisneros, D., Vaca, S., 2013. Intense interface seismicity triggered by a shallow slow slip event in the Central Ecuador subduction zone. Journal of Geophysical Research: Solid Earth 118, 2965–2981.
Van der Elst, N.J., Page, M.T., Weiser, D.A., Goebel, T.H., Hosseini, S.M., 2016. Induced earthquake magnitudes are as large as (statistically) expected. Journal of Geophysical Research: Solid Earth 121, 4575–4590.
van Thienen-Visser, K., Breunese, J.N., 2015. Induced seismicity of the Groningen gas field: History and recent developments. The Leading Edge 34, 664–671.
Verdon, J.P., Stork, A.L., 2016. Carbon capture and storage, geomechanics and induced seismic activity. Journal of Rock Mechanics and Geotechnical Engineering 8, 928–935. https://doi.org/10.1016/j.jrmge.2016.06.004
Wei, S., Avouac, J.-P., Hudnut, K.W., Donnellan, A., Parker, J.W., Graves, R.W., Helmberger, D., Fielding, E., Liu, Z., Cappa, F., 2015. The 2012 Brawley swarm triggered by injection-induced aseismic slip. Earth and Planetary Science Letters 422, 115–125.
White, R.A., Miller, A.D., Lynch, L., Power, J., 1998. Observations of hybrid seismic events at Soufriere Hills volcano, Montserrat: July 1995 to September 1996. Geophysical Research Letters 25, 3657–3660.
Wynants-Morel, N., Cappa, F., De Barros, L., Ampuero, J.P., submitted. Stress Perturbation From Aseismic Slip drives The Seismic Front During Fluid Injection In A Permeable Fault. Journal of Geophysical Research: Solid Earth submitted.
Zang, A., Oye, V., Jousset, P., Deichmann, N., Gritto, R., McGarr, A., Majer, E., Bruhn, D., 2014. Analysis of induced seismicity in geothermal reservoirs – An overview. Geothermics, Analysis of Induced Seismicity in Geothermal Operations 52, 6–21. https://doi.org/10.1016/j.geothermics.2014.06.005
Zecevic, M., Daniel, G., Jurick, D., 2016a. On the nature of long-period long-duration seismic events detected during hydraulic fracturingOn the nature of LPLD events. Geophysics 81, KS113–KS121.
Zecevic, M., De Barros, L., Bean, C.J., O'Brien, G.S., Brenguier, F., 2013. Investigating the source characteristics of long-period (LP) seismic events recorded on Piton de la Fournaise volcano, La Réunion. Journal of Volcanology and Geothermal Research 258, 1–11. https://doi.org/10.1016/j.jvolgeores.2013.04.009
Zecevic, M., De Barros, L., Eyre, T.S., Lokmer, I., Bean, C.J., 2016b. Relocation of long-period (LP) seismic events reveals en echelon fractures in the upper edifice of Turrialba volcano, Costa Rica. Geophysical Research Letters 43, 10,105-10,114. https://doi.org/10.1002/2016GL070427
Zhao, D., Kanamori, H., Negishi, H., Wiens, D., 1996. Tomography of the source area of the 1995 Kobe earthquake: evidence for fluids at the hypocenter? Science 274, 1891–1894.
Zuccarello, L., Burton, M.R., Saccorotti, G., Bean, C.J., Patanè, D., 2013. The coupling between very long period seismic events, volcanic tremor, and degassing rates at Mount Etna volcano. Journal of Geophysical Research: Solid Earth 118, 4910–4921.

ANNEXES

A1. Curriculum Vitae

DE BARROS Louis

Pacsé, 2 enfants
38 ans, né le 26/09/1981
Nationalité française

Géoazur, Université Cote d'Azur
Campus Azur, 250 rue A. Einstein, Les Lucioles 1
06560 Sophia Antipolis
+33 483618622
louis.debarros@geoazur.unice.fr

1) Expériences et formations

2012- **Maitre de conférences**, Géoazur (UMR 7329), Université Nice Sophia Antipolis

2008-2012 **Post-doctorat,** University College Dublin, Ireland

2007-2008 Attaché Temporaire Enseignement Recherche (**ATER**), Polytech' Grenoble, Université J. Fourier, Grenoble

2004-2007 **Doctorat** en géophysique : "Sensibilité et inversion des formes d'ondes sismiques en milieu poreux stratifié", LGIT - école Doctorale Terre-Univers-Environnement, Université J. Fourier, Grenoble

2004 **Master** recherche Terre-Univers-Environnement, mention Bien, U. J. Fourier, Grenoble

2004 **Diplôme d'ingénieur**, spécialité géotechnique, mention Bien, Polytech' Grenoble, U. J. Fourier

2) Activité d'enseignement

- **Résumé des activités d'enseignements**
  - Maître de conférences (Université Nice Sophia Antipolis) : 148h et 161h eq. TD en 2012-2013 et 2013-2014, puis ~200h eq. TD depuis
  - Enseignements en écoles d'été (5h : inverse problems in volcanology, Dublin, 2012) et école doctorale (mathematics for geoscientists, 2x15h, 2011-2012)
  - 1/2 ATER (Univ. J. Fourier, Grenoble ; 2007-2008) : 92h
  - Vacations (Univ. J. Fourier, Grenoble ; 2004-2007) :118h
- **Synthèse des enseignements effectués**

	Niveau	Hrs eq. TD	Année
Sismologie	L3	55 (x6)	2013-2020
Mécanique des sols	M1	40 (x5)	2014-2020
Géotechnique	M2	22 (x5)	2013-2019
Géological debate	L3	12 (x5)	2012-2017

Projet Professionnel et de recherche	M1	12(x2)	2018-2020
Géophysique appliquée	M1	36(x5)	2014-2019
Géophysique appliquée	L3	16(x5)	2013-2019
Rhéologie	L2/L3	24(x2)	2012-2013
Physique de la terre	L1	40	2012
Méthodes numériques	M1	24	2012
Mathematics for geoscientists	PhD	15(x2)	2011-2012
Mécanique des sols	L3	70	2005-2008
Notion de Géologie	L1	24(x2)	2005-2006

3) Encadrement doctoral et scientifique

- **Post-doctorat :**
  - **D. Rivet** (06/2014-09/2016 : financement Total puis UNS) sur les mesures des variations de vitesses sismiques associées à la réactivation artificielle de failles par injection d'eau haute pression.
- **Thèses :**

  Co-direction :
  - **M. Baques** (12/2019- financement IRSN-CEA, encadrement avec F. Courboulex) : Evolution spatio-temporelle de la sismicité de la zone Ubaye/Haute-Durance : apports pour la compréhension de la dynamique et de l'évolution des essaims de sismicité en domaine de faible déformation.
  - **N. Wynants** (09/2016-, MESR, encadrement à 50% avec F. Cappa -Pr UNS) : modélisation couplée de la réponse sismo-hydro-mécanique de zones de failles par modélisation numérique (1 article accepté)
  - **L. Duboeuf** (01/2015-02/2018, MESR, encadrement à 80 % avec A. Deschamps DR, UNS), sur l'analyse de la sismicité induite lors de la réactivation artificielle d'une zone de faille par injection d'eau haute pression (LSBB, Rustrel, 84), (3 articles)
  - **M. Zecevic** (09/2009-12/2013, ITN Quest), encadrement à 50 % avec C. Bean (UCD Dublin) sur "Long Period Seismic Events: Investigating Their Source Characteristics at Volcanoes and During Hydraulic Fracturing", (3 articles).
  - **T. Eyre** (09/2009-12/2013, UCD Dublin), encadré à 20 % avec C. Bean (UCD Dublin), sur "Investigating the source of long period seismicity at Turrialba volcano, Costa Rica". (3 articles).

Encadrement :

- **C. Chalumeau** (09/2018- ; P. Charvis) : Répliques du séisme de Pedernales (2016, Equateur)
- **B. Derode** (01/2010-07/2013 ; F. Cappa, Y. Guglielmi) : Réponse hydro-mécanique et sismique d'une zone de failles à une surpression fluide ;
- **R. Davy** (2007-2010, C. Bean) : mécanismes des sources des trémors harmoniques de l'Arenal
- **B. Dupuy** (09/2008-11/2011, J. Virieux et S. Garambois) : Modélisation numérique des ondes sismiques en milieux poreux (1 article).

- **Master**
  - **P. Danre** (M2 : 01-06/2020), avec F. Cappa : distribution spatio-temporelle des essaims sismiques et de la sismicité induite
  - **M. Baques** (M2 : 01-06/2018), avec M. Godano : répliques du séisme de Barcelonnette du 7/4/2014 (1 article)
  - **M. Hoch** (M1 : 04-06/2017), avec J. Trévisan : relation sismicité et barrages dans les Alpes du sud.
  - **L. Cordrie** (M1 : 06-07/2016), avec A. Deschamps : essaim sismique de Corinthe en 2015. (1 article en prép)
  - **M. Loiselet** (M1: 04-06/2016): imagerie sismique de zones de failles
  - **C. Caulet** (M1 : 05-08/2014 et L3 : 05-08/2013), avec I. Manighetti : segmentation des failles de l'Afar (1 article).
  - **B. Dupuy** (M2 : 03-08/2008), avec J. Virieux : Modélisation numérique des ondes sismiques en milieux poreux (1 article).
- **12 encadrements de stage de licence depuis 2013**

4) Publications scientifiques

- **Publications scientifiques** : 33 articles de rang A, 15 articles autres (résumés étendus avec peer-review, chapitres d'ouvrage); citations : 655, h-index: 15 (01/03/2020)
- **Conférences :** 85 communications dans des conférences internationales
- **Reviews** de plus de 40 articles pour Geophysical Research Letters, Journal of Geophysical Research, Geophysical Journal International, Journal of volcanology and geothermal research, Geophysics…

5) Distinctions

- **Grand prix Gouilloud-Schlumberger de l'Académie des Sciences**, 2017 (www.academie-sciences.fr/fr/Laureats/laureat-2017-du-prix-michel-gouilloud-schlumberger-louis-de-

barros.html).

- Médaille de l'Université de la Côte d'Azur (2018)
- Prime d'Encadrement Doctoral et de Recherche (**PEDR**) : 2016-2020

6) Projets scientifiques

- **Projet « Fluides et Failles »**
  - 2012-2017, financement Total (budget : 1.8 M€), PI R. Castilla & P. Henry,
  - Responsable du WP4 « Surveillance sismique », budget 550k€.

L'objectif de ce projet est la compréhension de la réponse des failles argileuses à une perturbation de pression de fluide. Des injections d'eau à haute pression ont été faites entre décembre 2013 et juin 2014 pour réactiver différentes zones d'une faille traversant les argilitites de la plate-forme expérimentale de Tournemire (IRSN, 12). L'instrumentation de surveillance comprenait 24 capteurs sismiques, pour 1) analyser la micro-sismicité induite et 2) suivre les variations des vitesses sismiques associées au mouvement de faille. Cette analyse se fait en collaboration avec la société Magnitude (84) et avec des hydro-mécaniciens (CEREGE Marseille, 3SR Grenoble, ENS Paris). Le travail de Post-doctorat de D. Rivet (2014-2015) a été financé sur ce projet.

- **ANR JCJC HYDROSEIS** *(https://projets.oca.eu/en/hydroseis-home)***:**
  - 2014-2019, financement ANR JCJC (budget 310 k€), PI F. Cappa
  - Responsable du WP2 « expérience et analyse des données », budget 160k€.

Les expériences de mise sous-pression d'un massif fracturé calcaire fracturé (LSBB, Rustrel) ont été réalisées entre février et avril 2015, avec une instrumentation de surveillance dense (pression, déformation, sismicité). L'analyse des données hydromécaniques et sismologiques est actuellement en cours, et devra permettre un changement d'échelle vers les zones sismogènes. Pour le bon déroulement de ce projet, j'ai obtenu des bourses de thèse (L. Duboeuf et N. Wynants financement MESR) et un an de post-doctorat (D. Rivet, 2016-2017, financement UNS).

- **Projet « FS » & « FS-B »:**
  - 2018-2022, Partenariat public (Swisstopo, IRSN…) – privé (Total, ANDRA,…), PI Y. Guglielmi, budget 1.5 M€,
  - Analyse et de la surveillance sismologique

Le projet « FS » a testé la réponse hydro-mécanique d'une faille en milieu argileux, dans le site expérimental du Mont Terri. Cette expérience préliminaire a donné des résultats importants sur le comportement hydro-mécanique des couvertures argileuses des réservoirs. Une seconde phase est en préparation (financement acquis pour la partie expérimentale, consortium d'entreprises (TOTAL, Andra, Chevron,…) et de partenaires publics (Swisstopo, Nagra…), pour des injections plus longues (6 mois), en utilisant différents fluides (eau, CO2), avec une densité beaucoup plus forte de capteurs. Je suis en charge de l'acquisition et du traitement des données sismologiques, pour permettre ensuite une interprétation conjointe avec les autres données.

- **Projets UBAYE :** 2019-2022, financement IRSN-CEA, PI L. De Barros et F. Courboulex, budget 165 k€

L'objectif de ce projet est de comprendre pourquoi cette zone des Alpes du sud a un taux anormalement fort de séismes, avec des alternances chocs principaux et essaims sismiques. En particulier, l'accent sera mis sur la caractérisation des processus et des forçages de la sismicité, en étudiant en détail les répliques du séismes du 07/04/2014 pour extrapoler et comparer les résultats à une plus grande échelle temporelle et à d'autres zones similaires. Ce projet finance la thèse de M. Baques (2019-).

- **Autres projets (participant, depuis 2012) :**
  - SEAFOOD (ANR & IDEX UCA^{JEDI}, PI A. Sladen) : développement et analyse de systèmes de mesures de déformation statique et sismologique par fibre optique.
  - LMI SVAN - Séismes et Volcans (IRD): Analyse des répliques du séismes de Pedernales (2016, Equateur) et de la sismicité sous Quito.
  - HPMS-Ca (Total, PI Y. Guglielmi, 2015-2017) : caractérisation multi-échelle, hydro-mécanique et géophysique, des carbonates du LSBB (Rustrel, 84)
  - REAKT (FP7, PI WP2 P. Bernard, 2011-2014) : sismicité du golfe de Corinthe ;
  - EPOST (ANR JC, PI M. Vergnole, 2015-2019) : Signature sismique à très court terme après les séismes ;

7) Autres activités et responsabilités

- **Responsabilités administratives**
  - Comité de sélection, Poste de Maitre de conférences, Université Côte d'Azur, 2019
  - Membre élu au Conseil Académique (CAC) de l'Université Côte d'Azur (2015-2019)
  - Membre élu au CPRH, section 35-36, Université Nice Sophia Antipolis (2015-)
  - Membre nommé au conseil de laboratoire de Géoazur (2015-2018)
- **Responsabilités pédagogiques**
  - Co-responsable du master STPE (2018-) (masterste.wixsite.com/accueil), Université Côte d'Azur
  - Co-responsable de la 3eme année de Licence Sciences de la Terre (2014-2018), Université Nice Sophia Antipolis
  - Membre du conseil pédagogique (2014-), département Sciences de la Terre, Université Nice Sophia Antipolis
  - Participation à la définition et à la mise en place des maquettes de master (2014 et 2017).

A2. Liste complète de publications

- **Publications (article de rang A)**

33. De Barros, L., F. Cappa, A. Deschamps, P. Dublanchet, 2020. Imbricated Aseismic Slip And Fluid Diffusion Drive A Seismic Swarm In The Corinth Gulf, Greece, *Geophysical Research Letters*, (revised)
32. Wynants-Morel, N., F. Cappa, L. De Barros, J.-P. Ampuero, 2020. Stress Perturbation From Aseismic Slip drives The Seismic Front During Fluid Injection In A Permeable Fault, *Journal of Geophysical Research: Solid Earth* (revised).
31. Petit C., L. De Barros, G. Duclaux, Y. Mazabraud, 2019. Why are there no earthquakes in the intracratonic Paris basin?, *Geosciences*, 9(12), 502
30. Sladen A., D. Rivet, J.P Ampuero, L. De Barros, Y. Hello, G. Calbris, P. Lamare, 2019. Distributed sensing of earthquakes and ocean-solid Earth interactions on seafloor telecom cables, *Nature Communication*, 10(1), 1-8
29. Huang Y., L. De Barros, F. Cappa, 2019. Illuminating the rupturing of microseismic sources in an injection-induced earthquake experiment, *Geophysical Research Letters*, doi: 10.1029/2019GL083856
28. Agurto-Detzel, H., Font, Y., Charvis, P., Régnier, M., Rietbrock, A., Ambrois, D., Paulatto, Alvarado A., Beck S., Courboulex, F., De Barros, L. et al. (2019). Ridge subduction and afterslip control aftershock distribution of the 2016 Mw 7.8 Ecuador earthquake. *Earth and Planetary Science Letters*, 520, 63-76.
27. De Barros, L., M. Baques+, M. Godano, A. Helmstteter, A. Deschamps, C. Larroque, F. Courboulex (2019) Fluid-Induced Swarms and Coseismic Stress Transfer: a Dual Process Highlighted in the Aftershock Sequence of the 7 April 2014 Earthquake (Ml 4.8, Ubaye, France), *Journal of Geophysical Research: Solid Earth*, doi:2018JB017226
26. De Barros, L., F. Cappa, Y. Guglielmi, L. Duboeuf+, J.-R. Grasso (2019) Energy of injection-induced seismicity predicted from in-situ experiments, *Scientific Reports*, 10.1038/s41598-019-41306-x
25. De Barros, L., Guglielmi, Y., Rivet, D., Cappa, F., & Duboeuf, L. (2018). Seismicity and fault aseismic deformation caused by fluid injection in decametric in-situ experiments. *Comptes Rendus Geoscience*, 350(8), 464-475 (invited)
24. Duboeuf+, L., De Barros, L., Cappa, F., Guglielmi, Y., Deschamps, A., & Seguy, S. (2017). Aseismic motions drive a sparse seismicity during fluid injections into a fractured zone in a carbonate reservoir. *Journal of Geophysical Research: Solid Earth*, 122(10), 8285-8304.
23. De Barros, L., Deschamps, A., Sladen, A., Lyon-Caen, H., & Voulgaris, N. (2017). Investigating dynamic triggering of seismicity by regional earthquakes: the case of the Corinth Rift (Greece). *Geophysical Research Letters*, 44(21).
22. Bletery, Q., A. M. Thomas, A. W. Rempel, L. Karlstrom, A. Sladen and L. De Barros (2016). Mega-earthquakes rupture flat megathrusts. *Science*, 354, pp 1027-1031
21. Rivet D., De Barros L., Guglielmi Y., Cappa F., Castilla R., Henry P.,(2016) Seismic velocity changes associated with aseismic deformations of a fault stimulated by fluid injection, *Geophysical Research Letters*, 43(18), 9563-9572.
20. Zecevic+ M., De Barros L., Eyre+ T. S., Lokmer I., Bean C. (2016) Relocation of Long Period (LP) seismic events reveals en echelon fractures in the upper edifice of Turrialba volcano, Costa Rica, *Geophysical Research Letters*, vol.43 (19), pp.10,105-10,114.
19. De Barros, L., G Daniel, Y Guglielmi, D Rivet, H Caron, X Payre, et al. (2016), Fault structure, stress, or pressure control of the seismicity in shale? Insights from a controlled experiment of fluid-induced fault reactivation, *J. Geophys. Res. Solid Earth*, 121, 4506–4522, doi:*10.1002/2015JB012633*.
18. Derode**+**, B., Guglielmi, Y., De Barros, L., & Cappa, F. (2015). Seismic responses to fluid pressure perturbations in a slipping fault. *Geophysical Research Letters*, *42*(9), 3197-3203.
17. Manighetti, I., Caulet+, C., De Barros, L., Perrin, C., Cappa, F., & Gaudemer, Y. (2015). Generic along-strike segmentation of Afar normal faults, East Africa: Implications on fault growth and stress heterogeneity on seismogenic fault planes. *Geochemistry, Geophysics, Geosystems*, *16*(2), 443-467.
16. Bean C. J., De Barros L., Lokmer I., Métaxian J.-P., O'Brien G., Murphy S., 2014, Long-period seismicity in the shallow volcanic edifice formed from slow-rupture earthquakes, Nature Geoscience, vol.7, pp.71-75, 2014

15. Eyre+ T.S., C. J. Bean, L. De Barros, F. Martini, I. Lokmer, M. M. Mora, J. F. Pacheco, G. J. Soto. A brittle failure model for long-period seismic events recorded at Turrialba volcano, Costa Rica, *Journal of Geophysical Research: Solid Earth*, *120*(3), 1452-1472.

14. De Barros L., Bean C. J., Zecevic+ M., Brenguier F., Peltier A. 2013. Eruptive fracture location forecasts from high-frequency events on Piton de la Fournaise Volcano, Geophysical Research Letters, vol.40, pp.1-5.

13. De Barros L., Lokmer I., Bean C. J., Origin of spurious single forces in the source mechanism of volcanic seismicity, Journal of Volcanology and Geothermal Research, vol.262, pp.1-6, 2013.

12. Eyre+, T.S., C.J. Bean, L. De Barros, G.S. O'Brien, F.Martini, I.Lokmer, M.M. Mora, J.F. Pacheco, G.J. Soto, 2013, Moment tensor inversion for the source location and mechanism of long period (LP) seismic events from 2009 at Turrialba volcano, Costa Rica, J. Volc. Geotherm. Res.,In press, doi :10.1016/j.jvolgeores.2013.04.016.

11. Zecevic+, M., L. De Barros, C. J. Bean, G. S. O'Brien, F., Brenguier, 2013, Investigating the source characteristics of long-period (LP) seismic events recorded on Piton de la Fournaise volcano, La Réunion. J. Volc. Geotherm. Res., Vol. 258, pp 1–11, Doi :10.1016/j.jvolgeores.2013.04.009

10. De Barros, L., F. Martini, C.J. Bean , A. Garcia-Yeguas , J. Ibanez. Magma storage below Teide volcano (Tenerife): evidence by scattered wavefields, Geophys. J. Int., 191 (2): 695-706, doi: 10.1111/j.1365-246X.2012.05637.x

9. Martini, F., Lokmer, I., Jonsdottir, K., De Barros, L., Möllhoff, M., Bean, C. J., Hauser, F., Doherty, J., Ryan, C. and Mongan, J. (2012), A passive low-frequency seismic experiment in the Albertine Graben, Uganda. Geophysical Prospecting. doi: 10.1111/j.1365-2478.2012.01083.x

8. Davi+, R., G.S. O'Brien, L. De Barros, I. Lokmer, C.J. Bean, P. Lesage, M.M, Mora. 2011. Seismic source mechanisms of tremor events recorded on Arenal vocano, Costa Rica. J. Volc. Geotherm. Res. 213-214:1-13

7. Dupuy+, B., L. De Barros, S. Garambois, J. Virieux, 2011. Wave propagation in heterogeneous porous media formulated in the frequency-space domain using a discontinuous Galerkin method, Geophysics, **76**, N13-N21

6. De Barros, L., I. Lokmer, C. Bean, G. O'Brien, G. Saccorotti, J.-P. Métaxian, L. Zuccarello, and D. Patanè, 2011. Source Mechanism of Long Period events recorded by a high-density seismic network during the 2008 eruption on Mt Etna, J. Geophys. Res., 116, B01304, doi:10.1029/2010JB007629.

5. O'Brien, G. S., I. Lokmer, L. De Barros, C. J. Bean G. Saccorotti, J-P Métaxian and D. Patanè, 2011. Time Reverse Location of Seismic Long-Period events recorded on Mt Etna. *Geophys. J. Int.*, 184(1): 452-462

4. De Barros, L., M. Dietrich and B. Valette, 2010. Full waveform inversion of seismic waves reflected in a stratified porous medium. *Geophys. J. Int.*, 182(3):1543–1556.

3. De Barros, L., C.J. Bean, I. Lokmer, G. Saccorotti, L. Zuccarello, G. O'Brien, J.-P. Métaxian, and D. Patanè, 2009. Source geometry from exceptionally high-resolution long period event observations at Mt Etna during the 2008 eruption. *Geophys. Res. Lett.*, 36. doi : 10.1029/2009GL041273.

2. De Barros, L., and M. Dietrich, 2008. Perturbations of the seismic reflectivity of a fluid-saturated depth-dependent poroelastic medium. *J. Acoust. Soc. Am.*, 123(3):1409-1420.

1. De Barros, L., H. A. Pedersen, J.-P. Métaxian, C. Valdes-Gonzalez, and P. Lesage, 2008. Crustal structure below Popocatépetl Volcano (Mexico) from analysis of Rayleigh waves. *J. Volc. Geoth. Res.*, 170(1-2) :5-11.

- **Autres articles (Résumés étendus, proceedings, chapitres d'ouvrages):**

15. Cappa F., L. De Barros, N. Wynants-Morel+, Y. Guglielmi, J. Birkholzer, C. Nussbaum, 2019. From aseismic slip to seismicity during fluid injection controlled by interactions between stress perturbation, permeability increases and fault structure, *53rd U.S. Rock Mechanics/Geomechanics Symposium, 23-26 June, New York ARMA*, 2019

14. Henry P., Guglielmi Y., Gout C., Dick P., Donzé F., Tsopela A., Neyens D., De Barros L., Durand J., 2019. Strain and flow pathways in a shale fault zone: An in-situ test of fault seal integrity, *Fifth International Conference on Fault and Top Seals, EAGE*. doi: 10.3997/2214-4609.201902318

13. Duboeuf+, L., L. De Barros, F. Cappa, Y. Guglielmi, A. Deschamps. A controlled in-situ fault activation experiment at meter-scale shows that high-pressure fluid injections mostly drive aseismic motion, *79th EAGE conference and exhibition*, Paris, 2017

12. Nussbaum C., Y. Guglielmi, L. De Barros, J. Birkholzer, and F. Cappa, Imaging the long-term loss of faulted caprock integrity: in-situ experiments in the Mont Terri rock laboratory, Switzerland, in *EAGE/SEG Research Workshop 2017*, Trondheim, Norway, 2017

11. De Barros, L., Daniel, G., Guglielmi, Y., Rivet, D., Caron, H., Payre, X., ... & Gourlay, M., What Controls the Occurrence of Seismicity in Shale? Lessons Learned from a Meter-Scale Fluid-Injection Experiment. In *Sixth EAGE Workshop on Passive Seismic,* Dubai, 2016

10. De Barros, L., B. Dupuy+, G. O'Brien, J. Virieux, S. Garambois, 2011. Using a poroelastic theory to reconstruct subsurface properties: numerical investigation, in *Seismic Waves, Research and Analysis*, ed. Dr K. Masaki, Intech

9. Martini, F., I. Lokmer, K. Jonsdottir, C. Bean, F. Hauser, M. Möllhoff, L. De Barros, J. Doherty, C. Ryan, J. Mongan, 2011. A passive low frequency seismic experiment in the Albertine Graben: basin structure control?, *EAGE Third Passive Seismic Workshop "Actively Passive!"* 2011, Athens, Greece

8. Dupuy+, B., L. De Barros, S. Garambois, J. Virieux, 2010. Discontinuous Galerkin method in frequency-space domain for wave propagation in 2D heterogeneous porous media . In: *80th international meeting, Society of Exploration Geophysicists, Expanded Abstracts 29,* Houston, p3054-3059

7. De Barros, L., G. S. O'Brien, C. Bean, 2010. Assessing velocity and impedance changes due to CO_2 saturation using interferometry on repeated seismic sources. In *72th EAGE Conference & Exhibition, Expanded abstract, Barcelona,* P402, p., 4921-4925.

6. Dupuy+, B., L. De Barros, J. Virieux, S. Garambois, 2010. Discontinuous Galerkin method in frequency-space domain to simulate wave propagation in 2D heterogeneous porous media. In *72th EAGE Conference & Exhibition, Expanded abstract, Barcelona,* P106, p 4149-4153.

5. Dupuy+, B., L. De Barros, J. Virieux, S. Garambois, 2010. *W*ave propagation in 2D heterogeneous porous media: Discontinuous Galerkin method in (x,ω) domain, *proceedings of 2010 iDUST inter Disciplinary Underground Science and Technology Conference, Apt, France,* N020.

4. De Barros L., and M. Dietrich, 2009. Estimation of poroelastic parameters from seismograms using Biot theory. In *POROMECHANICS IV, Proceedings of the IV Biot Conference, DEStech Publications, Inc., PA, USA eds. The Fourth Biot Conference on Poromechanics Columbia University, New York*, pp. 540-546.

3. De Barros L., and M. Dietrich, 2008. Sensitivity and inversion of full seismic waveform in stratified porous media for CO2 storage application, i-DUST 2008 Conference papers, Apt, France

2. De Barros, L., and M. Dietrich, 2007. Full waveform inversion of shot gathers in terms of poro-elastic parameters. In *69th EAGE Conference & Exhibition, Expanded abstract, London*, Vol. 5, P277, pp. 3071-3075.

1. De Barros, L., and M. Dietrich, 2006. First-order perturbations of the seismic response of fluid-filled stratified poro elastic media. In *76th international meeting, Society of Exploration Geophysicists, Expanded Abstracts, New Orleans,* pp. 2250-2254.

- **Communications internationales (avec résumés):**

2019

71. Guglielmi Y., J. Birkholzer, F. Cappa, L. De Barros, C. Nussbaum and J. Rutqvist, 2019. How Diffusion rate can control Induced Seismicity: Insights from two Fault Activation Experiments, *AGU, San Francisco*

70. Chalumeau+ C., H. Agurto-Detzel, L. De Barros, P. Charvis, Y. Font, A. Rietbrock, et al., 2019. Repeating aftershocks of the 16th April 2016 Mw 7.8 Pedernales (Ecuador) earthquake underline the interplay between afterslip and seismicity, *AGU, San Francisco*

69. Sladen S., D. Rivet, J.-P. Ampuero, L. De Barros, Y. Hello, G Calbris, P. Lamare, 2019. Distributed sensing of earthquakes and ocean-solid Earth interactions analysis using the fiberoptic telecom seafloor cable KM3NET offshore Toulon, France, *AGU, San Francisco*

68. Rivet D., A. Sladen, J.-P. Ampuero, L. De Barros, Y. Hello et al., 2019. Distributed sensing of earthquakes and ocean-solid Earth interactions using two orthogonal fiber optic telecom seafloor cables, offshore Methoni, Greece.

AGU, San Francisco

67. Wynants-Morel**+**, N., F. Cappa, and L. De Barros, 2019. The influence of fault permeability evolution and stress state on injection-induced seismicity, EGU2019-7324, *EGU General Assembly*

66. Birkholzer, J. T., Guglielmi, Y., Nussbaum, C., De Barros, L. and Cappa, F., 2019. The 2015 Mesoscale fault slip experiment at Mont Terri: Main findings, lessons learned, and next steps. *GSA Annual Meeting in Phoenix, Arizona, USA - 2019*

65. De Barros, L., M. Baques**+**, M. Godano, A. Helmstteter, A. Deschamps, C. Larroque, F. Courboulex (2019) Fluid-Induced Swarms and Coseismic Stress Transfer: a Dual Process Highlighted in the Aftershock Sequence of the 7 April 2014 Earthquake (Ml 4.8, Ubaye, France), SISM@LP-Swarm, ISTerre, Grenoble (invited)

64. Chalumeau**+** C., H. Agurto-Detzel, L. De Barros, P. Charvis, Y. Font, A. Rietbrock, et aL., 2019. Repeating aftershocks of the 2016 Mw 7.8 Pedernales (Ecuador) earthquake highlight interactions between afterslip and seismicity. ISAG, Ecuador

2018

63. Nussbaum C., Y. Guglielmi, L. De Barros, F. Cappa, J. Birkholzer, P. Bossart, 2018, Aseismic and Seismic Reactivation of a Velocity-Strengthening Clay-Rich Fault Zone: Example of the MtTerri Main Fault FS Experiment, Swiss Geosciences Meeting, Bern

62. Birkholzer J. T., Y. Guglielmi, C. Nussbaum, L. De Barros, F. Cappa, 2018, Seismic Reactivation of a Velocity-Strengthening Clay-Rich Fault Zone: Are Laboratory Experiments a Good Enough Indicator of Field-Scale Behavior? AGU Fall Meeting, Washington, 2018

61. Guglielmi Y., De Barros L., Cappa F., L. Duboeuf**+**, 2018. Seismic/Aseismic budget and its prediction from in-situ injection experiments, AGU Fall Meeting, Washington, 2018

60. De Barros, L., F. Cappa, L. Duboeuf+, N. Wynants-Morel+, Y Guglielmi, and A Deschamps. Aseismic motions drive a sparse seismicity during fluid injections into a fractured zone in a carbonate reservoir, CMWR 2018, Saint-Malo

59. Lokmer, I., L. De Barros, and J. Thun, 2018. Can we invert for shallow long-period volcanic sources with significant amount of shearing? EGU, Vienna

58. Font, Y. et al., 2018, Aftershock distribution of the M_w=7.8 April 16, 2016 Pedernales Earthquake in Ecuador subduction: constraints from 3D earthquake location, *2018 Seismology of the Americas*, Miami, Florida

2017

57. Cappa F., Y. Guglielmi, L. De Barros, N. Wynants-Morel**+** and L. Duboeuf**+**, 2017. Seismic and aseismic fault slip in response to fluid injection observed during field experiments at meter scale, AGU Fall Meeting, New Orleans, 2017

56. Cappa F., L De Barros, L Duboeuf+, Y Guglielmi, A Deschamps and S Seguy, 2017. Aseismic motions drive a sparse seismicity during fluid injections into a fractured zone in a carbonate reservoir, AGU Fall Meeting, New Orleans, 2017

55. Guglielmi Y., C.Nussbaum, J Birkholzer, L De Barros, and F Cappa, 2017. Permeability evolution associated to creep and episodic slow slip of a fault affecting clay formations: Results from the FS fault activation experiment in Mt Terri (Switzerland). AGU Fall Meeting , New Orleans, 2017 (invited speaker)

54. Agurto--Detzel, H., Font, Y., Charvis, et al., 2017. Aftershock analysis of the 2016 Mw7.8 Pedernales (Ecuador) Earthquake: seismotectonics, seismicity distribution and relationship with coseismic slip distribution, AGU Fall Meeting , New Orleans, 2017

53. Y. Font, H. Agurto, A. Alvarado, M. Régnier, F. Rolandone, P. Charvis, P.A. Mothes, J.-M. Nocquet, P. Jarrin, et al., Aftershock distribution of the Mw=7.8 April 16, 2016 Pedernales Earthquake in Ecuador subduction: constraints from 3D earthquake location, AGU Fall Meeting, New Orleans, 2017

52. Tsopela A., Guglielmi Y., FV Donze, L. De Barros, P. Henry, R. Castilla, C. Gout, 2017. Field Injection Test in the Host Rock nearby a Fault Zone-Stress Determination and Fault Hydraulic Diffusivity, AGU Fall Meeting, New Orleans, 2017

51. Guglielmi Y., L. de Barros, P.Henry, C.Nussbaum, F.Cappa and J.Birkholzer, 2017, Exploring induced seismicity from mesoscale field experiments, 2nd induced seismsicity workshop, Davos (Switzerland). Invited speaker

50. Nussbaum C., Y. Guglielmi, L. De Barros, J. Birkholzer, F. Cappa, 2017, Aseismic fault slip and leakage preceding an earthquake induced during an in-situ fault reactivation experiment in the Opalinus Clay, Mont Terri rock laboratory, 2nd induced seismicity workshop, Davos (Switzerland).

49. De Barros, L. et al., 2017. Aseismic motions versus seismicity during fluid injection experiments into in-situ fractured zones, Earthquake summer school, Cargese

48. De Barros, L. et al., 2017. Seismic and aseismic deformation induced by fluid injection in shale: insights from controlled in-situ experiment, Earthquake summer school, Cargese

2016

47. Tsopela A., Y. Guglielmi, F V Donze, L De Barros, P Henry, R Castilla, C. Gout, 2016. Exploration of the role of permeability and effective stress transfer effects on Earthquakes Migration in a Fault Zone induced by a Fluid Injection in the nearby host rock: Experimental and Numerical Result. AGU Fall Meeting , San Francisco, 2016

46. Bletery, Q., A. M. Thomas, A. W. Rempel, L. Karlstrom, A. Sladen and L. De Barros, 2016. How fault geometry controls earthquake magnitude, AGU, 2016

45. Guglielmi Y., De Barros, L., C.Nussbaum, J. Birkholzer, and F. Cappa. First results of aseismic fault slip and leakage preceding an earthquake induced during an in situ fault reactivation experiment in shales (Mont Terri FS experiment, Switzerland), Geological Society of America, Denver (USA)

44. Guglielmi, Y., T. Daley, D.Rivet, L.De Barros, F. Cappa, P. Henry, Coupling downhole hydromechanical tests with active seismic monitoring to characterize stimulated deep sedimentary fractures systems, ARMA, June 2016 Houston (invited)

43. Duboeuf+ , L., L. De Barros, A. Deschamps, F. Cappa, Y. Guglielmi, 2016. Seismic and aseismic slip measured during a meter-scale fluid injection experiment into a fault, ESC, Trieste, Italy

2015

42.. Bean, C.J, I. Lokmer, L. De Barros, and P. Benson, 2015, Shallow Long Period (LP) Seismicity Controlled by Deformation of the Volcano Edifice, AGU, Fall meeting, S43F-01, invited.

41. De Barros, L., Rivet D., Daniel, G. Guglielmi, Y. et al., 2015. Lithology, stress or pressure control of the seismicity in shale? Insights from a controlled experiment of fluid-induced fault reactivation. AGU Fall meeting**,** S13B-2842:

40. Rivet D., De Barros L., Guglielmi Y. & Castilla R. Monitoring in situ deformation induced by a fluid injection in a fault zone in shale using seismic velocity changes, AGU Fall meeting, S13B-2841

2014

39. De Barros, L., B. Derode, Y. Guglielmi, and F. Cappa, 2014. Seismic responses to fluid pressure perturbations in a slipping fault. Earthquakes summer school, Cargese.

38. M. Zecevic+**,** L. De Barros, C. Bean, F. Brenguier, and A. Peltier, 2014, The temporal and spatial evolution of pre-eruptive seismicity on Piton de la Fournaise, La Réunion Island. EGU2014-7227, Vienna.

37. C.J. Bean**,** I. Lokmer, L. De Barros, and D. Amitrano, 2014, Controls on upper edifice rheology and consequences for seismicity-deformation relationship on volcanoes (invited), EGU2014-15399, Vienna**.**

2013

36. Manighetti, I, De Barros, L., Caulet+, C., Perin, C. Cappa, F, 2013, Deterministic, self-similar slip and stress heterogeneity on seismogenic faults, Abstract T53E-07, 2013 Fall Meeting, AGU, San Francisco, Calif.

35. T. S. Eyre+, Christopher J. Bean, L. De Barros, I. Lokmer, G. S. O'Brien, F. Martini, M. M. Mora, J. F. Pacheco, and G.J. Soto (2013). A new approach to investigating the source mechanism of long period seismic events recorded at Turrialba volcano, Costa Rica *56th Annual Irish Geological Research Meeting*

34. C. J. Bean, L. De Barros, I. Lokmer, G. O'Brien, 2013, What causes shallow short-duration low-frequency seismic events on volcanoes? 3P1_2A-O21, IAVCEI 2013 Scientific Assembly - July 20 - 24, Kagoshima, Japan

33. Bean, CJ; Lokmer, I; De Barros, L; Eyre+, TS; Metaxian, J-P (2013) Shallow Long Period (LP) seismicity as signatures of shallow edifice deformation at volcanoes *American Geophysical Union Fall Meeting (AGU)* San Francisco, California, USA

32. T. S. Eyre+, C. J. Bean, L. De Barros, I. Lokmer, G.S. O'Brien, F. Martini, M.M. Mora, J. F. Pacheco, and G.J. Soto (2013) New insights into the source mechanism of long period seismic events recorded at Turrialba volcano, Costa Rica *IAVCEI Scientific Assembly* Kagoshima, Japan,

31. Zecevic+, M., De Barros, L., Lokmer, I., Eyre, T.S., and Bean, C.J. (2013) A new double-difference location method for LP event families: the ability to image structures within volcanoes *IAVCEI 2013 Scientific Assembly* Kagoshima, Japan,

2012

30. Zecevic+, M., De Barros, L., O'Brien, G.S, Bean, C.J. and Brenguier, F. (2012) Investigating the Source Characteristics of a Family of Long Period Events Recorded on Piton de la Fournaise, La Réunion, Using Moment Tensor Inversion *EGU General Assembly 2012* 14,

29. Zecevic+, M., De Barros, L., O'Brien, G.S, Bean, C.J. and Brenguier, F.; (2012) Investigating the Source Mechanisms of a Family of Long Period (LP) Events Recorded on Piton de la Fournaise, La Réunion *55th Annual Irish Geological Research Meeting, UCC Cork*

28. TS Eyre+, CJ Bean, L De Barros, GS O'Brien, F Martini, MM Mora, JF Pacheco, GJ Soto; Comparing the source mechanisms of long period (LP) volcano-seismic events recorded in 2009 and 2011 at Turrialba volcano, Costa Rica, *Geophys. Res. Abs.,vol. 14,* EGU General Assembly, 2012

27. Zecevic+, M., De Barros, L., O'Brien, G.S, Bean, C.J., Brenguier, F. (2012) *Source Characteristics of a Family of Long Period Events Recorded During an Intrusive Phase on Piton de la Fournaise, La Réunion*. QUEST 3rd Workshop 2012, Tatranska Lomnica, Slovakia

26. Cauchie+ L., G Saccorotti, C Bean, L de Barros, Detailed analysis of amplitude and recurrence times of LP activity at Mt. Etna Volcano, Italy. EGU General Assembly Conference Abstracts, 2012

2011

25. Zuccarello L., M. Aliotta, A. Cannata, C. Cassisi, L. De Barros, G. Di Grazia, P. Montalto, D. PatanèSeismo-Volcanic Monitoring Techniques at Mt. Etna, Conference A. RITTMANN, Catania

24. Zecevic+, M., De Barros, L., O'Brien, G.S, Bean, C.J. and Brenguier, F. (2011) Investigating Source Mechanisms of LP Events Recorded on Piton de la Fournaise, La Réunion *Fall Meeting, AGU* San Francisco,

23. CJ Bean, I Lokmer, L De Barros, 2011, Rheological controls on upper edifice stress-strain relationships from low frequency seismicity swarms and seismic wave scattering, AGU Fall Meeting Abstracts 1, 08

22. Eyre+, T.S., Bean, C.J., De Barros, L.,O'Brien, G.S., Martini, F., Mora, M.M., Pacheco, J.F., Soto, G.J. (2011) Investigating the Source Mechanism of Long Period Volcano-Seismic Events Recorded in 2009 and 2011 at Turrialba Volcano, Costa Rica, *55th Irish Geological Research Meeting, Cork, Ireland.*

21. Zecevic+, L. De Barros, M., G. O'Brien, C.J. Bean, F. Brenguier, 2011. Investigating Source Mechanisms of LP Events Recorded on Piton de la Fournaise, La Réunion, V33B-2633, 2011 AGU Fall Meeting

20. Zecevic+, M., L. De Barros, G. O'Brien, C.J. Bean, F. Brenguier, 2011. Analysis of source characteristics of LP events at Piton de la Fournaise, La Reunion, *Geophys. Res. Abs.,vol. 13,* EGU General assembly 2011, *Vienna, Austria*

19. De Barros, L., F. Martini, C. J. Bean, A. García Yeguas, J. M. Ibáñez, 2011. Magmatic storage below Teide volcano from reflected and scattered seismic waves, *Geophys. Res. Abs.,vol. 13,* EGU General assembly 2011, *Vienna, Austria*

18. Zecevic+, M., De Barros, L., O'Brien, G.S, Bean, C.J., Brenguier, F.; (2011) Moment Tensor Inversion for Mechanisms of LP Events Recorded on Piton de la Fournaise, La Réunion. QUEST 2nd Workshop 2011, Hveragerdi, Iceland

17. Lokmer, I., G. O'Brien, L. De Barros, and C.J. Bean, 2011, Mapping of alternative long-period sources into moment-tensor solutions, *Geophys. Res. Abs.,*vol. 13, EGU General assembly 2011, Vienna, Austria

16. Bean, C. J., L. De Barros, I. Lokmer, G. S. O'Brien, 2011. Long Period events: An unreliable indicator of conduit processes? , *Geophys. Res. Abs.,*vol. 13, EGU General assembly 2011, Vienna, Austria *(oral)*.

2010

15. Bean, C. J., L. De Barros, I. Lokmer, G. S. O'Brien, 2010. Long Period (LP) seismic events without conduit resonance: Implications for near surface fluid transport models on volcanoes, *2010 AGU Fall Meeting*

14. O'Brien, G. S. , I. Lokmer, L. De Barros, C. J. Bean, G. Saccorotti, J. Métaxian, D. Patanè, 2010. Time Reverse Imaging of Long-Period on Mt Etna, *2010 AGU Fall Meeting*

13. De Barros, L., I. Lokmer, G. S. O'Brien and C. Bean, 2010. Source characteristics inversion of long-period (LP) events recorded by a dense broadband network on Mt Etna, *European Seismology commission, 32nd General Assembly* Montpellier, France

12. Lokmer, I. , G.S. O'Brien, L. De Barros, and C. Bean, 2010. High-resolution spatio-temporal source inversion of a long-period (LP) sequence recorded by a dense broadband network. *Geophys. Res. Abs., Vol. 12, EGU General Assembly 2010, Vienna, Austria*

11. Davi+, R., G.S. O.Brien, I. Lokmer, C.J. Bean, P. Lesage, L. De Barros, 2010. Moment tensor inversion of tremor events at Arenal Volcano (Costa Rica). *Geophys. Res. Abs., Vol. 12,* EGU2010-9216, *EGU General Assembly, Vienna, Austria.*

10. G.S. O'Brien, L. De Barros, C.J. Bean and I.Lokmer, 2010. Current research directions at UCD Geophysics on monitoring and verification of CO2 storage *Royal Irish Academy CCS Conference, Dublin, Ireland (invited)*

9. De Barros, L. , G. O'Brien, C. J. Bean (2010) Assessing velocity and impedance changes using interferometry on repeated seismic sources for time lapse monitoring of CO2 geological storage *53rd Irish Geological Research Meeting, Belfast, Northern Ireland, UK*

8. Zecevic, M., De Barros, L., O'Brien, G.S, Bean, C.J.; (2010) *Preliminary Analysis of LP Events at Piton de la Fournaise, La Réunion*. QUEST 1st Workshop 2010, Capo Caccia, Sardinia: Workshops

7. De Barros, L., I. Lokmer, C. J. Bean, G. S. O'Brien, G. Saccorotti, L. Zuccarello, J.-P. Métaxian, D. Patanè (2010) Source characteristics of Long Period events from high resolution observations at Mt Etna during the 2008 eruption *53rd Irish Geological Research Meeting, Belfast, Northern Ireland, UK*

2009 and before

6. De Barros, L., I. Lokmer, C. J. Bean, G. S. O'Brien, G. Saccorotti, L. Zuccarello, J.-P. Métaxian, D. Patanè, 2009. Source characteristics of Long Period events from high resolution observations at Mt Etna during the 2008 eruption, *2009 AGU Fall Meeting, San Francisco*.

5. Bean C. J. , G. O'Brien, L. De Barros, S. Murphy, I. Lokmer, G. Saccorotti, D. Patanè, J.-P. Métaxian, 2009. Constraining Volcano Source Rheology and Mechanisms: 3D Full Wavefield Simulations and Very High Resolution Observations From Mt Etna. *2009 AGU joint assembly Toronto, Ontario, Canada* (oral, invited).

4. De Barros, L., Bean, C.J., Zuccarello, L., Saccorotti, G., O'Brien, G., Lokmer, I., Metaxian, J.P., 2009. Elements of the plumbing system beneath Etna Volcano from localisation of long-period events recording by a high density network, *52nd Irish Geological Research Meeting, Trinity College Dublin, Dublin, Ireland*

3. O'Brien, G, L. De Barros, C. J. Bean, 2009. New developments in numerical tools for monitoring the seismic response of sub-surface fluids. *Griffith Geoscience Research Seminar, Dublin, Ireland*

2. De Barros, L., and M. Dietrich (2008) Sensitivity and inversion of full seismic waveform in stratified porous media for CO2 storage application, 2007. *2th Interdisciplinary Deep Underground Science and Technology Conference, Apt, France*

1. De Barros, L., P. Lesage, H. A. Pedersen, J.-P. Métaxian and C. Valdès-Gonzalez, 2006. Crustal structure below Popocatépetl Volcano (Mexico) from analysis of Rayleigh waves. *X international meeting `Volcan de Colima`, Colima, Mexico*.

- **Thèse de doctorat**

De Barros, L. Sensibilité et inversion des formes d'ondes sismiques en milieu poreux stratifié. PhD thesis, Université J. Fourier, Grenoble, 2007 (tel.archives-ouvertes.fr/tel-00204917/).

Note: + *denotes PhD students I was involved in the supervision.*